Mathematical modelling of the formation of gold nanoparticles via the citrate synthesis method

Emmanuel Gbenga Agunloye

Department of Chemical Engineering

University College London

A thesis submitted for the degree of

Doctor of Philosophy of University College London

September 2018

I, Emmanuel Agunloye, confirm that the work presented in this thesis is my own. Where information has been derived from other sources, I confirm that this has been indicated in the thesis.

_____

Signature

_____

Date

To Jesus Christ, my Saviour

Abstract

This work presents a new model for predicting the evolution of the size of gold nanoparticles (GNPs) in the citrate synthesis method. In this method, the precursor is an acid solution of tetrachloroauric acid, while the reducing agent is a base solution of sodium citrate. The acid-base properties of the solutions influence how the size of the particles evolves during the synthesis. In the literature, various mechanistic theories have been proposed to explain this evolution. Turkevich et al. (1951), who pioneered this synthesis method, suggested the "organizer theory" also known as "nucleation-growth" mechanism. Recently, however, Wuithschick et al. (2015) proposed a "seed-mediated" mechanism, a nucleation-aggregation-growth mechanism. In investigating the synthesis, while Turkevich et al. (1951) used the conventional techniques such as the transmission electron microscopy (TEM), the scanning electron microscopy (SEM) and the UV-vis spectroscopy, Wuithschick et al. (2010) used a combination of X-ray absorption near edge spectroscopy (XANES) and small angle X-ray scattering (SAXS) along with the conventional techniques. This setup provides time-resolved in situ information on the formation of GNPs, thereby yielding reliable accounts of the synthesis mechanism. Nevertheless, only one mathematical model has been developed, that advanced by Kumar et al. (2007), which is based on the nucleation-growth theory proposed by Turkevich et al. (1951). This model had not been thoroughly tested.

In a part of this work, we investigate the model of Kumar et al. (2007) for different conditions of pH, temperature and initial reactant concentrations. To solve the model, we use the numerical code Parsival, which is developed for solving population balance equations. We test the model for different synthesis conditions studied experimentally by various researchers, for which experimental data are available in the literature. The model poorly predicts these data, because the Turkevich organizer theory does not account for the acid-base properties of chloroauric acid and sodium citrate.

Thereafter, we present a novel kinetic model based on the synthesis seed-mediated mechanistic description proposed by Wuithschick et al. (2015). In this description, the precursor concurrently reduces into gold atoms and hydroxylates into a passive form. The gold atoms then aggregate into seed particles, which finally react with the passive form of the precursor in a growth step. We validate the model using experimental data from the literature obtained for conditions in which the seed-mediated mechanism is valid. The predicted GNP final sizes closely agree with those obtained experimentally.

Finally, we present a modelling approach for the aggregation process in metal nanoparticles syntheses based on the theory proposed by Polte (2015). In this theory, metal atoms formed by reducing the precursor solution aggregate to larger sizes due to the Van der Waals' forces of attraction. Then, due to the electrostatic forces of repulsion induced by the "potential determining" ions, the nanoparticles eventually stop aggregating and become stabilized. Based on this theory, we develop a model for the aggregation process resulting from the interplay of the attractive and repulsive forces in the evolution of nanoparticles. Using this model, we describe how gold atoms aggregate into seed particle in the citrate synthesis method. Then, we couple this aggregation model with the model developed for the seed-mediated mechanism. To validate the model predictions, we employ the experimental data used to validate the seed-mediated mechanism. In addition to the GNP final sizes, this integrated model correctly predicts the size polydispersity and completely describes the final GNP particle size distribution.

Impact statement

Nanotechnology is one of the most important fields in contemporary and future science for research and development. It involves synthesizing, modifying, and applying nanoparticles. Because of its unique characteristics, gold nanoparticles are one of the most applied nanoparticles. In producing gold nanoparticles, researchers and industrialists employ the citrate synthesis method because it is cheap, simple and environmentally-friendly. However, like other nanoparticles syntheses, this synthesis method is poorly understood. Thus, it cannot be controlled or optimised, thereby undermining quality and profitability.

Modelling nanoparticles syntheses would help in improving quality and profitability. Since the beginning of nanotechnology 50 years ago, few contributions have been made in modelling nanoparticles syntheses. In the citrate synthesis method, for example, only a model developed for a batch reactor is available. In this Ph.D. work, we even found that this only model fails in describing the synthesis, creating a research gap.

Before reaching this conclusion, we thoroughly investigated and tested the model. To do so, we implemented the model in the commercial numerical code Parsival (this required altering the code considerably and was not a simple task), validated the results against experimental data, and critically discussed the model performance. We found out that this model failed to describe the synthesis satisfactorily. This work has been published in the international peer-reviewed journal Chemical Engineering Science.

Following the above findings and conducting extensive literature review, we developed a novel model for the citrate synthesis method. Then, we implemented and validated the results against experimental data. Our model excellently describes the synthesis. This work has also been published in the international peer-reviewed journal Chemical Engineering Science.

Furthermore, we developed a model for the aggregation process, a process that is common to most nanoparticles and in general, nanotechnology. We investigated the model in the citrate synthesis method. Then, we implemented and validated the results against experimental data. The aggregation model performs well.

In the near future and beyond, this Ph.D. work is therefore expected to make a great impact in the field of nanotechnology. The model can be used to investigate and control processes as well as design and optimise reactors in nanoparticle synthesis.

Publications

Journal articles:

1. Agunloye, E., Panariello, L., Gavriilidis, A., Mazzei, L., 2018, A Model for the Formation of Gold Nanoparticles in the Citrate Method, Chemical Engineering Science, *Chemical Engineering Science, 191*, 318-331. doi:10.1016/j.ces.2018.06.046
2. Agunloye, E., Gavriilidis, A., & Mazzei, L., 2017. A mathematical investigation of the Turkevich organizer theory in the citrate method for the synthesis of gold nanoparticles. *Chemical Engineering Science, 173*, 275-286. doi:10.1016/j.ces.2017.0

Conference articles:

3. Agunloye, E., Gavriilidis, A., & Mazzei, L., 2017. A mathematical investigation of the Turkevich organizer theory in the citrate method for the synthesis of gold nanoparticles. *19th International Conference on Nanoparticles*.

Conference presentations:

4. Agunloye, E., Gavriilidis, A., & Mazzei, L., 2018. *A model for the evolution of gold nanoparticles synthesised by the citrate method*. Presented at: III International Symposium on Nanoparticles/Nanomaterials and Applications.
5. Agunloye, E., Gavriilidis, A., & Mazzei, L., 2017. *Modelling investigation of gold nanoparticles formation in the citrate method*. Presented at: UK Colloids.

Acknowledgements

First and foremost, I would like to thank God for the successful completion of this thesis. He gave me inspiration, wisdom, health, and life to pursue this project to a conclusive end. I could fill entire pages in thanking Him as He deserves much more.

I would like to thank Dr. Luca Mazzei for his supervision. Having admired his teaching style during my M.Sc. programme, I was convinced he would be the right supervisor for my Ph.D. programme. Yes, the programme came with enormous challenges in both hard and soft skills. Nevertheless, he trained me to simplify the challenges. Sometimes, Luca and I had heated discussions. However, from these discussions, I derived my most valuable training.

I would like to thank Professor Asterios Gavriliidis for his criticisms, which I absorbed in good fate. He was my examiner-in-chief. I appreciate also the platform of his group – MAFUMA – for the meetings. In one of those meetings, Prof. Ivan Parkin (Dean of Science, and former head, Department of Chemistry, UCL) and Prof. Thanh Nguyen (Biophysics Group, Department of Physics & Astronomy, UCL), after listening to the scope of my project, exclaimed that the work was impossible – considering the intricacy of the citrate synthesis method. This same position was expressed by Dr. Jörg Polte, Department of Chemistry, Humboldt-Universität zu Berlin. In the end, however, God made it possible.

I would also like to thank Dr. Michael Wulkow, managing director of Computing in Technology GmbH (CiT), the company that developed the numerical code Parsival, for his support and the stimulating discussions.

I would want to appreciate the Nigerian government via the Petroleum Technology Development Fund and National Universities Commission, for funding my Ph.D. and M.Sc. programmes. Without this funding, my postgraduate degrees would not materialize.

These acknowledgements would be incomplete without mentioning the emotional support I enjoyed from Sadeoluwa Obikoya. This support made me less distracted in the course of the programme.

I must also mention the Redeemed Christian Church of God, Winners' Temple and her entire members, for providing me a religious and social place.

And in Nigeria, I appreciate the members of the Redemption Rights Christian Mission, for their prayers and steadfastness.

I would like to thank the many individuals that prayed for me and still do: My mum (Mrs Margaret Agunloye), Pastor Wole Oludipe, Pastor Rotimi Tenabe, my adopted parents

(Elder Ezekiel and Mrs Olabisi Ogundare) and the list goes on. I appreciate the contributions of my elder brothers: Jacob Agunloye, and David Agunloye. They both taught me mathematics at a tender age, before I clocked age ten. I still remember those days.

My experience at Birch Freeman High School, Mushin, Lagos State, Nigeria, taught me that with God all things are possible.

Finally, and once again, to the Alpha and Omega, the beginning and ending, the first and last, the Almighty God and Saviour Jesus Christ, I give all thanks.

Table of Contents

Chapter 1

General introduction

In this chapter, we introduce nanotechnology, and its significance. We also introduce the current research in nanotechnology. Thereafter, we introduce the objectives of this PhD study. Finally, we report the structure of the thesis.

1.1 Introduction to nanotechnology and its significance

Nanotechnology is a technology that explores materials with sizes in the range 1 – 100 nm for various applications (Liveri, 2006). It involves the synthesis of these materials, called nanoparticles, then their modification (or functionalization) and finally their application. It can be traced to the Roman Empire in the 4th Century AD. Artefacts from this period show glass cups plated with gold nanoparticles. Depending on its interaction with light, this plating induced different colours on the cup; red for absorbed light and green for reflected light (Leonhardt, 2007). One of the early laboratory investigations in nanotechnology was conducted in the 1850s by Michael Faraday (Faraday, 1857). In his work, Faraday inadvertently synthesized a ruby red solution of gold nanoparticles by reducing a solution of gold chloride with phosphorus. Notice that the colour of this solution is different from the bright yellow of bulk gold. Furthermore, more than 150 years after, the solution of gold nanoparticles synthesized by Faraday and kept at the Royal Institution in London remains ruby red and stable (Anonymous author @Royal Institution, 2014). Because of the difference in the properties of nanoparticles from those of the bulk material and their stability, nanotechnology offers a novel way of producing materials with selected physico-chemical properties that can be exploited in different applications.

Intrigued by the prospect of nanotechnology, at an American Physical Society meeting in 1959, Richard Feyman delivered a lecture titled: “There’s Plenty of Room at the Bottom”. As substances become smaller, they exhibit properties and functionalities different from those of the same material in the bulk state as well as from those of isolated atoms and molecules. This lecture, widely applauded by the audience, stimulated further research in nanotechnology (Feyman, 1959; Majumder et al., 2007). This research has been helped by three important things: the awareness of nanotechnology through conferences (such as those organised by the Foresight Institute of the USA), inventions of powerful techniques to

probe materials at the nano level (such as the scanning tunnelling microscope (STM) invented by Gerd Binning and Heinrich Rohrer of the IBM) and recognition of the work in nanotechnology (such as the Nobel prizes in Physics awarded to the inventors of STM in 1986, the Nobel prize in Chemistry awarded to the trio of Harry Kroto, Richard Smalley and Robert Curl in 1996, for discovering fullerene, and the Nobel Prize in Physics awarded to the duo of Andre Geim and Konstantin Novoselov in 2010, for discovering graphene).

Today, various consumer products come from nanotechnology. From the work of Vance et al. (2015) on data collection of the consumer product inventory in 24 countries in 2014, 1814 consumer products come from nanotechnology, up from only 54 consumer products in 2005. More than 40% of these products find applications in health care; the remaining 60% find applications in home and garden, electronics and computers, food and beverage, automotive, appliances and products for children. In the US, the worth of these products is estimated to be over $32 B. See Figure 1.1 for the pie chart on the applications of nanotechnology.

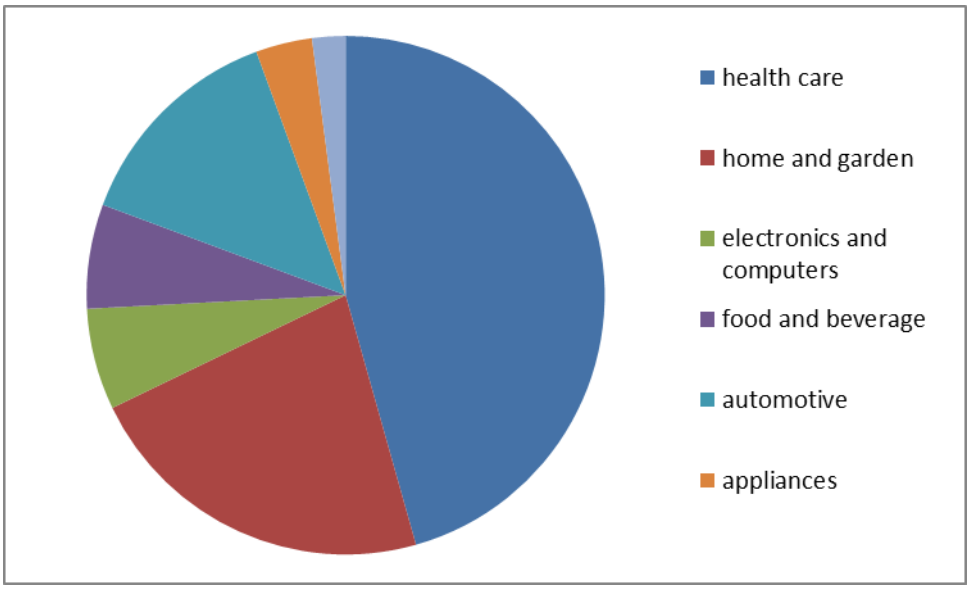

Figure 1.1 A pie chart showing the applications of nanotechnology in consumer products. Data from Vance et al. (2015).

Vance et al. (2015) further classified these products according to the type of nanoparticles used in them. Out of the inventory of products, however, Vance et al. reported information of the type of nanoparticles for only 51% of the products. The companies did not provide the type of nanoparticles used in the remaining 49% of the products. Out of the 51% consumer products (i.e. 923 out of 1814), consumer products from metal nanoparticles account for more than 70%; those from carbon, silicon and other nanoparticles account for the remaining

30%. Figure 1.2 shows the classification of the consumer products based on the nanoparticle type.

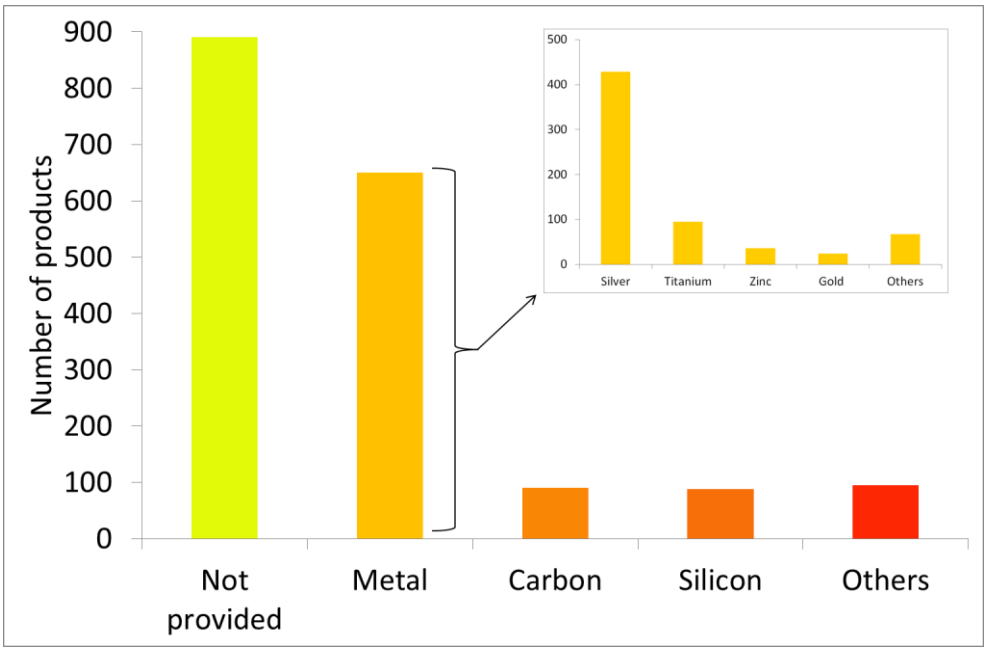

Figure 1.2 The classification of 1814 consumer products based on the nanoparticle type (49% of the consumer products do not present the composition or a detailed description of the type of nanoparticles). Data from Vance et al. (2015).

As shown, silver nanoparticles are the most frequently used nanoparticles. Apart from silver nanoparticles, the order of the most frequently used metal nanoparticles is titanium, zinc and gold. Notice that silver and gold belong to the same group in the periodic table called noble metals. Thus, bulk silver and gold may be interchanged. However, at the scale of nanoparticles, considering the difference in properties from the bulk, one needs research to justify interchanging silver and gold nanoparticles.

1.2 Current research in nanotechnology

Nanotechnology is one of the research areas identified by the US department of Commerce and the National Science Foundation as of national priority; others are biotechnology, information technology and cognitive science (Roco and Bairnbridge, 2002, Gutierrez, 2005). Nanotechnology through the National Nanotechnology Initiative, an initiative established in 2000 by the US government, to advance research and development in nanotechnology, received nearly $10 billion between 2000 and 2009 (Porter and Youtie, 2009). Thereafter, its yearly budget allocation increased. For example, in 2012 it received $3.7 billion (ANUI, 2012). Other developed countries are also investing in nanotechnology. Also in 2012, the European Union invested $1.2 billion, and Japan invested $750 million (ANUI, 2012). In

2015, the European Union through the European Physical Science Research Council awarded a £2.5M research grant to develop manufacturing technologies for the synthesis of nanoparticles for use in healthcare related applications (for example, antimicrobial materials, diagnostics, and cancer hyperthermia). This research, led by the Department of Chemical Engineering, University College London, comprises experts from the academia and industry. Other applications include catalysis, electronics and energy.

Recent studies have focused on the toxicity of nanoparticles on life. For example, Vazquez-Muñoz et al. (2017) investigated the effect of silver nanoparticles on various organisms for the lethal concentrations. In humans, Vazquez-Muñoz et al. found out that the lethal concentration of silver nanoparticles is $10\ \mu g/ml$. In another research study, Yah (2013) also investigated the effect of gold nanoparticles on humans. At a concentration of $450\ \mu g/ml$, he reported that gold nanoparticles are nontoxic. Furthermore, Giassudin et al. (2012) reported gold nanoparticles as nontoxic. Thus, in this work, we focus on gold nanoparticles as better substitutes than silver nanoparticles for health care related applications.

Gold nanoparticles (GNPs) have applications in many fields. In biomedicine, for example, they are used in cancer diagnosis and biological imaging. GNPs demonstrate excellent catalytic properties and high conductivity, which can be tuned by particle size, surface functionality, intraparticle separation and are influenced by the chemical environment. Such properties are exploited in various electrochemical and electrocatalytic sensors. These optical, optoelectronic, electrochemical and electrocatalytic properties are utilised for detection of biomolecules such as proteins, DNA, oligonucleotides, pathogens but also whole cancer cells which are important for healthcare applications (Yang et al., 2015; Dreaden et al., 2012; Zheng et al., 2014; Lane et al., 2015; Matias et al., 2017; Zhou et al., 2015). Even though bulk gold is inert, in the form of nanoparticles it displays high catalytic activity for a variety of reactions. These include oxidations of olefins, alcohols and alkanes, hydrogenations, and aminations (Corma and Garcia, 2008; Daniel and Astruc, 2004; Stratakis and Garcia, 2012). Geometrical properties, such as size and shape, determine how GNPs perform. When the size of Au nanoparticles approaches the Fermi wavelength of electrons (<2nm), molecule-like optical properties and size-dependent fluorescence appear (Zhou et al., 2015; Yang et al., 2015). Large GNPs have a longer electromagnetic field decay length, and provide higher sensitivity; hence, they are more efficient at enhancing Raman signals (Yang et al., 2015). For GNPs used in catalysis, size influences their performance. Catalytic activity of GNPs typically increases substantially as size decreases below 5 nm (e.g. CO oxidation). However, selectivity to desired products can increase or decrease with nanoparticle size, depending on the particular reaction (Hvolbæk et al., 2007; Hashmi and Hutchings, 2006).

Spherical GNPs with sizes from 10 to 150 nm can be produced via a synthetic route known as *the citrate method*. Many authors have explored this method for different applications and have investigated how the nanoparticles form when the precursor (a tetrachloroauric acid solution) reacts with the reducing agent (a trisodium citrate solution). However, the GNPs produced are usually polydisperse and irreproducible. Sometimes, the polydispersity (also known as the coefficient of variation – the ratio of standard deviation to the mean size – of the particle size distribution) can be ~ 40% (Ji et al., 2007), therefore undermining product quality.

Hypothetically, one can imagine that the synthesis involves mass transfer by mixing, reduction of the precursor by citrate, nucleation, growth, aggregation, and possibly breakage (Liveri, 2006; Pong et al., 2007; Ji et al., 2007). Ji et al. (2007) proposed two mechanisms, which can occur depending on the pH of the solution (dictated by the composition of the reagents). At low pH (i.e. a pH value in the range 3.0 – 6.5 when measured at 25^0 C), the dominant mechanism, after the reactions have taken place, is nucleation, aggregation, and intraparticle ripening, while at high pH (i.e. a pH value in the range 6.5 – 8.0 when measured at 25^0 C) it is nucleation and growth. The former is similar to the nucleation-aggregation-growth mechanism, which is gaining popularity, especially after the work by Polte et al. (2010) was published. In their work, these researchers used small angle X-ray scattering (SAXS) and X-ray absorption near-edge spectroscopy (XANES) to study the synthesis experimentally. They claimed that the number of particles reduces in the synthesis, which suggests aggregation; they thus advanced a nucleation-aggregation-growth mechanism. Conversely, the pioneering work of Turkevich et al. (1951) supported the second mechanism (nucleation-growth), and this is why this mechanism is also referred to as the Turkevich organizer theory. A mathematical model for the GNPs synthesis would help considerably to test these theories, and in particular whether only one mechanism really exists or more than one is possible depending on the solution pH. A model would also assist to design and optimise the reactors for the nanoparticle synthesis.

Kumar et al. (2007) developed such a model, basing it on the Turkevich organizer theory. In the model, the presence of dicarboxy acetone (DCA), which is formed during the synthesis, causes nucleation. However, according to the model, DCA decomposes in the presence of GNPs, and therefore eventually the nucleation process stops. The model involves material balance equations (for all reactants) and a population balance equation (for the nanoparticles), and assumes that the system is perfectly mixed. The material balance equations account for the reactions, while the population balance equation accounts for nucleation, growth and aggregation. Kumar et al. (2007) included aggregation so as to reflect the observation by Chow and Zukoski (1994) that particles aggregate when the

concentration of the precursor is very high. The assumptions of this model have been criticised (Doyen et al., 2010; Wuithschick et al., 2015). Gammon et al. (1997) proposed a nucleation step that does not require DCA. Doyen et al. (2010) confirmed that the amount of DCA, detected with the nuclei magnetic resonance, is insignificant and cannot cause nucleation. Wuithschick et al. (2015) reported that DCA does not promote nucleation. Also, the model does not account for the role played by the pH. It is important to further test the model of Kumar et al. (2007) and develop another mathematical model based on the nucleation-aggregation-growth mechanism.

1.3 Research objectives and questions

We aim to develop a robust mathematical model for the citrate synthesis method of gold nanoparticles able to describe the experimental observations reported in the literature and to correctly predict both the mean particle size and the particle size distribution of GNPs. We will develop a model based on the work of Polte et al (2010) (this work was later refined by Wuithschick et al. (2015)) assuming perfect mixing. We will start with perfect mixing because, modelling-wise, it is reasonable to start simple. Also, this synthesis is usually carried out in a batch system where perfect mixing is assumed. However, in reality, fluid dynamics affect the process. The developed model for perfect mixing can then be integrated with fluid dynamics. In this thesis, however, we will not do so. Therefore, we pursue the following objectives:

1. We intend to test the model developed by Kumar et al. (2007) for different conditions to see whether it is accurate, and whether the theory, on which it is based, is always applicable.
2. We will develop a model for the seed-mediated mechanism proposed by Wuithschick et al. (2015). At first, we will be using an approximate expression to model the aggregation process while we use reaction steps to model the nucleation and growth processes. Similarly, we will implement and test the model for different conditions.
3. Subsequently, we will develop a rigorous model for aggregation from the surface energy and surface charge of particles. The model will be a function of both the size of particles and the concentration of ions.

1.4 Structure of the thesis

In this thesis, we report how these outlined objectives have been achieved. To start with, we review the literature in Chapter 2. We review experimental investigations of the citrate synthesis method. From these investigations, we focus on the best mathematical approach

to model the synthesis. We also review how to solve the model before reporting past attempts in modelling the synthesis.

In Chapter 3, we test the Turkevich organizer theory by investigating the model of Kumar et al. (2007). We first review the model and then we test it under new conditions, by comparing its predictions to experimental data available in the literature. In testing the model, we consider factors such as the initial concentrations of the precursor and reducing agent, the initial and final pH of the reaction solution, and the temperature of the latter.

In Chapter 4, we briefly present the seed-mediated mechanism. Then, we report the reactions that occur in the synthesis according to this mechanism, their corresponding rate-order equations and the balance equations for the components. Finally, we present the solutions of the model and discuss the results.

In Chapter 5, we present a new aggregation model. Then, we employ the citrate synthesis as a case study for this aggregation model. This model comprises sub-models for reactions, gold atoms formation, aggregation and growth. Finally, we present the solutions of the model and discuss the results.

In Chapter 6, we report the conclusions of this PhD research and future work.

Chapter 2

Literature review

In this chapter, we review the literature from four perspectives. First, we review the experimental synthesis of gold nanoparticles with the focus on the citrate synthesis method of forming gold nanoparticles (GNPs) and its peculiar characteristics. As one of these characteristics, the synthesis solution involves multiple phases: continuous and discontinuous phases. Second, we review the mathematical framework that can handle these peculiar characteristics of the synthesis method. Third, we review briefly solution methods for the mathematical model. Finally, we review past work on modelling nanoparticle syntheses.

2.1 Experimental synthesis of gold nanoparticles

In the following, we discuss the significance of gold nanoparticles, and briefly introduce their synthesis methods. Then, we focus on the citrate synthesis method and its past experimental investigations. These investigations translated into various mechanistic descriptions of the synthesis. We then review these mechanistic descriptions.

2.1.1 Gold nanoparticles

Gold is present naturally in Earth's crust, having a relative abundance of 0.004 part per million (ppm). In the periodic table of elements, gold belongs to group 11 and period 6, corresponding to an atomic number of 79 with the electronic structure $[Xe]5d^{10}6s^{1}$ (Gimeno, 2008). The elements above gold in group 11 are copper and silver in periods 4 and 5 respectively. While period 3 comprises the first set of the transition metals, period 6 comprises the first set of the inner transition metals, called the lanthanides. Due to this electronic structure, gold is one of the least reactive metals, a property that explains why it occurs in its element form in bulk. This electronic structure also explains other interesting properties of gold: bright-colour, malleability, and ductility. These properties make gold useful as jewellery and investments. Although gold does not react under normal conditions, it reacts in an aqueous solution of highly oxidising hydrochloric and trioxonitrate acids, to produce tetrachloroauric acid. Gold can also react under other extreme conditions to produce substances such as gold (III) fluoride, gold (III) sulphide and other derived compounds from gold (Hanes et al., 1992). In spite of the applications of gold in bulk, many

more applications have continued to emerge for it at the nano level, where particle sizes range from 1 to 100 nm.

GNPs display many interesting characteristics such as colorimetry and reactivity. While bulk gold is bright yellow, GNPs display almost all the colours in the visible light from red to violet, depending on the size of the particles. GNPs with sizes 16, 25 and 147 nm are orange, red and violet, respectively (Frens, 1973). Because of these optical properties, GNPs linked with proteins find applications in biosensing. For example, GNPs linked by oligonucleotides provoke a red-to-blue colour change that is useful for DNA-sensing (Daniel and Astruc, 2004). In terms of its toxicity, GNPs linked with some proteins such as lysine are considerably non-toxic for biomedical applications (Alkilany and Murphy, 2010).

Being a relatively unreactive transition metal, GNPs also have applications in catalysis. The d-orbital electrons in gold interact with reacting species, to promote electron transfer during chemical reactions. Haruta et al. reported in 1989 that GNPs supported on Co_3O_4, Fe_2O_3, or TiO_2 were highly active catalysts, under high dispersion, for CO and H_2 oxidation, NO reduction, water-gas shift reaction, CO_2 hydrogenation, and catalytic combustion of methanol. Catalysis with GNPs (Huang et al., 2018), in particular the very active oxide-supported ones, is now an expanding area, and a large number of new catalytic systems for various reactions are now being explored. Other applications of GNPs include electronics, photodynamic therapy and therapeutic agent delivery.

In meeting these growing applications, GNPs can be synthesized by different methods, classified as top-down and bottom-up approaches (Liveri, 2006). In the top-down approach, bulk gold can be ground in a ball mill. Then, the resulting particles are air classified to recover nanoparticles. This method is not cheap and quick to manufacture GNPs; hence, it is not suitable for large scale production. For nanoparticles used in electronic applications, such as Si nanoparticles, the most widely used top-down method is lithography (Urban et al., 2010). In this method, a structured photo-resist layer, called the master template, partially embeds bulk Si. Under focused light, the exposed Si etches out to form Si nanoparticles. While milling can produce nanoparticles of size 100 nm, lithography can produce nanoparticles of size 20 nm. Nevertheless, lithography suffers from the same disadvantages as milling. Methods such as milling and lithography are also classified as solid-phase synthesis of nanoparticles.

In the bottom-up approach, nanoparticles form from sub-size particles such as atoms and molecules. Many gas and liquid-phase synthesis methods fall under this approach. In a typical gas-phase method, for example, bulk material evaporates in thermal plasma, which operates at 10, 000 K (Boulos, 1991). Then, nanoparticles form while cooling. This method

involves a top-down approach when breaking the bulk material to atoms in the plasma and a bottom-up approach when fusing the atoms to form nanoparticles during the cooling process. Inert-gas condensation operates similarly to the thermal plasma: bulk material vaporises in a vacuum chamber and then cools in an inert gas stream to produce gold nanoparticles (Belloni et al., 1998). With the gas-phase methods, nanoparticles of sizes 20 – 100 nm can be produced. However, like the solid-phase methods, these methods require a lot of energy.

Liquid-phase methods offer a one-stop panacea to the synthesis of nanoparticles in general and GNPs in particular. They are simple and cheap. They can also produce nanoparticles of sizes 1 – 200nm, which can be easily functionalised for potential applications. These methods involve many techniques in tuning the nanoparticles size, form and geometry. These many techniques are however mostly carried out in a colloidal system.

2.1.2 Colloidal systems

A homogeneous solution is formed when two or more substances exist together in a single phase. The molecules of the substances mix completely in one another. For example, the water-NaCl system forms a homogeneous solution. Conversely, some substances (e.g., polymers) are made up of macromolecules which do not dissolve, consequently forming a heterogeneous solution (each macromolecule can be identified with a microscope of sufficient resolution). These water-polymer systems are called colloids. To an unaided eye, these systems appear to be homogeneous, but at the microscale their heterogeneity becomes glaring. Hence, colloidal systems are also called micro-heterogeneous systems. Some systems are heterogeneous even to an unaided eye; these systems are called suspensions (Brady and Senese, 2004).

Colloidal systems are used in the synthesis of many nanoparticles; their advantages include safety, cost effectiveness and low energy requirement. The polymers for the synthesis are referred to as surfactants. These form cavities in which nanoparticles can form. They can assume various arrangements and can perform many functions, and are consequently used in diverse applications in nanotechnology.

A simple surfactant comprises a functional group head (the polar part) and an alkyl tail (the apolar part). The polar part dissolves in a polar medium while the apolar part dissoves in an apolar medium. This property makes surfactants assume various arrangements such as a film or a micelle of surfactant molecules. Figure 2.1.1 shows a typical surfactant (dodecanethiol) and a possible arrangement on a polar surface.

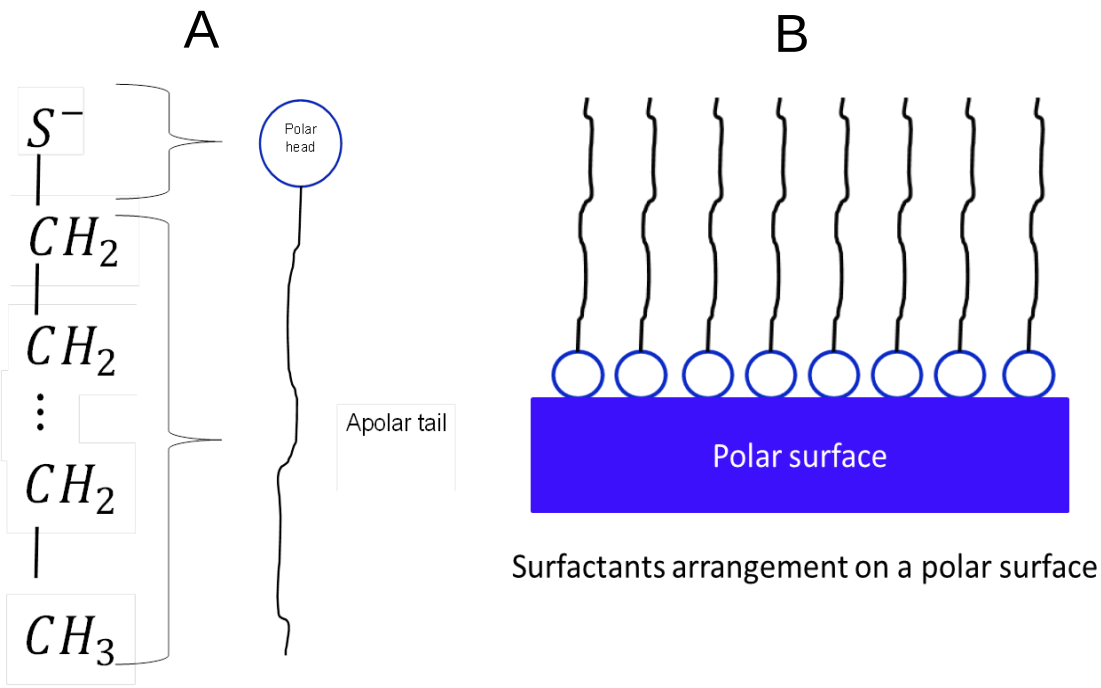

Figure 2.1.1: The structure and arrangement of dodecanethiol on a polar surface. A: Showing the skeletal structure of dodecanethiol having a polar head and an apolar tail; B: Showing a film arrangement of dodecanethiol on a polar surface.

The arrangement of surfactant molecules can either be formed before nucleation of nanoparticles in the reaction medium (Cushing et al. 2004, Liveri 2006) or in-situ along with nucleation (Cushing et al. 2004).

- **Before nucleation**. The configuration of surfactant molecules is formed before nucleation takes place. The produced molecules of the nanoparticles come together inside the structure formed by the surfactant molecules and therein nucleate. Surfactants in this case act as an 'organizer', as proposed by Turkevich et al. (1951). The nucleus starts growing and can only reach the space available in the cavity of the surfactants, becoming stabilized (Figure 2.1.2). The surfactants do not react in the course of the synthesis. An example is the Brust-Schiffrin method, in which dodecanethiol acts as the surfactant (Brust et al., 1994).

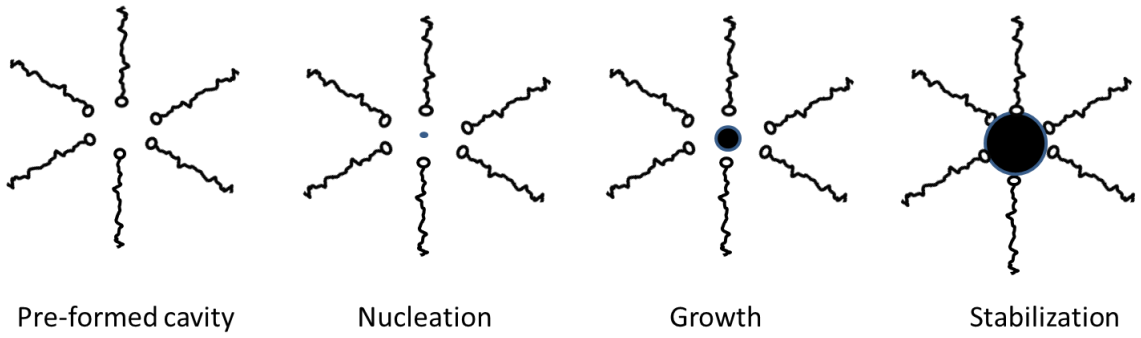

Figure 2.1.2: Showing how a nanoparticle forms, grows, and stabilizes in a pre-formed cavity.

- **In-situ**. In this case, the nucleus is formed and starts growing while the surfactants remain randomly distributed. After a while, the surfactants reach the surface of the growing nanoparticles, either by adsorption or by complexation, forming a cavity that prevents further growth of the nanoparticles. The latter are therefore stabilized. This mechanism is shown in Figure 2.1.3.

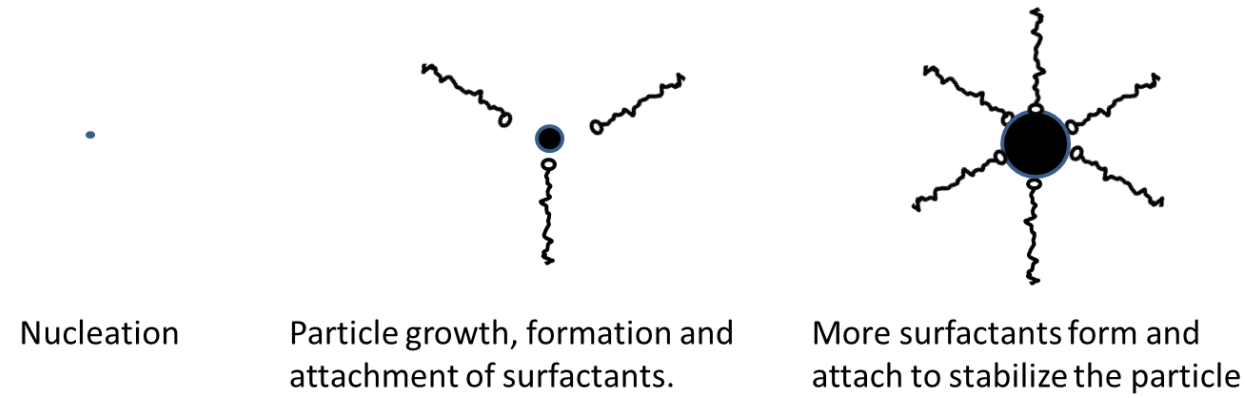

Figure 2.1.3: Showing how a nanoparticle grows and the surfactants become attached to stabilize it.

In this mechanism, the surfactants are produced in the course of the synthesis. After they are formed, they attach and stabilize the particles. An example is the citrate synthesis method. In this method, citrate, which is a reactant, or any of its derivatives, which are formed in the course of the synthesis, acts as a surfactant, and stabilizes GNPs. This synthesis is the focus of this research project. Below, we review the synthesis in detail.

2.1.3 Citrate synthesis method

The citrate synthesis method is commonly used to produce GNPs (Kumar et al., 2007). Upon reacting tetrachloroauric acid with sodium citrate in an aqueous solution, Hauser and Lynn (1940) reported the synthesis as a synthetic route of producing GNPs. In this synthesis method, the precursor is tetrachloroauric acid, the reducing agent is sodium citrate, and the solvent is water. In 1951, Turkevich et al. used techniques such as the electron microscopy to investigate the synthesis in a batch reactor under different process conditions (i.e. the synthesis temperatures and reactants' concentrations). In their standard synthesis condition, where the synthesis temperature is 100 ^{0}C and the initial concentrations of tetrachloroauric acid and sodium citrate are 0.255 and $1.938\ mol/m^3$, respectively, the authors reported in the final mixture spherical GNPs of a mean size of 20 nm. Furthermore, based on their experimental observation, they proposed a synthesis mechanism, called the organizer theory, a nucleation-growth mechanism, which describes how GNPs form in the citrate synthesis method. Because of this landmark contribution, the synthesis is otherwise called the Turkevich synthesis.

Many other authors have used this route to produce GNPs of varying sizes. Frens (1973) studied this synthesis and demonstrated that different sizes of GNPs can be obtained by changing the concentration of sodium citrate while keeping the concentration of chloroauric acid at about $0.3\ \mathrm{mol/m^3}$ at a synthesis temperature of 100 ^{0}C. This technique was slightly modified by Freund and Spiro (1985) to produce GNPs used for testing size-dependent catalytic properties of the particles. Abid (2003) used the synthesis to form different sizes of GNPs intended for laser and optical properties. However, unlike Frens (1973), Abid (2003) varied the concentration of both chloroauric acid and sodium citrate. Chow and Zukoski (1994) also explored the synthesis, this time by varying the concentration of chloroauric acid while keeping that of sodium citrate at $1.6\ mol/m^3$ at a synthesis temperature of 70 ^{0}C. Recent authors such as Ji et al. (2007), Zabetakis et al. (2012) and Wuithschick et al. (2015) have also investigated the synthesis. For authors who kept the initial precursor concentration constant at about $0.3\ \mathrm{mol/m^3}$ at the synthesis temperature of 100 ^{0}C, Figure 2.1.4 shows how the final particle mean size varies with the initial molar ratio of sodium citrate to tetrachloroauric acid.

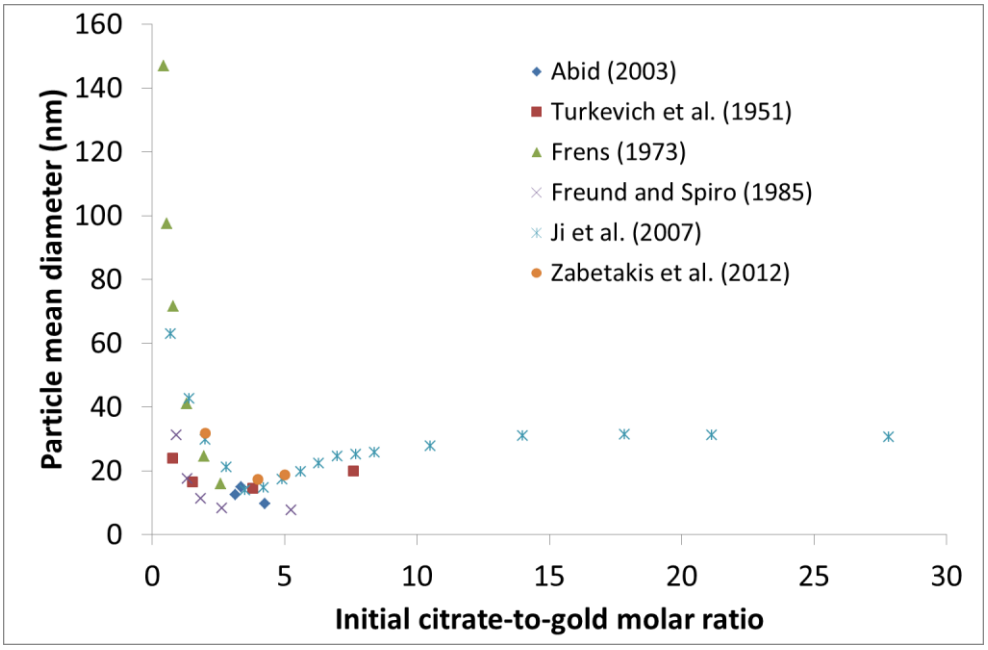

Figure 2.1.4: Final particle mean size of the citrate synthesis method for the initial precursor concentration constant at about $0.3\ \mathrm{mol/m^3}$ at the synthesis temperature of 100 ^{0}C from the investigations of various authors. Data from Abid (2003), Turkevich et al. (1951), Frens (1973), Freund and Spiro (1985), Ji et al. (2007) and Zabetakis et al. (2012).

As Figure 2.1.4 illustrates, the citrate synthesis method can be used to produce GNPs of sizes in the range 10 – 150 nm. This wide range and the spherical particle shape make the synthesis a common route for obtaining GNPs in various applications. However, the synthesis method is not reproducible and the products are usually polydisperse (i.e. wide particle size distribution). While conducting the synthesis, some authors have probed into the evolution of the reacting mixture so as to understand the formation of GNPs from the initial reactant mixture of tetrachloroauric acid and sodium citrate. For example, the reacting mixture changes in colour as the synthesis progresses. According to Frens (1973), after adding the reducing agent solution ($0.384\,mol/m^3$) to the precursor solution ($0.294\,mol/m^3$) at 100 ^{0}C, for various initial concentrations, the reacting mixture turns blue in about 25 - 80 s. In about 70 - 850 s, it turns brilliant red. Finally, the synthesis completes in a total time of 5 - 30 mins. The colour of the final mixture varies from red to orange to violet depending on the particle size distribution. Because of this colour change and the generation of particles, certain techniques have been used to investigate the citrate synthesis method.

2.1.4 Instrumentation techniques

Initially, the reacting mixture is an aqueous solution of the precursor and reducing agent. These react and produce GNPs in the particle phase as well as other by-products such as Cl^- (present in the unreacted precursor) in the liquid phase. Because of the many

components in the liquid phase, monitoring any of them in isolation would be impossible. On the other hand, the particle phase contains only gold particles of varying sizes. Thus, the instrumentation techniques employed by past authors to monitor the citrate synthesis method can be classified as particles image microscopy and particle radiation spectroscopy.

2.1.4.1 Particle image microscopy

Microscopy is the technique of using microscopes to view objects and areas of objects that cannot be seen with the naked eye (objects that are not within the resolution range of the normal eye). The smallest size the normal eye can recognize is about 0.1 mm. In contrast, nanoparticles are $10^3 - 10^5$ times smaller than this size. To monitor NP syntheses, the instrument must be able to magnify the particle size, at least, by about $10^3 - 10^5$. Usually, investigators apply this technique to the reacting mixture ex situ. In this case, they place a drop of the mixture on a screen and allow the drop to evaporate leaving behind only particles, which are then analysed under the microscope. Examples of microscopy instruments applied in NP syntheses include the scanning electron microscopy (SEM), transmission electron microscopy (TEM) and atomic force microscopy (AFM). Figure 2.1.5 shows TEM images. In this figure, the particle size has been magnified by about 10^5.

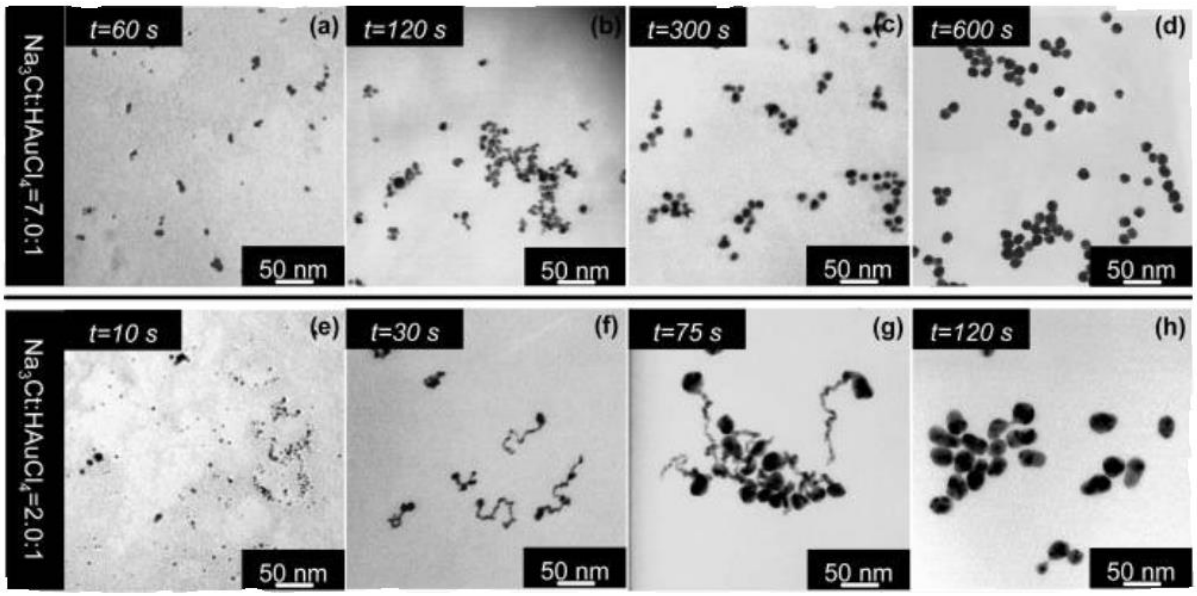

Figure 2.1.5: Time evolution of the TEM images of particles in the citrate synthesis method. Data from Ji et al. (2007).

2.1.4.2 Particle radiation spectroscopy

Spectroscopy is the technique of monitoring the interaction between matter and electromagnetic waves. As illustrated previously, the reacting mixture changes colour as the

synthesis progresses. To quantify this trend, investigators apply the radiation spectroscopy. As this trend can be observed by the eye, the frequencies (or the wavelengths) of the spectra must be in and around the visible light region of the electromagnetic waves; hence, the UV-Vis spectroscopy can be used to investigate the synthesis. This instrument generates the absorption spectrum of a substance within the visible light and ultra-violet wavebands. Using it, Haiss et al. (2007) reported the absorption spectrum of GNPs and the variation of the peak of the spectrum with the size of GNPs. Quantitatively therefore, the UV-Vis spectra can be used to determine the size of GNPs. Figure 2.1.6 shows the time evolution of the UV-Vis spectra of the citrate synthesis method.

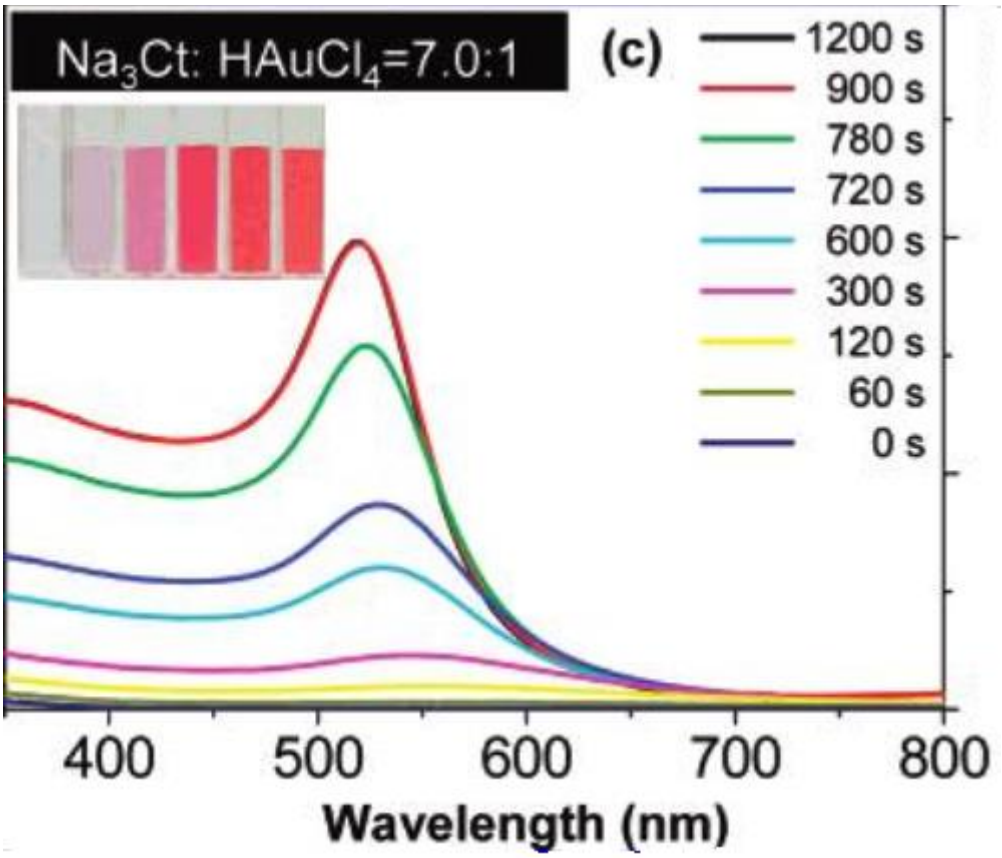

Figure 2.1.6: Time evolution of the UV-Vis spectroscopy in the citrate synthesis method. Data from Ji et al. (2007)

Also, since its discovery, X-rays have been used to study crystal structures. Since the wavelengths of X-rays are in the order of nanometres, they can interact with nanoparticles, indicating for example the number concentration of particles. Thus, X-rays can be used to investigate NP synthesis. Small-angle X-ray scattering (SAXS) and X-ray absorption near edge structure (XANES) are examples of the application techniques of X-rays.

Using these instrumentation techniques, one can describe the mechanism of the synthesis.

2.1.5 Mechanistic descriptions of the citrate synthesis method

From the investigation of the synthesis using various instrumentation techniques, previous authors proposed several (but quite different) mechanistic descriptions for the citrate synthesis method. These descriptions can be classified into: Turkevich organizer theory and seed-mediated mechanism. We review these mechanisms below.

2.1.5.1 Turkevich organizer theory

In their landmark work, Turkevich et al. (1951) investigated the citrate synthesis method to understand the mechanism of the synthesis. They carried out the citrate synthesis method at temperatures ranging from 15 – 100^0C and initial molar ratios of sodium citrate to tetrachloroauric acid from 1 to 7.5. For their investigation, they used the electron microscopy in combination with other analytical techniques described as the ultra-slit microscopy, nephelometry, nuclei isolation, titration and reaction analyses (Turkevich et al., 1951). They took portions of the reacting mixture of the citrate synthesis suspected of containing nuclei at different times, and transferred them into a growth medium consisting of a solution of 12×10^{-4} parts of hydroxylamine hydrochloride and 10×10^{-4} parts of tetrachloroauric acid. In this growth medium, nucleation did not take place. They relied on the description of a number of investigators that hydroxylamine hydrochloride, in slightly acid solution, inhibits the nucleation process. In neutral or basic solution, however, it is a nucleating agent. If the nuclei were present in the portions, hydroxylamine hydrochloride would reduce tetrachloroauric acid causing the nuclei to grow to a size convenient for them to count using a slit microscope. In the absence of nuclei and in a dust-free atmosphere, the growth medium undergoes no reduction of tetrachloroauric acid (Turkevich et al, 1951). Figure 2.1.7 shows a typical curve of the nucleation process in this synthesis.

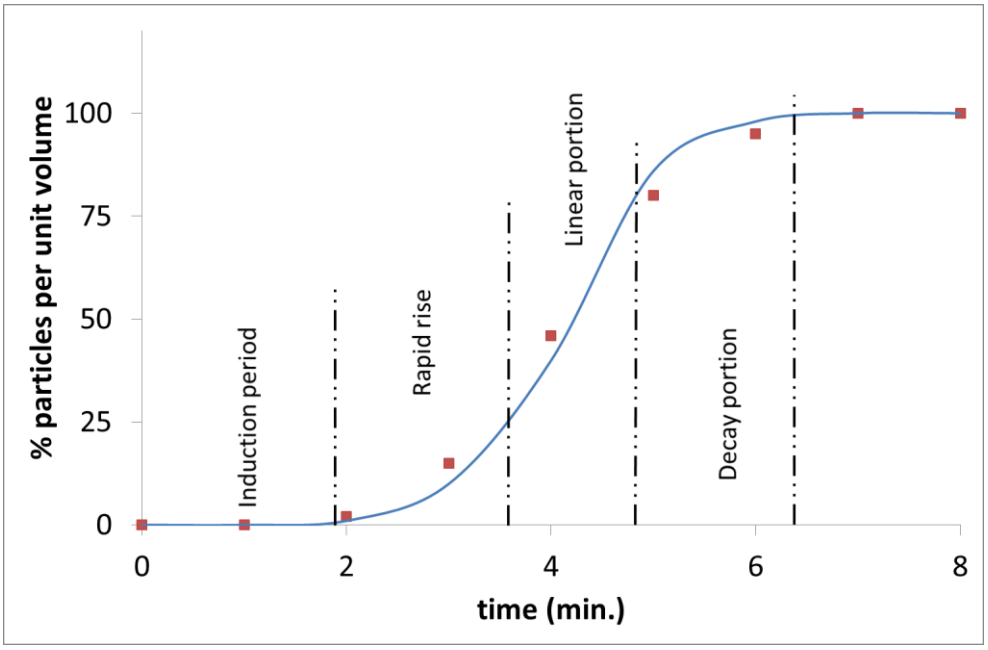

Figure 2.1.7 A typical curve of the nucleation process in the citrate synthesis method. The data refer to the synthesis studied by Turkevich et al. (1951) at 49 ^{0}C. The initial concentrations of precursor and reducing agent in the synthesis solution are equal to $0.255\ mol/m^3$ and $1.94\ mol/m^3$, respectively. (% particles per unit volume expresses the number of particles per unit volume as a percentage of the final number of particles per unit volume).

The nucleation curve in Figure 2.1.7 can be divided into four regions: an induction period, a rapid rise, which indicates the beginning of nucleation, a linear portion and finally a decay portion. This general nature of the curve is characteristic of an autocatalytic reaction (Turkevich et al., 1951). The cause of nucleation can be said to be absent at the beginning of the process, but it is produced in the course of the reaction. During the region of the linear portion, nucleation rate is at a maximum because the driving force for nucleation is also at a maximum. Thereafter, the nucleation rate starts declining to zero. The nucleation rate is the slope of the curve in Figure 2.1.7. If we assume that the nucleation rate is proportional to the amount of the substance which causes nucleation (the nucleating agent), the right-skewed distribution curve in Figure 2.1.8 shows a possible profile of the nucleating agent. In order to determine this substance, Turkevich et al. (1951) analysed the concentration profiles of auric, aurous and citrate ions. Excess sodium citrate was used in the experiments; thus, citrate could not be the nucleating agent. They measured the amount of the reacted auric ions with time by titrating the solution against thiosulphate. By the end of the nucleation process, less than 5% of auric ions had been used up. Thus, they concluded that neither

auric ions nor their reduced form, aurous ions, could be the nucleating agent. They did not report about testing for the presence of dicarboxy acetone.

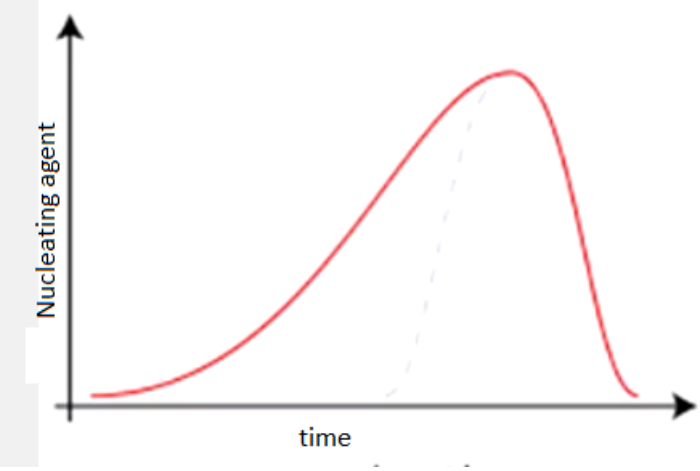

Figure 2.1.8 Possible profile of the nucleating agent with reaction time, to explain the nucleation curve in Figure 2.1.7

In order to understand the cause of nucleation, Turkevich et al (1951) used dicarboxy acetone directly as reducing agent. They assumed dicarboxy acetone to be the oxidation product of sodium citrate. Figure 2.1.9 shows the corresponding nucleation curve. In this figure, the induction period is much less than 0.1 min.

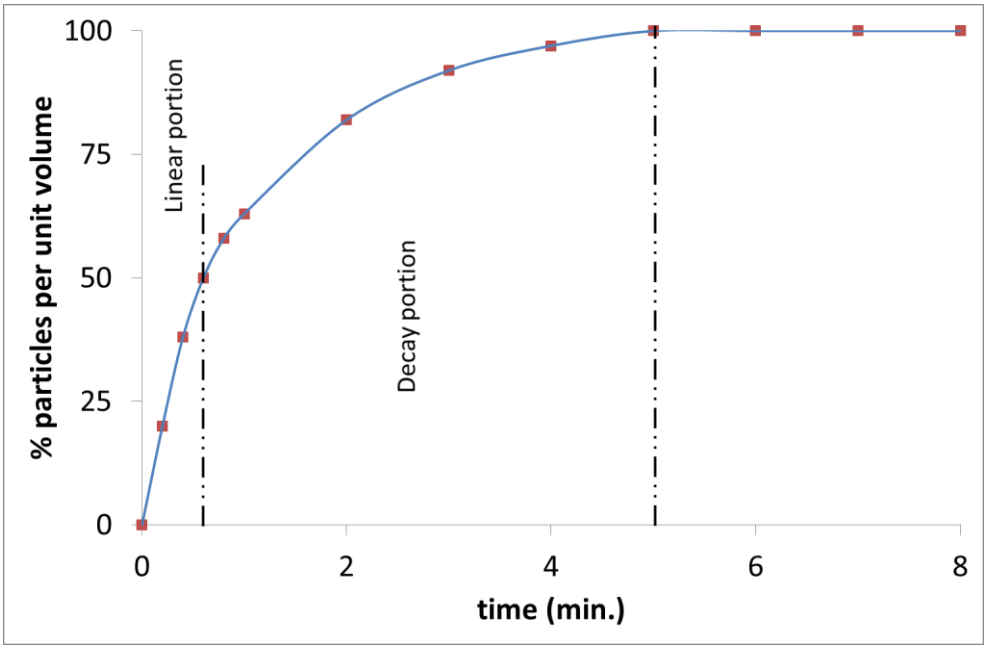

Figure 2.1.9: Nucleation curve of a gold sol produced by dicarboxy acetone. Data from Turkevich et al. (1951).

Turkevich et al (1951) explained the induction period in Figure 2.1.7 as the time required to produce the amount of dicarboxy acetone necessary for nucleation.

Also, the region of rapid rise is absent from Figure 2.1.9. The nucleation rate is a maximum at the start of nucleation and falls off exponentially. This indicates a first-order kinetic mechanism. One is therefore led to conclude that the autocatalytic nature of the nucleation reaction is due to the autocatalytic nature of the formation of dicarboxy acetone, while the first-order kinetic mechanism results from the unimolecular decomposition of a complex of dicarboxy acetone and gold ions (Turkevich et al., 1951).

Based on the foregoing, Turkevich et al (1951) advanced the 'organizer' mechanism for the formation of a nucleus. They discredited the possibility of nucleation due to the presence of impurities and pointed out that it was difficult to understand the nucleation process from the perspective of the fluctuation theory. Fluctuation theory postulates the formation of a supersaturated solution of atoms of metallic gold, some of which coalesce into a nucleus only when the statistical fluctuation of their concentration brings a sufficiently large amount of them together to form a particle size that is thermodynamically stable. This theory also explains nucleation due to the presence of impurities.

In the organizer theory, they claimed that the presence of a polydentate reducing agent (i.e. citrate) or its oxidation product provides the mechanism for the nanoparticle precursor (atoms) to arrange and nucleate (Turkevich et al., 1951). Kumar et al (2007) illustrated this using Figure 2.1.10. From this Figure, three Au^{+} ions can be tethered by a minimum of two dicarboxy acetone molecules.

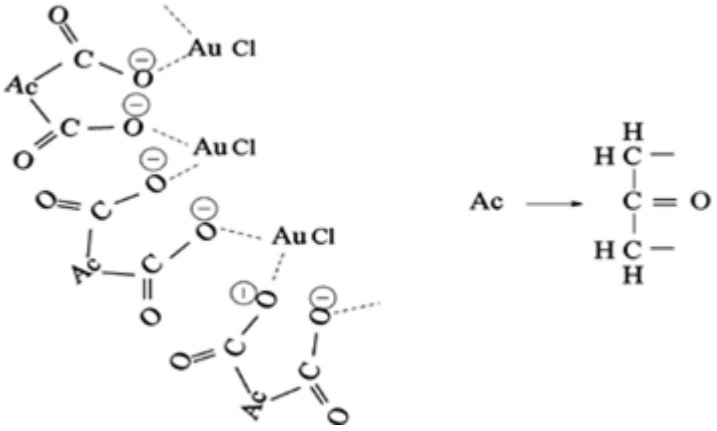

Figure 2.1.10 Illustration of complex of aurous species and dicarboxy acetone. Derived from Kumar et al. (2007)

Also, Turkevich et al (1951) observed that while nucleation stopped after about five minutes of the synthesis, reactions continued for a further two hours, largely by the growth process when conducting the synthesis at 49 ^{0}C. Nucleation stopped because the nuclei adsorb dicarboxy acetone and decompose it to acetone (Kumar et al., 2007). Turkevich et al (1951) supported this idea using an experiment on the growth process. They mixed a solution of

sodium citrate and tetrachloroauric acid together. Few minutes after, they added a colloid of GNPs. This recipe yielded a particle size distribution (PSD) of one maximum. However, when they added the colloid several minutes after the completion of the nucleation step, they obtained a PSD of two maxima, one due to nucleation and growth and the other due to the added colloid. See Figure 2.1.11 for typical particle size distributions of one maximum and two maxima reported by Turkevich et al. (1951), to support their idea.

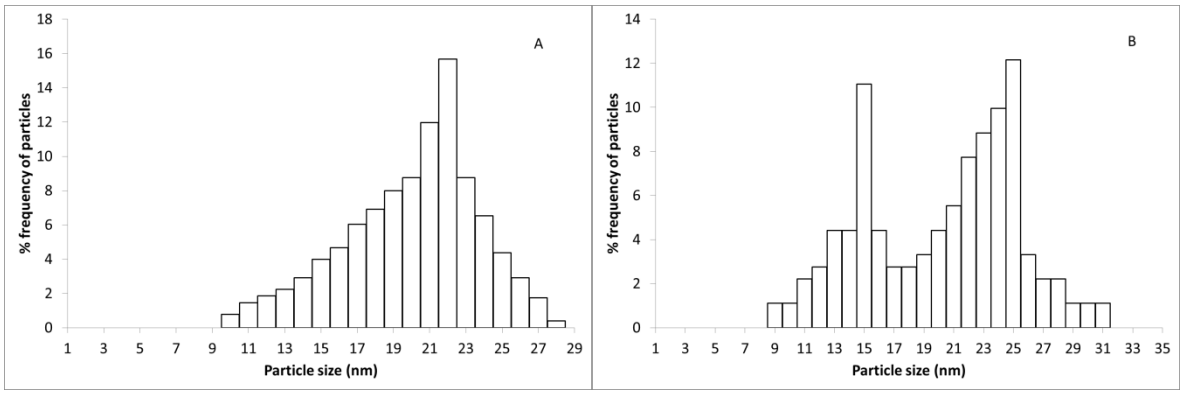

Figure 2.1.11: Showing typical particle size distributions of one maximum and two maxima reported by Turkevich et al. (1951).

Turkevich et al (1951) also made some findings on the growth process from their various experiments such as:

- The standard deviation of the nanoparticle size distribution does not change with growth.
- The ratio of particle sizes remains constant during growth.

They put in a growth medium, two colloids of gold whose PSDs have mean sizes of 20 and 30 nm, respectively, and obtained two PSDs with mean sizes of 40 and 60 nm. The standard deviations for both distributions remained almost unchanged. It is only if we assume that the growth rate is proportional to the size that the above scenario can hold.

The evidence outlined above supports the nucleation-growth mechanism proposed by Turkevich et al. (1951). Kumar et al. (2007) used this evidence and contributions from other authors to come up with the reaction steps for this synthesis although they pointed out that some of the steps were still not fully understood. Below, we describe these steps starting from tetrachloroauric acid.

The first step in the synthesis is to heat an aqueous solution of $HAuCl_4$ to its boiling point. Doing so yields auric chloride (Mellor, 1946). Thus, auric chloride becomes the main precursor for the reduction process. The chemical expression is:

$$HAuCl_4 \rightarrow AuCl_3 + HCl \quad (2.1.1)$$

At this stage, sodium citrate is introduced into the reactor while the reacting mixture is mechanically stirred. Both sodium citrate and auric chloride undergo a redox reaction; citrate becomes oxidized to dicarboxy acetone (DCA with the chemical formula: $(COO^-CH_2)_2C=O$) while auric chloride becomes reduced to aurous chloride according to the following oxidation and reduction reactions:

$$(COO^-CH_2)_2C(OH)COO^- \rightarrow (COO^-CH_2)_2C=O + CO_2 + H^+ + 2e^- \quad (2.1.2)$$

$$AuCl_3 + 2e^- \rightarrow AuCl + 2Cl^- \quad (2.1.3)$$

Combining eqs. (2.1.2) and (2.1.3) yields:

$$AuCl_3 + (COO^-CH_2)_2C(OH)COO^- \rightarrow AuCl + 2Cl^- + (COO^-CH_2)_2C=O + CO_2 + H^+ \quad (2.1.4)$$

Thereafter, DCA forms a complex with aurous chloride and facilitates the disproportionation of aurous chloride into gold atoms and auric chloride. This is in line with the Turkevich organizer theory. An illustration of the complex is shown in Figure 2.1.10. From this picture, a minimum of 2 DCA molecules and 3 aurous ions is required to form the complex. This complex continues to increase in the number of aurous ions and DCA molecules until it can produce a number of gold atoms sufficient to form a nucleus; hence, we have nucleation. The disproportionation reaction is given as:

$$3AuCl \xrightarrow{DCA} 2Au^0 + AuCl_3 \quad (2.1.5)$$

In this reaction, DCA behaves as a catalyst.

In the Turkevich organizer theory, GNPs grow when gold (I) ions disproportionate on the particle surface; the particle surface acts as a catalyst in this case. Kumar et al (2007) stated that diffusional resistances are negligible at the length scales of nanoparticles. They stated that citrate ions alongside their derivatives easily adsorb unto gold surface to form complexes. Unless the surface is sufficiently large and the concentration of gold (I) ions is high, the complexes will shield gold (I) ions from adsorbing onto the gold surface. Thus, the growth rate is assumed to be proportional to the surface area of the particle and the concentration of gold (I) ions; so, the chemical reaction occurs as:

$$3AuCl \xrightarrow{particles} 2Au^0 + AuCl_3 \quad (2.1.6)$$

In the standard Turkevich synthesis, nucleation stops after 10 minutes when conducting the synthesis at 49 ^{0}C. In the previous paragraph, we cited that DCA creates nuclei. Thus,

nucleation cannot stop unless either aurous chloride or DCA is exhausted. Turkevich et al (1951) reported that DCA decomposes on the gold surface. Similarly, Kumar et al (2007) reported that at the synthesis temperature, DCA degrades into acetone according to the following reaction step:

$$(COO^{-}CH_2)_2C=O + 2H_2O \rightarrow (CH_3)_2C=O + 2CO_2 + 2(OH)^{-} \quad (2.1.7)$$

We can obtain the overall stoichiometry of the reduction reaction as follows:

Multiply eq. (2.1.4) by 3:

$$3AuCl_3 + 3[(COO^{-}CH_2)_2C(OH)COO^{-}] \rightarrow 3AuCl + 6Cl^{-} + 3[(COO^{-}CH_2)_2C=O] + 3CO_2 + 3H^{+} \quad (2.1.8)$$

Substitute for $3AuCl$ using eq. (2.1.6):

$$3AuCl_3 + 3[(COO^{-}CH_2)_2C(OH)COO^{-}] \rightarrow 2Au^{0} + AuCl_3 + 6Cl^{-} + 3[(COO^{-}CH_2)_2C=O] + 3CO_2 + 3H^{+} \quad (2.1.9)$$

By collecting $AuCl_3$ on the LHS, the overall stoichiometry is:

$$2AuCl_3 + 3[(COO^{-}CH_2)_2C(OH)COO^{-}] \rightarrow 2Au^{0} + 6Cl^{-} + 3[(COO^{-}CH_2)_2C=O] + 3CO_2 + 3H^{+} \quad (2.1.10)$$

This overall stoichiometry suggests that to have a complete reaction, we need three moles of citrate and two moles of auric chloride. However, various authors have shown that a complete conversion can be obtained at a stoichiometric ratio of 0.43 (ratios below 1.5, however, have little or no practical significance because they produce large particles). It appears reasonable to conclude that some derivatives of citrate can also reduce auric chloride in the synthesis. We derive the additional reduction of auric chloride as follows.

Davies (1928) reported the reduction of tetrachloroauric acid using acetone. Since DCA degrades to acetone according to eq. (2.1.7), we write the reduction reaction as follows:

$$(CH_3)_2C=O + xAuCl_3 \rightarrow xAuCl + products \quad (2.1.11)$$

(Kumar et al. (2007) reported 'products'; they did not report the real substances. In this reaction, acetone becomes oxidised while reducing $AuCl_3$. 'Products' would therefore consist of the oxidation products of acetone. Evans and Sefton (1922) reported the oxidation products of acetone as CH_3COOH, H^{+} and CO_2. Furthermore, for a balance of atoms, Cl^{-} would also be produced. Thus, 'products' would be a combination of CH_3COOH, H^{+}, Cl^{-} and CO_2.)

In Eq. (2.1.11), the stoichiometry of acetone to auric chloride is assumed to be $1{:}x$. The value of x can be obtained from the stoichiometric ratio of 0.43 citrate to auric chloride, experimentally reported by past authors for a complete conversion of the precursor occurs. To do this, we express acetone in terms of citrate and then substitute this expression into Eq. (2.1.11) so that the latter would be in terms of citrate rather than acetone. Thereafter, we obtain the value of x by equating the ratio of citrate to auric chloride to 0.43. To express acetone in terms of citrate, we first express acetone in terms of DCA using Eq. (2.1.7) as:

$$(CH_3)_2C=O \rightarrow (COO^-CH_2)_2C=O + 2H_2O - 2CO_2 - 2(OH)^- \quad (2.1.12)$$

Then, we substitute for acetone in Eq. (2.1.11) and rearrange as:

$$(COO^-CH_2)_2C=O + 2H_2O + xAuCl_3 \rightarrow xAuCl + 2CO_2 + 2(OH)^- + product \quad (2.1.13)$$

We can then write Eq. (2.1.13) in terms of citrate by substituting for DCA using Eq. (2.1.10). From the latter, we have:

$$3[(COO^-CH_2)_2C=O] \rightarrow 2AuCl_3 + 3[(COO^-CH_2)_2C(OH)COO^-] - 2Au^0 - 6Cl^- - 3CO_2 - 3H^+ \quad (2.1.14)$$

We multiply Eq. (2.1.13) by 3 and then substitute for DCA using Eq. (2.1.14). After rearranging, we obtain:

$$(2+3x)AuCl_3 + 3[(COO^-CH_2)_2C(OH)COO^-] + 6H_2O \rightarrow 2Au^0 + 6Cl^- + 3CO_2 + 3H^+ + 3xAuCl + 6CO_2 + 6(OH)^- + 3product \quad (2.1.15)$$

Also, we can substitute for $3xAuCl \rightarrow 2xAu^0 + xAuCl_3$ in Eq. (2.1.15) and obtain

$$(2+3x)AuCl_3 + 3[(COO^-CH_2)_2C(OH)COO^-] \rightarrow 2Au^0 + x(2Au^0 + AuCl_3) + 3products + 9CO_2 + 6(OH)^- + 6Cl^- - 6H_2O + 3H^+ \quad (2.1.16)$$

By re-arranging Eq. (2.1.16), we obtain

$$(2+2x)AuCl_3 + 3[(COO^-CH_2)_2C(OH)COO^-] \rightarrow (2+2x)Au^0 + 3products + 9CO_2 + 6(OH)^- + 6Cl^- - 6H_2O + 3H^+ \quad (2.1.17)$$

Eq. (2.1.17) becomes the final overall reaction, from which x can be calculated using $citrate/gold = \sim 0.43$. $x = 2.49$. Thus, we explain the stoichiometric ratio of 0.43 by adding the following reduction reaction:

$$2.5AuCl_3 + (CH_3)_2C=O \rightarrow 2.5AuCl + products \quad (2.1.18)$$

However, Kumar et al. (2007) reported

$$4AuCl_3 + (CH_3)_2C=O \rightarrow 4AuCl + products \quad (2.1.19)$$

We think this was a mistake as the calculations above reveal.

We summarize the chemical reactions that describe the Turkevich organizer theory in Table 2.1.1.

Table 2.1.1: The chemical reactions that describe the Turkevich organizer theory (Mellor, 1946; Kumar et al., 2007)

$HAuCl_4 \rightarrow AuCl_3 + HCl$	(2.1.1)
$AuCl_3 + (COO^-CH_2)_2C(OH)COO^- \rightarrow AuCl + 2Cl^- + (COO^-CH_2)_2C = O + CO_2 + H^+$	(2.1.4)
$3AuCl \xrightarrow{DCA} 2Au^0 + AuCl_3$	(2.1.5)
$(COO^-CH_2)_2C = O + 2H_2O \rightarrow (CH_3)_2C = O + 2CO_2 + 2(OH)^-$	(2.1.7)
$3AuCl \xrightarrow{particles} 2Au^0 + AuCl_3$	(2.1.6)
$2.5AuCl_3 + (CH_3)_2C = O \rightarrow 2.5AuCl + products$	(2.1.18)

Next, we describe the experimental evidence provided by Wuithschick et al (2015) for the seed-mediated mechanism.

2.1.5.2 Seed-mediated mechanism

While the Turkevich organizer theory did not report aggregation, the seed-mediated mechanism involves nucleation, aggregation and growth in the particle phase. Aggregation in the citrate synthesis method was first reported by Chow and Zukoski (1994) while investigating the synthesis with a combination of the UV-Vis spectroscopy and electron microscopy. Using this set-up as well, Ji et al. (2007) reported a more extensive study, which first pointed out the role of pH and illustrated how it affects the effect of aggregation in the synthesis. In addition to this set-up, Polte et al. (2010) and Wuithchick et al. (2015) used a combination of XANES and SAXS techniques to investigate the synthesis. This equipment provides time-resolved in situ information on the size of nanoparticles of about 2 nm or larger and of their number concentration, offering a reliable account of the synthesis. Figure 2.1.12 shows the SAXS evidence for the presence of aggregation in the synthesis.

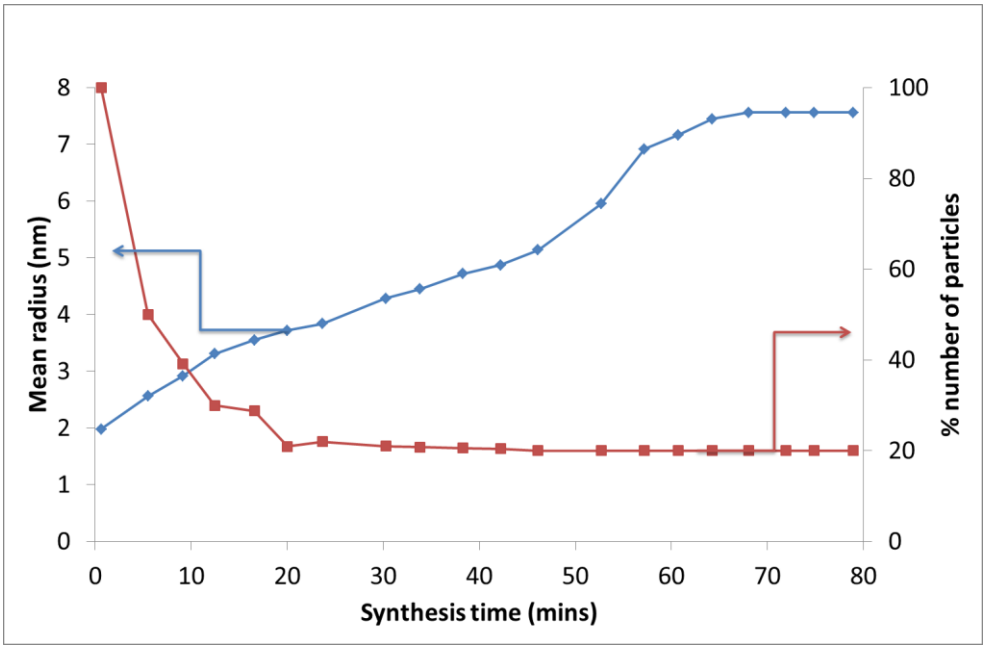

Figure 2.1.12: Evolution of the mean radius and of the percentage number of particles in the citrate synthesis method. The values of the initial concentrations of $HAuCl_4$ and Na_3Ct in the synthesis solution are $0.25\ mol/m^3$ and $2.5\ mol/m^3$, respectively. The mixture temperature is $75\ ^0C$. Data reproduced from Figure 2(d) of Polte et al. (2010).

From this figure, the number of particles is at the maximum early in the synthesis, declines for about one-third of the synthesis time, and remains constant thereafter. In the process, the polydispersity reduced (Polte et al., 2010). The maximum number of particles corresponds to the nucleated nanoclusters, which coalesce to form the seed particles, reflected in the decline of the particle number. Later on, the number of particles remains constant while particle size steadily rises. This suggests that particles stop coalescing and start growing.

Furthermore, in their standard condition, where the molar ratio of citrate-to-gold is 10, the initial precursor concentration in the synthesis solution at $100\ ^0C$ is $0.25\ mol/m^3$, Wuithschick et al. observed that particles aggregated into seed particles, which are about the same size. Then, these seed particles grew to the final GNPs. In their work, Wuithschick et al (2015) drew portions from the reacting mixture at different times and quenched them to normal temperature so as to stop the synthesis. They analysed the portions after four days and observed that the reactions still reached completion. The particles had slowly grown to the final size. The portions drawn after a particular time yielded the same particle mean size and polydispersity as the original mixture. These portions were said to have been drawn after the seed had been formed. Conversely, the portions drawn before this time yielded particles that were much bigger or smaller. Thus, Wuithschick et al (2015) proposed the

seed-mediated mechanism where GNPs aggregate until they reach a stable size; thereafter, they grow.

The seed size is determined by the colloidal stability of the mixture. The colloidal stability is a measure of aggregation of particles. As colloids become stable, particles aggregate less significantly. For the usual range of the Turkevich synthesis, seed size is constant (Polte et al., 2010). Polte et al (2010) tested this by adding an unreactive electrolyte $NaClO_3$ to the mixture. They reasoned as follows. As the ionic strength of the solution increases, the charges on particles increase, hence ensuring the colloidal stability of the mixture. In increasing the ionic strength, to preserve the chemistry of the synthesis, Polte et al. did not want to introduce into the synthesis solution a reactive electrolyte, hence employing $NaClO_3$ in the investigation. $NaClO_3$ did not have any effect on the stability (as the seed size remained constant) until when its concentration was 120 times more than $[AuCl_4]^-$. This observation made them conclude that within the usual range of the Turkevich synthesis, the seed size is constant. Subsequently, they explained the mechanism as follows: Au(III) reacts in two parallel directions: one forms Au(0) and the other forms the unreactive complex $[AuCl_{4-x}(OH)_x]^-$.The ratio of their rate constants is determined by the pH of the system which affects the gold equilibrium position. In an acidic pH, Au(III) preferably exists as $[AuCl_4]^-$. $[AuCl_4]^-$ reacts to form Au(0), gold atoms nucleate into gold nanoclusters. At the nanocluster level, particles are unstable so they aggregate to form seeds. $[AuCl_{4-x}(OH)_x]^-$ slowly begins to release Au atoms on the seeds, followed by a fast release i.e. slow and fast growth.

Also, pH affects the dynamics of this synthesis in a number of ways. For example, it affects the colloidal stability and the seed size. Similarly, it affects the precursor and reducing agent solutions, either of which can exist in different forms depending on the pH. The normal pH range for the synthesis is between 3 and 8. Within this range, the seed particle size is fixed. So, if more $[AuCl_4]^-$ reacts to form the seed monomers, more seed particles will be formed thus reducing the final size. At lower pH than this range, seed particle size increases because more ions are present to promote aggregation. In acidic pH, the precursor exists as $[AuCl_4]^-$ while as the pH increases, it becomes $[AuCl_{4-x}(OH)_x]^-$. Citrate, on the other hand, exists as Ct^{3-} in acid, but as CtH_3 in alkaline pH. Thus, pH determines both the state of the precursor and that of the reducing agent.

Polte et al (2010) also considered the role of dicarboxyl acetone (DCA) in the synthesis. They carried out experiments (i) with DCA used as the only reducing agent instead of citrate (ii) DCA added to a standard synthesis after seed particle formation, and (iii) DCA added to Na_3Ct before mixing with $HAuCl_4$. The first experiment produced a more polydisperse

mixture; they concluded that $HAuCl_4$ with DCA does not follow the seed mediated pathway. Both $HAuCl_4$ and DCA are acids; so, while $[AuCl_4]^-$ forms $[AuCl_{4-x}(OH)_x]^-$ as a parallel reaction to the formation of seeds, DCA directly forms GNPs in no particular order. In the second experiment, the final particle size and particle size distribution were similar to the results from the standard synthesis; however, the reaction was completed in half of the time. DCA promoted the growth process. In the third experiment, DCA only substantially reduced the reaction time. The outcomes further confirmed that DCA actually promotes the synthesis; Turkevich et al (1951) said it promotes the nucleation process while Polte et al (2010) said it promotes the growth process. Meanwhile, DCA should not produce more particles in experiment (ii) as expected by Polte et al (2010). Previous investigations by Turkevich et al (1951) confirmed DCA decomposes in the presence of seed particles. A valid argument against DCA as an organizer, however, was put forward by Doyen et al (2010). Doyen et al (2010) investigated the synthesis using nuclei magnetic resonance and found no evidence of DCA as an intermediate in the citrate method. A critical look at their report, however, revealed that DCA was present early in the synthesis. However, the strongest claim against DCA is the fact that, at the synthesis temperature, it decomposes more rapidly than the nuclei take to form so it cannot be available to promote nucleation. Wiig (1928) reported that DCA takes 1e-7 s to decompose while Turkevich et al. (1951) reported that it takes about 1 min. for nucleation to occur. Thus, as soon as DCA forms, it decomposes instantaneously before the inception of nucleation process.

In summary, the work by Polte et al (2010) revealed that the citrate synthesis method follows a seed-mediated mechanism. However, unlike the Turkevich organizer theory, we do not have the reaction steps for the seed-mediated mechanism. We transform the presented experimental evidence of Polte et al. (2010), Wuithschick et al. (2015) and other authors into reaction steps in Chapter 4.

In the following section, we present the mathematical framework to adopt in modelling the citrate synthesis method.

2.2 Mathematical modelling

We have thus far reviewed the citrate synthesis method, revealing how GNPs form in the reaction mixture. The reaction mixture consists of particles (GNPs) dispersed in the aqueous solution, to constitute a multiphase system of the liquid (or continuous) phase and the solid (or discontinuous) phase. We review modelling approaches for the two phases as follows.

2.2.1 Continuous phase

In chemical processes, the basic governing equations are the laws of the conservation of mass, momentum and energy. In deriving these governing equations, we consider a control volume. Depending on the state of the control volume, the governing equations can be derived from two approaches: Lagrangian and Eulerian. In the former, the control volume moves at the same velocity as the local fluid while in the latter, the control volume is fixed. We adopt the Eulerian approach in deriving the governing equations in this work. For the material balance, we write:

$$Acc = (In - Out) + Gen \tag{2.2.1}$$

where Acc is the mass accumulation rate (i.e. the rate of change of mass of a component in the control volume V), $In - Out$ is the net mass flow rate of the component entering V and Gen is the mass generation rate (i.e. the mass of the component generated within the control volume per unit time). By convention, the conservation laws are written in terms of moles because in chemical reactions, the combination of reactants is expressed accurately using their moles. The mole $M_i(t)$ of component i present at time t in V is:

$$M_i(t) = \int_V C_i(\boldsymbol{x}, t)dV \tag{2.2.2}$$

where $C_i(\boldsymbol{x}, t)$ is the molar concentration of component i and it is a function of both physical space and time.

By definition, the accumulation term in Eq. (2.2.1) is given as:

$$Acc = \frac{M_i(t+dt)-M_i(t)}{dt} = \frac{d}{dt}\left(\int_V C_i(\boldsymbol{x}, t)dV\right) = \int_V \frac{\partial C_i}{\partial t}dV \tag{2.2.3}$$

The last passage in the equation above holds because V is fixed; that is, it is not a time-dependent integration domain.

The term $(In - Out)$ in Eq. (2.2.1) is contributed by two processes: convection and diffusion. Thus, we have:

$$(In - Out) = (In - Out)_{conv} + (In - Out)_{diff} \tag{2.2.4}$$

For the term $(In - Out)_{conv}$, due to the fluid velocity $\boldsymbol{u_f}$, component i flows in and out of the control volume V. This control volume has a physical control surface denoted by $\boldsymbol{S}$ and its differential surface is denoted by $d\boldsymbol{S}$. In terms of the unit vector, $d\boldsymbol{S} = \boldsymbol{n}dS$. By convention, the unit vector is directed outward. Thus, we have:

$$(In - Out)_{conv} = -\int_S C_i \boldsymbol{u_f}.d\boldsymbol{S} \tag{2.2.5}$$

Using the Gauss theorem, Eq. (2.2.5) becomes:

$$(In - Out)_{conv} = -\int_V \boldsymbol{\nabla_x}.\left(C_i \boldsymbol{u_f}\right)dV \tag{2.2.6}$$

For the term $(In - Out)_{diff}$, component i diffuses in and out of the control volume V. By the convention of the unit vector and applying the Gauss theorem, the expression is:

$$(In - Out)_{diff} = -\int_S \boldsymbol{J}_i.d\boldsymbol{S} = -\int_V \boldsymbol{\nabla_x}.(\boldsymbol{J}_i)dV \tag{2.2.7}$$

where $\boldsymbol{J}_i$ is the diffusive flux of component i. In the absence of external forces and temperature gradient, $\boldsymbol{J}_i$ can be expressed using the Fick's law of diffusion as (Ranade, 2002):

$$\boldsymbol{J}_i = -D_{im}\boldsymbol{\nabla_x}C_i \tag{2.2.8}$$

where D_{im} is the diffusion coefficient for component i in the mixture. In terms of the binary diffusion coefficient D_{ij} of component i relative to component j, D_{im} can be expressed as (Ranade, 2002):

$$D_{im} = \frac{1-y_i}{\sum_{j.j\neq i} y_j/D_{ij}} \tag{2.2.9}$$

y_i is the mole fraction of component i.

For the last term in Eq. (2.2.1), the generation term, we have:

$$Gen = \int_V r_i(\boldsymbol{x},t)\,dV \tag{2.2.10}$$

where $r_i(\boldsymbol{x},t)$ is the rate of generation of component i per unit volume from various reactions and it is a function of both physical space and time.

Substituting the equations into Eq. (2.2.1), we have:

$$\int_V \frac{dC_i}{dt}dV = -\int_V \boldsymbol{\nabla_x}.\left(C_i\boldsymbol{u_f}\right)dV + \int_V \boldsymbol{\nabla_x}.(D_{im}\boldsymbol{\nabla_x}C_i)dV + \int_V r_i(\boldsymbol{x},t)\,dV \tag{2.2.11}$$

Eq. (2.2.11), when re-arranged, becomes:

$$\int_V \left[\frac{\partial C_i}{\partial t} + \boldsymbol{\nabla_x}.\left(C_i\boldsymbol{u_f}\right) - \boldsymbol{\nabla_x}.(D_{im}\boldsymbol{\nabla_x}C_i) - r_i\right]dV = 0 \tag{2.2.12}$$

Since this equation has to be satisfied for an arbitrary control volume, assuming that the integrand function is continuous, we conclude that it must be:

$$\frac{\partial C_i}{\partial t} = -\boldsymbol{\nabla_x}.\left(C_i\boldsymbol{u_f}\right) + \boldsymbol{\nabla_x}.(D_{im}\boldsymbol{\nabla_x}C_i) + r_i \tag{2.2.13}$$

We can simplify this equation by imposing some conditions. The synthesis of GNPs in citrate synthesis is usually carried out in a batch reactor with good mechanical stirring (Turkevich et al., 1951). Consequently, the reactor is well-mixed. By implication, the properties of the fluid do not depend on physical space; C_i, $\boldsymbol{u_f}$ and r_i only depend on time. Hence, the diffusion term in Eq. (2.2.13) vanishes, because no concentration gradients are present. Similarly, the convective term also vanishes. The system is a batch reactor with no boundaries through the component can enter or leave the reactor. As C_i only depends on time, Eq. (2.2.13) becomes:

$$\frac{dC_i}{dt} = r_i \tag{2.2.14}$$

(In Appendix A, we have also derived Eq. (2.2.14) using the averaging theory. For details of this derivation, we refer the reader to Appendix A.)

Eq. (2.2.14) is an ordinary differential equation (ODE) of C_i with respect to time that describes any aqueous component in the citrate synthesis method for a batch reactor. r_i can be expressed in terms of the reactants' concentrations. Expressions for r_i would depend on the mechanism of the synthesis, which can be the Turkevich organizer theory or the seed-mediated mechanism. We discuss in detail the expressions for r_i in these mechanisms in Chapters 3 and 4.

2.2.2 Discontinuous phase

The discontinuous phase contains GNPs with a number concentration of $6.09 \times 10^{17}\ 1/m^3$. To estimate the latter, we employ the experimental condition of Turkevich et al. (1951), where the initial precursor concentration $C_{HAuCl_4} = 0.255\ mol/m^3$ yielded particles with a final mean diameter $s_f = 20.0\ nm$ lying in the interval $[18.5\ nm, 21.5\ nm]$. With this narrow interval, we assumed the GNP distribution as monodisperse and used the expression:

$$C_{HAuCl_4}/\rho m_v {s_f}^3$$

for the estimate. In this expression, ρ is the molar density of gold, taken as $10^5\ mol/m^3$, m_v is the particle volume shape factor (which we set equal to $\pi/6$, assuming that the particles are spherical).

This system of particles can be modelled at different levels of details. At the most fundamental level (or the microscale), the particles are considered individually. This approach involves modelling the formation of nuclei and describing how each nucleus grows and aggregates. Tracking individual particles (that is, tracking how ~$10^{17}\ 1/m^3$ particles evolve in the synthesis) is computationally extremely demanding and, in most cases,

unnecessary. We will not adopt this approach. On the other hand, the macroscale approach treats this system of particles effectively as a bulk (a single particle) using their average values, such as the mean size of GNPs. However, the quality of GNPs depends not only on the mean particle size, but more importantly on the particle size distribution (PSD). The PSD or more generally the number density function (NDF) is the framework of the population balance equations (PBEs) – the NDF is a mathematical function that describes how these particles relate with one another. The PBEs describe how the NDF, under the influence of processes such as nucleation, growth and aggregation, evolves in time, internal particle space (such as the particle size) and physical space.

Below, we introduce the concept of the NDF, followed by the derivation of the PBEs. We then consider how all the terms in the PBEs representing nucleation, growth and aggregation can be expressed under the section treating the problem of closure.

2.2.2.1 Number density function

The particle size s is assumed to be a continuous variable characterizing the state of the nanoparticles. No two nanoparticles have exactly the same size (say, the size of particle A is $4.12345 \dots\ nm$ while that of particle B is $4.12344 \dots nm$): a (nano)particle size distribution is therefore present. This is true in general, for any variable characterizing the nanoparticles. The velocity $\boldsymbol{u}$ at which each nanoparticle moves in physical space, for instance, differs from particle to particle: a (nano)particle velocity distribution is thus also present. The distribution of the nanoparticle population over all the variables that characterize the state of each particle (here assumed to be size and linear velocity) can be expressed as a number density function, denoted as $f_n(s, \boldsymbol{u}, \boldsymbol{x}, t)$. By definition, $f_n(s, \boldsymbol{u}, \boldsymbol{x}, t)\ ds d\boldsymbol{u} d\boldsymbol{x}$ represents the number of particles at time t present in a differential volume $d\boldsymbol{x}$ around a point $\boldsymbol{x}$ in physical space that have size in the range ds around s and velocity in the range $d\boldsymbol{u}$ around $\boldsymbol{u}$. Therefore, $f_n(s, \boldsymbol{u}, \boldsymbol{x}, t)$ represents the number of particles per unit phase-space volume, where phase space is the abstract space given by the union of size, velocity and physical spaces. Notice that the number of particles having size equal to s (or having velocity equal to $\boldsymbol{u}$) is statistically zero. Conversely, the number of particles with size in a given size *range* is nonzero. For instance, the number of particles with size in the range $[s_1, s_2]$ per unit velocity-space volume and physical-space volume is finite and equal to:

$$\int_{s_1}^{s_2} f_n(s, \boldsymbol{u}, \boldsymbol{x}, t) ds \tag{2.2.15}$$

The number of particles with size in the range $[s_1, s_2]$ per unit physical-space volume (with any possible velocity) is instead given by:

$$\int_{\Omega_{\boldsymbol{u}}} \int_{S_1}^{S_2} f_n(s, \boldsymbol{u}, \boldsymbol{x}, t) ds \, d\boldsymbol{u} \tag{2.2.16}$$

where $\Omega_{\boldsymbol{u}}$ represents the domain of variation of the particle velocity vector (for each rectangular velocity component this domain is assumed to extend from $-\infty$ to $+\infty$).

The total number of particles per unit physical-space volume (with any possible size and velocity) is given by:

$$\int_{\Omega_{\boldsymbol{u}}} \int_{\Omega_s} f_n(s, \boldsymbol{u}, \boldsymbol{x}, t) ds \, d\boldsymbol{u} \tag{2.2.17}$$

where Ω_s represents the domain of variation of the particle size (assumed to extend from 0 to $+\infty$).

Finally, the number of particles present in a vessel occupying a region $\Omega_{\boldsymbol{x}}$ of physical space (with any possible size and velocity) is given by:

$$\int_{\Omega_{\boldsymbol{x}}} \int_{\Omega_{\boldsymbol{u}}} \int_{\Omega_s} f_n(s, \boldsymbol{u}, \boldsymbol{x}, t) ds \, d\boldsymbol{u} \, d\boldsymbol{x} \tag{2.2.18}$$

2.2.2.2 Derivation of the generalized population balance equation

Following the Eulerian approach previously discussed for the continuous phase, we consider a fixed arbitrary control volume $\boldsymbol{\Lambda_\psi}$ in phase space. $\boldsymbol{\Lambda_\psi}$ is the union of three disjointed control volumes: $\boldsymbol{\Lambda_s}$ in particle size space, $\boldsymbol{\Lambda_u}$ in velocity state space and $\boldsymbol{\Lambda_x}$ in physical space. In deriving the number balance equation over this control volume, we follow the balance equation previously reported in Eq. (2.2.1). In this case, the accumulation rate Acc is the rate of change of the number of particles in the control volume; the convective term $(In - Out)$ is the net number flow rate of particles entering the control volume; and the generation rate Gen is the number of particles generated within the control volume per unit time. The number $N(t)$ of particles present at time t in the control volume $\boldsymbol{\Lambda_\psi}$ is:

$$N(t) = \int_{\Lambda_{\boldsymbol{x}}} \int_{\Lambda_{\boldsymbol{u}}} \int_{\Lambda_s} f_n(s, \boldsymbol{u}, \boldsymbol{x}, t) ds \, d\boldsymbol{u} \, d\boldsymbol{x} = \int_{\Lambda_{\boldsymbol{\psi}}} f_n(\boldsymbol{\psi}, t) d\boldsymbol{\psi} \tag{2.2.19}$$

where $\boldsymbol{\psi}$ is the phase-space position vector that combines s, $\boldsymbol{u}$ and $\boldsymbol{x}$**.** Let us now derive an expression for each term of Eq. (2.2.1). First, we can write:

$$Acc = \frac{N(t+dt) - N(t)}{dt} = \frac{d}{dt} \int_{\Lambda_{\boldsymbol{\psi}}} f_n(\boldsymbol{\psi}, t) d\boldsymbol{\psi} = \int_{\Lambda_{\boldsymbol{\psi}}} \frac{\partial}{\partial t} f_n(\boldsymbol{\psi}, t) d\boldsymbol{\psi} \tag{2.2.20}$$

The last passage in the equation above holds because $\boldsymbol{\Lambda_\psi}$ is fixed; that is, it is not a time-dependent integration domain.

Considering the physical space, the convective flow can be expressed as:

$$(In - Out)_{\boldsymbol{x}} = -\int_{\boldsymbol{\Lambda_s}} \int_{\boldsymbol{\Lambda_u}} \int_{\boldsymbol{\partial \Lambda_x}} f_n(s, \boldsymbol{u}, \boldsymbol{x}, t)\boldsymbol{u}.\, d\boldsymbol{S_x}\, d\boldsymbol{u}\, ds \tag{2.2.21}$$

where $\boldsymbol{\partial \Lambda_x}$ denotes the boundary of the physical-space domain $\boldsymbol{\Lambda_x}$. Using the Gauss theorem, Eq. (2.2.21) becomes:

$$(In - Out)_{\boldsymbol{x}} = -\int_{\boldsymbol{\Lambda_\psi}} \boldsymbol{\nabla_x}.\,(f_n(\boldsymbol{\psi}, t)\boldsymbol{u})d\boldsymbol{\psi} \tag{2.2.22}$$

Here, $\boldsymbol{\nabla_x}.$ is the divergence operator in physical space. Being an internal coordinate, $\boldsymbol{u}$ can be removed from the divergence sign, and the integrand in Eq. (2.2.22) could be rewritten as $\boldsymbol{u}.\boldsymbol{\nabla_x} f_n$.

Similar expressions can be obtained for the convective terms in velocity and size spaces. For the former, we obtain:

$$(In - Out)_{\boldsymbol{u}} = -\int_{\boldsymbol{\Lambda_\psi}} \boldsymbol{\nabla_u}.\,(f_n(\boldsymbol{\psi}, t)\dot{\boldsymbol{u}})d\boldsymbol{\psi} \tag{2.2.23}$$

where $\dot{\boldsymbol{u}}$ is the particle acceleration (assumed to be a known function of $\boldsymbol{\psi}$). For the contribution related to the particle size space, it is:

$$(In - Out)_s = -\int_{\boldsymbol{\Lambda_\psi}} \frac{\partial}{\partial s}(f_n(\boldsymbol{\psi}, t)G_s)d\boldsymbol{\psi} \tag{2.2.24}$$

where G_s is the growth rate (assumed to be a known function of $\boldsymbol{\psi}$).

The generation term accounts for events such as nucleation, aggregation and breakage. These events give rise to sudden appearance of particles as against what happens with the convective terms, where particles move gradually into and out of the control volume. We express this term as:

$$Gen = \int_{\boldsymbol{\Lambda_\psi}} h_n(\boldsymbol{\psi}, t)d\boldsymbol{\psi} \tag{2.2.25}$$

Putting all the terms together, we obtain:

$$\int_{\boldsymbol{\Lambda_\psi}} \frac{\partial}{\partial t} f_n(\boldsymbol{\psi}, t)d\boldsymbol{\psi} = -\int_{\boldsymbol{\Lambda_\psi}} \boldsymbol{\nabla_x}.\,(f_n(\boldsymbol{\psi}, t)\boldsymbol{u})d\boldsymbol{\psi} - \int_{\boldsymbol{\Lambda_\psi}} \boldsymbol{\nabla_u}.\,(f_n(\boldsymbol{\psi}, t)\dot{\boldsymbol{u}})d\boldsymbol{\psi} - \int_{\boldsymbol{\Lambda_\psi}} \frac{\partial}{\partial s}.\,(f_n(\boldsymbol{\psi}, t)G_s)d\boldsymbol{\psi} + \int_{\boldsymbol{\Lambda_\psi}} h_n(\boldsymbol{\psi}, t)d\boldsymbol{\psi} \tag{2.2.26}$$

Eq. (2.2.26), when re-arranged, becomes:

$$\int_{\boldsymbol{\Lambda_\psi}} \left[\frac{\partial}{\partial t} f_n(\boldsymbol{\psi}, t) + \boldsymbol{\nabla_x}.\,(f_n(\boldsymbol{\psi}, t)\boldsymbol{u}) + \boldsymbol{\nabla_u}.\,(f_n(\boldsymbol{\psi}, t)\dot{\boldsymbol{u}}) + \frac{\partial}{\partial s}.\,(f_n(\boldsymbol{\psi}, t)G_s) - h_n(\boldsymbol{\psi}, t)\right] d\boldsymbol{\psi} = 0 \tag{2.2.27}$$

Since this equation has to be satisfied for an arbitrary control volume, assuming that the integrand function is continuous, we conclude that it must be:

$$\frac{\partial}{\partial t} f_n(\boldsymbol{\psi}, t) = -\boldsymbol{\nabla}_{\boldsymbol{x}}.(f_n(\boldsymbol{\psi}, t)\boldsymbol{u}) - \boldsymbol{\nabla}_{\boldsymbol{u}}.(f_n(\boldsymbol{\psi}, t)\dot{\boldsymbol{u}}) - \frac{\partial}{\partial s}.(f_n(\boldsymbol{\psi}, t)G_s) + h_n(\boldsymbol{\psi}, t) \quad (2.2.28)$$

Eq. (2.2.28) is referred to as generalized population balance equation (GPBE). The term *generalized* indicates that the particle velocity is included in the set of independent variables that specify the particle state. The solution of Eq. (2.2.28) yields the function f_n, which completely characterizes the system, telling how the particles move in physical space, how their linear momenta evolve and how their sizes vary (sizes vary from the nucleus size to the final size of the particle). The GBPE is an eight-dimensional integro-partial-differential equation; thus, it is extremely difficult to solve. To simplify it, we impose some conditions as follows.

2.2.2.3 Simplified population balance equation

Like we did for the continuous phase, we impose the experimental conditions of a well-mixed batch reactor on the GPBE. In addition, the only particle internal coordinate of gold nanoparticles of interest in various applications is particle size. We also consider that the volume of the reactor is fixed. In the citrate synthesis method, the volume of the reacting mixture is fixed. Thus, we simplify the GPBE by imposing the following conditions:

- Only particle size is considered as the particle internal property.
- The batch reactor is perfectly mixed.
- The volume of the reactor is fixed.

We will consider how these conditions affect the GPBE.

First, only the particle size s is considered as particle internal property. This condition will reduce the dimensionality of eq. (2.2.28) from eight to five (because the three coordinates of the particle velocity are no longer considered as variables characterizing the particle state) and transform the generalized population balance equation to the more conventional population balance equation (PBE) often used to model crystallization processes. The PBE is obtained by integrating eq. (2.2.28) over the velocity space. This strategy would produce a mean velocity conditioned on the size, which is no longer an independent particle state coordinate. We implement this integral transform as follows:

$$\int_{\Omega_{\boldsymbol{u}}} \left[\frac{\partial}{\partial t} f_n + \boldsymbol{\nabla}_{\boldsymbol{x}}.(f_n\boldsymbol{u}) + \boldsymbol{\nabla}_{\boldsymbol{u}}.(f_n\dot{\boldsymbol{u}}) + \frac{\partial}{\partial v}.(f_n G_s) - h_n\right] d\boldsymbol{u} = 0 \quad (2.2.29)$$

The first term in eq. (2.2.29) is transformed as:

$$\int_{\Omega_{\boldsymbol{u}}} \frac{\partial}{\partial t} f_n(s, \boldsymbol{u}, \boldsymbol{x}, t)\, d\boldsymbol{u} = \frac{\partial}{\partial t} n(s, \boldsymbol{x}, t) \quad (2.2.30)$$

where n is the number of particles per size space volume per physical space volume, mathematically expressed as:

$$n(s, \boldsymbol{x}, t) \equiv \int_{\Omega_{\boldsymbol{u}}} f_n \, d\boldsymbol{u} \tag{2.2.31}$$

The second term is transformed as:

$$\int_{\Omega_{\boldsymbol{u}}} \boldsymbol{\nabla}_{\boldsymbol{x}} \cdot (f_n \boldsymbol{u}) \, d\boldsymbol{u} = \boldsymbol{\nabla}_{\boldsymbol{x}} \cdot \int_{\Omega_{\boldsymbol{u}}} (f_n \boldsymbol{u}) \, d\boldsymbol{u} = \boldsymbol{\nabla}_{\boldsymbol{x}} \cdot (n(s, \boldsymbol{x}, t) \langle \boldsymbol{u} \rangle_{av}) \tag{2.2.32}$$

where

$$\langle \boldsymbol{u} \rangle_{av} \equiv \frac{\int_{\Omega_{\boldsymbol{u}}} (f_n \boldsymbol{u}) d\boldsymbol{u}}{\int_{\Omega_{\boldsymbol{u}}} f_n d\boldsymbol{u}} = \frac{\int_{\Omega_{\boldsymbol{u}}} (f_n \boldsymbol{u}) d\boldsymbol{u}}{n(s, \boldsymbol{x})} \tag{2.2.33}$$

$\int_{\Omega_{\boldsymbol{u}}} (f_n \boldsymbol{u}) \, d\boldsymbol{u}$ and $n(s, \boldsymbol{x})$ are the first and the zeroth moments respectively of the NDF over the velocity space while $\langle \boldsymbol{u} \rangle_{av}$ is an average velocity conditioned on s. Velocity is no longer an independent variable in eq. (2.2.32).

The third term is transformed by splitting the triple integral into its components as:

$$\int_{\Omega_{\boldsymbol{u}}} \boldsymbol{\nabla}_{\boldsymbol{u}} \cdot (f_n \dot{\boldsymbol{u}}) \, d\boldsymbol{u} = \int_{-\infty}^{+\infty} \int_{-\infty}^{+\infty} \int_{-\infty}^{+\infty} \left[\frac{\partial}{\partial u_1} (f_n \dot{u}_1) + \frac{\partial}{\partial u_2} (f_n \dot{u}_2) + \frac{\partial}{\partial u_3} (f_n \dot{u}_3) \right] du_1 du_2 \, du_3 \tag{2.2.34}$$

If we take the innermost integral on the first term on the right-hand side of eq. (2.2.34), we have:

$$\int_{-\infty}^{+\infty} \frac{\partial}{\partial u_1} (f_n \dot{u}_1) du_1 = [f_n \dot{u}_1]_{-\infty}^{+\infty} \tag{2.2.35}$$

f_n declines rapidly as we move away from its mean and goes to zero when u_1 diverges. This makes eq. (2.2.35), and hence eq. (2.2.34), vanish.

For the transformation of the fourth term, as we did in eq. (2.2.32), we have

$$\int_{\Omega_{\boldsymbol{u}}} \frac{\partial}{\partial s} \cdot (f_n G_s) \, d\boldsymbol{u} = \frac{\partial}{\partial s} \int_{\Omega_{\boldsymbol{u}}} (f_n G_s) \, d\boldsymbol{u} = \frac{\partial}{\partial s} (n \langle G_s \rangle) \tag{2.2.36}$$

where

$$\langle G_s \rangle \equiv \frac{\int_{\Omega_{\boldsymbol{u}}} (f_n G_s) d\boldsymbol{u}}{\int_{\Omega_{\boldsymbol{u}}} f_n d\boldsymbol{u}} = \frac{\int_{\Omega_{\boldsymbol{u}}} (f_n G_s) d\boldsymbol{u}}{n(s, \boldsymbol{x})} \tag{2.2.37}$$

$\langle G_s \rangle$ is an average growth rate conditioned on s. It is a function of the particle-size and the position in the physical space.

The fifth term remains the expression for both source and death terms, contributed by nucleation and aggregation. It is transformed as:

$$H_n \equiv \int_{\Omega_{\boldsymbol{u}}} h_n \, d\boldsymbol{u} \tag{2.2.38}$$

Now, putting all the terms together, we have:

$$\frac{\partial}{\partial t} n + \boldsymbol{\nabla}_{\boldsymbol{x}} . (n\langle \boldsymbol{u} \rangle_{av}) + \frac{\partial}{\partial s} (n\langle G_s \rangle) - H_n = 0 \tag{2.2.39}$$

Next, we will apply the second assumption: the fluid-particle system is well-mixed. This implies that all the functions, including the NDF, do not depend on real-space coordinates: nothing changes in space. Thus, we will integrate eq. (2.2.39) over the physical space $\Omega_{\boldsymbol{x}}$ as:

$$\int_{\Omega_{\boldsymbol{x}}} \left[\frac{\partial}{\partial t} n + \boldsymbol{\nabla}_{\boldsymbol{x}} . (n\langle \boldsymbol{u} \rangle_{av}) + \frac{\partial}{\partial s} (n\langle G_s \rangle) - H_n \right] d\boldsymbol{x} = 0 \tag{2.2.40}$$

The first term,

$$\int_{\Omega_{\boldsymbol{x}}} \frac{\partial}{\partial t} n(s, \boldsymbol{x}, t) \, d\boldsymbol{x} = \frac{\partial}{\partial t} \bar{f}(s, t) \tag{2.2.41}$$

where $\bar{f}$ is the number of particles per size space volume, mathematically expressed as:

$$\bar{f}(s, t) \equiv \int_{\Omega_{\boldsymbol{x}}} n(s, \boldsymbol{x}, t) \, d\boldsymbol{x} \tag{2.2.42}$$

On the second term, the product $n\langle \boldsymbol{u} \rangle_{av}$ represents the particle flux. We distinguish a portion $\boldsymbol{\partial \Omega_{x,in}}$ of the physical boundary $\boldsymbol{\partial \Omega_x}$ through which particles enter the physical volume and a portion $\boldsymbol{\partial \Omega_{x,out}}$ through which particles leave the system. Other parts of the boundary are impervious to the transport of particles making the particle flux zero. Thus, the second term becomes:

$$\int_{\partial \Omega_{\boldsymbol{x}}} (n(s, \boldsymbol{x}) \langle \boldsymbol{u} \rangle_{av}) . d\boldsymbol{S}_{\boldsymbol{x}} = \int_{\partial \Omega_{x,in}} (n(s, \boldsymbol{x}) \langle \boldsymbol{u} \rangle_{av}) . d\boldsymbol{S}_{\boldsymbol{x}} + \int_{\partial \Omega_{x,out}} (n(s, \boldsymbol{x}) \langle \boldsymbol{u} \rangle_{av}) . d\boldsymbol{S}_{\boldsymbol{x}} \tag{2.2.43}$$

For a batch reactor, since the synthesis is usually carried out in a batch reactor, Eq. (2.2.43) is zero.

The third term:

$$\int_{\Omega_{\boldsymbol{x}}} \frac{\partial}{\partial s} (n\langle G_s \rangle) d\boldsymbol{x} = \frac{\partial}{\partial s} \int_{\Omega_{\boldsymbol{x}}} (n\langle G_s \rangle) d\boldsymbol{x} = \frac{\partial}{\partial s} \left(\bar{f} \langle G_s \rangle_{av} \right) \tag{2.2.44}$$

where

$$\langle G_s \rangle_{av} \equiv \frac{\int_{\Omega_{\boldsymbol{x}}} (n\langle G_s \rangle) d\boldsymbol{x}}{\int_{\Omega_{\boldsymbol{x}}} n d\boldsymbol{x}} = \frac{\int_{\Omega_{\boldsymbol{x}}} (n\langle G_s \rangle) d\boldsymbol{x}}{\bar{f}(s)} \tag{2.2.45}$$

$\langle G_s \rangle_{av}$ has now been averaged over both the velocity space and the physical space; it only depends on the particle-size.

The fourth term remains the expression for both source and death term, mathematically expressed as:

$$\bar{H}_n \equiv \int_{\Omega_x} H_n \, d\boldsymbol{x} \tag{2.2.46}$$

Thus, eq. (2.2.40) is written as:

$$\frac{\partial}{\partial t}\bar{f}(s) + \frac{\partial}{\partial s}\left(\bar{f}.\langle G_s\rangle_{av}\right) - \bar{H}_n = 0 \tag{2.2.47}$$

Next, we divide eq. (2.2.47) by the reacting volume V, which is fixed, as

$$\frac{1}{V}\frac{\partial}{\partial t}\bar{f}(s,t) + \frac{1}{V}\frac{\partial}{\partial s}\left(\bar{f}.\langle G_s\rangle_{av}\right) - \frac{1}{V}\bar{H}_n = 0 \tag{2.2.48}$$

Further, we write eq. (2.2.48) as:

$$\frac{\partial}{\partial t}f(s,t) + \frac{\partial}{\partial s}(f.\langle G_s\rangle_{av}) - H_V = 0 \tag{2.2.49}$$

where $f(s,t) \equiv \bar{f}(s,t)/V$ and $H_V \equiv \bar{H}_n/V$

Eq. (2.2.49) is the PBE, which can be employed to describe the size evolution in processes such as crystallization and nanoparticle synthesis (for instance, the citrate synthesis method). The PBE is unclosed because the growth term $\langle G_s\rangle_{av}$ and the net source term H_V are unknown. The birth and death terms that can affect GNPs, as revealed by the mechanisms, are the nucleation and aggregation processes. One needs to derive expressions that relate these terms (that is nucleation, growth and aggregation) to the NDF or its moments. Once this has been done, the problem of closure is overcome and the equation can be solved.

2.2.3 The closure problem for particles dispersed on the size

In this section, we address the closure problem. To do this, we derive the constitutive equations for nucleation, growth and aggregation.

2.2.3.1 Nucleation process

Nucleation is the generation of the smallest particles from the aqueous phase. These particles are called nuclei. If the nuclei do not have single size, being instead continuously distributed over the size coordinate, we model the nucleation process by employing a probability density function (PDF), denoted as $\pi_N(s|\boldsymbol{x},t)$. By definition, $\pi_N(s|\boldsymbol{x},t)ds$ gives the probability that a nucleus that appears at time t in the real-space point x have size in the differential range ds around the point s. Then, we can write:

$$H_N(s,\boldsymbol{x},t) = n_N(s,\boldsymbol{x},t)\pi_N(s|\boldsymbol{x},t) \tag{2.2.50}$$

Here $H_N(s,\boldsymbol{x},t)$ and $n_N(s,\boldsymbol{x},t)$ are defined so that $H_N(s,\boldsymbol{x},t)dsd\boldsymbol{x}$ gives the number of nuclei with size in the range ds around the point s generated per unit time in the real-space region $d\boldsymbol{x}$ around the point $\boldsymbol{x}$, while $n_N(s,\boldsymbol{x},t)d\boldsymbol{x}$ gives the number of nuclei with size s formed per unit time in the region $d\boldsymbol{x}$ around the point $\boldsymbol{x}$. If locally all the nuclei have equal size $s_N(\boldsymbol{x},t)$, it is:

$$\pi_N(s|\boldsymbol{x},t) = \delta[s - s_N(\boldsymbol{x},t)] \rightarrow H_N(s,\boldsymbol{x},t) = n_N(s,\boldsymbol{x},t)\delta[s - s_N(\boldsymbol{x},t)] \quad (2.2.51)$$

so that:

$$\int_0^\infty H_N ds = \int_0^\infty n_N(s,\boldsymbol{x},t)\delta[s - s_N(\boldsymbol{x},t)]ds = n_N[s_N(\boldsymbol{x},t),\boldsymbol{x},t] \quad (2.2.52)$$

This result confirms the physical interpretation of the function $n_N(s,\boldsymbol{x},t)$ given above. The closure problem is finding expressions for $n_N(s,\boldsymbol{x},t)$ and $\pi_N(s|\boldsymbol{x},t)$. Often Eq. (2.2.51) is employed, so that an expression for $s_N(\boldsymbol{x},t)$ is needed instead of the PDF; the nucleus size is then often assumed to be uniform and constant. For example, in Kumar et al. (2007) it is assumed that $s_N(\boldsymbol{x},t) = 2\ nm$.

The model for $n_N(s,\boldsymbol{x},t)$, on the other hand, depends on the mechanism of nucleation. Here, we report the classical nucleation theory model, because this is a classical model that has been used often in the literature in modelling nucleation (Mersman, 2001; Jones, 2000; Robb and Privman, 2008). However, this model is inconsistent with the mechanistic theories for the citrate synthesis of gold nanoparticles. As discussed in Section 2.1.5, these mechanistic theories are the organizer theory of Turkevich et al. (1951) and the seed-mediated mechanism of Wuithschick et al. (2015)). The nucleation models based on these theories will be presented later in Chapters 3 and 4, respectively.

The classical nucleation theory model is based on the mechanism of burst-nucleation and growth. By this mechanism, popularly called the Lamer model, the concentration of atomic gold builds up slowly to the saturation point, and then to a critical supersaturation level. After this level, additional increase in concentration leads to burst nucleation that immediately lowers the supersaturation level of gold in the solution below the critical supersaturation; thus, the nucleation process stops. The nuclei then grow by consuming atomic gold until the concentration returns to the saturation point. Lamer model is based on the classical nucleation theory; Robb and Privman (2008), for instance, used this approach to model the nucleation process in the synthesis. Below, we present the classical nucleation theory.

Classical nucleation theory (CNT)

CNT is the most common theoretical model used to understand the nucleation process. CNT postulates that nucleation only occurs in a supersaturated solution when statistical

fluctuation brings a number of monomers together required to form thermodynamically stable clusters, called nuclei. These nuclei grow and eventually appear as a new phase. If the nucleation takes place without any existing crystal or foreign object, the process is called homogeneous nucleation. If foreign objects or impurities are present, they provide sites that promote nucleation. This is called heterogeneous nucleation. Homogeneous and heterogeneous nucleation processes are classified as primary nucleation because they occur without solution-own crystals. In the presence of solution-own crystals, nucleation is even more enhanced. This is called secondary nucleation.

We discuss homogeneous nucleation below. Turkevich et al (1951) ruled out that the presence of impurities caused nucleation in the synthesis of gold nanoparticles by the citrate synthesis method. Also, we will not discuss secondary nucleation. The mechanism of secondary nucleation requires the crystal to provide a sufficient surface for nucleation to occur. Because precipitation crystals are small (order of nanometre), secondary nucleation is absent in precipitation (Sohnel and Garside, 1992) and then absent in nanoparticle nucleation.

Homogeneous nucleation

For molecules to nucleate in solution, their concentration must be higher than the saturation concentration C_{eq} (also called the equilibrium concentration). C_{eq} is the maximum amount of solute, at a particular temperature and pressure, that can dissolve in a solvent and form a homogeneous solution. In our case, the synthesis is carried out at a constant temperature in an aqueous solution. As the reactions progress, the concentration of atomic gold in the solution increases. When the concentration of solute C is below C_{eq}, the solution is undersaturated; in this case, all solute molecules are in a single phase with the solvent. At this stage, the solvent can still dissolve additional solute. When the concentration becomes equal to C_{eq}, the solution cannot dissolve any additional solute. Any additional molecules produced will exist in another phase; the solution is said to be supersaturated. These molecules fluctuate and form clusters. They can form clusters of two, three or more particles. However, these clusters also disintegrate into molecules; the solution is at the metastable region. As the concentration increases, fluctuation brings more molecules together and the cluster number increases until a stage when nucleation occurs. At this stage, the cluster continues to grow rather than disintegrate. If impurities are present, nucleation is facilitated. The supersaturation required for heterogeneous nucleation is lower than that of homogeneous nucleation. Even much lower supersaturation is required for nucleation when the system contains existing crystals (secondary nucleation). Figure 3.1 shows the separate regions of solubility.

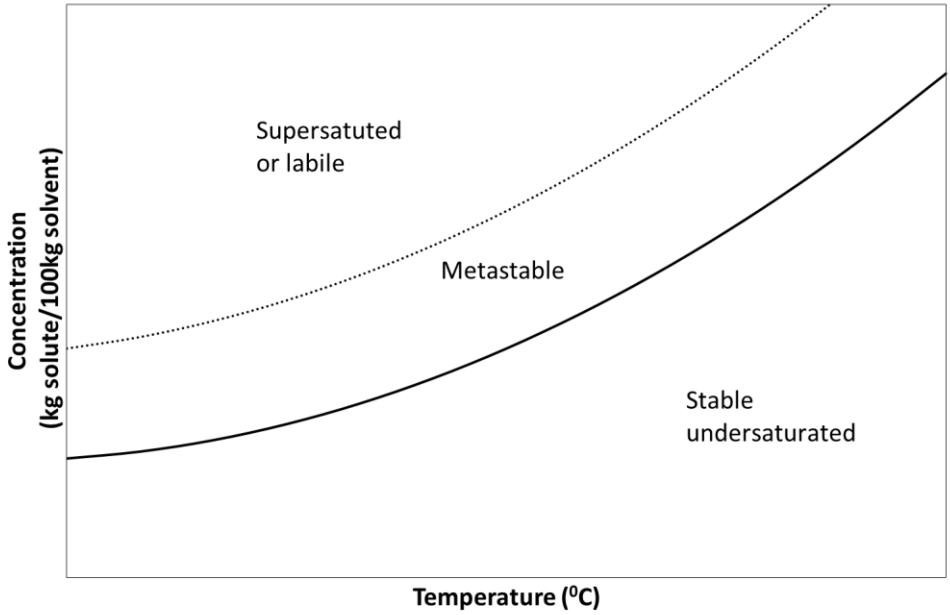

Figure 2.2.1 Showing the three separate regions of solubility. Figure from Jones (2002)

These regions are:

1. Undersaturated region – in this region, the solute concentration is below the saturation concentration and the solutes are wholly in solution.
2. Metastable region – in this region, the solute concentration is larger than the saturation concentration. The solution maintains its supersaturation for a certain period without nucleation. From the creation of supersaturation to the appearance of the first nucleus is the induction period. As supersaturation increases, the induction time is reduced. When the supersaturation reaches a certain point, nucleation becomes rapid. The gap between this point and the saturation point is referred to as the metastable width (Tung et al., 2009).
3. Labile region – in this region, the solutes nucleate rapidly. This rapid nucleation depletes solute concentration in the solution and quickly brings it back to the metastable region. The formed nuclei then grow by consuming the solute until the concentration returns to the saturation concentration.

In the following sections, we treat the models for the thermodynamics and kinetics of homogeneous nucleation, and use the model to understand how supersaturation affects it.

Thermodynamics of homogeneous nucleation

To determine if a solution will undergo homogeneous nucleation, we consider its chemical potential difference $\Delta\lambda$ given by (Liveri, 2006):

$$\Delta\lambda = \lambda_{sat} - \lambda_{sol} = bk_BT \ln\frac{c_{eq}}{c} = bk_BT \ln\frac{1}{\hat{S}} = -bk_BT \ln\hat{S} \quad (2.2.53)$$

where b is the dissociation number of a monomer (for example in the crystallization of $NaCl$, $b = 2$ as $NaCl$ dissociates into $Na^+ + Cl^-$), k_B Boltzmann constant, T the temperature, and $\hat{S}$ the supersaturation ratio. As $\hat{S}$ increases, the chemical potential difference increases.

The Gibb's free energy for the nucleation process will be the sum of the energy required to form the particle volume (bulk energy – exothermic) and the energy required to form the particle surface (surface energy – endothermic); it is given by:

$$\Delta G_{hom} = N\Delta\lambda + K_N N^{2/3}\gamma_s \quad (2.2.54)$$

where $K_N \equiv m_a\left(\frac{v_m}{m_v}\right)^{2/3}$; m_a and m_v are the area and volume shape factors; v_m is the monomer volume.

N is the number of monomers and γ_s is the interfacial surface energy for the cluster.

The magnitude of the exothermic term $N\Delta\lambda$ is proportional to N and increases with increasing $\hat{S}$. On the other hand, the magnitude of the endothermic term $K_N N^{2/3}\gamma_s$ is proportional to $N^{2/3}$. As $\hat{S}$ increases, N increases; the exothermic term increases faster than the endothermic term to generate the plot of ΔG_{hom} against N shown in Figure 2.2.2.

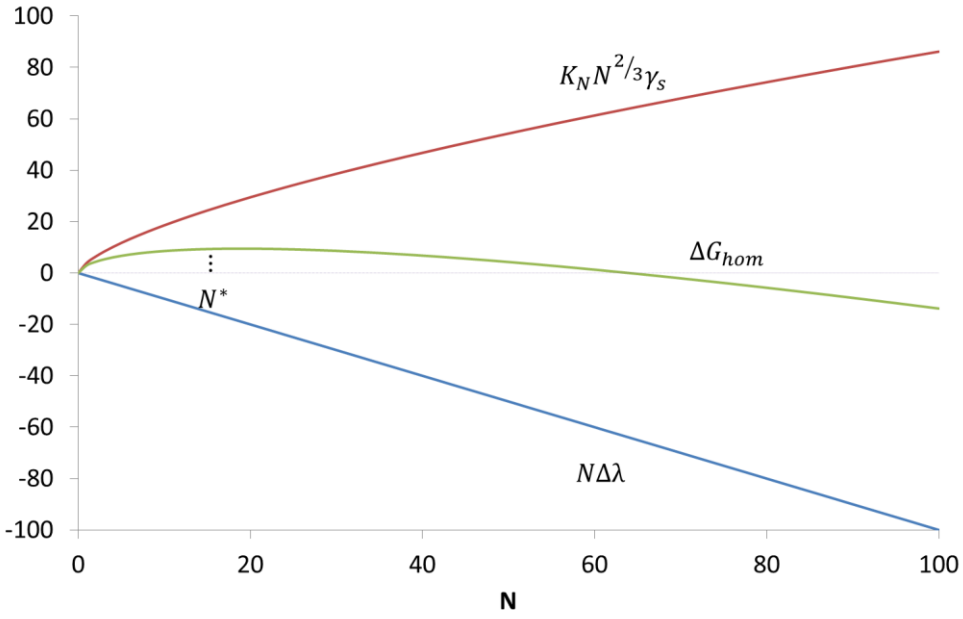

Figure 2.2.2 Dependence of the Gibbs free energy on N. Figure from Liveri (2006)

ΔG_{hom} is maximum at N^*, the critical nucleus. This maximum point is obtained by differentiating ΔG_{hom} in eq. (2.2.54) with respect to N and equating the result to zero. We have:

$$\Delta G^*_{hom} = \frac{4K_N^3\gamma_S^3}{27\Delta\mu^2} = \frac{4K_N^3\gamma_S^3}{27(bk_BT\ln\hat{S})^2} \quad (2.2.55)$$

$$N^* = \frac{-8K_N^3\gamma_S^3}{27\Delta\mu^3} = \frac{8K_N^3\gamma_S^3}{27(bk_BT\ln\hat{S})^3} \quad (2.2.56)$$

Eqs. (2.2.55) and (2.2.56) reveal that as the supersaturation increases, the number of molecules required to form a thermodynamically stable nucleus decreases; the energy barrier similarly decreases. Let us now proceed to the kinetics of nucleation and obtain an expression for the rate of homogeneous nucleation.

Kinetics of homogenous nucleation

Assuming that a nucleus is formed by the following steps:

$A_1 + A_1 \rightarrow A_2$

$A_2 + A_1 \rightarrow A_3$

$\vdots$

$A_{n-1} + A_1 \rightarrow A_n$ (a nucleus)

This scheme is described by the successive addition of monomers. Aggregation is not allowed i.e.

$A_i + A_j \rightarrow A_{i+j}$ where $i, j \geq 2$.

The critical nucleus is thermodynamically stable. Once formed, it will grow rather than disintegrate if another molecule impinges on it; hence, we have nucleation. The rate of nucleation n_N will be equal to the product of the number concentration of the critical nuclei and the rate of impingement of monomers; this is mathematically expressed as (Sohnel and Garside, 1992):

$$n_N = k_N * C_{N^*} * Z \quad (2.2.57)$$

where C_{N^*} is the number concentration of the critical nuclei, k_N is the impingement rate of monomers on the critical nuclei and Z is the Zeldovich factor. We obtain the expression for each term below.

If we assume that the cluster size distribution C_N is caused by random collisions of monomers and can be described by a Boltzmann distribution, we obtain

$$C_N = C_1 \exp\left(-\frac{\Delta G_{hom_N}}{k_B T}\right) \tag{2.2.58}$$

where C_1 is the number concentration of monomers, ΔG_{hom_N} is the energy needed to form a cluster of N monomers. Before the critical nuclei, ΔG_{hom_N} increases as N increases; so, C_N decreases following an exponential decay. For the critical nuclei, we have

$$C_{N^*} = C_1 \exp\left(-\frac{\Delta G^*_{hom}}{k_B T}\right) = C_1 \exp\left(-\frac{4K_N^3 \gamma_S^3}{27 k_B T (b k_B T \ln \hat{S})^2}\right) \tag{2.2.59}$$

As expected, this concentration increases with increasing supersaturation.

k_N is the rate at which monomers impinge on the critical nuclei. If we assume that monomers impinge by diffusion, Fick's law holds. In the radial coordinate, we have:

$$k_N = D_0 A \frac{dC_1}{dx} \tag{2.2.60}$$

where D_0 is the diffusion coefficient of monomers, A is the area of the critical cluster given as $4\pi x^2$ for a sphere (in this case, x is the radial coordinate), and dC_1/dx is the concentration gradient of the monomers as they approach the critical cluster. Before the start of nucleation, the concentration of monomer remains the same so we assume their impingement rate k_N is constant. Thus:

$$k_N = D_0 4\pi x^2 \frac{dC_1}{dx} \tag{2.2.61}$$

Integrating Eq. (2.2.61), we have

$$C_1 = -\frac{k_N}{D_0 4\pi x} + \mathcal{M} \tag{2.2.62}$$

$\mathcal{M}$ is the constant of integration. Say (as a boundary condition) at $x = r$ (the radius of the cluster), $C_1 = 0$, by this, we imply that every monomer that hits the critical nuclei is incorporated (in other words, the incorporation rate is much larger than the diffusion rate); and at $x = r + \delta$, $C_1 = C_1^0$ (C_1^0 is the bulk concentration of the monomers), by this, we imply that diffusion only occurs across δ. Eq. (2.2.62) becomes

$$M = 0 + \frac{k_N}{D_0 4\pi r} \tag{2.2.63}$$

$$C_1 = \frac{k_N}{D_0 4\pi}\left[\frac{1}{r} - \frac{1}{x}\right] \tag{2.2.64}$$

By the second boundary condition, we have:

$$C_1 = \frac{k_N}{D_0 4\pi}\left[\frac{1}{r} - \frac{1}{r+\delta}\right] \tag{2.2.65}$$

For nanoparticles, r is small; thus we can assume δ is much larger than r. Eq. (2.2.65) becomes

$$k_N = D_0 4\pi r C_1 \tag{2.2.66}$$

$k_N * C_{N^*}$ gives the rate for the interaction between monomer and the critical cluster; it calculates the rate at equilibrium.

Z corrects for the imbalance from equilibrium. Mersmann et al (2001) reported an expression for Z for the critical nucleus N^* as

$$Z = \frac{1}{N^*}\sqrt{\frac{\Delta G^*_{hom}}{3\pi k_B T}} \tag{2.2.67}$$

Inserting Eqs (2.2.59), (2.2.66) and (2.2.67) for C_{N^*}, k_N and Z respectively in Eq. (2.2.57), we have

$$n_N = D_0 4\pi r \frac{1}{N^*}\sqrt{\frac{\Delta G^*_{hom}}{3\pi k_B T}} {C_1}^2 \exp\left(-\frac{4K_N^3\gamma_S^3}{27k_BT(bk_BT\ln\hat{S})^2}\right) \tag{2.2.68}$$

We can as well relate C_1 to the molar concentration of solute, C as

$$C_1 = \frac{C - C_{eq}}{\rho^* \frac{\pi}{6} {s_0}^3} \tag{2.2.69}$$

where C_{eq} is the solubility of the solute, ρ is the molar density of the solute and s_0 is the diameter of a monomer. When we substitute for C_1 in eq. (2.2.68), we have

$$n_N = k_o \exp\left(\frac{-4K_N^3\gamma_S^3}{27(k_BT)^3(b\ln\hat{S})^2}\right) \tag{2.2.70}$$

where:

$$k_o = D_0 2\pi s_0 \sqrt{\frac{\Delta G^*_{hom}}{3\pi k_B T}} \left(\frac{C - C_{eq}}{\rho^* \frac{\pi}{6} {s_\alpha}^3}\right)^2 \tag{2.2.71}$$

In the literature, other expressions for k_o are reported. For example, Sohnel and Garside (1992) reported:

$$k_o = \frac{D_0}{{s_0}^5 N^*}\left[\frac{4\Delta G^*_{hom}}{3\pi k_B T}\right]^{\frac{1}{2}} \tag{2.2.72}$$

which is simpler than Eq. (2.2.71). Using Eq. (2.2.72), we have

$$n_N(s, \boldsymbol{x}, t) = \frac{D_0}{{s_0}^5 N^*}\left[\frac{4\Delta G^*_{hom}}{3\pi k_B T}\right]^{\frac{1}{2}} \exp\left(\frac{-4K_N^3\gamma_S^3}{27(k_BT)^3(b\ln\hat{S})^2}\right) \tag{2.2.73}$$

The dominant effect of the degree of supersaturation on the time required for spontaneous nucleation to take place can be calculated using eq. (2.2.73). For a cubic critical nucleus of $BaSO_4$ (Sohnel and Garside, 1992), $T = 25^0C$, $Y = 0.233\ kg/mol$, $\rho = 4500\ kgm^{-3}$, $\gamma_s = 0.136\ Jm^{-2}$, $D_0 = 10^{-9}m^2s^{-1}$ and $b = 1$.

For a cube,

$K_N = 6{v_0}^{2/3}$; where the molecular volume, $v_0 = \frac{Y}{\rho \times N_A} = \frac{0.233}{4500 \times 6.023 \times 10^{23}} = 8.60 \times 10^{-23}m^3$; $K_N = 1.169 \times 10^{-14}$

s_0 can be calculated using $s_0 = {v_0}^{1/3} = (8.60 \times 10^{-23}m^3)^{1/3} = 4.41 \times 10^{-10}m$.

The induction time t_{ind}, the time required by the first nucleus to form, is given as (Sohnel and Garside, 1992):

$$t_{ind} = \frac{1}{n_N V} \qquad (2.2.74)$$

where V is the volume of the solution and we take it as $1\ m^3$ for this exercise.

Table 2.2.1: Comparison of the nucleation rates with supersaturation. Data from Sohnel and Garside (1992)

$\hat{S}$	k_o	exp	n_N	t_{ind}	
1	0	∞	0	∞	
10	4.48E+36	5.1E-176	2.3E-139	1.40E+131	yrs
100	1.79054E+37	1.5E-44	2.69E-07	43.08736	days
120	1.93512E+37	2.82E-41	0.000546	30.52583	mins
140	2.06E+37	8.73E-39	0.179917	5.558126	sec

Table 2.2.1 shows the nucleation rate of $BaSO_4$ as the supersaturation increases from 1 to 140. It can be seen that the metastable region would be $1 \leq \hat{S} \leq 120$. Within this region, the induction time for the first crystal ranges from infinity to several years and then to days. The characteristic time for homogeneous nucleation at $\hat{S} = 100$ is 43 days. One will have to wait for that long, mathematically, before nucleation can ever occur. Once the value of $\hat{S}$ is increased further to 140, the characteristic time is reduced to ~6s. The metastable curve in Fig. 2.2.1 (and so the width of the metastable region) depends on the time that one is willing to wait, for nuclei to appear. It is a subjective quantity, not an objective one. The saturation curve, conversely, is an objective quantity. By further increasing $\hat{S}$, nucleation becomes spontaneous and uncontrollable.

To employ the CNT, we need the solubility curve. For metal nanoparticles synthesis, Polte (2015) argued that the solubility of the metal atoms in a solvent such as water is not exactly known; their solubility should be extremely small (effectively $C_{eq} = 0$) (Polte, 2015). So, Polte (2015) assumed that supersaturation effectively occurs as long as metal atoms are in the solution (i.e. as long as all the reduced metal atoms are not part of a cluster or particle). Consequently in modelling nucleation in gold nanoparticles synthesis, Kumar et al. (2007) (the only past authors to have modelled the citrate synthesis method) employed a different approach. This approach involves accounting for the chemical reaction, producing nuclei. As this reaction depends on the mechanism, we report the submodels for nucleation when modelling the mechanistic theories of the citrate synthesis, in Chapters 3 and 4.

2.2.3.2 Growth process

Both Turkevich et al (1951) and Wuithschick et al (2015) proposed the growth process as a step in their respective mechanisms. Unlike aggregation, it involves the addition of new monomers into the characteristic arrangement of a particle. Growth typically follows an initial stage of either homogeneous or heterogeneous (surface catalyzed) nucleation, unless a "seed" crystal (secondary nucleation), purposely added to start the growth, is present. The presence of available monomers due to supersaturation and of the crystal surface is therefore essential for growth to occur. Since it involves the attachment of monomers on the surface, certain factors affect the growth rate. Chief amongst these is supersaturation which indicates the availability of monomers. Growth models contain terms that show their dependence on supersaturation. Other factors are crystal size, temperature, pH, and the presence of impurities. As we will see, crystal size is a common parameter to most growth models indicating how size generally affects growth.

As discussed in the previous section on the classical nucleation theory, following burst-nucleation, growth would occur by consuming atomic gold until the concentration returns to the saturation point. Gold atoms would move from the bulk of the solution unto the particle surface either solely by diffusion or a combination of convection and diffusion and then integrate into the surface of the particles. Mass transfer or surface integration or a combination of both mechanisms can control the growth process. For growth controlled by mass transfer (that is, mass transfer limited), the growth rate decreases with size while for growth rate controlled by surface integration, the rate is independent of size (Turkevich et al., 1951; Viswanatha and Sarma, 2007). The experiments by Turkevich et al (1951) revealed growth controlled by surface integration while that by Wuithschick et al (2010) revealed that both mechanisms (i.e. diffusion and surface-integration controlled) are present at different stages of the synthesis. Also, temperature affects the diffusivity of monomers, a term in the diffusion-controlled growth models. The activity of a substance can be influenced by pH and

the presence of impurities. In the modelling of the seed-mediated mechanism presented in Chapter 4, the gold atoms that grow the particles come from $AuCl_3(OH)^-$. The mixture pH determines the amount of $AuCl_3(OH)^-$, hence the growth rate. Similarly, impurities can be deposited on the particle surface, preventing further growth.

In the bulk of the solution, the solute has the maximum concentration, corresponding to the supersuration of the solution. Unless the solution is perfectly stagnant, the fluid convection transports monomers (solute) from the bulk to around the particle surface, called the boundary layer. Outside the boundary layer, convection dominates, while inside the boundary layer convection and diffusion are both important (in the direction normal to the particle surface diffusion is expected to be dominant). The attachment is enhanced by either a high concentration of monomers that gather on the surface or a cavity on the particle surface that can easily accommodate monomers, called the kink site. These two processes (i.e. mass transport and surface integration) occur in series and affect one another; the slower determines the growth rate. Figure 2.2.3 shows how the concentration of solute in the solution varies around a growing particle. The driving forces for mass transfer (convection and diffusion) and surface integration are $c - c'$ and $c' - c_{eq}$, respectively, where $c =$ bulk concentration, $c' =$ concentration at the particle surface, $c_{eq} =$ equilibrium concentration (Garside and Sohnel, 1992). Curve 1 represents the profile of a surface-integration-controlled growth. The concentration gradient between the particle surface and the bulk solution is so small as to be negligible; the characteristic time for diffusion is very small when compared to that of surface integration. In this case, increasing the bulk concentration will increase the driving forces for both diffusion and surface integration of monomers thereby enhancing the growth process. Curve 2 represents the profile of diffusion-controlled growth. The characteristic time of the diffusion process is far larger than that of the surface-integration process. Curve 3 represents what happens when both processes have comparable characteristic times; neither mechanism dominates.

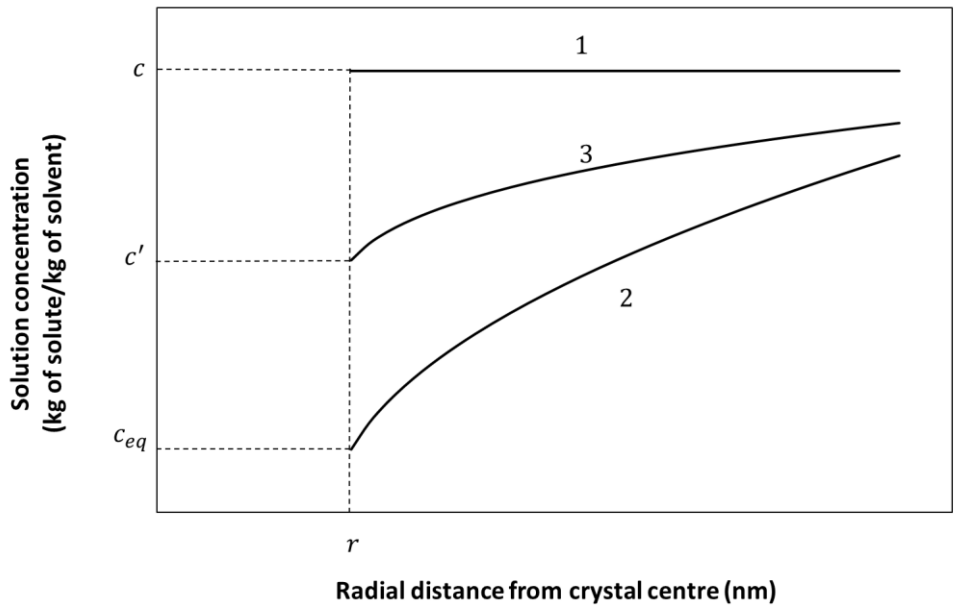

Figure 2.2.3 Solute concentration within the boundary layer surrounding a particle when growth is controlled by surface reaction (1), by mass transfer in the solution (2) and by both mechanisms (3). $c =$ bulk concentration, $c' =$ concentration at the particle surface, $c_{eq} =$ equilibrium concentration (Garside and Sohnel, 1992).

In a solid-liquid system, c_{eq} is the maximum amount of solid (usually called the solute) that can be in solution at a given temperature and pressure. This concentration is also called the solubility; its value can be read from the solubility curve of the solute in solution. For solid-liquid systems such as NaCl-water, it increases with temperature (Mullin, 2001). For metal nanoparticles, however, as previously mentioned, Polte (2015) argued that $c_{eq} = 0$. Nevertheless, mass transfer or surface integration or a combination of both mechanisms controls the growth process. We consider how to model each growth mechanism below.

Growth controlled by mass transfer

Monomers move from the bulk solution to the particle surface through the convection and diffusion processes. We can enhance this mass transfer if we stir the solution vigorously as in the case of a well-mixed solution, but monomers still have to diffuse through the boundary layer before reaching the crystal surface. We report the model for the diffusion-controlled process below.

Diffusion is governed by Fick's law, which reads:

$$\mathrm{j} = -D_0 A \frac{\partial C}{\partial r} \qquad \text{(diffusive molar flow rate of solute in solution)} \qquad (2.2.75)$$

where D_0 is the diffusivity of the solute in the solvent, A is the surface area of a single spherical particle and $\partial C/\partial r$ is the partial derivative of the solute concentration with respect to the radial coordinate r.

In this case, we assume that the boundary layer thickness is much larger than the particle radius and that convection is absent within the boundary layer. Thus, monomers move by diffusion from the bulk solution to the particle surface. Also, the particle is assumed to be spherical, and by symmetry, the concentration of the solute is assumed to depend on the radial coordinate only. We can express j as the product of the molar density of the solute in the solid phase ρ, the particle surface area A and growth rate G_s:

$$-\mathrm{j} = \rho A G_s \tag{2.2.76}$$

In this equation, the amount of solute diffusing grows the particle.

Eq. (2.2.75) can be reformulated in terms of the growth rate as:

$$G_s = D_0 V_m \frac{\partial C}{\partial r} \tag{2.2.77}$$

where V_m denotes the molar volume of solute, that is, the inverse of ρ. The concentration profile, and in turn the concentration gradient can be obtained by writing (and solving) a mass balance on the solute written in the polar coordinates for only the radial component. In this derivation, the term $(In - Out)$ in Eq. (2.2.1) is only caused by diffusion and the term Gen is zero. The mass balance thus is:

$$\int \frac{\partial C}{\partial t} 4\pi r^2 dr = -\int \frac{\partial}{\partial r} . \left(D_0 4\pi r^2 \frac{\partial C}{\partial r} \right) dr \tag{2.2.78}$$

When re-written, we have:

$$\frac{\partial C}{\partial t} = -D_0 \frac{1}{r^2} \frac{\partial}{\partial r} \left(r^2 \frac{\partial C}{\partial r} \right) \tag{2.2.79}$$

Let us assume steady state, so that $\partial C/\partial t = 0$. To justify this assumption, we consider the time scales of the concentration profile evolution and of the growth process. If the former is much smaller than the latter - that is, if the growth process is very slow compared with the time the concentration profile takes to change significantly - then the process can be modelled using the *quasi-steady-state approximation*. Then, it is:

$$\frac{d}{dr} \left(r^2 \frac{dC}{dr} \right) = 0 \tag{2.2.80}$$

In this equation, the concentration is a function of the radius only.

Integrating Eq. (2.2.80), yields:

$$\frac{dC}{dr} = \frac{\mathcal{M}}{r^2} \tag{2.2.81}$$

A further integration gives:

$$C(r) = \mathcal{N} - \frac{\mathcal{M}}{r} \tag{2.2.82}$$

where $\mathcal{M}$ and $\mathcal{N}$ represent integration constants, whose values one finds by introducing boundary conditions.

At $r = r_c$ (particle radius), $C = C_{eq}$. The assumption here is that the concentration at the surface is at equilibrium as the rate of surface integration is very fast.

At $r = r_c + \delta$, $C = C_0$. Here δ is the thickness of the boundary layer; its value is much larger than the particle radius as previously assumed (mathematically one can take it to be infinite; the solution of the differential equation is insensitive to the value chosen for δ, as long as $\delta/r_c \gg 1$) and C_0 is the bulk concentration.

Thus, we have

$$\frac{C - C_{eq}}{C_0 - C_{eq}} = \left(1 + \frac{r_c}{\delta}\right)\left(1 - \frac{r_c}{r}\right) \tag{2.2.83}$$

Differentiating gives:

$$\frac{dC}{dr} = \left(\frac{r_c}{r^2}\right)\left(1 + \frac{r_c}{\delta}\right)(C_0 - C_{eq}) \tag{2.2.84}$$

At $r = r_c$

$$\frac{dC}{dr} = \left(\frac{1}{r_c}\right)\left(1 + \frac{r_c}{\delta}\right)(C_0 - C_{eq}) \tag{2.2.85}$$

Substituting this equation into (2.2.77), we have

$$G_s = \frac{D_0 V_m}{r_c}\left(1 + \frac{r_c}{\delta}\right)(C_0 - C_{eq}) \tag{2.2.86}$$

Since diffusion layer thicknesses are typically of the order of microns, in the case of nanoparticles, $\delta \gg r_c$ (Viswanatha and Sarma, 2007). Thus, Eq. (2.2.86) reduces to:

$$G_s = \frac{D_0 V_m}{r_c}(C_0 - C_{eq}) \tag{2.2.87}$$

From eq. (2.2.87), the concentration drops from C_0 to C_{eq} over a distance of the order of the particle radius. This means that far away from the particle surface (say, at a distance equal to ten particle radii) the concentration is almost constant, So, as long as we choose δ much larger than the particle radius, the value of δ is irrelevant.

Eq. (2.2.87) can be used when $\delta \gg r_c$. We encounter this situation when either r_c is very small, as in nanoparticles, or δ is very large, which is the case in a virtually motionless medium.

For other cases, however, δ takes on a clear physical meaning: it is the thickness of the layer within which the solute concentration varies significantly (in other words, it represents the length scale of the mass transfer process). Its value, consequently, has to be determined. Eq. (2.2.87) can be related to the overall mass transfer coefficient as:

$$G_s = \frac{D_0 V_m}{r_c}\left(1 + \frac{r_c}{\delta}\right)(C_0 - C_{eq}) \equiv k_{MT}(C_0 - C_{eq})V_m \qquad (2.2.88)$$

From which,

$$\frac{D_0}{r_c}\left(1 + \frac{r_c}{\delta}\right) = k_{MT} \qquad (2.2.89)$$

One can estimate the value of k_{MT} using the empirical relations available in the literature, expressed in terms of the Sherwood (Sh), Reynolds (Re) and Schmidt (Sc) numbers. Cussler (2009) reports these relations as:

$$Sh = 2 + 0.6(Re)^{1/2}(Sc)^{1/3} \text{ where } \quad Sh = \frac{2k_{MT}r_c}{D_0},\ Re = \frac{2\rho_f u_f r_c}{\mu} \text{ and } Sc = \frac{\mu}{\rho_f D_0} \qquad (2.2.90)$$

where ρ_f and μ, are the fluid density and viscosity, respectively; u_f is the magnitude of the velocity of the fluid flowing around the particle.

Considering Eqs. (2.2.89) and (2.2.90), when the fluid is stationary i.e. $u_f = 0, Sh$ will be equal to 2 (its minimum value) and δ will tend to infinity (as expected). Eq. (2.2.87) can therefore be used, as suggested before. But for finite values of u_f, and therefore of Re, δ is finite and decreases with Re. When mixing becomes vigorous, the mass transfer coefficient k increases, and so δ decreases. So, the mass transfer becomes very efficient and the bottleneck is now the surface integration.

Growth controlled by surface integration

The transportation of solute in solution unto the boundary layer of a crystal is followed by surface integration. The growth process is surface integration controlled when the mass transfer coefficient is much larger than the surface integration rate constant (in other words, the integration reaction is slower than the mass transfer processes). Using the concept of resistances, the inverse of rate constants, we quantitatively compare growth controlled by mass transfer or surface integration or both in Appendix B. For details about this comparison, we refer the reader to Appendix B. Here, we write a material balance assuming that the accumulation on the particle is only caused by surface integration. We assume that

D_0 is very large thereby making the concentration gradient due to mass transfer almost zero. The surface integration is proportional to the product of particle surface and concentration gradient (usually raised to a number). Eq. (2.2.1) can be written as:

$$\frac{d}{dt}\left[\frac{4}{3}\pi r^3.\rho\right] = k_{SI}\left(C_0 - C_{eq}\right)^m 4\pi r^2 \tag{2.2.91}$$

where k_{SI} and m are the reaction growth rate constant and order of the reaction, respectively.

Simplifying this equation yields:

$$G_s = 2\frac{dr}{dt} = 2\frac{k_{SI}}{\rho}\left((C_0 - C_{eq})\right)^m \tag{2.2.92}$$

Considering Eq. (2.2.92), G_s is independent of the real-space, velocity-space, size-space. Thus, $G_s = \langle G_s \rangle = \langle G_s \rangle_{av}$.

In modelling the growth process for the citrate synthesis method, Kumar et al. (2007) employed surface-integration-controlled model, arguing that D_0 is very large for nanoparticles synthesis. We report their expression in Chapter 3, on modelling the Turkevich organizer theory.

For the seed-mediated mechanism, on the other hand, we investigate the experimental data of Polte et al. (2010) in Chapter 4, to arrive at the growth controlling mechanism and hence the corresponding growth model.

2.2.3.3 Aggregation process

The work by Polte et al (2010) corroborated previous suggestions by Chow and Zukoski (1994) that GNPs aggregate during the synthesis by the citrate reduction method. Nanoparticles aggregate when some smaller nanoparticles come together to form a bigger nanoparticle. This process leads to both the disappearance of smaller particles (a death term) and the appearance of bigger particles (a source term). Although we can imagine that any number of particles can come together and aggregate, binary aggregation is the most probable. Therefore, we will restrict our model to binary aggregation and consider both source and death terms, represented as H^+ and H^- respectively.

The number of particle pairs where the first particle has size in the range $d\bar{s}$ around the size $\bar{s}$ and is located in the region $d\overline{\boldsymbol{x}}$ around the point $\overline{\boldsymbol{x}}$, and the second particle has size in the range $d\hat{s}$ around the size $\hat{s}$ and is located in the region $d\hat{\boldsymbol{x}}$ around the point $\hat{\boldsymbol{x}}$ is given by the following expression, which is valid if the particles are statistically unrelated:

$$f(\bar{s}, \overline{\boldsymbol{x}}, t) f(\hat{s}, \hat{\boldsymbol{x}}, t) d\bar{s} d\hat{s} d\overline{\boldsymbol{x}} d\hat{\boldsymbol{x}} \tag{2.2.93}$$

Some of these pairs aggregate. The fraction of this number that on average does so is expressed by means of an aggregation frequency and is defined to be:

$$\omega_A(\bar{s},\hat{s},\overline{\boldsymbol{x}},\widehat{\boldsymbol{x}},t)f(\bar{s},\overline{\boldsymbol{x}},t)f(\hat{s},\widehat{\boldsymbol{x}},t)d\bar{s}d\hat{s}d\overline{\boldsymbol{x}}d\widehat{\boldsymbol{x}} \tag{2.2.94}$$

The particles generated by the aggregation process have size in the range ds around the point s and lie in the differential region $d\boldsymbol{x}$ around the point $\boldsymbol{x}$. If we assume that two particles can aggregate solely if they find themselves in the same differential region of real space, as physical intuition suggests, then also the particles generated lie in the same real-space region, and so it is:

$$\overline{\boldsymbol{x}} \equiv \widehat{\boldsymbol{x}} \equiv \boldsymbol{x} \qquad \rightarrow \qquad \omega_A(\bar{s},\hat{s},\overline{\boldsymbol{x}},\widehat{\boldsymbol{x}},t) = \widetilde{\omega}_A(\bar{s},\hat{s},t)\delta(\overline{\boldsymbol{x}}-\boldsymbol{x}) \tag{2.2.95}$$

The fraction of particle pairs that on average aggregates, the first particle having size in the range $d\bar{s}$ around $\bar{s}$ and the second having size in the range $d\hat{s}$ around $\hat{s}$, with both particles lying in the region $d\boldsymbol{x}$ around the point $\boldsymbol{x}$, can be expressed as follows:

$$\widetilde{\omega}_A(\bar{s},\hat{s},t)f(\bar{s},\overline{\boldsymbol{x}},t)f(\hat{s},\boldsymbol{x},t)\delta(\overline{\boldsymbol{x}}-\boldsymbol{x})d\bar{s}d\hat{s}d\overline{\boldsymbol{x}}d\boldsymbol{x} \tag{2.2.96}$$

The size of the particles generated can be easily calculated. If we assume that all the particles have the same density and shape factor, we can write:

$$s^3 = \bar{s}^3 + \hat{s}^3 \tag{2.2.97}$$

Now, to obtain the total number of particles with size in the range ds around the size s located in the region $d\boldsymbol{x}$ around the point $\boldsymbol{x}$ generated by the aggregation process, we must integrate Eq. (2.2.96) over $\bar{s}$, letting $\bar{s}$ span the interval $(0, s)$ and making $\hat{s}$ vary accordingly so as to satisfy Eq. (2.2.97), and over $\overline{\boldsymbol{x}}$, letting the latter span the entire space. We then need to divide by 2 to eliminate the redundancy in the calculation (the integral considers the contribution of each particle pair twice; for more details, we refer to the literature, for instance to Ramkrishna, 2000). The result is:

$$H_A^+(s,\boldsymbol{x},t)dsd\boldsymbol{x} = (1/2)\int_0^s \widetilde{\omega}_A(\bar{s},\hat{s},t)f(\bar{s},\boldsymbol{x},t)f(\hat{s},\boldsymbol{x},t)d\bar{s}d\hat{s}d\boldsymbol{x} \tag{2.2.98}$$

The left-hand side of this equation is in terms of the variable s, whereas the right-hand side is in terms of the variable $\hat{s}$. However, for a fixed value of $\bar{s}$, these two variables are related via Eq. (2.2.97). We can thus change variable and write Eq. (2.2.98) as follows:

$$H_A^+(s,\boldsymbol{x},t)dsd\boldsymbol{x} = (1/2)\int_0^S \widetilde{\omega}_A(\bar{s},\hat{s},t)f(\bar{s},\boldsymbol{x},t)f(\hat{s},\boldsymbol{x},t)|\partial_s\hat{s}(s,\bar{s})|d\bar{s}dsd\boldsymbol{x} \tag{2.2.99}$$

Since it is:

$$|\partial_s\hat{s}(s,\bar{s})| = \left|(s^3-\bar{s}^3)^{-2/3}\right|s^2 \tag{2.2.100}$$

we finally obtain:

$$H_A^+(s,\boldsymbol{x},t)dsd\boldsymbol{x} = (s^2/2)\int_0^s \widetilde{\omega}_A[(\bar{s},\hat{s}(s,\bar{s}),t)]f(\bar{s},\boldsymbol{x},t)f[\hat{s}(s,\bar{s}),\boldsymbol{x},t)](s^3-\bar{s}^3)^{-2/3}d\bar{s}dsd\boldsymbol{x} \tag{2.2.101}$$

This is again for the particles with size in the range ds around s. A part of these particles, however, aggregates; this leads to the following loss:

$$H_A^-(s,\boldsymbol{x},t)dsd\boldsymbol{x} = f(s,\boldsymbol{x},t)\int_0^\infty \widetilde{\omega}_A[(\bar{s},\hat{s}(s,\bar{s}),t)]f(\bar{s},\boldsymbol{x},t)d\bar{s}dsd\boldsymbol{x} \tag{2.2.102}$$

The expression above gives the number of particles with size in the range ds around s that aggregate per unit time in the region $d\boldsymbol{x}$ around the real-space point $\boldsymbol{x}$. We then write:

$$\begin{aligned} &H_A(s,\boldsymbol{x},t) = \\ &(s^2/2)\int_0^s \widetilde{\omega}_A[(\bar{s},\hat{s}(s,\bar{s}),t)]f(\bar{s},\boldsymbol{x},t)f[\hat{s}(s,\bar{s}),\boldsymbol{x},t)](s^3-\bar{s}^3)^{-2/3}d\bar{s} - \\ &f(s,\boldsymbol{x},t)\int_0^\infty \widetilde{\omega}_A[(\bar{s},\hat{s}(s,\bar{s}),t)]f(\bar{s},\boldsymbol{x},t)d\bar{s} \end{aligned} \tag{2.2.103}$$

This is the number of particles which aggregation forms per unit time and phase-space volume. The problem of closure is now finding an expression for the aggregation frequency.

Expression for aggregation frequency

Particles of sizes below 1 μm diffuse and exhibit Brownian motion. Smoluchowski (1917) was the first to derive an expression for the aggregation frequency of particles describing Brownian motion. From this derivation, Smoluchowski reported the aggregation kernel between two particles of sizes $\bar{s}$ and $\hat{s}$ as (Hunter, 1995):

$$\widetilde{\omega}_A(\bar{s},\hat{s},t) = 2\pi(D_{\bar{s}}+D_{\hat{s}})(\bar{s}+\hat{s}) \tag{2.2.104}$$

From the Stokes-Einstein equation, diffusivity is expressed as (Hunter, 1995):

$$D_{\bar{s}} = \frac{k_B T}{3\pi\bar{s}\mu} \tag{2.2.105}$$

k_B, T and μ are the Boltzmann constant, temperature and fluid viscosity.

Thus, we can express $\widetilde{\omega}_A(\bar{s},\hat{s},t)$ as:

$$\widetilde{\omega}_A(\bar{s},\hat{s},t) = 2\pi(D_{\bar{s}}+D_{\hat{s}})(\bar{s}+\hat{s}) = \frac{2k_B T}{3\mu}\left(\frac{1}{\bar{s}}+\frac{1}{\hat{s}}\right)(\bar{s}+\hat{s}) \tag{2.2.106}$$

Eq. (2.2.106) is the well-known Brownian aggregation kernel.

If the aggregating particles are about the same size, then a size-independent kernel results:

$$\widetilde{\omega}_A = 8k_B T/3\mu \tag{2.2.107}$$

In contrast, particles of disparate sizes have high rate of aggregation because of the vigorous diffusion of the smaller particle towards its sluggish larger partner. Smoluchowski called Eq. (2.2.106) the fast aggregation kernel. In order to account for the fact that not all collisions are successful at producing a new aggregate, $\widetilde{\omega}_A$ is divided by a stability factor W. This stability factor is a number between 1 and ∞. When $W = 1$, fast aggregation is obtained; while, when $W = \infty$, no aggregation occurs. There are many factors that can impede aggregation. In our case, we consider the effect of surface charges and their electric potential.

The effect of surface charges

Surface charges can be positive or negative and can induce either attraction or repulsion between particles depending on the surrounding charges. Let us consider a positively charged GNP. The GNP will attract a layer of tightly-held negative charges around it; this layer, in turn, will attract another layer of positive charges. These two layers of opposite charges around the initial positively charged GNP are called the electric double layer. This second layer is loosely associated with the particle. It is made of free ions that move in the fluid under the influence of electric attraction and thermal motion rather than being firmly anchored. It is thus called the "diffuse layer".

Nanoparticles with surface charges will aggregate only if the cumulative effect of both diffusion and electrostatic interaction brings the nanoparticles together. Fuch (1960) first derived a model for this cumulative effect for monodisperse particles. Subsequently, other authors such as Bogush and Zukoski (1991) derived the expression for spherical particles of sizes $\bar{s}$ and $\hat{s}$. The expression for the aggregation kernel with surface charge is (Bogush and Zukoski, 1991; Hunter, 1995):

$$\frac{\widetilde{\omega}_A}{W} = \frac{4\pi(D_{\bar{s}} + D_{\hat{s}})}{\int_{(\bar{s}+\hat{s})/2}^{\infty} \frac{\exp\left[{E_T}/{k_B T}\right]}{x^2} dx} \tag{2.2.108}$$

x is the distance between the particles, which varies from $(\bar{s} + \hat{s})/2$, when the two particles are in contact, to infinity. E_T is the total interaction energy, taken to be the sum of the energy due to the Van der Waal's force of attraction and that due the charge repulsion (Hunter, 1995). We review how to model E_T under the DLVO theory.

As E_T increases, $\widetilde{\omega}_A/W$ decreases, therefore Eq. (2.2.108) represents the slow aggregation while Eq. (2.2.106) represents the fast aggregation. Substituting Eq. (2.2.106) into Eq. (2.2.108) yields the expression for W as:

$$W = \frac{(\bar{s}+\hat{s})}{2} \int_{(\bar{s}+\hat{s})/2}^{\infty} \frac{\exp\left[{E_T}/{k_B T}\right]}{x^2} dx \tag{2.2.109}$$

DLVO theory

The interaction of colloidal particles due to the forces of attraction and repulsion is described in the popular DLVO theory, named after Derjaguin, Landau, Verwey and Overbreek (Derjaguin and Landau, 1941; Verwey and Overbreek, 1948). In this theory, the total interaction energy E_T between two particles is the sum of the Van der Waals energy of attraction and electrostatic energy of repulsion. We review this theory as follows.

For the expression of E_T, we write:

$$E_T = E_A + E_R \tag{2.2.110}$$

where E_A is the Van der Waals energy of attraction and E_R is the electrostatic energy of repulsion. By definition, energy is the ability to do work; it is the energy required to overcome a resistance (force) over a distance, mathematically expressed as:

$$E = -\int \boldsymbol{F}.d\boldsymbol{x} \tag{2.2.111}$$

where $\boldsymbol{F}$ is the force along the path $d\boldsymbol{x}$ associated with the energy E. We assume this distance to be one-dimensional in the radial direction. Thus, we write:

$$E = -\int F.dx \tag{2.2.112}$$

For colloidal particles, F is caused by the charges on the particles. For two particles of charges q_1 and q_2 separated by a distance x, using the power law, F can be expressed as (Israelachvili, 2011):

$$F = B\frac{q_1.q_2}{x^n} \tag{2.2.113}$$

where B is a constant and n is an integer. In the Coulomb's law,

$$B = 1/4\pi\epsilon_0\epsilon_c \tag{2.2.114}$$

and $n = 2$. In other power laws, n is greater than 2. In the Lennard-Jones equation, for example, n is 7 (for the attractive force) and n is 13 (for the repulsive force). Substituting Eq. (2.2.113) into Eq. (2.2.112) and integrating, we have:

$$E = \frac{B}{n-1}\frac{q_1.q_2}{x^{n-1}} \tag{2.2.115}$$

In the Lennard-Jones version of Eq. (2.2.115), $(n-1)$ is 6 (for the Van der Waals' force of attraction) and $(n-1)$ is 12 (for the electrostatic force of repulsion). Hence, this equation is called the "6-12" potential equation (Israelachvili, 2011).

These charges q_1 and q_2 can be expressed in terms of the concentrations of electrons on the particles and of the particle volumes. We write:

$$q_1 = \int_{v_{p1}} \rho_{e1} dv_{p1};\ q_2 = \int_{v_{p2}} \rho_{e2} dv_{p2} \tag{2.2.116}$$

where ρ_{e1} and ρ_{e2} are the electron densities due to the ions attached to the particles of particle-volumes v_{p1} and v_{p2}, respectively. Substituting Eq. (2.2.116) into Eq. (2.2.115), we have:

$$E = Q \frac{\int_{v_{p1}} \rho_{e1}\, dv_{p1} \int_{v_{p2}} \rho_{e2} dv_{p2}}{x^{n-1}} \tag{2.2.117}$$

where

$$Q = \frac{B}{n-1} \tag{2.2.118}$$

We employ Eq. (2.2.117) for an expression for the Van der Waals' energy of attraction, where $(n-1) = 6$. For spherical particles of diameters $\bar{s}$ and $\hat{s}$, Eq. (2.2.117) becomes (Polte 2015):

$$E_A = -\frac{\pi^2 \rho_{e1} \rho_{e2}}{6} Q \left[\frac{2\bar{s}\hat{s}}{4q^2-(\bar{s}+\hat{s})^2} + \frac{2\bar{s}\hat{s}}{4q^2-(\bar{s}-\hat{s})^2} + \ln\left(\frac{4q^2-(\bar{s}+\hat{s})^2}{4q^2-(\bar{s}-\hat{s})^2}\right)\right] \tag{2.2.119}$$

where q is the centre to centre distance between the two particles. For two identical spherical particles, an approximate expression of Eq. (2.2.119) is (Polte, 2015):

$$E_A = -\frac{\pi^2 \rho_{e1} \rho_{e2} Q \bar{s}}{24D} = -\frac{A_H \bar{s}}{24D} \tag{2.2.120}$$

where D is the particle surface to particle surface distance, given as:

$$D = (q - \bar{s}) \tag{2.2.121}$$

and A_H is the Hamaker constant, given in Eq. (2.2.120) as $A_H = \pi^2 \rho_{e1} \rho_{e2} Q$.

Eq. (2.2.120) shows the Van der Waals' potential energy of attraction for charged particles is inversely proportional to the separation distance, whereas for point charges such as the electrons, the Van der Waals' potential energy of attraction is inversely proportional to the sixth power of the separation distance as shown in Eq. (2.2.115).

While the Van der Waals' energy of attraction brings about aggregation of nanoparticles, the electrostatic energy of repulsion stabilizes them. As described before, two layers of opposite charges form around nanoparticles in ionic solutions (the electric double layer). Because of the electric double layer, nanoparticles repel one another. To describe this repulsion, DLVO used the Stern-Gouy-Chapman theory. In this theory, two particles distance D apart carry

equal negative charges. The surroundings, on the other hand, contain positively-charged ions, called counterions. This is illustrated in Figure 2.2.4A. Figure 2.2.4B, on the other hand, illustrates (as a function of the distance x) the distribution of the density of the counterions ρ_x, the corresponding electrostatic charge potential ψ_x and electric field $\mathbf{E}_x$.

The electrostatic charge potential at any point is the energy required to bring a unit positive charge from infinity to the point; it indicates the energy due to the electric field generated by charges around the point. The electric field, on the other hand, is the electric force per unit charge; it is directed from a more positive point (or location) to a less negative point (or location). From these definitions, the electrostatic charge potential and electric field are related by Eq. (2.2.111). By convention, for an isolated unit positive charge, the force is in the positive direction (directed outwards the charge) thus making its electrostatic charge potential positive, while for an isolated unit negative charge, the force is in the negative direction (directed inwards the charge) thus making its electrostatic charge potential negative. Therefore, at the surfaces in Figure 2.2.4, the charge is the most negative (the surface charge potential ψ_s) while at the middle ($D/2$), the charge is the least negative (ψ_0).

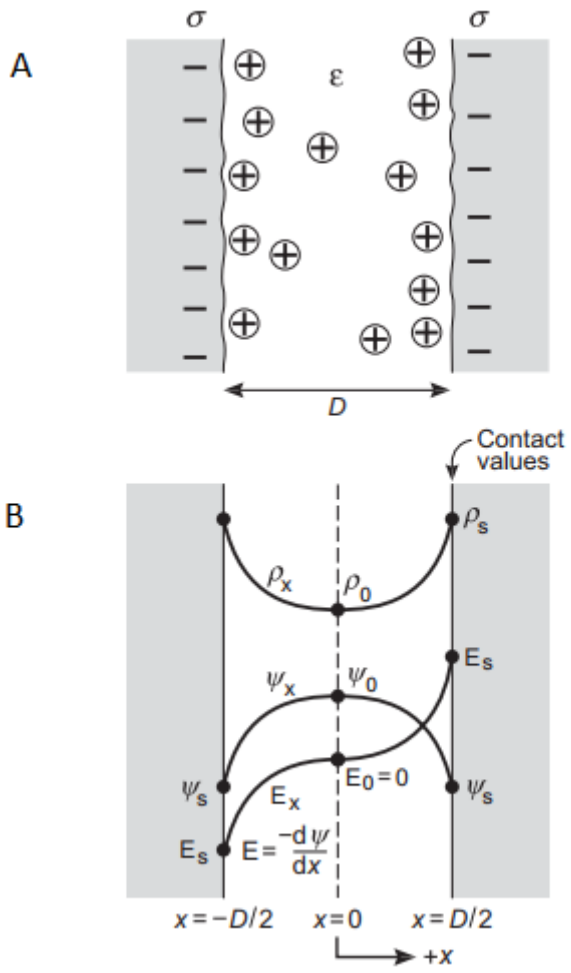

Figure 2.2.4: Two negatively charged surfaces of surface charge density ψ_s separated a distance D in water. The only ions in the space between them are the counterions that have dissociated from the surfaces. The counterion density profile ρ_x and electrostatic charge potential ψ_x are shown schematically in the lower part of the figure. The "contact" values are ρ_s, ψ_s and $\mathbf{E}_s = -[d\psi/dx]_s$. Figure obtained from Israelachvili (2011).

Assuming the system in Figure 2.2.4 to be in equilibrium, then the chemical potential λ would be the same from point to point. For two points I and II, we can then write:

$$\lambda^I = \lambda^{II} \tag{2.2.122}$$

Using the Nernst equation of thermodynamics, we express the chemical potential as Israelachvili (2011):

$$\lambda^x = ze\psi_x + k_B T \ln(\rho_x/\rho^0) \tag{2.2.123}$$

where z is the oxidation state of the ions and e is the amount of charge on an electron. ρ^0 is the density of counterions in the surroundings before applying the charged surfaces; its value can be taken to be the same throughout the surroundings.

At $x = 0$, we have:

$$\lambda^0 = ze\psi_0 + k_B T \ln(\rho_0/\rho^0) \tag{2.2.124}$$

Equating Eqs (2.2.123) and (2.2.124) and rearranging, we have:

$$\rho_x = \rho_0 \exp[-ze(\psi_x - \psi_0)/k_B T] \tag{2.2.125}$$

In Israelachvili (2011), Eq. (2.2.125) is given as:

$$\rho_x = \rho_0 \exp[-ze\psi/k_B T] \tag{2.2.126}$$

where $\psi = \psi_x - \psi_0$ (2.2.127)

Eq. (2.2.126) is the Boltzmann distribution of counterions. The x dependence of ψ is expressed using the Poisson equation given as:

$$ze\rho_x = -\epsilon_0 \epsilon_c \frac{d^2\psi}{dx^2} \tag{2.2.128}$$

Using Eq. (2.2.126) to substitute for ρ_x; Eq. (2.2.128) when rearranged becomes:

$$\frac{d^2\psi}{dx^2} = -\frac{ze}{\epsilon_0 \epsilon_c}\rho_0 \exp[-ze\psi/k_B T] \tag{2.2.129}$$

Eq. (2.2.129) is called Poisson-Boltzmann equation. Given one boundary condition, this equation can be solved for $\mathbf{F}$, the electric force. Similarly, given two boundary conditions, this equation can be solved for ψ and then the Boltzmann equation in (2.2.126) can be solved for ρ_x.

For solutions with dilute ion concentrations, where ψ is very small, Debye and Hückel linearized Eq. (2.2.129) as (Polte, 2015):

$$\frac{d^2\psi}{dx^2} = \frac{z^2 e^2 \rho_0 \psi}{\epsilon_0 \epsilon_c k_B T} - \frac{ze\rho_0}{\epsilon_0 \epsilon_c} \tag{2.2.130}$$

Between the charged surfaces in Figure 2.2.4, we have only one type of charges: unit-positive charges. In reality, different types of charges are present, some negative and some positive. Usually, the charges on the two surfaces or particles result from the attachment of some ions in the solution. To account for the different types of charges, Debye and Huckel reported the equations as (Polte, 2015):

$$\frac{d^2\psi}{dx^2} = \psi \sum_i \frac{z_i{}^2 e^2 \rho_0}{\epsilon_0 \epsilon_c k_B T} - \sum_i \frac{z_i e \rho_0}{\epsilon_0 \epsilon_c} \tag{2.2.131}$$

where i represents the species of charges.

In the overall ionic solution, the total positive charges cancel out the total negative charges. Thus, the solution is neutral. For this solution, the second term on the right-hand side of Eq. (2.2.131) is zero. Thus, Eq. (2.2.131) becomes:

$$\frac{d^2\psi}{dx^2} = \kappa^2\psi \tag{2.2.132}$$

where

$$\kappa = \left(\sum_i \frac{z_i^2 e^2 \rho_0}{\epsilon_0 \epsilon_c k_B T}\right)^{1/2} \tag{2.2.133}$$

κ is the inverse of the Debye length, also called the thickness of the diffuse layer.

A simple solution to Eq. (2.2.132) is:

$$\psi = \psi_0 \exp(-\kappa x) \tag{2.2.134}$$

with the electrostatic charge potential $\psi = \psi_0$ at $x = 0$. (The phrase "simple solution" was used by Polte (2015) because Eq. (2.2.132) can have other solutions. For example, another solution is $\psi = \psi_0 \exp(\kappa x)$.)

This equation gives the profile of the electrostatic charge potential. By definition of electrostatic charge potential, the equation refers to the interaction energy of point charges such as electrons and positrons.

For the interaction energy for charged surfaces, we need to account for the surfaces and their separation. Israelachvili (2011) reasoned in terms of the pressure of the ions between the surfaces, called the osmotic pressure, before obtaining the expression for the interaction energy. Assuming ideal gas behaviour and then uniform pressure, Israelachvili (2011) derived an expression for the repulsive pressure. We report this expression as:

$$P_r(D) = k_B T\left(\sum_i \rho_{i,D} - \sum_i \rho_{i,\infty}\right) \tag{2.2.135}$$

where P_r is the repulsive pressure when the charged surfaces are D distance apart. This pressure is assumed to be uniform everywhere within the surfaces. $\sum_i \rho_{i,D}$ is the total number density of the ions on each surface or particle. This number density is the same for identical surfaces or particles. $\sum_i \rho_{i,\infty}$ is the total number density of the ions on the surface when the charged surfaces are sufficiently far apart. Each number density can be expressed in terms of its density in the bulk of the solution $\rho_{i,0}$ using the Boltzmann distribution in Eq. (2.2.126). For an ionic solution containing mono-positive and mono-negative ions such as NaCl, $z = +1$ for Na^+ and $z = -1$ for Cl^-. Thus, Eq. (2.2.135) becomes:

$$P_r(D) = k_B T \left[\left(\rho_{Na,0} \exp[-ze\psi/k_B T] + \rho_{Cl,0} \exp[+ze\psi/k_B T] \right) \Big|_D - \left(\rho_{Na,0} \exp[-ze\psi/k_B T] + \rho_{Cl,0} \exp[+ze\psi/k_B T] \right) \Big|_\infty \right] \quad (2.2.136)$$

When the distance between the charged surfaces is infinity, Israelachvili (2011) took the charges on the surface to be zero (that is $\psi_\infty = 0$). Further, Israelachvili (2011) assumed that in the bulk, $\rho_{Na,0} = \rho_{Cl,0} = \rho_0$. Thus, Eq. (2.2.136) becomes:

$$P_r(D) = k_B T \rho_0 [(\exp[-ze\psi_D/k_B T] + \exp[+ze\psi_D/k_B T] - 2)] \quad (2.2.137)$$

Eq. (2.2.137) can be expressed as:

$$P_r(D) = 2k_B T \rho_0 [\cosh(ze\psi_D/k_B T) - 1] \quad (2.2.138)$$

where

$$\cosh(ze\psi_D/k_B T) = \frac{\exp[-ze\psi_D/k_B T] + \exp[+ze\psi_D/k_B T]}{2} \quad (2.2.139)$$

For solutions with dilute ion concentrations, where ψ_D is very small ($\psi_D < 25\, mV$), Israelachvili (2011) used the Taylor series expansion and approximated Eq. (2.2.138) as:

$$P_r(D) \approx \frac{z^2 e^2 {\psi_D}^2 \rho_0}{k_B T} \quad (2.2.140)$$

where in Eq. (2.2.138), $\cosh(ze\psi_D/k_B T)$ has been substituted as:

$$\cosh(ze\psi_D/k_B T) \approx 1 + \frac{(ze\psi_D/k_B T)^2}{2} \quad (2.2.141)$$

Using Eq. (2.2.134) to substitute for ψ_D, Eq. (2.2.140) when rearranged becomes:

$$P_r(D) \approx \frac{z^2 e^2 {\psi_0}^2 \rho_0}{k_B T} \exp(-\kappa D) \quad (2.2.142)$$

Depending on the geometry of the charged surfaces, Eq. (2.2.142) can be used to obtain the electrostatic force of repulsion and then the corresponding electrostatic energy of repulsion. For spherical particles, Dejaguin derived the equations for obtaining the force of repulsion and its corresponding energy of interaction from the osmotic pressure. These equations are based on the Dejaguin approximation. In this approximation, the sizes of the particles are considered to be infinity when compared to the distance between them. In other words, the surface curvature is neglected and it is regarded as flat. To obtain the equation for the force, Eq. (2.2.142) is multiplied by a differential area between the particles. The result is then integrated over the charged surfaces and their separation. We report the equation for the force of repulsion as (Israelachvili, 2011):

$$F_R = \frac{\pi\bar{s}\hat{s}}{\bar{s}+\hat{s}}\int_D^\infty P_r(x)dx = \frac{\pi\bar{s}\hat{s}}{\bar{s}+\hat{s}}\frac{z^2e^2{\psi_0}^2\rho_0}{k_BT\kappa}\exp(-\kappa D) \quad (2.2.143)$$

According to (Israelachvili, 2011), the corresponding energy of interaction can then be obtained by a further integration as:

$$E_R = \int_D^\infty F_R dx = \frac{\pi\bar{s}\hat{s}}{\bar{s}+\hat{s}}\frac{z^2e^2{\psi_0}^2\rho_0}{k_BT\kappa^2}\exp(-\kappa D) \quad (2.2.144)$$

From Eqs (2.2.119) and (2.2.144), we can then substitute in Eq. (2.2.110) for the total interaction energy for two spherical particles of sizes $\bar{s}$ and $\hat{s}$, x distance apart as:

$$E_T = -\frac{\pi^2\rho_{e1}\rho_{e2}}{6}Q\left[\frac{2\bar{s}\hat{s}}{4q^2-(\bar{s}+\hat{s})^2}+\frac{2\bar{s}\hat{s}}{4q^2-(\bar{s}-\hat{s})^2}+\ln\left(\frac{4q^2-(\bar{s}+\hat{s})^2}{4q^2-(\bar{s}-\hat{s})^2}\right)\right]+\frac{\pi\bar{s}\hat{s}}{\bar{s}+\hat{s}}\frac{z^2e^2{\psi_0}^2\rho_0}{k_BT\kappa^2}\exp(-\kappa x) \quad (2.2.145)$$

This type of expression of E_T allows calculating W using Eq. (2.2.109). For other geometries of interacting charged particles, the expression for E_T is different. However, these different expressions yield a similar profile for E_T. Figure 2.2.5 shows this typical profile as the green curve; the blue and red curves show the profiles of E_A and E_R, respectively. The green curve characteristically has a maximum point, called the energy barrier. Based on this typical profile of E_A, past authors simplified the expression of E_T and then of W. We review their approach to simplify these expressions as follows.

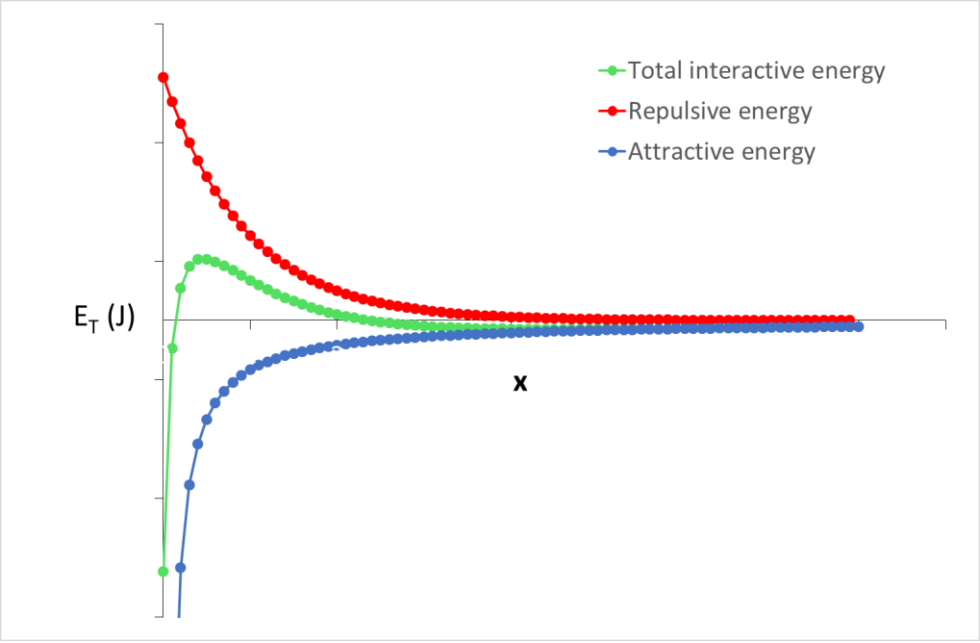

Figure 2.2.5: A typical profile of the total interaction energy with distance x between two charged particles.

Simplified expressions for E_T and W

In terms of energy barrier between two spherical particles of sizes $\bar{s}$ and $\hat{s}$, Reerink and Overbreek (1954) derived an expression for W. This expression is (Marchisio and Fox, 2012):

$$W = \frac{2\kappa}{\bar{s}+\hat{s}} \exp\left[{E_{agg}}/{k_B T} \right] \tag{2.2.146}$$

where E_{agg} is the energy barrier for aggregation (i.e. the maximum value of the green curve in Fig. 2.2.5). Since $W(\bar{s},\hat{s})$ is a dimensionless number, $2\kappa/(\bar{s}+\hat{s})$ in Eq. (5.2.4) should be dimensionless. However, considering $1/\kappa$ has a dimension of L, $2\kappa/(\bar{s}+\hat{s})$ has the dimension of L^{-2}. Thus, Eq. (2.2.146) is incorrect. In Chapter 5 on modelling the aggregation process, we derive the correct expression of Eq. (2.2.146).

Further, Reerink and Overbreek (1954) reported a simpler expression for W than Eq. (2.2.146). In doing this, they considered identical spherical particles where $\bar{s} = \hat{s}$ and employed the Taylor series expansion on an expression for E_T simpler than Eq. (2.2.145) about the value of x corresponding to the energy barrier E_{agg}. This value of x is the thickness of the electric double layer i.e. $x = \kappa^{-1}$ (Israelachvili, 2011). The final expression is:

$$\ln W = -g_1 \ln C_e + g_2 \tag{2.2.147}$$

where C_e is the concentration of potential determining ions (these are the ion species that induce surface charge on the particles), while g_1 and g_2 are constants. The value of g_1 depends on the surface potential, while the value of g_2 depends on the physical system only (Reerink and Overbreek, 1954). Reerink and Overbreek tested Eq. (2.2.147) using a colloid of silver iodide particles in aqueous barium nitrate and then reported almost linear curves of $\ln W$ vs $\ln C_e$ thus confirming the linear relationship in Eq. (2.2.147). Thereafter, Kumar et al. (2007) employed the expression in Eq. (2.2.147) for W in their model for the citrate synthesis method. We present their model in Chapter 3. We also present another modelling approach for W and the aggregation process in Chapter 5.

However, on reviewing the mathematical derivation of Reerink and Overbreek (1954), we observed some inconsistencies with Figure 2.2.5. To support our discussions in Chapters 3 and 5, we report the inconsistencies as follows.

First, Reerink and Overbreek (1954) did not start with Eqs. (2.2.109) and (2.2.145). Instead of Eq. (2.2.109) for W, they started with

$$W = 2\int_0^{\infty} \exp(E_T/kT)\frac{dx_s}{(x_s+2)^2} \tag{2.2.148}$$

where

$$x_s \equiv \frac{2D_0}{\bar{s}} \tag{2.2.149}$$

where D_0 is the shortest distance between the particles. Based on this definition, D_0 should be zero since the particles should be in contact when they aggregate. However, according to Reerink and Overbreek (1954), it is finite and nonzero. We think that D_0 should be x, the distance between the particles, not the shortest distance between them.

Notice that the two particles have equal size $\bar{s}$. Notice also two things: the integration in Eq. (2.2.148) is from $x_s = 0$ to $x_s = \infty$, and the denominator of the integral function is $(x_s + 2)$. When derived from Eq. (2.2.109) assuming $D_0 = x$, the integration should be from $x_s = 2$ to $x_s = \infty$, and the denominator should be x_s.

Also, instead of Eq. (2.2.145), Reerink and Overbreek (1954) started with

$$E_T = -\frac{A_H}{12x_s} + B_r\ \exp(-\kappa_s x_s) \tag{2.2.150}$$

where $B_r = 2.31 \times 10^{-6}\bar{s}\frac{\alpha^2}{z^2}$ (2.2.151)

$$\kappa_s = \kappa\bar{s}/2 \tag{2.2.152}$$

$$\alpha = \frac{\exp(|z|e\psi_0/2k_BT)-1}{\exp(|z|e\psi_0/2k_BT)+1} \tag{2.2.153}$$

and $|z|$ is the magnitude of the potential determining ion.

Next, Reerink and Overbreek (1954) employed the Taylor series expansion on E_T in Eq. (2.2.150) about the value of x_s corresponding to the energy barrier E_{agg}, denoted as x_{sm}. As previously mentioned, this value corresponds to $x = \kappa^{-1}$. The Taylor series expansion of E_T about the point $x_s = x_{sm}$ is:

$$E_T(x_s) = E_{agg} + \left.\frac{dE_T}{dx_s}\right|_{x_s=x_{sm}}(x_s - x_{sm}) + \frac{1}{2}\left.\frac{d^2E_T}{dx_s{}^2}\right|_{x_s=x_{sm}}(x_s - x_{sm})^2 \tag{2.2.154}$$

where we have neglected higher-order terms (Reerink and Overbreek, 1954). The figure reported by Reerink and Overbreek (1954) for $E_T(x_s)$ with the peak at $x_s = x_{sm}$ is similar to Figure 2.2.5, where the peak is at $x = \kappa^{-1}$. As in Figure 2.2.5, for $x_s = x_{sm}$ it is:

$$\left.\frac{dE_T}{dx_s}\right|_{x_s=x_{sm}} = 0 \tag{2.2.155}$$

Thus, Eq. (2.2.154) becomes:

$$E_T(x_s) = E_{agg} + \frac{1}{2}\frac{d^2E_T}{dx_s{}^2}\Big|_{x_s=x_{sm}} (x_s - x_{sm})^2 \quad (2.2.156)$$

If we use this relation in Eq. (2.2.148), this yields:

$$W = \frac{2}{(x_{sm}+2)^2} \exp\left(E_{agg}/k_BT\right) \int_0^\infty \exp[-p^2(x_s - x_{sm})^2]\, dx_s \quad (2.2.157)$$

$$\text{where } p = \left(-\frac{1}{2k_BT}\frac{d^2E_T}{dx_s{}^2}\Big|_{x_s=x_{sm}}\right)^{1/2} \quad (2.2.158)$$

Reerink and Overbreek (1954) replaced the lower limit in the integral in Eq. (2.2.157) by $-\infty$, claiming that this replacement introduces only a negligible error. Subsequently, they calculated the integral as:

$$\int_{-\infty}^{\infty} \exp[-p^2(x_s - x_{sm})^2]\, dx_s = \frac{\sqrt{\pi}}{p} \quad (2.2.159)$$

From this equation, Eq. (2.2.157) becomes:

$$W = \frac{\sqrt{\pi}}{p}\frac{1}{(x_{sm}+2)^2} \exp\left(E_{agg}/k_BT\right) \quad (2.2.160)$$

To obtain E_{agg}, Reerink and Overbreek (1954) differentiated Eq. (2.2.150) with respect to x_s and then equated the derivative to zero at $x_s = x_{sm}$. Doing so yields:

$$B_r \exp(-\kappa_s x_{sm}) = \frac{A_H}{12\kappa_s x_{sm}{}^2} \quad (2.2.161)$$

Combining Eqs (2.2.150) and (2.2.161), we have:

$$E_{agg} = E_T(x_{sm}) = \frac{A_H}{12x_{sm}}\left(\frac{1}{\kappa_s x_{sm}} - 1\right) \quad (2.2.162)$$

Furthermore, Reerink and Overbreek (1954) considered a case where $E_{agg} = 0$. In the figure of Reerink and Overbreek (1954), which is similar to Figure 2.2.5, this case occurs when $E_R = 0$ i.e. there is no electrostatic repulsion. As previously mentioned, Reerink and Overbreek (1954) employed this case to derive the expression in Eq. (2.2.147), which was used in the model of Kumar et al. (2007), discussed in Chapter 3.

To satisfy this case, Eq. (2.2.162) becomes:

$$\kappa_s x_{sm} = 1 \quad (2.2.163)$$

We rewrite Eq. (2.2.163) as:

$$\left(\frac{1}{\kappa_s x_{sm}} - 1\right) = \pm \ln \kappa_s x_{sm} \tag{2.2.164}$$

This equation satisfies Eq. (2.2.163). In Eq. (2.2.164), the right-hand side can carry a positive or a negative sign. In their derivation, Reerink and Overbreek (1954) employed Eq. (2.2.164) with only the negative sign on the right-hand side. However, they did not disclose why they employed only this option.

Following Reerink and Overbreek (1954), we substitute the right-hand side of Eq. (2.2.164) (with the negative sign only) into Eq. (2.2.162):

$$E_{agg} = -\frac{A_H}{12 x_{sm}} \ln \kappa_s x_{sm} \tag{2.2.165}$$

W can then be expressed by substituting Eq. (2.2.165) into (2.2.160). Rearranging the results, we have:

$$\ln W = \ln\left(\frac{\sqrt{\pi}}{p} \frac{1}{(x_{sm}+2)^2}\right) - \frac{A_H}{12 x_{sm} k_B T} \ln \kappa_s x_{sm} \tag{2.2.166}$$

We can express Eq. (2.2.166) as a function of the concentration of potential determining ions. To do this, we further rearrange Eq. (2.2.166) as:

$$\ln W = -\frac{A_H}{12 x_{sm} k_B T} \ln \kappa_s - \frac{A_H}{12 x_{sm} k_B T} \ln x_{sm} + \ln\left(\frac{\sqrt{\pi}}{p} \frac{1}{(x_{sm}+2)^2}\right) \tag{2.2.167}$$

Further, we substitute κ_s using Eq. (2.2.152) to obtain Eq. (2.2.167) in terms of κ and $\bar{s}$. Then, we substitute for κ using Eq. (2.2.133), recognising that:

$$C_e = \sqrt{\sum_i {z_i}^2 e^2 \rho_0} \tag{2.2.168}$$

After rearranging, these substitutions transform Eq. (2.2.167) as:

$$\ln W = -\frac{A_H}{12 x_{sm} k_B T} \ln C_e - \frac{A_H}{12 x_{sm} k_B T} \ln\left(\frac{x_{sm}\bar{s}}{2\sqrt{\epsilon_0 \epsilon_c k_B T}}\right) + \ln\left(\frac{\sqrt{\pi}}{p} \frac{1}{(x_{sm}+2)^2}\right) \tag{2.2.169}$$

Now we substitute back for p. To do this, first we find $d^2E_T/{dx_s}^2$ using Eq. (2.2.150) and then substitute its value at $x_s = x_{sm}$ into Eq. (2.2.158). We differentiate Eq. (2.2.150) twice as:

$$\frac{d^2 E_T}{{dx_s}^2} = -\frac{A_H}{6{x_s}^3} + {\kappa_s}^2 B_r \exp(-\kappa_s x_s) \tag{2.2.170}$$

Using (2.2.161), Eq. (2.2.170) at $x_s = x_{sm}$ becomes:

$$\left.\frac{d^2 E_T}{{dx_s}^2}\right|_{x_s = x_{sm}} = -\frac{A_H}{6{x_{sm}}^3} + \frac{A_H \kappa_s}{12{x_{sm}}^2} = \frac{A_H}{12{x_{sm}}^3}(\kappa_s x_{sm} - 2) \tag{2.2.171}$$

Substituting this into Eq. (2.2.158), we have:

$$p = \left(\frac{A_H}{24{x_{sm}}^3 k_B T} (2 - \kappa_s x_{sm}) \right)^{1/2} \tag{2.2.172}$$

Using Eq. (2.2.172), we can now substitute for p in Eq. (2.2.169). Doing so, we have:

$$\ln W = -\frac{A_H}{12 x_{sm} k_B T} \ln C_e - \frac{A_H}{12 x_{sm} k_B T} \ln \left(\frac{x_{sm} \bar{s}}{2\sqrt{\epsilon_0 \epsilon_c k_B T}} \right) + \ln \left(\frac{\sqrt{\pi}}{\left(\frac{A_H}{24{x_{sm}}^3 k_B T} (2 - \kappa_s x_{sm}) \right)^{1/2}} \frac{1}{(x_{sm}+2)^2} \right) \tag{2.2.173}$$

Reerink and Overbreek (1954) assumed that apart from C_e, every other term in Eq. (2.2.173) is a constant. Thus, they proposed that W varies with C_e according to Eq. (2.2.147).

However, Eq. (2.2.173) shows that W also varies with size $\bar{s}$. As previously shown, another limitation of this equation is that it assumes $E_R = 0$; no stabilization by the repulsion energy. In spite of these limitations, Kumar et al. (2007) employed Eq. (2.2.173) to derive an expression for the aggregation process in the citrate synthesis method. As we see in chapter 3, this expression fails to accurately describe the aggregation process.

In our attempt to model the aggregation process accurately, however, we employ Eq. (2.2.109) and derive an equation for W in terms of particle size. This equation follows the theory proposed by Polte (2015) to describe the aggregation process. We discuss this theory and the derived equation that describes it in chapter 5.

In concluding this section, we have reviewed the mathematical framework to adopt in modelling the formation of gold nanoparticles in the citrate synthesis method. In the population balance modelling for the particle phase, based on the investigations of past authors, we have discussed how to model processes such as nucleation, growth and aggregation.

2.3 Methods of solution

The reviewed mathematical model comprises the ordinary differential equations (ODEs) in the continuous phase (Eq. (2.2.13) and the integro-partial-differential equation in the discontinuous phase (the population balance equation in Eq. (2.2.49)). For ODEs, analytical solutions are only possible for some cases. These cases include ODEs where the dependent and independent variables can be separated to the different sides of an equation, and ODEs that are linear and homogeneous. Nonlinear ODEs are solved numerically starting from the initial conditions. The numerical methods used for solving ODEs include the Euler, modified-Euler and Runge-Kutta methods (Stroud and Booth, 2003; Hornberger and Wiberg, 2005). In the Euler method, for example, the domain of the independent variable,

which is time t in Eq. (2.2.13), is first divided into time steps Δt. Then, the dependent variables, which are the concentrations in Eq. (2.2.13), are calculated using:

$$C_i(t + \Delta t) = C_i(t) + \frac{dC_i}{dt}\Delta t \tag{2.3.1}$$

At the initial condition (i.e. $t = 0$), $C_i(0)$ is specified. Eq. (2.3.1) is therefore iterated until the final simulation time t_f. As $\Delta t \to 0$, the results approach the values obtainable if the equation were to be solved analytically. Other numerical methods such the modified-Euler and Runge-Kutta methods follow a similar procedure as the Euler method.

The integro-partial-differential equation, as shown in the population balance equation (PBE), poses even higher difficulty and complexity than the ODEs. Excluding the aggregation term, this equation reduces to a partial differential equation (PDE). For PDEs, analytical solutions may be possible using separation of variables, Laplace and Fourier transforms (Kreyzig, 1999; Stroud and Booth, 2003). For many cases, however, like the ODEs, PDEs are solved numerically using numerical techniques such as the finite difference methods. In Appendix C, we present some functions employed as solutions in describing experimentally obtained particle size distributions. We refer the reader to this appendix for more details.

For the PBEs in particular, numerical techniques employed such as the method of moments first focus on manipulating the NDF so that the PBE is in the form of an ODE. Then, by following a similar procedure as the Euler method, the resulting ODE is transformed into algebraic equations in the form of Eq. (2.3.1). In the method of moments, the PBE is averaged in the particle-size space by multiplying by s^n and integrating over s from zero to infinity (Randolph and Larson, 1971). Applying the method of moments to Eq. (2.2.49), we have:

$$\int_0^\infty \left[\frac{\partial}{\partial t}f(s,t) + \frac{\partial}{\partial s}(f.\langle G_s\rangle_{av}) - H_V\right]s^n ds = 0 \tag{2.3.2}$$

Reversing the order of differentiation and integration on the first term, we have:

$$\frac{d}{dt}\int_0^\infty f(s,t)s^n ds = \frac{dm_n(t)}{dt} \tag{2.3.3}$$

where $m_n(t)$ is the nth integer moment of the particle size distribution per unit volume of solution, mathematically expressed as

$$m_n(t) \equiv \int_0^\infty f s^n ds \tag{2.3.4}$$

The second term of Eq. (2.3.2) can be integrated by parts as:

$$\int_0^\infty \frac{\partial}{\partial s}(f.\langle G_s\rangle_{av})s^n ds = (f.\langle G_s\rangle_{av})s^n|_\infty - (f.\langle G_s\rangle_{av})s^n|_0 - \int_0^\infty n(f.\langle G_s\rangle_{av})s^{n-1}ds \tag{2.3.5}$$

We assume that f vanishes faster than any other function as s diverges, a property referred to as regularity condition (Mazzei, 2008). Thus, the expected number of particles with infinite sizes is zero. This makes the first term on the right-hand side of Eq. (2.3.5) vanish. Since the size of a nucleus is not zero, for most applications, the second term may also be taken as zero at $s = 0$ (Mazzei, 2008). Thus, the second term in Eq. (2.3.2) yields:

$$\int_0^\infty \frac{\partial}{\partial s}(f.\langle G_s\rangle_{av})s^n ds = -\int_0^\infty n(f.\langle G_s\rangle_{av})s^{n-1} ds \tag{2.3.6}$$

The form of $\langle G_s\rangle_{av}$ determines the final form of Eq. (2.3.6). From the surface-reaction controlled growth in Section 2.2.3.2 (Eq. (2.2.92)), $\langle G_s\rangle_{av}$ is a constant. Thus, Eq. (2.3.6) becomes:

$$\int_0^\infty \frac{\partial}{\partial s}(f.\langle G_s\rangle_{av})s^n ds = -n\langle G_s\rangle_{av} m_{n-1}(t) \tag{2.3.7}$$

While for the diffusion-controlled growth, $\langle G_s\rangle_{av}$ is given by (Eq. (2.2.87). Thus, Eq. (2.3.36) becomes:

$$\int_0^\infty \frac{\partial}{\partial s}(f.\langle G_s\rangle_{av})s^n ds = -nD_0V_m(C_0 - C_{eq})m_{n-2}(t) \tag{2.3.8}$$

The third term in Eq. (2.3.2) can be integrated as:

$$\int_0^\infty H_V s^n ds = \bar{\bar{H}}_V(m_k, t) \qquad n = 0,1,2 \ldots \geq k \tag{2.3.9}$$

In the citrate synthesis method, the growth process is controlled by surface reaction as we see in Chapters 3 and 4. Putting all the terms together, for surface reaction controlled growth, Eq. (2.3.2) becomes:

$$\frac{dm_n(t)}{dt} - n\langle G_s\rangle_{av} m_{n-1}(t) - \bar{\bar{H}}_V(m_k, t) = 0 \qquad n = 0,1,2 \ldots \geq k \tag{2.3.10}$$

Eq. (2.3.10) is an ODE that describes the particle phase. Coupling and solving numerically Eqs (2.3.2) and (2.3.10) would yield results of concentrations and moments for the fluid-particle system. From these results, we can derive some properties of the particle size distribution. For example, the particles mean size can be obtained in terms of the moments from the general expression:

$$\text{Mean size, } s_{j+1,j} = \frac{m_{j+1}}{m_j} \tag{2.3.11}$$

where $s_{1,0}$, $s_{2,1}$, $s_{3,2}$, and $s_{4,3}$ represent the number-mean, length-mean, area-mean and weight-mean sizes, respectively. For specific expressions for these mean sizes, we refer the reader to Appendix C.

Furthermore, the standard deviation σ of the particle size distribution can be derived from the size moments as follows:

$$\sigma^2 = \frac{\int_0^\infty (s - s_{1,0})^2 f ds}{\int_0^\infty f ds} = \frac{m_2}{m_0} - \left(\frac{m_1}{m_0}\right)^2 \quad (2.3.12)$$

As the set of moments (m_n) increases, more information about the particle size distribution can be obtained. To completely reconstruct the particles size distribution, however, we need to generate an infinite number of size moments.

Due to increasing computing ability, discretizing the NDF in the PBEs is becoming an attractive method of solution. In the quadrature method of moments (QMOM), for example, the NDF is discretized into a number of particle classes, each having a weighting function and a particular size. These particle classes then replace the NDF in the PBE. As these particle classes evolve by the transport equation, the particle classes are obtained for various time steps. Usually, the QMOM works with about ten classes of particles (Mazzei, 2008). Using discretization techniques, Kumar and Ramkrishna (1995) reported a method of solving PBEs, called the fixed pivot. In this method, the authors divided the NDF into about 100 bins. Then, they obtained the zeroth moment of the PBE within each bin, yielding how the number concentration of particles within the bin evolves in time, an ODE. This ODE is then solved numerically. As the name suggest in the fixed pivot, the sub-region of the particle-state space is fixed.

To make the sub-region dynamic, Wulkow et al. (2001) developed the adaptive Galerkin method. The h-p Galerkin method is a finite element scheme that divides the size space into a number of nodes h and represents each node with an algebraic equation of order p, hence the name h-p. The nodes and the equations, when brought together, yield the particle size distribution. The nodes are separated by the size step Δs. In determining Δs, the h-p Galerkin method adapts to the particle size distribution and refines the number of nodes as the simulation progresses. The first node is fixed as the initial minimum size s_{min} while the number of subsequent nodes and their locations are generated by searching the semi-infinite size space (i.e. from s_{min} to ∞) for particles.

The method solves the population balance equation within a time step that guarantees the specified accuracy. The accuracy refers to the difference between the solutions (the concentrations of the fluid components and PSD) at time t and time $t + \Delta t$. This time step, called the actual time step Δt_a, is obtained using the Rothe method (see Wulkow et al. (2001) for details).

In this work, to solve the PBE and material balance equations, we used the numerical code called Parsival, which is based on the h-p Galerkin method and developed by Wulkow for commercial purposes. We test the numerical accuracy of Parsival in Appendix D. We refer the reader to this appendix for details.

2.4 Review of modelling of the synthesis of NPs

To accurately describe the synthesis of nanoparticles in general and the citrate synthesis method in particular, the synthesis model must be derived using the mathematical framework discussed previously and must be based on the mechanism of the synthesis. Following different (but less fundamental) approaches, however, past authors have attempted to model NP synthesis.

In 1997, Finke and Watzky followed a macroscopic approach for metal nanoparticles synthesis and reported a model for calculating the final particle mean diameter. In deriving this model, they assumed a two-step mechanism for nanoparticle syntheses. This mechanism involves a slow nucleation step, which forms nuclei of a particular size, and an autocatalytic growth step, which grows the nuclei to the final diameter. This model requires as inputs the initial precursor concentration, rate constants for the nucleation and growth steps, and the nucleus size. For most nanoparticles syntheses, Finke and Watzky (1997) observed that the time profile of the precursor concentration is sigmoidal, in which the concentration remains almost constant at the beginning of the synthesis, then decreases rapidly mid-way into the synthesis and finally tails off at the end. Figure 2.4.1 shows the typical time profile of the precursor concentration. From the period of constant concentration at the beginning, called the induction period, Finke and Watzky obtained the kinetic rate constant for the nucleation step while from the mid-way slope of the profile, they obtained the kinetic rate constant of the growth step.

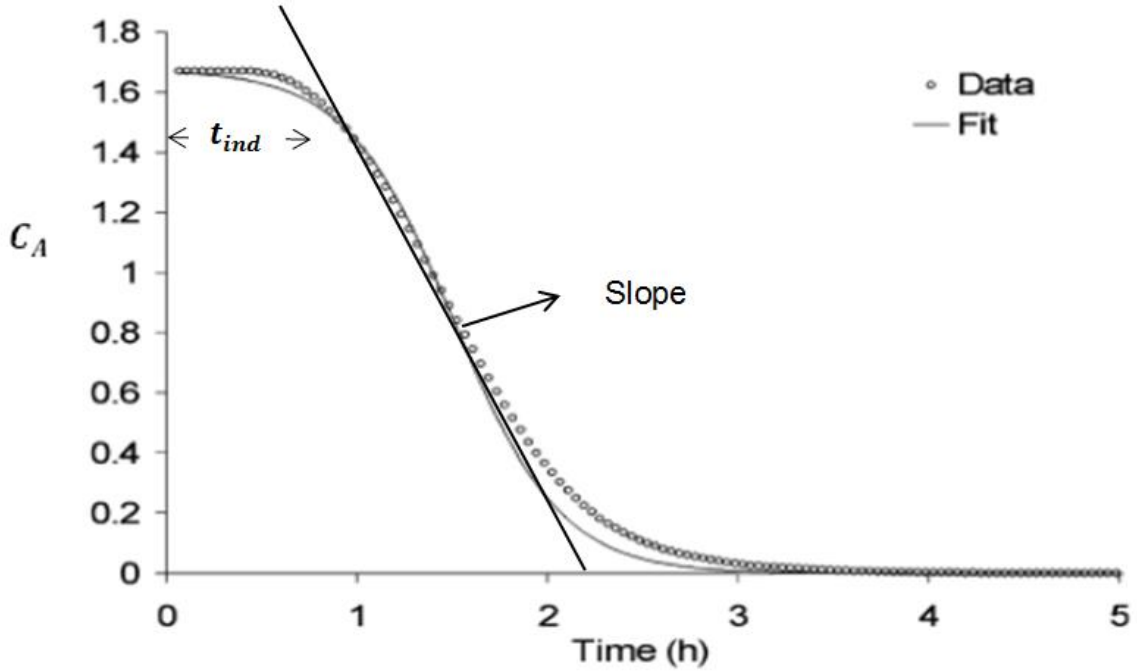

Figure 2.4.1: A typical time profile of the precursor concentration (C_A) in the nanoparticle synthesis showing how to determine the induction time (t_{ind}) and slope. Data from Finke and Watzky (1997).

Schematically, this mechanism is represented as:

Nucleation: $$A \overset{k_n}{\rightarrow} B \tag{2.4.1}$$

Growth: $$A + B \overset{k_g}{\rightarrow} 2B \tag{2.4.2}$$

where A represents the precursor; B represents the particles; k_n and k_g are the rate constants for the nucleation and growth steps, respectively. For more information, we refer the reader to Finke and Watzky (1997).

The total material balance at any instant for a well-mixed batch reactor is given as:

$$C_{A,0} = C_A + C_B \tag{2.4.3}$$

where per unit volume of the synthesis mixture, $C_{A,0}$ is the initial mole of A in the liquid phase, C_A is the mole of A in the liquid phase at any instant, and C_B is the mole of B in the liquid phase at any instant, noting that according to Eq. (2.4.1) one mole of A yields one of B.

For component A, its time evolution derived from the component material balance equation for a well-mixed batch reactor is:

$$-\frac{dC_A}{dt} = k_n C_A + k_g C_A C_B \tag{2.4.4}$$

From Figure 2.4.1, k_n and k_g can be calculated as (Finke and Watzky, 1997):

$$k_n = \frac{1}{t_{ind}} \; ; \; k_g = \frac{slope}{{C_{A,0}}^2} \tag{2.4.5}$$

where t_{ind} is the induction time and $C_{A,0}$ is the initial precursor concentration.

From Eq. (2.4.3), we substitute for C_B in Eq. (2.2.4) and re-arrange as:

$$\frac{dC_A}{k_n C_A + k_g C_A (C_{A,0} - C_A)} = -dt \tag{2.4.6}$$

The left-hand side of this equation can be resolved as:

$$\frac{dC_A}{k_n C_A + k_g C_A (C_{A,0} - C_A)} = \left\{ \frac{1}{(k_n + k_g C_{A,0}) C_A} + \frac{k_g}{(k_n + k_g C_{A,0})\left(k_n + k_g (C_{A,0} - C_A)\right)} \right\} dC_A \tag{2.4.7}$$

Integrating Eq. (2.4.6) and then rearranging, we have:

$$\ln C_A / \left(k_n + k_g (C_{A,0} - C_A)\right) = (k_n + k_g C_{A,0})(t + \mathcal{M}) \tag{2.4.8}$$

where $\mathcal{M}$ is the constant of integration, calculated from the initial condition, where $t = 0$ and $C_A = C_{A,0}$ as follows:

$$\mathcal{M} \equiv \frac{\ln(C_{A,0}/k_n)}{(k_n + k_g C_{A,0})} \tag{2.4.9}$$

Substituting for $\mathcal{M}$ in Eq. (2.4.8) and then re-arranging, we have:

$$C_A = \frac{\frac{k_n}{k_g} + C_{A,0}}{1 + \frac{k_n}{k_g C_{A,0}} \exp\left[-(k_n + k_g C_{A,0}) t\right]} \tag{2.4.10}$$

Finke and Watzky (1997) obtained the final mean diameter, s_f as follows. From Eq. (2.4.10), they first obtained the residual concentration of A ($C_{A,ind}$) at the induction time ($t = t_{ind}$). From this concentration, they reported the equation for the number concentration of nuclei as:

$$\frac{(C_{A,0} - C_{A,ind})V}{mole\ of\ one\ nucleus} = \frac{1}{mole\ of\ one\ nucleus} \frac{\left(\frac{k_n}{k_g} + C_{A,0}\right)V}{\left[1 + \frac{k_n}{k_g C_{A,0}} \exp\left[-(k_n + k_g C_{A,0}) t\right]\right]} \tag{2.4.11}$$

where V is the volume of the reacting mixture. The mole of A in one nucleus can be determined from the number of atoms that form the nucleus N^* as:

$$mole\ of\ one\ nucleus = \frac{N^*}{N_A} \tag{2.4.12}$$

where N_A is the Avogadro's number, equal to 6.02×10^{23}.

Then, Finke and Watzky assumed the number concentration of nuclei to be equal to the final number concentration of particles. They obtained the latter from the initial precursor concentration and final mean diameter as:

$$\frac{C_{A,0}V}{m_v s_f^3 \rho} \tag{2.4.13}$$

where m_v is the volume shape factor of the particles and ρ is the molar density of the particles. By assuming the shape of the particles to be spherical, Finke and Watzky (1997) reported the value of m_v as $\pi/6$.

Finally, they equated Eq. (2.4.11) to Eq. (2.4.13) to obtain the final mean diameter as:

$$s_f = \left[\frac{N^*}{m_v \rho N_A} \frac{1}{1 - \frac{k_n + k_g C_{A,0}}{k_g C_{A,0} + k_n \exp[-(k_n + k_g C_{A,0})t]}} \right]^{1/3} \tag{2.4.14}$$

This equation can only yield the final mean diameter; it does not yield information about the size distribution of the particles. Also, to predict the final mean diameter, we need the value N^*, which was not reported by Finke and Watzky (1997); they did not employ experimental data of particle sizes to validate the predictions of their model. Their contribution was only reporting the feasibility of transforming this two-step mechanism into a mathematical model.

Robb and Privmann (2007) also made a similar contribution: the feasibility of modelling the LaMer mechanism of burst nucleation and growth for nanoparticle synthesis in solution. This model follows the master equation. Like the population balance equation (PBE), the master equation is based on the probability density function of particle sizes. However, in the master equation, each particle is in a transition state due to the attachment and detachment of monomers. The model did not converge and Robb and Privman (2007) did not validate the model predictions against experimental data. Instead of employing the master equation, past authors have used the PBE equation to describe nanoparticles synthesis. For example, Lazarri et al. (2017) used the PBE to describe the synthesis of semiconductor nanoparticles (of cadmium and selenium) and then validated their model predictions. Also for other nanoparticles, Liu et al. (2014) reported a model for the synthesis of silver nanoparticles from silver nitrate. In their model, Liu et al. assumed a two-stage mechanism of nucleation and growth and used the PBE to describe the synthesis. All these models are not based on first principles and are based on very strong assumptions, which are unlikely to reflect reality.

For the citrate synthesis method, however, the only predictive model available in the literature is that developed by Kumar et al. (2007). The authors used the PBE to describe the synthesis based on the Turkevich organizer theory. We review this model in the following chapter.

Chapter 3

Mathematical Investigation of the Turkevich Organizer Theory

In this chapter, we investigate and thoroughly test the mathematical model developed by Kumar et al. (2007) for the description of the synthesis of gold nanoparticles by the citrate method. The model, based on the "Turkevich organizer theory", is able to predict the evolution of the nanoparticle size distribution. In the following introduction, we report the motivation and structure of the chapter.

Parts of this chapter have been published:

Agunloye, E., Gavriilidis, A., & Mazzei, L., 2017. A mathematical investigation of the Turkevich organizer theory in the citrate method for the synthesis of gold nanoparticles. *Chemical Engineering Science, 173*, 275-286. doi:10.1016/j.ces.2017.0

3.1 Introduction

In 1951, Turkevich and co-workers pioneered the citrate reduction method, investigating how the GNPs evolve during the synthesis using electron microscopy. Their findings made them advance the popular "Turkevich organizer theory". In the synthesis, sodium citrate reduces chloroauric acid to aurous ions and concurrently oxidizes to dicarboxy acetone. Subsequently, by bringing together (that is, by "organizing") a sufficient number of aurous ions, dicarboxy acetone causes gold nuclei to form. Concurrently, it also decomposes into acetone, eventually arresting the nucleation process. Once this has happened, the remaining aurous ions make the nuclei grow. This justifies why this theory is also referred to as "nucleation-growth" theory.

Subsequently, Frens (1973) studied this synthesis and demonstrated that different sizes of GNPs can be obtained by changing the concentration of sodium citrate while keeping the concentration of chloroauric acid at about $0.3\ mol/m^3$. This technique was slightly modified by Freund and Spiro (1985) to produce GNPs used for testing size-dependent catalytic properties of the particles. Abid (2003) used the synthesis to form GNPs of different size intended for laser and optical properties. However, unlike Frens (1973), Abid (2003) varied the concentration of both chloroauric acid and sodium citrate. Chow and Zukoski (1994) also explored the synthesis, this time by varying the concentration of chloroauric acid while

keeping that of sodium citrate at $1.6\ \mathrm{mol/m^3}$. Unexpectedly, they observed that the particles aggregated. In 2007, Kumar and co-workers rationalized these experimental data, developing a model for the synthesis based on the mechanism proposed by Turkevich et al. (1951). The model predictions fitted reasonably well the data of the latter and of many of the other researchers mentioned above [for details, we refer to Kumar et al. (2007)].

Recently, nevertheless, with the advent of new techniques such as the small angle X-ray scattering and X-ray absorption near edge spectroscopy, many authors have investigated the synthesis, stressing the importance of the role played by the pH of the reaction solution. Ji et al. (2007), for example, reduced the polydispersity of the particles by increasing the pH of the solution. They observed that the nucleation-growth mechanism occurs only when the pH is above 6.5. Below, they observed that GNPs evolve by nucleation, aggregation and intraparticle ripening. Similarly, when performing the synthesis at 75 ^{0}C, for initial pH values of the precursor between 3 and 5, Wuithschick et al. (2015) reported that nuclei aggregate until forming particles of stable size, which they called seeds. Thereafter, these grow into the final GNPs. This description is referred to as “seed-mediated” mechanism. Moreover, in a recent publication, Kettemann et al. (2016) discussed the importance of the speciation of the precursor and reducing agent at different pH. This aspect of the synthesis is not accounted for in the theory of Turkevich et al. (1951) and, consequently, in the model developed by Kumar et al. (2007).

In light of this evidence, in this chapter we intend to test the Turkevich organizer theory by investigating the model of Kumar et al. (2007). We first review the model and then we test it under new conditions, by comparing its predictions to experimental data available in the literature. In testing the model, we consider factors such as the initial concentrations of the precursor and reducing agent, the initial and final pH of the reaction solution, and the temperature of the latter.

3.2 Review of the mathematical model

In this section, we briefly review the mathematical model developed by Kumar et al. (2007) for the GNPs synthesis by the citrate method. The model comprises material balance equations for the reactants and the products involved in the synthesis and a population balance equation (PBE) that describes how the particle size distribution (PSD) of the nanoparticles evolves. Before reporting such equations, we first clarify what compounds are present and what chemical reactions occur.

3.2.1 Chemical reactions

The components accounted for in the model are auric ions, citrate ions, aurous ions, dicarboxy acetone and acetone, represented by T, C, M, S and D, respectively. All the other reaction products are lumped in one fictitious component P. Five chemical steps are present:

Homogeneous reduction: $T + C \xrightarrow{k_c} M + S$ (1)

Nucleation: $3M \xrightarrow{k_n, S} \text{nucleus} + T$ (2)

Heterogeneous disproportionation: $3M \xrightarrow{k_h, \text{particles}} T + \text{particle mass}$ (3)

Degradation of dicarboxy acetone: $S \xrightarrow{k_s} D$ (4)

Reduction of acetone: $D + 2.5T \xrightarrow{k_d} 2.5M + P$ (5)

Reaction 1 yields the reactants required in the subsequent steps. The reaction rate is assumed to be first-order with respect to both reactants (by implication, this step is an elementary step). The reaction yields aurous ions and dicarboxy acetone.

From the Turkevich organizer theory, dicarboxy acetone (S) organizes aurous ions (M) in the nucleation step (reaction 2). This step requires two molecules of dicarboxy acetone to organize three aurous ions. When a sufficient number of aurous ions are brought together, they disproportionate to form a nucleus. The reaction rate is assumed to be third-order and second-order with respect to aurous chloride and dicarboxy acetone, respectively. Kumar et al. (2007) assumed that the nucleus has a known volume v_0, thus containing ρv_0 moles of gold, where ρ denotes the molar density of gold. This step stops when either dicarboxy acetone or aurous ions are no longer available.

While step 2 occurs, so does step 3, which leads to particle growth. However, to take place, the latter requires the surface of particles. Thus, this step cannot occur before nuclei are formed. Steps 2 and 3 compete for aurous ions. For reaction 3, the rate is assumed to be first-order with respect to aurous chloride. As we will see in Section 3.4, unless a significant particle concentration is present in the system, the consumption rate of aurous ions by step 3 is negligible compared to that of step 2, the latter step being present until dicarboxy acetone (the catalyst for step 2) is fully degraded. This mechanism makes it possible to decouple nucleation from particle growth.

Reaction 4 represents the degradation of dicarboxy acetone. As mentioned, this step is crucial, since it limits nucleation and allows decoupling it from particle growth. The reaction rate is assumed to be first-order.

Reaction 5 occurs when the ratio of citrate to chloroauric acid is below unity. Acetone acts as a second reducing agent, converting the precursor into GNPs. The reaction rate is assumed to be first-order with respect to both reactants (Kumar et al. (2007) made this assumption for this reaction step as it is similar to reaction 1; they are both reducing T to M). In the model of Kumar et al. (2007), the stoichiometric coefficient of component T is 4, whereas we have used the value 2.5. The reason has been explained in Section 2.1.1. The value 4 reported in the original model may be a typo. However, our simulations showed that, for the conditions investigated, the change in value of the coefficient does not affect the results significantly (in particular, the PSD and the mean size of the particles vary negligibly). As we will see in Section 3.4, reactions 2 and 4 determine the mean size. Because reaction 5 is much slower than these two reactions, varying the coefficient affects negligibly the mean size. Table 3.2.1 summarizes the chemical reactions, their corresponding kinetic rate equations and kinetic constants (we report in Section 3.4 how the values of these constants were obtained).

Table 3.2.1. Summary of the chemical reactions, their corresponding kinetic equations and rate constants

Chemical Reactions	Kinetic rate equations, r	Kinetic rate constants, k
$T + C \overset{k_c}{\rightarrow} M + S$	$r_T = -k_c C_T C_C$	$k_c = 1.25\ m^3/(mol.s)$
$3M \overset{k_n,S}{\longrightarrow} \text{nucleus} + T$	$r_{M1} = -3k_n \rho v_0 {C_M}^3 {C_S}^2$	$k_n = N_{av}\ 1.67 \times 10^{-3}\ (m^3/mol)^5\ 1/(m^3.s)$
$3M \xrightarrow{k_h,\text{particles}} T + \text{particle mass}$	$r_{M2} = -3k_h C_M \int_{v_0}^{\infty} v^{2/3} P(v) dv$	$k_h = 2.5 \times 10^{-4}\ m^3/(m^2.s)$
$S \overset{k_s}{\rightarrow} D$	$r_S = -k_s C_S$	$k_s = 1 s^{-1}$
$D + 2.5T \overset{k_d}{\rightarrow} 2.5M + P$	$r_D = -k_d C_T C_D$	$k_d = 4 \times 10^{-1}\ m^3/(mol.s)$

3.2.2 Balance equations

Assuming that the reaction solution is perfectly mixed (which implies that all intensive properties, such as temperature and concentrations, are uniform), we can select as control volume the region (of constant volume V) occupied by the mixture contained in the batch

reactor in which the synthesis occurs. The material balance equations of the mixture components are then those reported below.

Auric chloride

This is reduced by citrate in step 1 and may be reduced by acetone in step 5. On the other hand, it is produced when aurous ions disproportionate in the nucleation and in the growth steps. The material balance equation is:

$$\frac{dC_T}{dt} = -k_c C_T C_C - k_d C_T C_D + k_n \rho v_0 {C_M}^3 {C_S}^2 + k_h C_M \int_{v_0}^{\infty} v^{2/3} P(v) dv \qquad (3.2.1)$$

where *C* denotes the molar concentration of the reactants in mol/m^3 (the subscript indicating which component is being considered), *k* the reactions rate constants (the subscript indicating which reaction is being considered), v the nanoparticle volume (notice that this is not a constant, but a variable characterizing the internal state of the particles) and $P(v)$ the particle size distribution (this, in addition to the independent variable v shown explicitly, depends on the time as well). (The internal coordinate characterizing particles, as used by Kumar et al. (2007), is the particle-volume. In Section 3.3, we revert to the particle-size and relate terms in this chapter to those in Chapter 2.)

Citrate

Citrate appears only in step 1 as a reactant. The material balance equation is:

$$\frac{dC_C}{dt} = -k_c C_T C_C \qquad (3.2.2)$$

Aurous chloride

This is produced in steps 1 and 5, when auric chloride is reduced, but is consumed in steps 2 and 3. Therefore, the material balance equation is:

$$\frac{dC_M}{dt} = k_c C_T C_C + k_d C_T C_D - 3k_n \rho v_0 {C_M}^3 {C_S}^2 - 3k_h C_M \int_{v_0}^{\infty} v^{2/3} P(v) dv \qquad (3.2.3)$$

Dicarboxy acetone

This is consumed by the reaction in step 4 and generated by the reaction in step 1. Note that in the nucleation step dicarboxy acetone acts as a catalyst, and therefore it is not consumed. The material balance equation is:

$$\frac{dC_S}{dt} = k_c C_T C_C - k_s C_S \qquad (3.2.4)$$

Acetone

The material balance equation for acetone is obtained similarly and reads:

$$\frac{dC_D}{dt} = k_s C_S - \frac{1}{2.5} k_d C_T C_D \quad (3.2.5)$$

Gold nanoparticles

We describe the particle population using the number density function (NDF) $P(v,t)$, which is the number of GNPs per unit volume of physical and particle-volume space at time t. In other words, $P(v,t)$ is defined so that $P(v,t)\,dv$ represents the number of particles per unit volume of physical space with volume in the range dv around v at time t. The evolution of $P(v,t)$ is governed by the population balance equation and reflects the effects of the nucleation, growth and aggregation processes taking place in the mixture. The nucleation and growth rates are modelled as follows:

$$H_N(v) = 2k_n {C_M}^3 {C_S}^2\, \delta(v - v_0) \quad (3.2.6)$$

$$G_v(v) = 2\frac{k_h}{\rho} C_M v^{2/3} \quad (3.2.7)$$

where $\delta(v - v_0)$ is a Dirac delta function centered on the nucleus volume v_0. The factor 2 on the right-hand side of the equations above appears because in reactions 2 and 3, for each mole of T that forms, two moles of gold atoms generate.

Although the model is based on a nucleation-growth mechanism, it accounts also for aggregation, in light of the experimental results that Chow and Zukoski (1994) found at high citrate concentrations. So, the aggregation submodel plays an important role only under some process conditions (clarified in Section 3.4), and is given by:

$$B(v) - D(v) = \frac{1}{2}\int_{v_0}^{v} \frac{q(v - v', v')}{W} P(v - v')\, P(v')\, dv' - P(v) \int_{v_0}^{\infty} \frac{q(v, v')}{W} P(v')\, dv' \quad (3.2.8)$$

The first and second terms represent particle birth and death caused by aggregation, respectively. q and W are the aggregation kernel and stability factor, respectively. The former is given by:

$$q(v, v') = \frac{2K_B T}{3\mu}\left(\frac{1}{v^{1/3}} + \frac{1}{v'^{1/3}}\right)\left(v^{1/3} + v'^{1/3}\right) \quad (3.2.9)$$

where K_B, T and μ are the Boltzmann constant, the temperature of the mixture and the viscosity of the fluid, respectively. The stability factor is given by the expression reported below. We discovered a typo in the equation for W reported by Kumar et al. (2007). The authors confirmed (via email correspondence) that the correct expression is:

$$\ln W = \frac{560}{\varphi} \log_{10}\left[\left(3C_{C_0} + C_{T_0}\right) \times 10\right] + 27.5 \quad (3.2.10)$$

where C_{T_0} and C_{C_0} are the initial molar concentrations of chloroauric acid and sodium citrate, respectively, and φ is the surface charge, given by:

$$\varphi = -90[f_a + 1.5(1 - f_a)] \quad ; \quad f_a = \frac{1}{1+0.1C_C/(C_T+C_M)} \tag{3.2.11}$$

Note that W depends on C_{T_0} and C_{C_0}. These are the initial concentrations of T and C, and so do not change with time. The only variable in Eq. (3.2.10) is φ, which can assume a maximum numerical value of -90 when $f_a = 1$ and a minimum numerical value of -135 when $f_a = 0$. Thus, $560/\varphi$ varies from -6.22 to -4.15; the order of magnitude does not change, and W changes little as the synthesis progresses. This is unexpected. Rather, W should increase significantly and tend to infinity with time so as to stabilize the particles and prevent them from aggregating indefinitely.

Furthermore, Kumar et al. (2007) obtained Eq. (3.2.10) based on the expression of Reerink and Overbreek (1954), previously reported in Eq. (2.2.147) in Chapter 2. In deriving their expression for the aggregation process, Reerink and Overbreek (1954) did not account for stabilization by the repulsion energy, prevalent in metal nanoparticles synthesis. Also in this expression, they ignored the size dependence, as shown in Eq. (2.2.173). For details of these inconsistencies, we refer the reader to Section 2.2.3.3 in Chapter 2.

Finally, the population balance equation reads:

$$\partial_t P(v) = -\partial_v[G_v(v)P(v)] + H_N(v) + B(v) - D(v) \tag{3.2.12}$$

The first term on the right-hand side of the equation models is, as usual, convection; in this case, however, it is convection in particle-volume space (not in real space). The other three terms represent generation owing to nucleation and aggregation. For further details about the expressions reported above, we refer to Kumar et al. (2007).

3.3 Model implementation in Parsival

As shown, the model comprises material balance equations for the reacting species and a population balance equation for the GNPs. The former are ordinary differential equations, while the latter is an integro-partial-differential equation. Their combination yields a complex model that can only be solved numerically. To this end, we employed a commercial code called Parsival. This simulation tool is designed for the integration of population balance equations in which the number density function representing the particle population, as well as any other intensive variable such as concentration, are uniform in space. The form of the population balance equation that Parsival solves is shown in Eq. (3.3.1) where it is assumed that the system is closed and uniform (that is, perfectly mixed).

$$\partial_t f(s) = -\partial_s[G_s(s)f(s)] + nucleation + source\ agglomeration - sink\ agglomeration \quad (3.3.1)$$

$f(s)$ represents number of particles per unit particle diameter per physical space volume at time t, $G_s(s)$ the corresponding growth rate.

The equation reveals that in Parsival particle property is described in terms of the diameter s; while, in the original model, it is described in terms of the volume v. We present the transformation as follows. We start by writing:

$$v \equiv m_v s^3 \quad (3.3.2)$$

where v and s are the particle volume and diameter, respectively, while m_v is the volume shape factor. Thus,

$$dv = 3m_v s^2 ds \quad (3.3.3)$$

Next, by definition:

$$P(v,t)dv \equiv f(s,t)ds \quad (3.3.4)$$

where $f(s,t)$ is the new NDF (which gives the number of particles per particle length per volume of the entire mixture). Substituting for dv in eq. (3.3.4), we obtain:

$$P(v,t) = \left(\frac{1}{3m_v s^2}\right) f(s,t) \quad (3.3.5)$$

Similarly, we can show that:

$$\delta(v - v_0) = \left(\frac{1}{3m_v s^2}\right) \delta(s - s_0) \quad (3.3.6)$$

Next, we substitute in the model expressions in terms of v such as:

$$\int_{v_0}^{\infty} v^{2/3} P(v)dv = {m_v}^{2/3} \int_{s_0}^{\infty} s^2 f(s,t)ds \quad (3.3.7)$$

$$\delta(v - v_0) 2k_n {C_M}^3 {C_S}^2 = \frac{\delta(s-s_0)}{3m_v s^2} 2k_n {C_M}^3 {C_S}^2 \quad (3.3.8)$$

$$2\frac{k_h}{\rho} C_M \frac{\partial}{\partial v}.\left(v^{2/3} * P(v,t)\right) = \frac{2}{9}\frac{k_h}{\rho}\left(\frac{1}{{m_v}^{4/3}}\right) C_M \frac{1}{s^2}\frac{\partial f(s,t)}{\partial s} \quad (3.3.9)$$

$$\partial_t P(v) = \left(\frac{1}{3m_v s^2}\right) \partial_t f(s) \quad (3.3.10)$$

For the aggregation submodel, first we substitute eq. (3.3.2) for v in eq. (3.2.9) to finally give:

$$q(v,v') = \widetilde{\omega}_A(s,s') = \frac{2k_B T}{3\mu}\left(\frac{1}{s} + \frac{1}{s'}\right)(s + s') \quad (3.3.11)$$

Similarly for the term $q(v-v',v')$, if we first write:

$$v - v' = m_v \xi^3 \text{ where } \qquad \xi^3 \equiv s^3 - s'^3 \tag{3.3.12}$$

Thus,

$$\widetilde{\omega}_A(\xi, s') = \frac{2k_B T}{3\mu}\left(\frac{1}{\xi} + \frac{1}{s'}\right)(\xi + s') \tag{3.3.13}$$

This relation, along with the following ones:

$$P(v') = \frac{f(s')}{3m_v s'^2} \;\; ; \quad P(v-v') = \frac{f(\xi)}{3m_v \xi^2} \;\; ; \quad dv' = 3m_v s'^2 ds' \tag{3.3.14}$$

allow us to write:

$$\frac{1}{2}\int_{v_0}^{v} \frac{q(v-v',v')}{W} P(v-v')\,P(v')\,dv' = \frac{1}{2}\int_{s_0}^{s} \frac{\widetilde{\omega}_A(\xi,s')}{W} \frac{f(\xi)f(s')}{3m_v\xi^2} ds' \tag{3.3.15}$$

and:

$$P(v)\int_{v_0}^{\infty} \frac{q(v,v')}{W} P(v')\,dv' = \frac{f(s)}{3m_v s^2}\int_{s_0}^{\infty} \frac{\widetilde{\omega}_A(s,s')}{W} f(s')\,ds' \tag{3.3.16}$$

By substituting above equations, we obtain the population balance equation implemented in Parsival as:

$$\frac{\partial f(s,t)}{\partial t} = -\frac{2}{3}\frac{k_h}{\rho} C_M \left(\frac{1}{m_v^{1/3}}\right)\frac{\partial f(s,t)}{\partial s} + \delta(s-s_0) 2k_n {C_M}^3 {C_S}^2 + \frac{1}{2}\int_{s_0}^{s} \frac{\widetilde{\omega}_A(\xi,s')}{W}\frac{s^2}{\xi^2} f(\xi) f(s') ds' -$$

$$f(s,t)\int_{s_0}^{\infty} \frac{\widetilde{\omega}_A(s,s')}{W} f(s')\,ds' \tag{3.3.17}$$

Also, Parsival works on mass basis and expresses the material balances in terms of mass per unit time, while the original model is on mole basis and expresses the material balances in terms of moles per unit time. These are reported below. In the equations, Y is the molecular weight (the subscript indicating the component being considered).

Auric chloride

$$\frac{d[C_T\, Y_T\, V]}{dt} = Y_T V\left[-k_c C_T C_C - k_d C_T C_D + k_n \rho v_0 {C_M}^3 {C_S}^2 + k_h {m_v}^{2/3} C_M \int_{s_0}^{\infty} s^2 f(s,t) ds\right] \tag{3.3.18}$$

Citrate

$$\frac{d[C_C\, Y_C\, V]}{dt} = -Y_C V[k_c C_T C_C] \tag{3.3.19}$$

Aurous chloride

$$\frac{d[C_M\, Y_M\, V]}{dt} = Y_M V\left[k_c C_T C_C + k_d C_T C_D - 3k_n \rho v_0 {C_M}^3 {C_S}^2 - 3k_h {m_v}^{2/3} C_M \int_{s_0}^{\infty} s^2 f(s,t) ds\right] \quad (3.3.20)$$

Dicarboxy acetone

$$\frac{d[C_S\, Y_S\, V]}{dt} = Y_S V[k_c C_T C_C - k_s C_S] \quad (3.3.21)$$

Acetone

$$\frac{d[C_D\, Y_D\, V]}{dt} = Y_D V\left[k_s C_S - \frac{1}{2.5} k_d C_T C_D\right] \quad (3.3.22)$$

All other products

$$\frac{d[C_P\, Y_P\, V]}{dt} = Y_P V\left[\frac{1}{2.5} k_d C_T C_D\right] \quad (3.3.23)$$

Population balance equation

$$\partial_t f(s) = -\,\partial_s[G_s(s) f(s)] + H_N(s) + B(s) - D(s) \quad (3.3.24)$$

with:

$$H_N(s) = 2k_n {C_M}^3 {C_S}^2 \delta(s - s_0) \quad (3.3.25)$$

$$G_s(s) = \frac{2}{3} \frac{k_h}{{m_v}^{1/3}} \frac{C_M}{\rho} \quad (3.3.26)$$

$$B(s) = \frac{1}{2} \int_{s_0}^{s} \frac{\tilde{\omega}_A(\xi, s')}{W} \frac{s^2}{\xi^2} f(s',t) f(\xi,t) ds' \qquad \text{with} \qquad \xi \equiv (s^3 - s'^3)^{1/3} \quad (3.3.27)$$

$$D(s) = f(s,t) \int_{s_0}^{\infty} \frac{\tilde{\omega}_A(s,s')}{W} f(s',t)\, ds' \quad (3.3.28)$$

$$\tilde{\omega}_A(s,s') = \frac{2k_B T}{3\mu}\left(\frac{1}{s} + \frac{1}{s'}\right)(s + s') \quad (3.3.29)$$

where m_v is the particle volume shape factor (which we set equal to $\pi/6$, assuming that the particles are spherical).

Eq. (3.3.24) is a detailed form of Eq. (2.2.49). In association with the other equations written above, the closure problem identified for the latter in Chapter 2 has now been resolved. Comparing them, $\langle G_s \rangle_{av} = G_s(s)$, and $H_V = H_N(s) + B(s) - D(s)$.

By Eq. (3.3.25), the nucleation model, as it depends on the mechanism of nucleation, accounts for the reaction step where 2 molecules of DCA must organize 3 molecules of

aurous chloride for nucleation to occur, following the Turkevich organizer theory. See Figure 2.1.10 for the illustration of the theory.

By Eq. (3.3.26), the growth model, as it also depends on the mechanism of growth, accounts for the heterogeneous disproportionation of auric chloride on the particle surface, as shown in reaction 3. The reaction order of this surface reaction is one.

For the aggregation model, when combined, Eqs. (3.3.27) and (3.3.28) are identical to Eq. (2.2.103). Similarly for the aggregation frequency, Eq. (3.3.29) is identical to Eq. (2.2.106).

The nucleation term in the PBE involves a Dirac delta function. Because of its discontinuity, this function cannot be implemented in Parsival; therefore, we resorted to a similar but smooth function: a Gaussian distribution with mean equal to s_0 (that is, the size assumed for the nuclei) and an extremely small standard deviation.

In the synthesis no nanoparticles are initially present. We could implement this initial condition in Parsival, but an initial NDF that is identically zero may lead to numerical convergence problems. So, we initialized the problem employing the same Gaussian distribution (a normal) used for modelling nucleation, making sure that the mass (or number) of particles initially present was vanishingly small and thus irrelevant.

We will show that these assumptions (i.e., initial particle mass and initial form of the NDF) do not affect the results.

3.4 Implementation check

To check that the model had been correctly implemented in Parsival, we reproduced some of the results obtained by Kumar et al. (2007). Parsival requires values for the seven parameters used in the model, i.e., k_h, k_n, k_s, k_d, k_c, ρ and v_0. Kumar et al. (2007) obtained the values for k_h, k_n and k_s via best-fit, by requiring that the model results should fit the data of Frens (1973). They fixed k_c to render the synthesis time of the same order of magnitude as that experimentally determined at 100 ^{0}C. Also, they assumed a value for k_d smaller than k_c to reflect that the time the process takes to complete is larger when a limited amount of citrate is present (as opposed to the case in which citrate is in excess). They took the value of ρ from the literature and assumed a nucleus size of 2 nm (Turkevich et al. (1951) reported this size as the nucleus size based on their experimental investigation). We employed the same values in our simulations. These are:

$$k_c = 1.25\,\frac{m^3}{mol.s} \quad ; \quad k_n = N_{av}\,1.67\times10^{-3}\left(\frac{m^3}{mol}\right)^5\frac{1}{m^3.s} \quad ; \quad k_s = 1\,\frac{1}{s}$$

$$k_h = 2.5 \times 10^{-4}\ \frac{m^3}{m^2.s} \quad ; \quad k_d = 4 \times 10^{-1}\frac{m^3}{mol.s}$$

$$\rho = 1 \times 10^5\ \frac{mol}{m^3} \quad ; \quad v_0 = 4.18\ \times 10^{-27} m^3$$

From these values, we can obtain approximate characteristic times for the various reactions of the synthesis as follows.

3.4.1 Reactions characteristic times

We estimate the characteristic time for each of the five reactions involved in the citrate method to determine how the reactions progress relative to each other. The characteristic time of a reaction indicates how long the reaction requires to convert a significant amount of the limiting reactant.

Reaction 1

The synthesis begins with the reduction of chloroauric acid by citrate (reaction 1), which produces aurous chloride and dicarboxy acetone.

Assuming that $C_{T_0} = C_{C_0} = 0.3\ mol/m^3$, and given the stoichiometry of the reaction, we can write (the equality of C_{T_0} and C_{C_0}, and the stoichiometry of one would help in illustrating this concept of characteristic times):

$$\frac{dC_T}{dt} = -k_c C_T C_C = -k_c {C_T}^2 \qquad (3.4.1)$$

The characteristic time is therefore equal to:

$$\tau_c \sim \frac{1}{k_c C_{T_0}} = \frac{1}{1.25 \times 0.3} s \sim 1\ s$$

Since this is a second-order reaction, the time that the reaction takes to reduce the concentration of component T to 10% of its original value is ca. $10\,\tau_c$. Over a time τ_c the reagent concentration reduces to about 50% of its original value. The characteristic time of this reaction is $\tau_c \sim 10\ s$.

Reaction 2

$$\frac{dC_M}{dt} = -\left(3k_n \rho v_0 {C_S}^2\right){C_M}^3 \qquad (3.4.2)$$

$C_{M_{max}} = C_{S_{max}} = 0.3\ mol/m^3$ are the maximum concentration values for M and S, if we assume that reaction 1 is complete. Assuming that S does not react (in this reaction it behaves as a catalyst, and, for the time being, we do not consider reaction 4, which consumes S), in the equation above the variable C_S can be replaced with the constant $C_{S_{max}}$. Thus, the reaction is third-order and we can write:

$$\tau_n \sim \frac{1}{\left(3k_n \rho v_0 {C_{Smax}}^2\right){C_{Mmax}}^2}$$

$$\tau_n = \frac{1}{3 \times 1.0053 \cdot 10^{21} \times 10^5 \times 4.18 \cdot 10^{-27} \times 0.3^4} s = 98.72s \sim 100\ s$$

Because this is a third-order reaction, the time that the reaction takes to reduce the concentration of component M to 10% of its original value is ca. $50\,\tau_n$. Over a time τ_n the reagent concentration reduces to about 58% of its original value.

The values reported above hold in the assumption that C_S is constant. But reaction 4 depletes component S, reducing its concentration significantly in about one second (see below). Accordingly, over this time interval, C_S decreases, making τ_n increase rapidly. So, reaction 2 in the end proceeds for a very short time.

Reaction 3

We take the nuclei number density to be equal to $10^{17}\ 1/m^3$ (refer to Section 3.4.2). Assuming that nucleation and growth are fully decoupled and that, once nucleation is over, no aggregation takes place, the particle number density can be taken equal to $10^{17}\ 1/m^3$. So, we can estimate the order of magnitude of the particle surface per unit volume of physical space as follows:

$$\int_{v_0}^{\infty} v^{2/3} P(v) dv \sim \left(4.18 \times 10^{-27}\right)^{2/3} \times 10^{17} = 0.26\, m^2/m^3$$

We can then write:

$$\frac{dC_M}{dt} = -\left(3k_h \int_{v_0}^{\infty} v^{2/3} P(v) dv\right) C_M \qquad (3.4.3)$$

Therefore, the reaction is first-order and the characteristic time is:

$$\tau_{h1} \sim \frac{1}{3k_h \int_{v_0}^{\infty} v^{2/3} P(v) dv} = \frac{1}{3 \times 2.50 \cdot 10^{-4} \times 0.26} s = \ 5{,}128\ s$$

In the above, we assumed the total surface area as that of the nuclei. However, with time, this total surface area increases and would reduce τ_{h1}. If we calculate the time scale based on the final size, which is 37.5 nm for $C_{T_0} = C_{C_0} = 0.3\ mol/m^3$, we have $\int_{v_0}^{\infty} v^{2/3} P(v) dv \sim (2.76 \times 10^{-23})^{2/3} \times 10^{17} = 91.35\ m^2/m^3$, so that $\tau_{h2} = 14.6\, s$. Thus, the growth process starts slowly with a time constant of $5128\, s$ and ends rapidly with a time constant of $14.6\, s$. We thus took the effective growth time constant τ_h to be $\sim 10^2\, s$, as intermediate value closer to that related to the order of magnitude of the final particle surface per unit volume of physical space.

The time scale estimated here gives the order of magnitude of the time required for 99% conversion of gold into GNPs when $C_{T_0} = C_{C_0} = 0.3\ mol/m^3$.

Reaction 4

This is a first-order reaction, and so:

$$\tau_s \sim \frac{1}{k_s} = \frac{1}{1.00} s \sim 1\ s \qquad (3.4.4)$$

A significant amount of S therefore degrades in about one second, stopping reaction 2 prematurely.

In the presence of dicarboxy acetone, aurous chloride converts according to reaction 2, whose characteristic time is $\tau_n \sim 10^4\, s$. Concurrently, dicarboxy acetone degrades into acetone according to reaction 4, whose characteristic time is $\tau_s \sim 1\, s$. Once dicarboxy acetone is consumed, reaction 2 stops. Therefore, reaction 2 has barely started when it stops. However, quite a lot of nuclei are formed ($\sim 10^{17}\ nuclei/m^3$). According to reaction 3, the residual aurous chloride grows the formed nuclei. The characteristic time of this reaction is $\tau_h \sim 10^2\, s$. The last reaction is the second reduction of auric chloride by acetone, occurring only when the ratio of citrate to chloroauric acid is less than unity. The synthesis, nevertheless, is usually carried out with citrate in excess, and therefore we did not estimate the characteristic time of this final reaction.

As previously pointed out, the model also accounts for aggregation; nevertheless, particles only aggregate significantly under certain conditions. For the condition employed in estimating the reactions' characteristic times above, aggregation is insignificant. We show this as follows.

3.4.2 Aggregation characteristic time

NPs are most likely to aggregate when their concentration is the highest. To estimate the characteristic time of the aggregation process, we consider the scenario where the aggregation rate is at its maximum value.

According to Marchisio & Fox (2013), the aggregation characteristic time is given by:

$$\tau_a \sim \frac{W}{q(v_s,v_s)N_c} \tag{3.4.5}$$

Here N_c is the characteristic number concentration of NPs in the system and v_s is the characteristic volume of the NPs. We will consider the minimum value of W, because this favours aggregation. From Eqs. 3.2.10 and 3.2.11, the minimum value is obtained when $f_a = 1$, which gives $\varphi = -90\ mV$. Therefore, it is:

$$\ln W = -\frac{560}{90}\log_{10}\left[\left(3C_{C_0} + C_{T_0}\right) \times 10\right] + 27.5$$

$$= -\frac{560}{90}\log_{10}[(0.9 + 0.3) \times 10] + 27.5; W = 1.06 \times 10^9$$

At the conditions at which the synthesis is conducted, $T = 373\ K$, $\rho = 10^5\ mol/m^3$ and $\mu = 2.74 \times 10^{-4}\ kg/(m.s)$. Since $K_B = 1.38 \times 10^{-23}\ J/K$, Eq. 3.2.9 gives:

$$q(v_s, v_s) = \frac{2K_BT}{3\mu}\left(\frac{1}{v_s^{1/3}} + \frac{1}{v_s^{1/3}}\right)\left(v_s^{1/3} + v_s^{1/3}\right) = \frac{8K_BT}{3\mu} = 5 \times 10^{-17}\ m^3/s$$

The number of NPs per unit volume of physical space that would form before aggregation starts taking place if reaction 2 went to completion is equal to:

$$N_{c,max} = \frac{2}{3}\frac{C_{T_0}}{\rho v_0} \tag{3.4.6}$$

As seen above, to complete, reaction 2 requires $50\ \tau_n$ (i.e. $5{,}000\ s$). But reaction 4 will permit reaction 2 to proceed only for about one second. Therefore, it is:

$$N_c = \frac{2}{3 \times 5{,}000}\frac{C_{T_0}}{\rho v_0} = 9.4 \times 10^{16}\ 1/m^3$$

Thus, replacing these results in Eq. (3.4.5), we obtain:

$$\tau_a \sim \frac{1.06 \times 10^9}{5 \times 10^{-17} \times 9.4 \times 10^{16}} = 2.26 \times 10^8\ s \sim 10^8\ s$$

This is the characteristic time of the aggregation process for the initial conditions used in the synthesis. It gives an estimate of the time required by aggregation to take place significantly.

However, aggregation does not occur in all synthesis conditions. We will point out the conditions that favour aggregation when discussing how the model predicts the data of Chow and Zukoski (1994) in Section 3.4.4. Before that, we discuss the results from the simulations obtained by using the initial conditions adopted previously by Frens (1973) and subsequently by Kumar et al. (2007). The latter, Case 1, will illustrate that in the Turkevich organizer theory particles evolve via the nucleation and growth processes; the former, Case 2, will illustrate the conditions that favour aggregation.

3.4.3 Case 1

Kumar et al. (2007) employed the experimental data of Frens (1973), which were obtained by keeping C_{T_0} constant at $0.3\ mol/m^3$ while changing C_{C_0} from 0.12 to $0.76\ mol/m^3$ at 100 ^{0}C. These initial conditions translate into citrate to gold ratios from about 0.4 to 2.5. *They reported their numerical solutions (the mean diameter of the particles) when 99% of gold had converted to GNPs*, basing this criterion on the fact that the first and higher-order processes included in the model take infinite time to complete (Kumar et al., 2007). In the simulations, for the case where $C_{T_0} = C_{C_0} = 0.3\ mol/m^3$, this criterion translated into a synthesis time of $\sim 10^2\ s$. The synthesis times for other cases may be longer or shorter, depending on the initial conditions.

Figure 3.4.1 reports the numerical predictions of the mean particle diameter obtained by us in Parsival and by Kumar et al. (2007), along with the experimental findings of Frens (1973). Kumar et al. extended the numerical predictions beyond a ratio of 2.5, considering values up to 7. Our predictions agree reasonably well with those of Kumar et al., with a maximum deviation within 5%. To illustrate how we obtained this agreement, let us analyse the results further. For the case in which $C_{T_0} = C_{C_0} = 0.3\ mol/m^3$, the characteristic time for aggregation ($\sim 10^8\ s$) is much longer than the synthesis time ($\sim 10^2\ s$). Therefore, aggregation is insignificant, and the mean size of the particles is $48\ nm$, as reported by Kumar et al. The particles form at $2\ nm$ (the nucleus size) and then grow to their final size. We can calculate the amount of gold that forms the nuclei as follows:

$$\frac{amount\ of\ gold\ for\ both\ nucleation\ and\ growth}{amount\ of\ gold\ for\ nucleation\ only} = \frac{0.3}{x} = \frac{48^3}{2^3} \rightarrow x = 2.17 \times 10^{-5}\ mol/m^3 \quad (3.4.7)$$

Thus, the nuclei concentration that Kumar et al. (2007) obtained is:

$$\frac{x}{\rho v_0} = \frac{2.17 \times 10^{-5}\ mol/m^3}{1 \times 10^5\, mol/m^3\ \times 4.18\ \times 10^{-27} m^3} = 5.19 \times 10^{16}\ nuclei/m^3$$

In our simulations, we obtained $5.23 \times 10^{16}\ nuclei/m^3$ (less than 0.8% deviation from the value above). Because these values are very close, our predictions closely agree with those of Kumar et al. (2007).

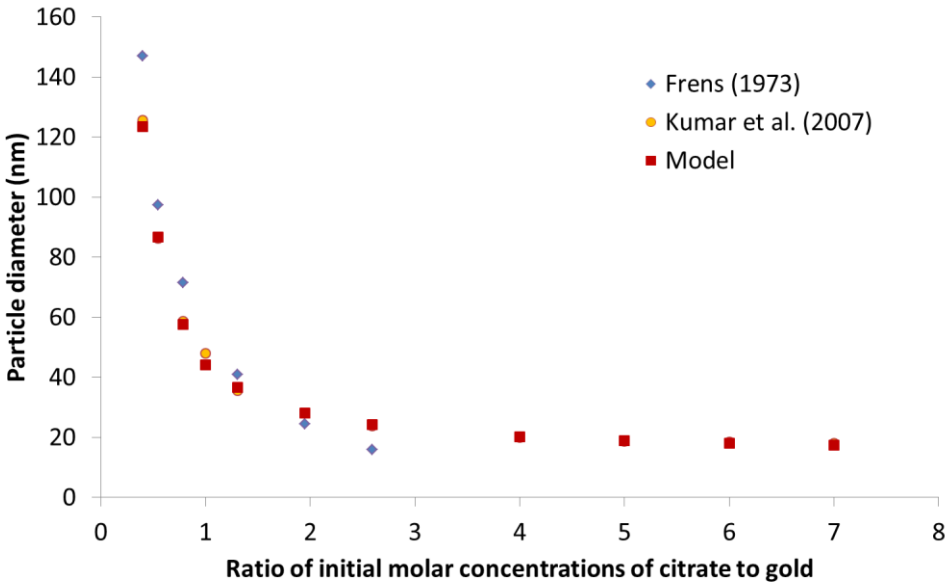

Figure 3.4.1. Comparison of the predictions of the model implemented in this work for Case 1 with those of the model of Kumar et al. (2007) and with the data of Frens (1973). (Like Kumar et al. (2007), we have reported the results in terms of the mean particle diameter).

Citrate reacts with auric ions to produce aurous ions and dicarboxy acetone. The stoichiometric ratio of citrate to gold, obtained by combining reactions 1 to 5, is 1.5 (refer to Kumar et al., 2007). DCA organizes the aurous ions in the nucleation step (reaction 2), but concurrently degrades into acetone (reaction 4). When C_{C_0}/C_{T_0} is less than 1.5, the amount of DCA is limited by the concentration of citrate. Thus, as this ratio decreases, the rate of nucleation decreases. Because the concentration of the precursor is kept constant, the nuclei produced grow to bigger sizes.

When C_{C_0}/C_{T_0} is higher than 1.5, the amount of DCA is limited by the concentration of chloroauric acid, which is kept constant. Hence, as the ratio increases, the rate of nucleation remains almost constant, yielding GNPs of almost identical mean size.

3.4.4 Case 2

Kumar et al. (2007) used this case to emphasize the role of aggregation, which was insignificant for the conditions examined above. The experimental results that they tried to

reproduce were those of Chow and Zukoski (1994). The latter varied C_{T_0} from 0.02 to $1.26\,mol/m^3$ while keeping C_{C_0} and the temperature constant at $1.60\,mol/m^3$ and 70 ^{0}C, respectively, and reported that the nanoparticles aggregated. Although the temperature was different from Case 1, Kumar et al. used the same values of the reaction rate constants. In our investigation, we did the same, not accounting for the temperature effect, inasmuch as our goal in this preliminary part of the work was to reproduce the values reported by Kumar et al. and discuss our findings.

With these conditions citrate is always in excess, so that chloroauric acid determines the amount of DCA formed. Using the same criterion of 99% of gold converted to GNPs and following the reasoning in Section 3.4.1, the synthesis times for $C_{T_0} = 0.1\,mol/m^3$ and $C_{T_0} = 1.26\,mol/m^3$ are $\sim 10^3\ s$ and $\sim 10\ s$, respectively. Figure 3.4.2 shows the predictions of the model that we implemented and those obtained by Kumar et al., compared with the experimental data of Chow and Zukoski (1994). The model of Kumar et al. does not match the experimental data very well; however, the results seem to yield a correct trend, showing that the mean diameter decreases to a minimum value and then increases when the initial concentration of tetrachloroauric acid is increased. This, as Kumar et al. reported, shows that the aggregation process observed by Chow and Zukoski does occur. The predictions of the model which we implemented in Parsival, however, do not show this trend (see Figure 3.4.2 for the predictions trend at 99% of gold converted to GNPs).

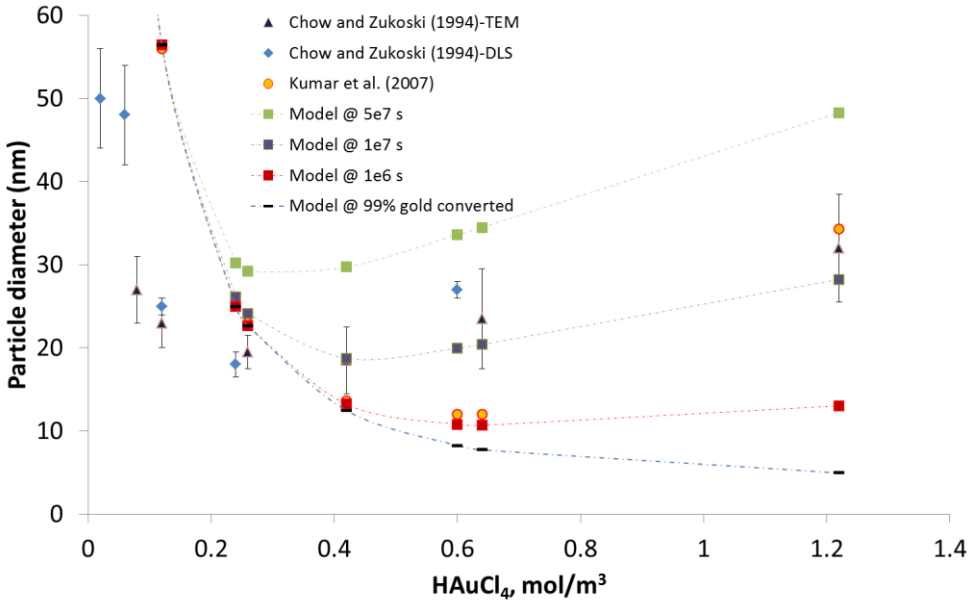

Figure 3.4.2. Comparison of the predictions of the model implemented in this work for Case 2 with those of the model of Kumar et al. (2007) and with the data of Chow and Zukoski

(1994). The figure illustrates how aggregation affects the mean particle size at different simulation times.

To investigate the reason for this difference, we estimated the characteristic times of the aggregation process for $C_{T_0} = 0.1\,mol/m^3$ and $C_{T_0} = 1.26\,mol/m^3$. The times we obtained are $\tau_a \sim 10^9\,s$ and $\tau_a \sim 10^3\,s$, respectively (refer to Section 3.4.2 for details). At these lowest and highest initial concentrations of tetrachloroauric acid, the characteristic times of aggregation (10^9 and $10^3\,s$) are much longer than the corresponding synthesis times (10^3 and $10\,s$, respectively). We therefore concluded that the results reported by Kumar et al. in this case could not be obtained using the 99% conversion criterion previously described.

When $C_{T_0} = 0.1\,mol/m^3$ (the lowest initial concentration of tetrachloroauric acid), the citrate to gold ratio is 16. In these conditions, about $4 \times 10^{14}\ nuclei/m^3$ form, hence consuming $1.7 \times 10^{-7}\,mol/m^3$ of auric ions (see Sections 3.4.1 and 3.4.2 for details). These nuclei grow to an estimated mean particle diameter of $168\,nm$ (this value is not shown in Figure 3.4.2). For the highest initial concentration of tetrachloroauric acid, however, $C_{T_0} = 1.26\,mol/m^3$, about $1.3 \times 10^{20}\ nuclei/m^3$ form, thus consuming $5.34 \times 10^{-2}\,mol/m^3$ of auric ions. These nuclei grow to an estimated mean particle diameter of $5.65\,nm$. Hence, within the synthesis time, the particle diameter decreases when the initial concentrations of tetrachloroauric acid increase. This agrees with our numerical results.

To obtain the trend reported by Kumar et al., we ran the simulation for much longer times than the synthesis times to allow particles to aggregate. The model predictions at different simulation times (10^6, 10^7 and $5 \times 10^7\,s$) are also shown in Figure 3.4.2. Since the characteristic time for aggregation at $C_{T_0} = 1.26\,mol/m^3$ is $10^3\,s$, by $10^6\,s$ the NPs have started to aggregate, increasing the mean particle diameter from $4.96\,nm$ to $10.3\,nm$. As C_{T_0} decreases, the particle concentration decreases while τ_a increases, the particles requiring longer times to aggregate significantly. By $10^6\,s$, the mean size for $C_{T_0} = 1.26\,mol/m^3$ has increased to more than twice the value obtained at 99% gold converted to particles; conversely, for $C_{T_0} = 0.42\,mol/m^3$, for instance, the mean size has only increased from $12.5\,nm$ to $13.2\,nm$.

We should note that in the model of Kumar et al. particles aggregate indefinitely; this is because the stability factor W, which should increase with time, remains constant. As shown in Section 3.2, W depends on the *initial* concentrations C_{T_0} and C_{C_0}, not on the current concentrations C_T and C_C. Figure 3.4.2 reveals this indefinite aggregation: the longer the

simulation time, the larger the mean particle diameter. We can infer that, as the simulation time tends to infinity, the particles would coalesce into one aggregate. This is clearly at variance with the experimental evidence.

To make the model correctly reflect the experimental evidence, which indicates that aggregation must eventually stop, in the equation for the stability factor, Eq. (3.2.10), we replaced the initial concentrations, C_{T_0} and C_{C_0}, with the current ones, C_T and C_C. The model, however, did not improve. As C_T and C_C decrease due to the reactions, W, and in turn the aggregation time, increase. Because C_T and C_C eventually reach constant values (but do not both vanish), W and the aggregation time also reach constant values. Accordingly, the aggregation time never diverges and the particles aggregate indefinitely at constant rate. However, several authors, such as Chow and Zukoski (1994) and Ji et al. (2007), reported that the aggregation process becomes less significant as particle size increases. Therefore, the expression for W must be a function of, and should increase with, particle size.

Because particles aggregate indefinitely in the model, we retain the criterion of 99% of gold converted to GNPs to obtain the simulation time and use the corresponding mean size in testing the model in Section 3.5.

3.4.5 Effects of our assumptions in the model implementation

We ran four simulations to check the effect of the reactor volume and of the initial particle size distribution on the results of the model. In the model of Kumar et al. (2007), it was assumed that the system was perfectly mixed. This implies that the properties of the system are uniform in physical space and therefore do not depend on the location in physical space. It also implies that the reactor volume should not affect the results of the model. To check this, we varied the reactor volume, keeping the initial concentration of the reactants constant. We used two reactor volumes of 2 and $10\ m^3$, respectively. To check the effect of the initial particle size distribution, we used two distributions of different shapes (see Figure 3.4.3), denoted as D1 and D2. In all cases, the initial particle mass was set to 1e-20 kg; this is a negligible amount, which reflects the fact that initially no particles are really present in the system (note that, as already mentioned, using an initial distribution that vanishes identically over the entire size space is not recommended). In all cases, the final mean size of the particle was the same, equal to 46.5 nm. So, as expected, neither the volume nor the shape of the initial distribution affects the numerical results.

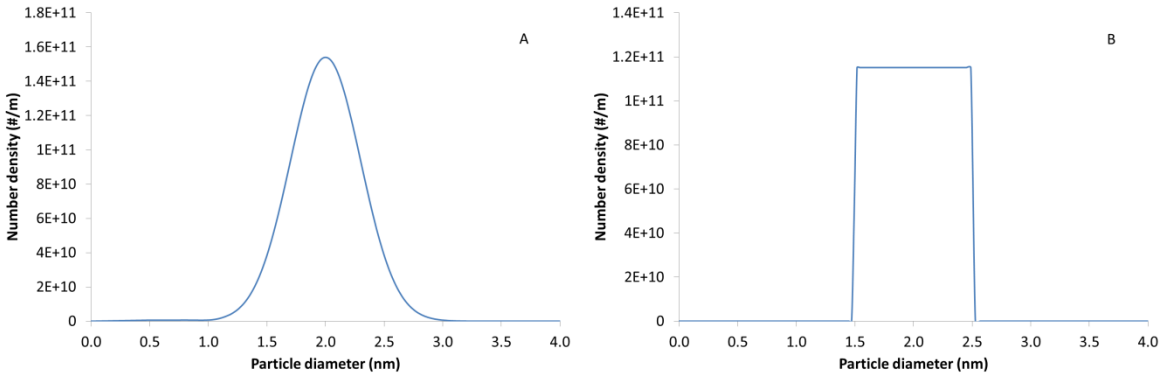

Figure 3.4.3. Particle size distributions used to initialize the simulations and for describe the nucleation process in Parsival. Distribution D1 is on the left, while distribution D2 is on the right.

Furthermore, to test the numerical accuracy in Parsival, in Appendix D, we present another experimental problem involving a crystallization process and solve it using the numerical code. We refer the reader to this appendix for more information.

3.5 Testing of the model

In the previous sections, we reported and solved the model developed by Kumar et al. (2007); also, we compared our results to those of Kumar et al. (2007). In this section, we test the model using experimental data available in the literature to assess whether the Turkevich organizer theory, on which the model is based, rightly describes the synthesis. Kumar et al. used the discussions in Case 1 (Section 3.4) to illustrate that the organizer theory is generally valid for the citrate reduction method. After employing the work of Frens (1973) to estimate the parameters used in the model and predicting his experimental data with excellent agreement, Kumar et al. reported that the same model parameters gave good predictions for the work of Turkevich et al. (1951), Freund and Spiro (1985), and Abid (2003). We believe the model well reproduced these data because these researchers used initial conditions similar to those of Frens, whose work Kumar et al. fitted to make the predictions from the nucleation-growth model accurate. In Case 2 we showed how the model failed to predict the data of Chow and Zukoski (1994) and the inconsistencies in temperature and simulation times. In this section, we employ new data to test the model.

Many other researchers have investigated the synthesis experimentally and in recent times have emphasized the significant role of pH in the synthesis (both the initial and final pH), which determines how particles evolve in the synthesis. For example, Ji et al. (2007) observed that NPs evolve by nucleation, aggregation and growth when the final pH of the mixture is below 6.5, while they evolve by nucleation and growth when the final pH of the

mixture is above 6.5. In the same way, Wuithschick et al. (2015) stated that the synthesis follows the seed-mediated mechanism (which is consistent with the nucleation-aggregation-growth description of the synthesis) when the initial pH is equal to 3.5. This mechanism of the synthesis can be explained on the basis of the chemical properties of the precursor and reducing agent, which are a strong acid and a weak base, respectively.

The precursor, tetrachloroauric acid, completely ionizes in an aqueous solution to release hydrogen ions and tetrachloroauric ions. In the presence of a base, hydroxyl ions replace chloride species in tetracloroauric ions to yield from monohydroxylated to tetrahydroxylated species. The speciation of the latter depends on the pH. The more hydroxylated the species is, the less reactive it is [whilst monohydroxylated trichloroauric ions can be reduced, species from dihydroxylated dichloroauric ions do not react, unless the pH is lowered (Ji et al., 2007)]. The model developed by Kumar et al. (2007) does not account for these pH effects, solely accounting for how the tetrachloroauric acid reduces in the synthesis.

The reducing agent, on the other hand, performs three important roles: reduces the precursor, supplies the hydroxyl ions and stabilizes the NPs, preventing aggregation. These additional reactions and processes render the synthesis complex to describe. Wuithschick et al. (2015) identified the factors affecting the final size as temperature, the initial concentrations of the precursor and reducing agent, and the initial and final pH. Thus, we used these factors to test the model. First, we tested the model against the work of Wuithschick et al. (2015) and Turkevich et al. (1951) for the effect of temperature. Second, we tested it against the work by Takiyama (1958), carried out at 80 ^{0}C. Third, we employed the works of Zabetakis et al. (2012) and Li et al. (2011) to test the model for the effect of the initial pH of the precursor. Lastly, we used the data of Ji et al. (2007) to test the role of the final pH of the mixture. For these experimental data, no error bars are reported because they are not available in the literature.

3.5.1 Effect of temperature

In their publication, Kumar et al. (2007) only tested the model for the Turkevich organizer theory at the usual synthesis temperature of 100 ^{0}C. In the literature, however, authors such as Turkevich et al. (1951) and Wuithschick et al. (2015) have investigated the effect of temperature on the final particle diameter. The former reported the mean sizes at 70, 80 and 100 ^{0}C for initial concentrations of $C_{T_0} = 0.26\ mol/m^3$ and $C_{C_0} = 1.9\ mol/m^3$, while the latter reported the mean sizes as the temperature changed from 23 to 100 ^{0}C for initial concentrations of $C_{T_0} = 0.25\ mol/m^3$ and $C_{C_0} = 2.5\ mol/m^3$. In both cases, citrate was in excess. To test the model at temperatures different from 100 ^{0}C, we require the activation

energies for the reactions involved in the synthesis so as to obtain their corresponding reaction rate constants. Out of five reactions, only four have their activation energies reported in the literature. Turkevich et al. (1951) reported the activation energies for the nucleation step (reaction 2) and growth step (reaction 3) as 10 and $9.1\ kcal/mol$ respectively; Wiig (1928) reported an activation energy for the reaction of dicarboxy acetone decomposition (reaction 4) of $23.1\ kcal/mol$. Using molecular modelling, Ojea-Jiménez and Campanera (2012) obtained the activation energy of the reduction step by citrate (reaction 1) as $34\ kcal/mol$. The last reaction (reaction 5), as we discussed, occurs only when the ratio of the initial concentrations of sodium citrate to tetrachloroauric acid is below unity. Therefore, in these investigations, reaction 5 was insignificant.

Figure 3.5.1A shows how the mean particle diameter changes with temperature for the data of Wuithschick et al. (2015). The model poorly predicts the experimental data. Starting from 23 ^{0}C, the mean size from experiment decreases with temperature and reaches a minimum value at around 60 ^{0}C before increasing. In contrast, the model predicts that the size decreases from 23 ^{0}C, where the mean diameter is 24.5 nm, to 40 ^{0}C, where the mean diameter is 21.5 nm, remaining constant thereafter. In this range of temperatures, the characteristic time of aggregation remains essentially constant at $10^7\ s$ (see Section 3.4.2 for details). However, the synthesis time decreases with increasing temperature. At 23 ^{0}C, the synthesis time is $10^9\ s$, a value obtained following the reasoning in Section 3.4.1, where the reaction rate constants at this temperature are used. As the synthesis time is longer than the time constant for aggregation, the particles aggregate, attaining a final mean size of 24.5 nm. At higher temperature, the effect of aggregation decreases as the synthesis time decreases. Therefore, the mean size decreases. By 50 ^{0}C, aggregation has stopped affecting the mean size, because the synthesis time is now much shorter than the characteristic time of aggregation. When the effect of aggregation is negligible, as highlighted in Section 3.4, the balance between the nucleation step (reaction 2) and the decomposition of dicarboxy acetone (reaction 4) determines the final mean size, which remains constant at 21.3 nm with increasing temperature. To explain this profile, in Table 3.5.1, we report the values of the rate constants of reactions 2 and 4, and their ratio at different temperatures. The ratio (k_n/k_s) remains constant, and this explains why the final mean size is constant as well. However, the experimental data do not remain constant with temperature; so, the balance between reactions 2 and 4 does not describe the synthesis. This aspect, consequently, is not properly captured by the model of Kumar et al.

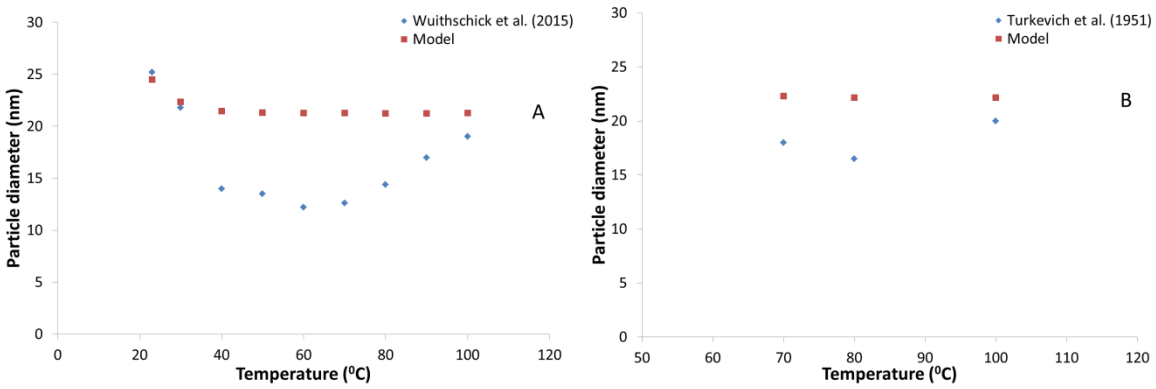

Figure 3.5.1. Comparison of the model predictions at different temperatures with the data of (A) Wuithschick et al. (2015) and (B) Turkevich et al. (1951).

Table 3.5.1. Values of the rate constants of reactions 2 and 4 with temperature.

Temperature (^{0}C)	k_n	k_s	k_n/k_s
23	6.61E+15	6.57E-06	1.01E+21
30	2.51E+16	2.50E-05	1.01E+21
40	1.53E+17	1.52E-04	1.01E+21
50	8.29E+17	8.25E-04	1.01E+21
60	4.07E+18	4.05E-03	1.01E+21
70	1.82E+19	1.81E-02	1.01E+21
80	7.48E+19	7.44E-02	1.01E+21
90	2.84E+20	2.83E-01	1.01E+21
100	1.01E+21	1.00E+00	1.01E+21

The seed-mediated mechanism proposed by Wuithschick et al. (2015) describes the synthesis and explains the profile of the final mean size with temperature shown in Figure 3.5.1A. According to this mechanism, nuclei generate after citrate reduces tetrachloroauric acid. These nuclei aggregate to form bigger particles. Similarly, particles containing two or more nuclei can also aggregate. Nevertheless, particle aggregation stops for particles with sizes equal to the seed size [see Wuithschick et al. (2015) for more information]. The seeds

subsequently grow to the final particle size. Thus, the seed-mediated mechanism occurs according to the order: nucleation, aggregation and growth. Among these processes, aggregation is the most sensitive to temperature. Temperature affects both the aggregation kernel q and the stability factor W, both of which determine the aggregation rate (Marchisio and Fox, 2013). For an aqueous system, Wang et al. (2010) reported that aggregation is insignificant below 60 ^{0}C for the reaction conditions which Wuithschick et al. (2015) investigated. Temperature also affects the rates of the nucleation and growth processes, as the Arrhenius equation illustrates. At low temperatures, both rates decrease so that only few nuclei form, and these grow slowly. Since the reaction mixture is left until all the precursor is converted, the few nuclei formed at 23 ^{0}C reach a large final size. As the temperature increases from 23 to 60 ^{0}C, the nucleation rate increases, forming more nuclei and leaving behind a smaller amount of precursor. The latter grows the many nuclei to smaller final sizes. For these initial conditions, as observed in Figure 3.5.1A, aggregation becomes significant above 60 ^{0}C. As the temperature rises from 60 ^{0}C, particle aggregation increases the final particle size.

3.5.2 Effect of initial $HAuCl_4$ concentration

Another investigation of the Turkevich synthesis that did not follow the usual method of changing citrate concentration at a fixed concentration of tetrachloroauric acid was that by Takiyama (1958). This investigation predated the work of Frens and provides additional data with which to test the model. Takiyama studied the synthesis at 80 ^{0}C and $C_{C_0} = 3.88\ mol/m^3$ while changing C_{T_0} from 0.05 to $1.28\ mol/m^3$; so, citrate is in excess. In solving the model for these initial conditions, we used the values of the reaction rate constants and other parameters at the operating temperature. Figure 3.5.2 shows the model predictions along with the corresponding experimental data. For the model predictions, which do not agree with the data, the profile of the mean particle diameter with the initial concentration of gold resembles that of Figure 3.4.2 (this was expected, because the operating conditions in this study resemble those of Case 2, discussed in Section 3.4.4). As the synthesis is at 80 ^{0}C, the synthesis time is far shorter than the aggregation characteristic time, so that the role of aggregation is negligible and only nucleation and growth affect the particle size distribution. If we assume that the two latter processes are fully decoupled (as shown in Section 3.4), the concentration of nuclei formed equals the concentration of particles in the final reaction mixture. As revealed in Section 3.4.2, to determine the concentration of nuclei N_c, we need to know the maximum concentration of nuclei $N_{c,max}$, the characteristic time for nucleation τ_n and the characteristic time for the decomposition of dicarboxy acetone τ_s. The expression $N_c = (\tau_s/\tau_n)N_{c,max}$ is found. If we consider the lowest concentration of precursor

considered, $C_{T_0} = 0.05\, mol/m^3$, following the reasoning presented in Section 3.4.1, we obtain $\tau_s = 10\, s$, $\tau_n = 10^6\, s$ and $N_{c,max} = 7.97 \times 10^{19}\ nuclei/m^3$, which results into $N_c = 4.26 \times 10^{14}\ nuclei/m^3$. This estimate is of the same order of magnitude as the value obtained from the model numerical solution ($2.13 \times 10^{14}\ nuclei/m^3$). In forming these nuclei, $\rho v_0 N_c = 1.78 \times 10^{-7}\ mol/m^3$ of the precursor converts. The concentration of the precursor that is left is $\sim 0.05\ mol/m^3$. Using Eq. (3.4.7), the remaining amount grows the nuclei to:

$$\sqrt[3]{\left(\frac{0.05}{8.9 \times 10^{-8}} \times 2^3\right)} = 165\, nm$$

For the highest precursor concentration, $C_{T_0} = 1.28\, mol/m^3$, on the other hand, the model numerical solution yields a nuclei concentration of $3.32 \times 10^{20}\ nuclei/m^3$, which is $\sim 10^6$ times the concentration of nuclei obtained for $C_{T_0} = 0.05\, mol/m^3$. These more concentrated nuclei grow to a mean size of $3.4\, nm$. Thus, as we move from $C_{T_0} = 0.05\, mol/m^3$ to $1.28\, mol/m^3$, the mean particle diameter decreases from $165\, nm$ to $3.4\, nm$.

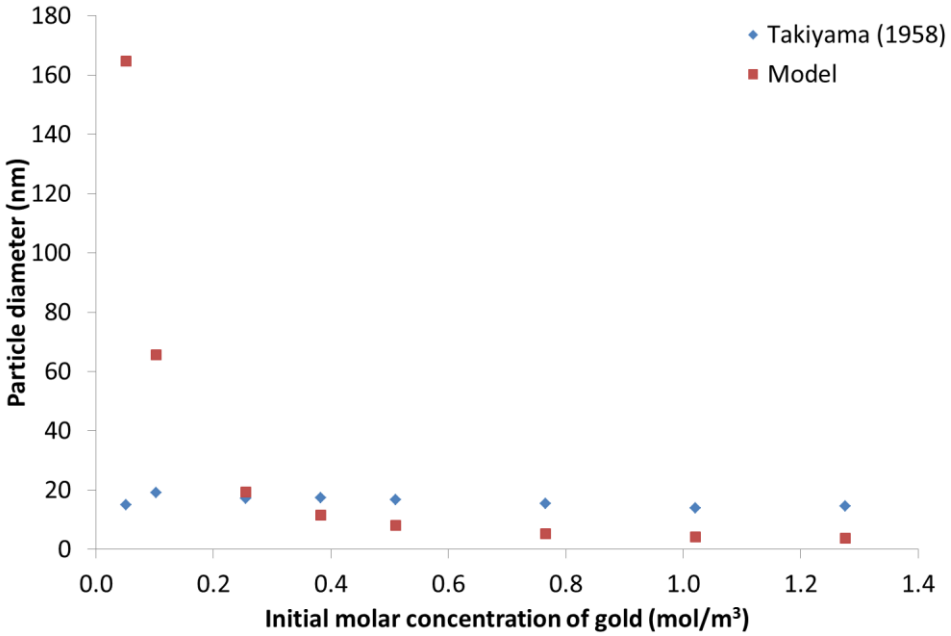

Figure 3.5.2. Comparison of the model predictions at different gold concentrations with the data of Takiyama (1958).

The seed mediated mechanism, on the other hand, explains the experimental profile in Figure 3.5.2. The final mean size increases slightly from $15\, nm$ at $C_{T_0} = 0.05\, mol/m^3$ to $19\, nm$ at $C_{T_0} = 0.10\, mol/m^3$ and then remains almost constant afterwards. Because the sodium citrate solution can supply OH^-, the precursor can undergo two reactions: reduction

to form the nuclei and passivation by OH^-. The passivation can produce monohydroxylated species of the precursor; even in the presence of much OH^-, it can produce higher hydroxylated species of the precursor. The monohydroxylated species reduces to gold and grows the particles while the higher hydroxylated species cannot reduce to gold, leaving behind unconsumed gold in the solution. At $C_{T_0} = 0.05\, mol/m^3$, the ratio of citrate to gold is 80, producing much OH^- that can form higher hydroxylated species. The mean size is small as some of the precursor is lost to the formation of higher hydroxylated species. As C_{T_0} increases, the ratio of citrate to gold decreases, producing a smaller amount of OH^-. Therefore, more precursor converts to gold nanoparticles, increasing the mean size. As C_{T_0} increases further, more precursor goes through the reduction step and produces many nuclei and seeds. Although more precursor also forms the monohydroxylated species that can grow the seeds, the balance between the number of seeds and the amount of gold available to grow them keeps the final mean size almost constant.

3.5.3 Effect of initial pH of $HAuCl_4$ (aq)

To test the effect of the initial pH of the precursor, we employed the initial conditions of the work by Zabetakis et al. (2012). They synthetized the NPs at different initial concentrations ($0.3 - 2.0\ mol/m^3$) of the precursor at a temperature of 100 ^{0}C, keeping the citrate to gold ratio (denoted as R) constant. They considered R values of 2, 3, 4 and 5. We obtained the initial pH values from the initial concentrations of tetrachloroauric acid, which is a strong acid. Figure 3.5.3 shows the model predictions against the experimental data for the effect of the initial pH of tetrachloroauric acid for all the values of R investigated. The model predictions are unsatisfactory. They generally increase as the initial pH rises, unlike the experimental data that decrease and then increase, hence presenting a minimum. Low initial pH translates into high concentration of tetrachloroauric acid. For instance, for $R = 2$ (i.e., the lowest pH considered, equal to 2.93), $C_{T_0} = 1.2\, mol/m^3$. From the simulation, this concentration yields $\sim 10^{20}\ nuclei/m^3$, consuming $4.18 \times 10^{-2}\, mol/m^3$ of T. Since aggregation is insignificant, these nuclei can only grow to a mean size of $3.9\, nm$, consuming the remaining quantity of T. The highest pH of 3.53, on the other hand, corresponds to $C_{T_0} = 0.3\, mol/m^3$, and generates $\sim 10^{18}\ nuclei/m^3$. To form, these nuclei consume $4.18 \times 10^{-4}\, mol/m^3$ of T and grow to a bigger mean diameter. So, in the numerical simulations, as the initial pH increases, the mean diameter increases.

The seed-mediated mechanism describes the behaviour observed experimentally. Low initial pH translates into a small amount of OH^-, which can only passivate a small portion of the precursor. Most of the precursor converts into gold and produces several nuclei. These

nuclei aggregate to form the seeds. On how the reaction condition favours aggregation, Wuithschick et al. observed vigorous aggregation at low pH that becomes less significant as the initial pH increases. Thus, at low pH, because of the effect of aggregation, the several nuclei aggregate to form larger seeds, producing larger final particles. As the initial pH increases, the amount of OH^-, which passivates the precursor, increases. The amount of the precursor that converts into gold decreases, yielding fewer nuclei. Because aggregation becomes less significant, these fewer nuclei aggregate less into smaller seeds, producing final smaller particles. As the initial pH increases further, even more precursor becomes passive. A small portion of the precursor reduces to even fewer nuclei. However, according to Wuithschick et al., increasing the initial pH at this stage does not significantly reduce the seed size. Thus, the fewer nuclei yield fewer seeds. Then, the passive form of the precursor, which increases with the initial pH, grows the fewer seeds to larger particles.

Li et al. (2012) published a work similar to that of Zabetakis et al. (2012). They used different initial concentrations of tetrachloroauric acid at a constant citrate-to-gold ratio of 4. Figure 3.5.4 shows their data with the corresponding model predictions; the trends are similar to those reported by Zabetakis et al., and similar considerations to those already discussed hold.

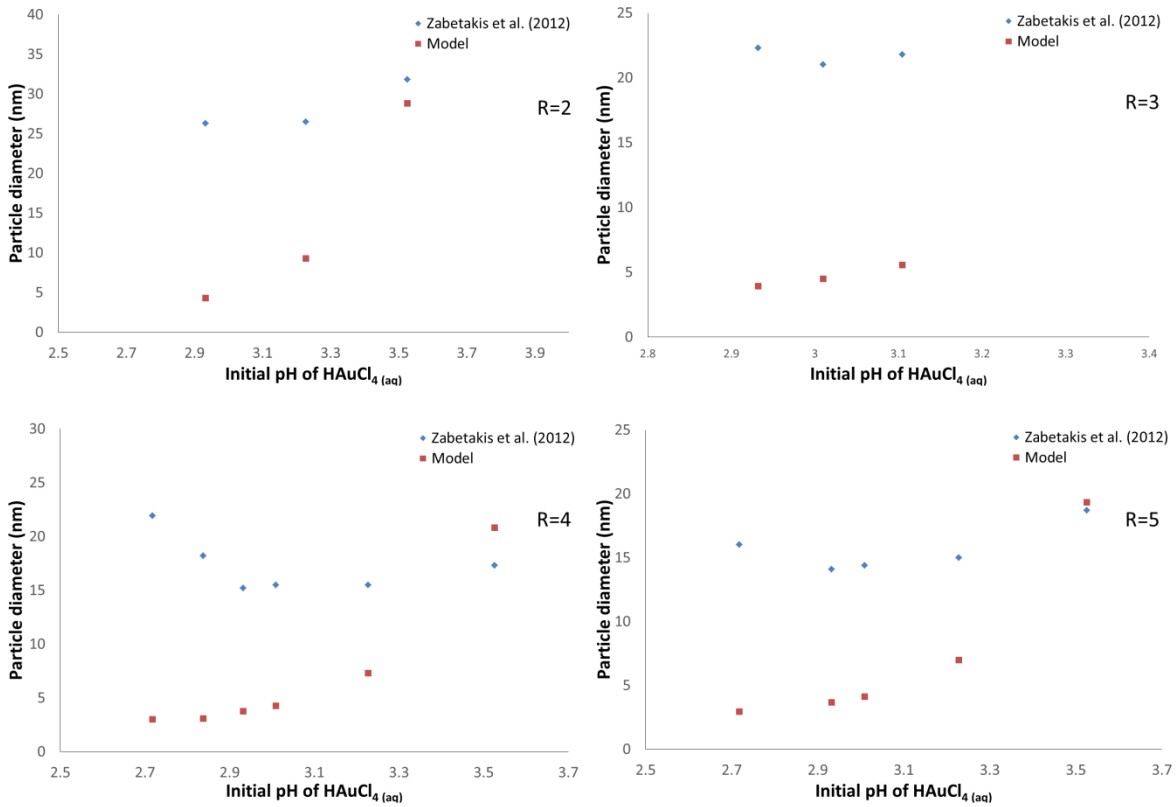

Figure 3.5.3. Comparison of the model predictions at different initial pH with the data of Zabetakis et al. (2012). R represents the ratio of citrate to gold.

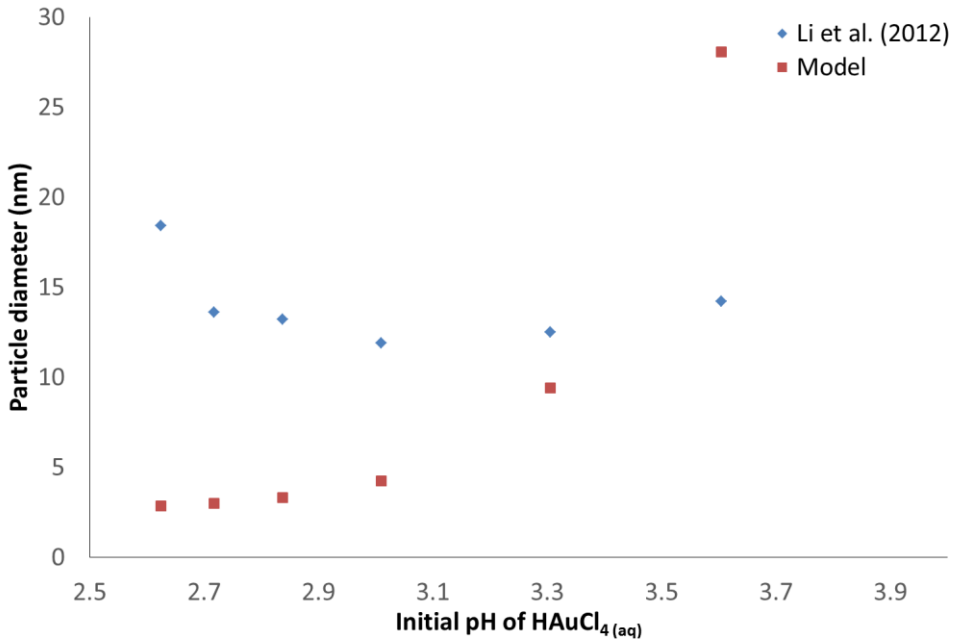

Figure 3.5.4. Comparison of the model predictions at different initial pH with the data of Li et al. (2012).

3.5.4 Effect of final pH of the mixture

As previously mentioned, Ji et al. (2007) have reported that the mechanism of the synthesis depends on the final pH of the reaction mixture: at low pH the mechanism involves nucleation, aggregation and then growth, while at high pH it involves only nucleation and then growth. Calculating the final pH of the reacting mixture requires detailed knowledge of the thermodynamics of the synthesis, which is currently not available in the literature. The dissociation of sodium citrate depends on the pH, which in turn depends on the sodium citrate concentration. Along with reporting the values of the citrate to gold ratios considered, Ji et al. (2007) measured the corresponding final pH of the synthesis. They varied C_{C_0} from $0.23\,mol/m^3$ to $6.92\,mol/m^3$ while keeping both C_{T_0} and the temperature constant at $0.25\,mol/m^3$ and 100 ^{0}C, respectively. Figure 3.5.5 shows their data along with the model predictions at 99% of gold converted to GNPs. With this criterion, aggregation is insignificant in the simulation. For the model predictions, as the final pH increases, the mean particle diameter decreases. While, for the experimental data, the mean particle diameter decreases until the final pH reaches 6.5 and then increases. The lowest final pH of 4.15 corresponds to $C_{C_0} = 0.23\,mol/m^3$ and a citrate to gold ratio $R = 0.9$. For this ratio, in the model, citrate is the limiting reactant and determines the amount of DCA that forms the nuclei. The concentration of the latter is $\sim 10^{17}\ nuclei/m^3$. These nuclei then grow to a mean size of $71.6\,nm$. Increasing the final pH corresponds to increasing C_{C_0} so that citrate becomes in excess and C_{T_0} starts determining the amount of DCA that forms the nuclei. The highest final pH of 6.92 corresponds to $C_{C_0} = 6.92\,mol/m^3$. At this pH, $C_{T_0} = 0.25\,mol/m^3$ and the concentration of nuclei results to be $\sim 10^{19}\ nuclei/m^3$, $\sim 10^2$ times larger than that of the lowest pH. The nuclei concentration therefore varies from $10^{17}\ nuclei/m^3$ at the minimum final pH to $10^{19}\ nuclei/m^3$ at the maximum final pH. As C_{T_0} is constant at $0.25\,mol/m^3$, the final mean size decreases with increasing pH.

It is still the seed-mediated mechanism by Wuithschick et al. (2015) that explains the experimental data, just as Ji et al. (2007) also explained the synthesis in their report using two mechanisms: nucleation-aggregation-growth when the pH is below 6.5 and nucleation-growth when the pH is above 6.5. Both explanations, by Ji et al. (2007) and Wuithschick et al. (2015), stem from the acid-base properties of the precursor and reducing agent. From thermodynamics, tetrachloroauric ion converts reversibly to the monohydroxylated form, both ions being present in equal amounts at the pH of 6.5. pH below 6.5 shifts the equilibrium to tetrachloroauric ion while pH above 6.5 shifts it to the monohydroxylated form. At the lowest final pH of 4.15, almost all the precursor forms nuclei; only a small portion (or even none) of it becomes hydroxylated. This produces several nuclei that then aggregate to form large

particles. As the final pH increases, aggregation starts playing a less significant role, and therefore the particle diameter decreases until the final pH is 6.5. Above 6.5, less of the precursor forms nuclei while more becomes hydroxylated, so that less particles form, which later grow when the hydroxylated precursor reacts on the particle surface. Thus, the increase in size after the pH of 6.5 is due to fewer particles growing bigger, whereas the increase in size below the pH of 6.5 is due to several particles aggregating into bigger sizes.

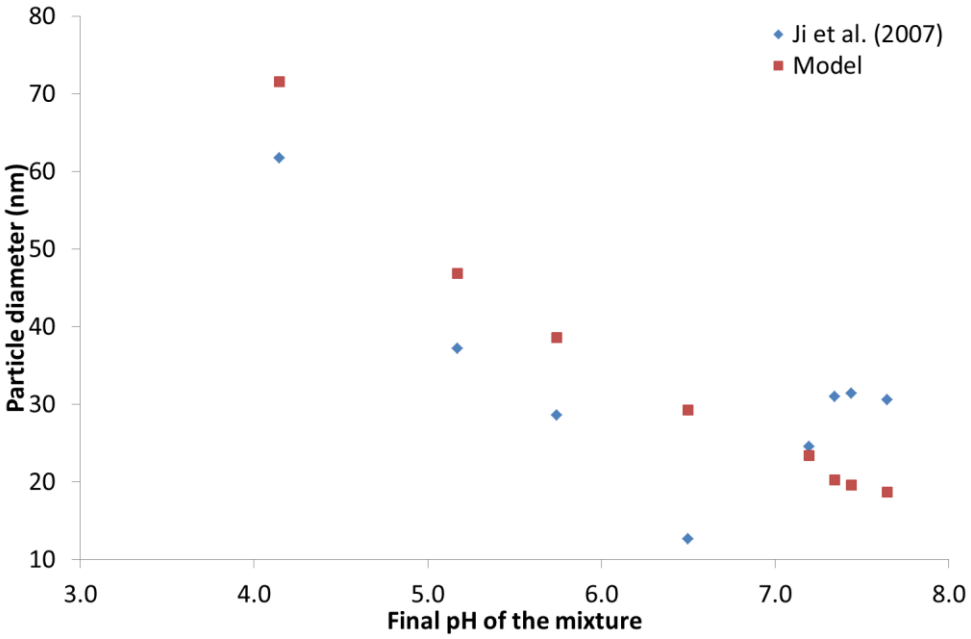

Figure 3.5.5. Comparison of the model predictions at different final pH with the data of Ji et al. (2007).

3.6 Concluding remarks

This work investigated the mathematical model developed by Kumar et al. (2007) for the synthesis of gold nanoparticles by means of the citrate method. This is the only model, based on the Turkevich organizer theory, available in the literature. The model accounts for five reaction steps, one of which produces dicarboxy acetone, which organizes gold in the nucleation step. While DCA decomposes, the particles grow by the deposition of the residual precursor on their surfaces. GNPs evolve by the nucleation-growth mechanism, as proposed

by Turkevich et al. (1951). Although Kumar et al. (2007) included a submodel for aggregation, this submodel does not play a significant role over the synthesis time.

Further, we tested the model for different conditions of temperature, concentrations and pH using various experimental data from the literature. The model performed poorly in describing the synthesis. We believe that this is because the five chemical steps over which the model of Kumar et al. is built do not reflect the chemistry of the synthesis accurately. Because the precursor and reducing agent are a strong acid and a weak base, respectively, their acid-base properties cover an important role in the synthesis. As a weak base, the reducing agent releases OH^- in water. The precursor, on the other hand, can be reduced and/or hydroxylated. Kumar et al. only modelled the reduction step that produces the nuclei but did not consider the hydroxylation step. Subsequently, these nuclei aggregate into seeds, which then grow by reacting with the hydroxylated precursor. Using the seed-mediated mechanism proposed by Wuithschick et al. (2015), we were able to qualitatively explain the experimental data reported by the researchers.

In the light of this work, it is necessary that a new model be derived for the citrate method. Since the seed-mediated mechanism of Wuithschick et al. (2015) seems to be able to convincingly describe the trends observed experimentally, this model should be based on this mechanistic theory along with all the chemical steps that reflect the acid-base properties of the precursor and reducing agent. These steps include reducing and hydroxylating the precursor to gold atoms and the passive form of the precursor, respectively, aggregating gold atoms to the seed particles, and growing the latter to the final GNPs by reacting with the passive precursor. We develop this model in the following chapter.

Chapter 4

A New Model Based on the Seed-mediated Mechanism

In this chapter, we report the development, implementation and validation of a novel mathematical model for the synthesis of gold nanoparticles by the “citrate synthesis method” based on a mechanistic description recently reported in the literature. This mechanism involves various reactions and processes, such as nucleation, aggregation and growth. To model the reactions, we adopted rate-order equations, some of which we derived using experimental data from the literature. The model is based on a population balance equation, which is coupled with a number of mass balance equations for the reactants involved in the synthesis. We validated the model predictions using experimental data from the literature. In the following introduction, we report the motivation and structure of the chapter.

Parts of this chapter have been published:

Agunloye, E., Panariello, L., Gavriilidis, A., Mazzei, L., 2018. A Model for the Formation of Gold Nanoparticles in the Citrate Method, *Chemical Engineering Science, 191*, 318-331. doi:10.1016/j.ces.2018.06.046

4.1 Introduction

In the past, researchers explained the GNPs synthesis through the pioneering work of Turkevich et al. (1951), who suggested that the particles form via a nucleation-growth mechanism. According to this mechanistic description of the synthesis, tetrachloroauric acid reacts with sodium citrate to form gold chloride and dicarboxy acetone (DCA). Subsequently, the latter (which acts as nucleation agent) organizes gold chloride to form gold nuclei, while decomposing into acetone. Its decomposition eventually prevents the generation of new nuclei (nucleation stops), leaving behind unconsumed gold chloride that reacts on the surface of the particles thereby making them grow. Nucleation and growth are therefore decoupled.

Kumar et al. (2007) developed a mathematical model for the description of the GNPs synthesis, basing it on such a theory. In Chapter 3, we tested the model for different synthesis conditions studied experimentally by various researchers, for which results are available in the literature. The model poorly predicted the experimental data, because the

Turkevich organizer theory does not account for the acid-base properties of the precursor and reducing agent.

In the last decade, however, new evidence has emerged indicating that the particles aggregate significantly during the synthesis, aggregation taking place after nucleation but before growth (Wuithschick et al., 2015). Further evidence has shown that changing the pH value at which the synthesis is conducted affects the processes of nucleation, aggregation and growth, and influences the final size of the particles (Ji et al., 2007). For example, the effect of aggregation, which occurs significantly at low pH values, decreases when the pH increases, while an opposite trend is found for growth. This behaviour is due to the chemistry of the precursor and reducing agent, which are a strong acid and a weak base, respectively. In addition, both of them exist in different forms depending on the value of the mixture pH: the precursor can exist as $AuCl_4^-$, $AuCl_3(OH)^-$, $AuCl_2(OH)_2^-$, $AuCl(OH)_3^-$ and $Au(OH)_4^-$, whilst the reducing agent can exist as Ct^{3-}, CtH^{2-}, CtH_2^- and CtH_3. Only pH values between 3 and 8, measured at room temperature, favour the synthesis (Ji et al., 2007). While investigating the synthesis within this pH range, Wuithschick et al. (2015) proposed the so-called “seed-mediated mechanism”, in which nuclei generate “seed particles”, which then grow into the particles of final size.

In this chapter, we develop a new model for the synthesis based on the seed-mediated mechanism. This mechanism originates from the thermodynamics and kinetics of the synthesis. Thermodynamics allows identifying the chemical components and their amounts at quasi-equilibrium and final equilibrium states (later on, we will explain the concept of quasi-equilibrium in the context of the citrate synthesis method). Kinetics, on the other hand, provides the rates of the reactions involved in the synthesis. In developing the model, we take into account the thermodynamics of the substances involved in the synthesis. Then, we derive rate-order equations for the reactions that occur in the pH range of interest for the synthesis analysed. To predict the evolution of concentrations and particle size distribution, we derive mass balance equations for the fluid components and a population balance equation (PBE) for the GNPs. These describe the synthesis according to the seed-mediated mechanism of Wuithschick et al. (2015). While the mass balance equations are ordinary differential equations, the PBE is an integro-partial-differential equation. Their combination yields a complex model that can only be solved numerically. To solve it, we employ the commercial numerical code Parsival. For the initial conditions, we adopt the process conditions that other researchers previously used in this synthesis method to produce GNPs. We then compare the model predictions to experimental data from the literature.

Based on the foregoing, this chapter involves different concepts such as nanotechnology, analytical chemistry, thermodynamics and kinetics, and population balance modelling. To clearly convey these concepts, we have classified them into a main contribution, and supporting information. This chapter presents the main contribution while Appendix E presents the supporting information. Nevertheless, the supporting information is not less important; it is required to understand the main contribution. Section 4.2 of the main contribution briefly presents the seed-mediated mechanism. Section 4.3 reports the reactions that occur in the synthesis according to this mechanism, their corresponding rate-order equations and the balance equations for the components. Section 4.4 presents the solutions of the model and discusses the results. Finally in this chapter (of the main contribution), Section 4.5 reports the concluding remarks. The supporting information in Appendix E contains six sections: Section 4.A discusses the thermodynamics of the citrate synthesis method; Section 4.B discusses the experimental evidence for the seed-mediated mechanism; Section 4.C reports some quasi-equilibrium calculations; and Sections 4.D, 4.E, and 4.F discuss rate calculations for various steps in the seed-mediated mechanism. We refer the reader to Appendix E.

4.2 Seed-mediated mechanism

In this section, we describe how gold nanoparticles evolve in the citrate synthesis method according to the seed-mediated mechanism of Wuithschick et al. (2015). For this synthesis, two solutions are prepared, one containing tetrachloroauric acid and the other containing sodium citrate in water. The aqueous medium renders the acid-base properties of precursor and reducing agent possible, dissociating according to the following equilibrium reaction:

$$H_2O \rightleftarrows H^+ + OH^- \qquad (4.2.1)$$

At 25 ^{0}C, the equilibrium constant $K_{a,w}$ of the dissociation of water, expressed as $K_{a,w} = C_{H^+}.C_{OH^-}$, is equal to 10^{-14} (Sandler, 2006), where C_{H^+} and C_{OH^-} denote the concentrations of H^+ and OH^-, respectively, measured in mol/dm^3 (here and below, C denotes the molar concentration of a reactant, in the units just given, the subscript indicating the component being considered). The acid-base property of an aqueous medium is usually indicated by the value of the pH, expressed as $pH \equiv -\log_{10} C_{H^+}$. In distilled water, $C_{H^+} = C_{OH^-}$. Hence, for distilled water at 25 ^{0}C, $pH = 7$, which is regarded as the neutral pH. The value of the neutral pH, nevertheless, changes with temperature, because $K_{a,w}$ is temperature-dependent. For example, at the standard synthesis temperature of 100 ^{0}C, the value of the neutral pH is 5.6.

Apart from Eq. (4.2.1), in the precursor solution, tetrachloroauric acid, which is a strong acid, completely ionizes according to:

$$HAuCl_4 \rightarrow H^+ + AuCl_4{}^- \quad (4.2.2)$$

The H^+ ions produced in Eq. (4.2.2) shift the equilibrium position of Eq. (4.2.1) to the left so that the amount of OH^- ions present in the solution is negligible. So, even if OH^- can hydroxylate $AuCl_4{}^-$ to the species $AuCl_3(OH)^-$, $AuCl_2(OH)_2{}^-$, $AuCl(OH)_3{}^-$ and $Au(OH)_4{}^-$, their equilibrium amounts in the precursor solution are negligible. To illustrate this, we present a sample calculation in Section 4.A.1 in the supporting information (SI) to Chapter 4, placed in Appendix E. So, in the tetrachloroauric solution, the precursor exists almost entirely as $AuCl_4{}^-$ and the pH of this solution is equal to $-\log_{10} C_{HAuCl_4}$.

On the other hand, the reducing agent solution of sodium citrate is a base solution that contains a significant amount of OH^- because citrate consumes H^+ ions and shifts the equilibrium of Eq. (4.2.1) to the right according to the following reactions:

$$Na_3Ct \rightarrow 3Na^+ + Ct^{3-} \quad (4.2.3)$$

$$Ct^{3-} + H^+ \rightleftarrows CtH^{2-} \quad ; 1/K_{R3} \quad (4.2.4)$$

$$CtH^{2-} + H^+ \rightleftarrows CtH_2{}^-; 1/K_{R2} \quad (4.2.5)$$

$$CtH_2{}^- + H^+ \rightleftarrows CtH_3 \quad ; 1/K_{R1} \quad (4.2.6)$$

where the K_{Ri}'s are the equilibrium constants of the reactions reported, whose values at 25 ^{0}C are 7.41×10^{-4}, 1.74×10^{-5} and 3.98×10^{-7}, respectively (Serjeant and Dempsey, 1979). Because the amount of OH^- ions is larger than that of H^+ ions, the value of the pH of the reducing agent solution is above 7 at 25 ^{0}C. To illustrate this, we present a sample calculation in Section 4.A.2 of the SI.

Upon adding the reducing agent solution to the precursor solution in the synthesis, usually carried out at 100 ^{0}C in a well-mixed batch reactor, a number of reactions can occur at different rates. For example, Pines et al. (1997) reported $\sim 10^{-11}\ s$ as the time scale for reactions involving H^+ ions to reach completion at 23 ^{0}C. Hence, we expect the equilibrium reactions in Eqs. (4.2.1) and (4.2.4) to (4.2.6) to occur almost instantaneously. Wuithschick et al. (2015) confirmed this expectation experimentally: they reported that the reactions attain equilibrium in less than 2 s at 23 ^{0}C (notice that the time resolution of the instrument that they used was of seconds). Because of these fast reactions (fast compared to the other reactions involved in the synthesis), the synthesis mixture reaches a temporary equilibrium state, henceforth referred to as "quasi-equilibrium" state, before other reactions begin to occur significantly. When this state is reached, the amount of OH^- is significant and can convert $AuCl_4{}^-$ into the hydroxylated forms previously reported. To illustrate this, we provide a sample calculation in Section 4.A.3 of the SI.

The speciation of chloroauric acid can in principle yield various hydroxylated species, namely, $AuCl_3(OH)^-$, $AuCl_2(OH)_2{}^-$, $AuCl(OH)_3{}^-$ and $Au(OH)_4{}^-$. Peck et al. (1991) investigated the speciation reactions of the precursor solution using both UV-Vis and Raman spectroscopy and reported that below a pH value of 6.2 (measured at about 25 ^{0}C) $AuCl_4{}^-$ is the dominant species, whilst in the pH range 6.2 - 8.4 $AuCl_4{}^-$ and $AuCl_3(OH)^-$ dominate. At larger values of the pH, the higher hydroxylated species dominate, starting with $AuCl_2(OH)_2{}^-$ and then moving to the others in succession. So, we assume that within the pH range 3-8, in which the synthesis is conducted, OH^- only hydroxylates $AuCl_4{}^-$ into $AuCl_3(OH)^-$. Referred to as "passivation step", this reaction occurs significantly over a time scale of $\sim 30\ s$ at 100 ^{0}C (Wuithschick et al., 2015).

Moreover, $AuCl_4{}^-$ (gold oxidation state of $+3$) converts into Au (gold oxidation state of zero) by the reducing action of the sodium citrate solution; this occurs significantly over a time scale similar to that characterizing the passivation reaction at 100 ^{0}C (Wuithschick et al., 2015). Therefore, after a time of about a minute, all the gold initially present in the precursor is (prevalently) either in the form of atomic gold or of $AuCl_3(OH)^-$. In the remaining 20 min of the synthesis, all the gold converts into nanoparticles, as reported by researchers such as Ji et al. (2007), Frens (1973) and Wuithschick et al. (2015).

To understand the mechanism of the synthesis, Polte et al. (2010) and Wuithschick et al. (2015) investigated it using a combination of small-angle X-ray scattering and X-ray absorption near-edge structure along with the other conventional techniques of transmission electron microscopy, surface electron microscopy and UV-Vis. This equipment provides time-resolved in situ information on the size of nanoparticles of about 2 nm or larger and of their number concentration, offering a reliable account of the synthesis. For the synthesis carried out at 75 ^{0}C, Polte et al. (2010) reported this information for a total synthesis time of 80 min (in Figure 2(d) of their article). We have reproduced this figure in Figure 4.B.1 in Section 4.B of the SI. From this figure, we see that in the time interval between 20 and 80 min the aggregation process is absent, because the particle number concentration is constant. Before 20 min, however, the aggregation process is present, because the number concentration of particles decreases. To determine whether the growth process is also present before this time, we further analysed Figure 4.B.1. From this analysis, reported in Section 4.B.1 of the SI, we can state that the growth process is nearly insignificant before this time. So, in developing a mathematical model, it can be assumed that in the synthesis the aggregation process is entirely decoupled from the growth process. According to Wuithschick et al. (2015), the nanoparticles stop aggregating when they reach about the same size, which is referred to as "seed" size. Then, these "seed particles" grow into the final NPs by reacting with the hydroxylated precursor, which we assume to be in the form of

$AuCl_3(OH)^-$ considering the pH range of interest in the citrate synthesis method. Based on these explanations, we present the seed-mediated mechanism as shown in Figure 4.2.1. $AuCl_4^-$ passivates into $AuCl_3(OH)^-$ and concurrently reduces into atomic gold. As gold atoms generate, they aggregate forming particle seeds; growth is not entirely absent, but its contribution is much less significant and thus is neglected. Finally, the gold present in $AuCl_3(OH)^-$ grows the seeds into NPs; during this step aggregation is absent.

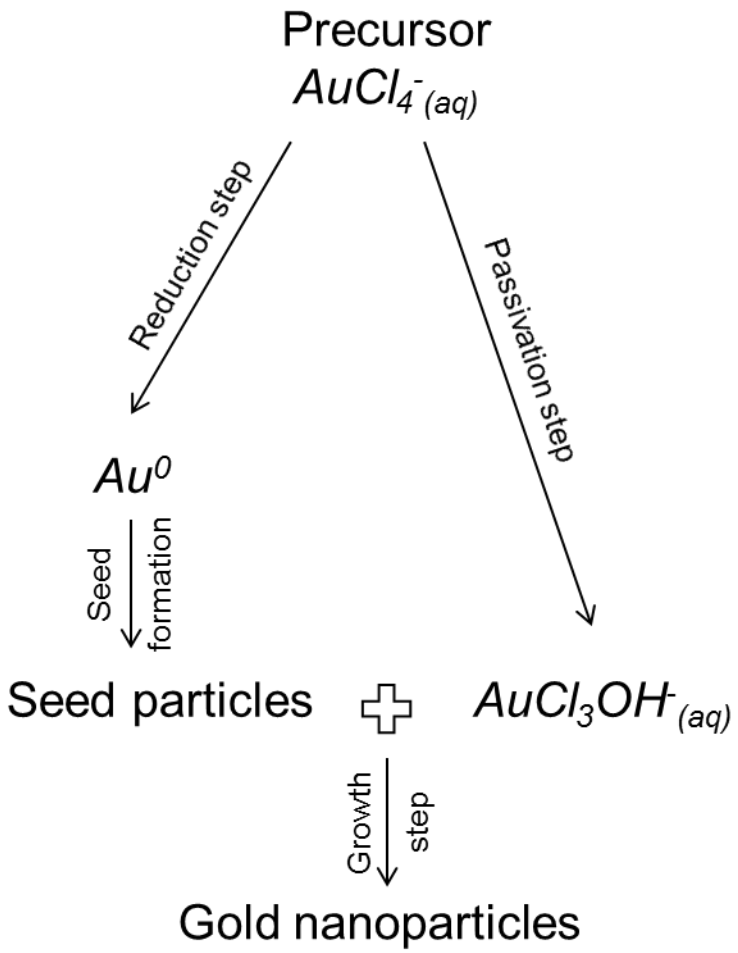

Figure 4.2.1. Reaction scheme in the seed-mediated synthesis mechanism describing how the gold in the precursor evolves into GNPs in the citrate synthesis method.

4.3 Model development

In this section, we derive a model for the GNP citrate synthesis based on the seed-mediated mechanism as presented in Figure 4.2.1. The precursor solution is mixed with the reducing agent solution to form the *synthesis solution*, where GNPs then form. The reduction, passivation and growth steps involve chemical reactions, while the seed formation step

involves solely the aggregation process. For the chemical reactions, we first derive balanced chemical equations and then develop their rate equations, whilst for the seed formation step we suggest a method for calculating the seed diameter that is applicable for initial molar ratios of sodium citrate to gold (more precisely to tetrachloroauric acid) equal to or greater than five. For initial molar ratios with these values, as illustrated in Section 4.C of the SI, the values of the pH of the synthesis solution at quasi and final equilibrium are approximately equal. Based on this observation, we derive a model for the synthesis.

4.3.1 Precursor reduction step

In the reduction step $AuCl_4^-$ converts into gold atoms owing to the reducing action of the sodium citrate solution. As a result of the speciation reactions of citrate, given by Eqs. (4.2.4), (4.2.5) and (4.2.6), the reducing agent can be Ct^{3-}, CtH^{2-}, CtH_2^-, CtH_3 or a combination thereof. Using molecular thermodynamic simulations, Ojea-Jiménez and Campanera (2012) reported that the reducing agent is CtH_2^-, while Kettermann et al. (2016) suggested that it is CtH^{2-}. We tested both alternatives, using data about the kinetics of the synthesis reported by Ji et al. (2007). From this test, we concluded that CtH_2^- is the most likely form of the reducing agent, as discussed in Section 4.D.3 of the SI.

For the conversion of the precursor into gold atoms, Kumar et al. (2007) reported the overall balanced chemical equation in the form:

$$2AuCl_3 + 3[(COO^-CH_2)_2C(OH)COO^-] + 3H^+ \rightarrow 2Au^0 + 3(CH_3)_2C=O + 9CO_2 + 6Cl^- \quad (4.3.1)$$

In this equation, $AuCl_3$ appears as precursor and Ct^{3-} as reducing agent. However, several authors, such as Ji et al. (2007), Doyen et al. (2012) and Wuithchick et al. (2015), do not report the reaction in this form because, as said in Section 4.2, in the precursor solution gold is in the form of $AuCl_4^-$. Substituting $AuCl_3$ with $AuCl_4^- - Cl^-$ and Ct^{3-} with $CtH_2^- - 2H^+$, we can express Eq. (4.3.1) in terms of $AuCl_4^-$ and CtH_2^-. Rearranging the chemical species as reactants and products yields:

$$2AuCl_4^- + 3(CH_2COOH)_2C(OH)COO^- \rightarrow 2Au^0 + 8Cl^- + 3(CH_3)_2C=O + 9CO_2 + 3H^+ \quad (4.3.2)$$

Eq. (4.3.2) is the balanced chemical equation for the reduction step. The stoichiometry of this reaction requires three moles of CtH_2^- to reduce two moles of $AuCl_4^-$.

We assume that the kinetics of the reduction step follows a rate law. This means that the reaction rate is proportional to the product of the concentrations of the reactants, each

concentration raised to a coefficient (Fogler, 2004). Therefore, we write the rate r_r for the reaction between $AuCl_4^-$ and CtH_2^- in the form:

$$r_r = k_r \, C_{AuCl_4^-}{}^{l} . C_{CtH_2^-}{}^{n} \tag{4.3.3}$$

where r_r is the formation rate of gold atoms in $mol/(m^3.s)$, k_r is the reduction rate constant, and l and n are the rate orders of $AuCl_4^-$ and CtH_2^-, respectively.

While investigating the synthesis in the presence of an excess of sodium citrate, Chakraborty et al. (2016) found that Eq. (4.3.3) is first-order with respect to $AuCl_4^-$; that is, $l = 1$. So, we can write:

$$r_r = k_r \, C_{AuCl_4^-} . C_{CtH_2^-}{}^{n} \tag{4.3.4}$$

To obtain the values of k_r and n, one needs data for r_r and the corresponding values of $C_{AuCl_4^-}$ and $C_{CtH_2^-}$. To obtain values for r_r, one requires data of the time evolution of the concentration of gold atoms present in the GNPs. Hendel et al. (2014) do not report data of this kind, but give relevant information. In particular, for nanoparticles synthesized with different initial precursor concentrations, they correlated the amount of gold initially present in the precursor to the UV-Vis absorbance at 400 nm obtained at the end of the synthesis. By doing so, they observed that such quantities are linearly related. Because all the gold in the precursor converts into nanoparticles, they concluded that the UV-Vis absorbance at 400 nm is proportional to the amount of gold atoms present in the solid phase. Consequently, one can use data of the time evolution of the UV-Vis absorbance at 400 nm to determine the time evolution of the concentration of gold atoms present in the solid phase. However, since the data of Hendel et al. (2014) were obtained at the end of the synthesis only, we could not use them to determine r_r (no time-resolved data are available). To this end, we instead used the data of Ji et al. (2007), who investigated the synthesis at $100\,^0C$ for a fixed initial value of precursor concentration, equal to $0.25\,mol/m^3$, and an initial value of the citrate-to-gold molar ratio varying between 0.7 and 28 (values referred to the synthesis solution). Ji et al. reported the time evolution of the UV-Vis spectra in the wavelength band between 400 to 800 nm for three initial conditions; furthermore, for these and many more initial conditions, they reported the time evolution of the UV-Vis peaks of the absorption spectra. One can obtain values for r_r by using either the entire UV-Vis spectra or the values of their peaks. From the UV-Vis spectra, one can determine the values of the UV-Vis absorbance at 400 nm and subsequently the concentration of gold in the solid phase. Since these data are time-resolved, one can therefore determine the corresponding values of r_r. The disadvantage of this method is that the spectra are available only for three initial precursor concentrations,

and so just three values for r_r can be found. Many more values are instead available for the peaks; for this reason, we used the time evolution of the UV-Vis peaks.

One consideration is in order here. Note that using the values of the UV-Vis peaks is possible since, when normalized, their time evolution is nearly identical to that of the normalized UV-Vis absorbance at 400 nm. To demonstrate this, in Section 4.D.1 of the SI we compare the time evolutions of the normalized UV-Vis absorbances (at 400 nm) and peaks (the normalized values are obtained by dividing the actual values of the absorbance by the respective maximum absorbance values, which correspond to those at the end of the synthesis). As we can observe, the time evolutions are nearly identical. This implies that also the UV-Vis peaks are linearly related to the concentration of gold in the solid phase. Therefore, we obtained the amount of gold atoms in the solid phase produced from the reduction step using the time evolution of the peaks. These data are reported in Figure 2S (b) of the work of Ji et al. (2007).

We used these data in the limit $t \to 0$. This is because the gold atoms in the solid phase can form via both the reduction and growth steps, as illustrated in Figure 4.2.1; However, in the limit $t \to 0$, because the growth step occurs solely in the presence of particles, only the reduction step plays a role. Thus, to obtain the values of k_r and n, we only used the data of r_r, and of the corresponding values of $C_{AuCl_4^-}$ and $C_{CtH_2^-}$, in this limit. In Section 4.D.2 of the SI, we also show how to obtain from Figure 2S (b) the value of the rate r_r in the limit $t \to 0$, which we denote as $r_{r,0}$. The values of $C_{AuCl_4^-}$ and $C_{CtH_2^-}$ for vanishingly short times, denoted as $C_{AuCl_4^-,0}$ and $C_{CtH_2^-,0}$, are those at quasi-equilibrium, which are attained in the synthesis solution when, after mixing the precursor solution with the reducing agent solution, the fast reactions involving H^+ ions have reached equilibrium but $AuCl_4^-$ has not significantly reacted. A sample calculation of how to obtain the values of $C_{AuCl_4^-,0}$ and $C_{CtH_2^-,0}$ for the citrate-to-gold molar ratio of 0.7 is given in Section 4.A of the SI.

For $t \to 0$, we write Eq. (4.3.4) as follows:

$$r_{r,0} = k_r \, C_{AuCl_4^-,0} \, . \, C_{CtH_2^-,0}{}^n \tag{4.3.5}$$

This equation can be expressed equivalently as:

$$\log\left(\frac{r_{r,0}}{C_{AuCl_4^-,0}}\right) = n \log C_{CtH_2^-,0} + \log k_r \tag{4.3.6}$$

By plotting $\log\left(r_{r,0}/C_{AuCl_4^-,0}\right)$ against $\log C_{CtH_2^-,0}$ for several initial molar ratios of citrate-to-gold, we obtain a straight line. The values of n and $\log k_r$ correspond to the slope and intercept of this line. For the data of Ji et al. (2007), Figure 4.3.1 shows the plot of Eq.

(4.3.6). Notice that to plot the values of $\log(r_{r,0}/C_{AuCl_4^-,0})$ and $\log C_{CtH_2^-,0}$ in the positive quadrant of the x-y plane, as done in Figure 4.3.1, we multiplied both sides of Eq. (4.3.6) by -1; thus, the intercept of the line is equal to $-\log k_r$.

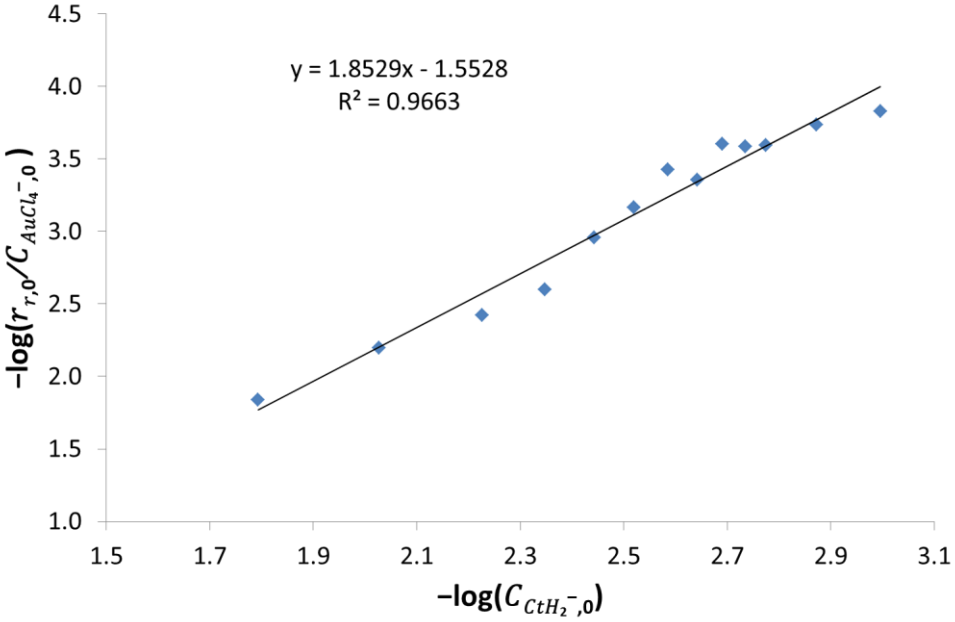

Figure 4.3.1. Plot of $y = -\log(r_{r,0}/C_{AuCl_4^-,0})$ vs $x = -\log C_{CtH_2^-,0}$ to determine the order of CtH_2^- and the kinetic constant in the reduction rate equation. The experimental data, obtained at $100\ ^0C$, are taken from Ji et al. (2007).

From Figure 4.3.1, we can calculate the reaction order with respect to CtH_2^-. This is given by the slope of the curve and is equal to $n = 1.85$. The reduction rate constant at $100\ ^0C$, on the other hand, is equal to:

$$k_r = 10^{1.55}[m^3/mol]^{1.85}\ 1/s = 35.48\ [m^3/mol]^{1.85}\ 1/s$$

We can thus write the reduction rate equation as:

$$r_r = k_r C_{AuCl_4^-} . C_{CtH_2^-}{}^{1.85} \qquad (4.3.7)$$

4.3.2 Precursor passivation step

As previously discussed, the passivation step occurs when OH^- reacts with a portion of $AuCl_4^-$ to form $AuCl_3(OH)^-$, since higher hydroxylated forms of the precursor are present in negligible amounts within the pH range of interest for the synthesis, which is between 3 and 8 when the pH is measured at 25 ^{0}C (Peck et al., 1991). We write the chemical reaction as:

$$AuCl_4^- + OH^- \rightarrow AuCl_3(OH)^- + Cl^- \qquad (4.3.8)$$

A rate equation for this step has been reported by Paclawski et al. (2012) in the form:

$$r_p = k_p C_{AuCl_4^-} . C_{OH^-} \quad (4.3.9)$$

where r_p is the passivation rate and k_p is the rate constant; the reaction is first-order with respect to both reactants. For the value of k_p, Paclawski et al. (2012) refer to Hanes et al. (1992), in which it is reported that $k_p = 0.0052\ m^3/(mol \cdot s)$ at 16 ^{0}C.

To determine the value of k_p at the standard synthesis temperature of 100 ^{0}C, we employ the experimental data of Wuithschick et al. (2015), who reported, at different temperatures, the times that $AuCl_4^-$ takes to convert significantly when hydroxylating into $AuCl_3(OH)^-$ for fixed initial concentrations of tetrachloroauric acid and $NaOH$ in solution. These data refer to values of the mixture pH falling within the range in which the amounts of the higher hydroxylated forms of the precursor are negligible (Peck et al., 1991). Table 4.3.1 shows these data. From these, we can obtain the value of the activation energy of the passivation reaction.

Table 4.3.1. Characteristic time of the passivation reaction at different temperatures. The experimental data are taken from Wuithschick et al. (2015).

Temperature (^{0}C)	Reaction time (s)
46	2150
65	250
75	150
88	80
95	40

As the initial concentrations of $HAuCl_4$ and $NaOH$ do not change, k_p is proportional to the inverse of the reaction time τ_p, the proportionality constant, denoted as b, not depending on the reaction temperature. The reasoning for this proportionality is presented in Section 4.E.1 of the SI. We can thus write:

$$k_p = \frac{b}{\tau_p} \quad (4.3.10)$$

Therefore, the Arrhenius equation for this step can be written as:

$$\frac{b}{\tau_p} = k_0 \exp[-E_a/RT] \quad (4.3.11)$$

where k_0 and E_a are the pre-exponential factor and activation energy, respectively, while T is the temperature in Kelvin and R is the universal gas constant. Rearranged, Eq. (4.3.11) becomes:

$$\ln\left(\frac{1}{\tau_p}\right) = \ln\left(\frac{k_0}{b}\right) - \frac{E_a}{RT} \qquad (4.3.12)$$

A plot of $\ln(1/\tau_p)$ versus $1/T$, based on the experimental data of Wuithschick et al. (2015), is shown in Figure 4.3.2. The slope of the line is equal to $-\,9070.2\,K$. Thus, we obtain:

$$E_a = 9070.2\,K \times\ 8.31\,J/(mol.K) = 75373\ J/mol$$

Given that $k_p(16\,^0C) = 0.0052\,m^3/(mol\cdot s)$, we can write:

$$0.0052\,m^3/(mol\cdot s) = k_0 \exp(-\,75373/(8.31\times 289))\,m^3/(mol\cdot s)$$

whence:

$$k_0 = 2.22\times 10^{11}\ m^3/(mol.s)$$

Then, the Arrhenius equation for the passivation rate constant reads:

$$k_p = 2.22\times 10^{11}\exp[-\,75373/RT] \quad m^3/(mol\cdot s) \qquad (4.3.13)$$

Thus, at 100 ^{0}C, we have:

$$k_p(100\,^0C) = 2.22\times 10^{11}\exp[-\,75373/(8.31\times 373)] = 6.1\,m^3/(mol\cdot s)$$

By an indirect method, reported in Section 4.F of the SI, we obtained an estimated value of $1.9\,m^3/(mol\cdot s)$ for k_p at 100 ^{0}C, confirming that the (more reliable) value found here is reasonable.

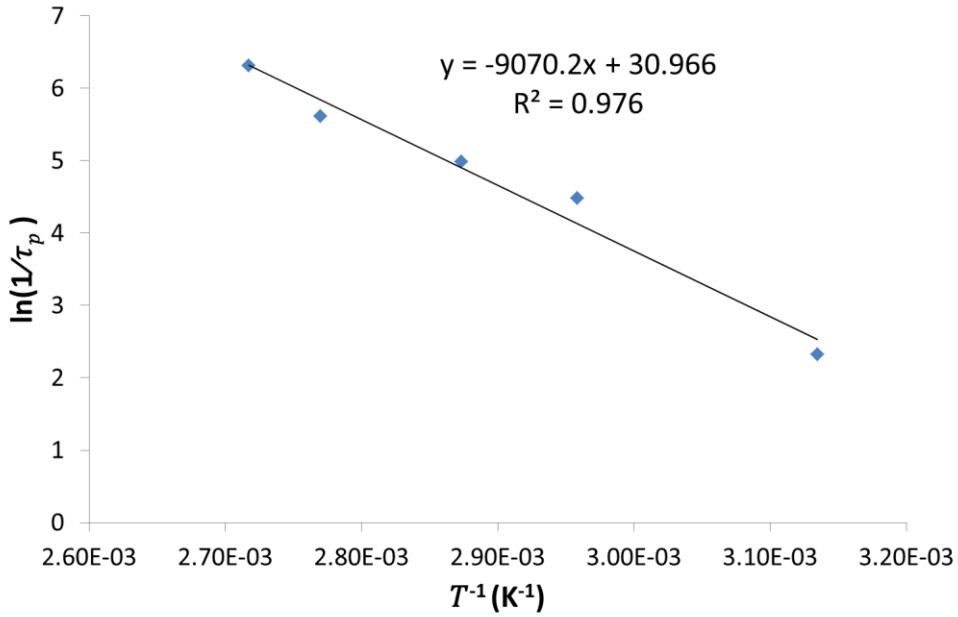

Figure 4.3.2. Plot of $y = \ln(1/\tau_p)$ vs $x = 1/T$ to determine the activation energy of the passivation step. The experimental data, where the initial precursor concentration is constant at $0.25\ mol/m^3$, are taken from Wuithschick et al. (2015).

4.3.3 Seed growth step

The growth step involves a *continuous* increase of the size of the seed particles that occurs when the gold atoms produced from the reduction of $AuCl_3(OH)^-$ integrate onto the surface of the seed particles (shown in Figure 4.2.1). Using molecular thermodynamic simulations, Ojea-Jiménez and Campanera (2012) reported that the reducing agent for this step is CtH^{2-}. We can therefore write the balanced chemical equation for this step as a reaction between $AuCl_3(OH)^-$ and CtH^{2-} by substituting in Eq. (4.3.2) $AuCl_4{}^-$ with $AuCl_3(OH)^- + Cl^- - OH^-$ and $CtH_2{}^-$ with $CtH^{2-} + H^+$. This gives:

$$2AuCl_3(OH)^- + 3(CH_2COO^-)_2C(OH)COOH \xrightarrow{particle\ surface} 2Au + 6Cl^- + 2OH^- + 9CO_2 + 3(CH_3)_2C = O \qquad (4.3.14)$$

where we have explicitly indicated that this reaction occurs on the surface of the gold nanoparticles.

Eq. (4.3.14) is the balanced chemical equation for the growth step. Like the reduction step, its stoichiometry requires that (on the particle surface) three moles of CtH^{2-} reduce two moles of $AuCl_3(OH)^-$.

The growth model depends on the controlling mechanism. The two mechanisms are mass transfer and surface reaction (Mersmann, 2001). Here we assume that growth is controlled by the latter mechanism. This assumption is based on an analysis of the experimental data reported in Figure 2 (d) of the article of Polte et al. (2010), which presents the time evolution of the particle mean size (Figure 4.B.1 in Section 4.B of the SI reproduces this figure). The data reveals that the growth rate is constant over a large time interval; only towards the end of the synthesis it first appears to increase slightly and then it progressively decreases, eventually vanishing. The decrease is expected and is due to the depletion of the driving force (that is, of the concentration of $AuCl_3(OH)^-$). For growth controlled by mass transfer (that is, mass transfer limited), the growth rate decreases with size (Viswanatha and Sarma, 2007; also see Eq. (2.2.88) in Chapter 2). Since this behaviour is not observed experimentally, we assume that surface reaction controls particle growth. A more detailed analysis is provided in Section 4.B of the SI. The same assumption was also made by Kumar et al. (2007). In deriving the growth model, we thus assume that the growth rate follows a rate law that depends on the concentrations of the reactants (that is, $AuCl_3(OH)^-$ and CtH^{2-}) and on the specific particle surface. So, we write:

$$\frac{dC_{Au}}{dt} = A\, k_g\, C_{AuCl_3(OH)^-}{}^{g}.C_{CtH^{2-}}{}^{h} \tag{4.3.15}$$

where C_{Au} represents the moles of gold atoms present in the particles per unit volume of mixture; this concentration, consequently, increases only because of growth (since nucleation is absent), and so dC_{Au}/dt is directly related to the rate of change of the particle size (see Section 4.B for further details). Also, in Eq. (4.3.15), k_g is the reaction constant, A is the particle surface area per unit volume of mixture, and g and h are the reaction orders for $AuCl_3(OH)^-$ and CtH^{2-}, respectively.

Eq. (4.3.15) contains three constants: k_g, g and h. We take g and h to be equal to one, following Turkevich et al. (1951), who reported the order of the two reactants in the growth process to be unity. Thus, we have:

$$\frac{dC_{Au}}{dt} = A\, k_g\, C_{AuCl_3(OH)^-}.C_{CtH^{2-}} \tag{4.3.16}$$

To determine the value of k_g, we still employ the data in Figure 2 (d) of the article of Polte et al. (2010), where the initial concentrations of the precursor and reducing agent in the synthesis solution are $0.25\ mol/m^3$ and $2.5\ mol/m^3$, respectively, and the solution temperature is $75\ ^0C$. As this figure describes the time evolution of the mean size, we can obtain the growth rate ds_m/dt from Eq. (4.3.16) as:

$$\frac{ds_m}{dt} = \left(\frac{m_a}{3\rho m_v}\right) k_g \, C_{AuCl_3(OH)^-} \, C_{CtH^{2-}} \quad (4.3.17)$$

where m_a is the particle area shape factor (which we set equal to π, assuming that the particles are spherical), ρ is the molar density of gold, taken to be $10^5 \ mol/m^3$ (Kumar et al., 2007), m_v is the particle volume shape factor (which we set equal to $\pi/6$, assuming that the particles are spherical) and s_m is the mean particle diameter. See Section 4.B of the SI for the derivation of this equation.

As previously illustrated, the mean particle size can be affected by seed formation (caused by aggregation) and growth. In the range 20 to 70 min in the Figure 2 (d), the particles no longer aggregate, since the number concentration of particles is constant. However, the particle mean size increases; this can only be due to growth. At any particular time within this time interval, we can calculate the values of ds_m/dt, $C_{AuCl_3(OH)^-}$, $C_{CtH^{2-}}$ and A, and then obtain the value of k_g from Eq. (4.3.17). From the calculations reported in Section 4.B of the SI, at $75\ ^0C$ the constant k_g is equal to $2.0 \times 10^{-6}\, m^4/(mol.s)$.

To obtain the value of k_g at 100^0C, we employ additional experimental data reported by Polte et al. (2010) for the same initial concentrations of precursor and reducing agent but at two other temperatures: 85 and $100\ ^0C$. These additional data show that the time scale of the growth step, which is the time required for the particle size to change significantly due to growth, decreases from about 40 mins at $75\ ^0C$ to about 23 and 15 min at 85 and $100\ ^0C$, respectively (Polte et al., 2010). From these times, we can calculate the activation energy of the growth step. Similarly to what we discussed in relation to the passivation step, we can relate the constant k_g to the inverse of the growth time scale τ_g as follows:

$$k_g = \frac{b}{\tau_g} \quad (4.3.18)$$

where b is a proportionality constant. The reasoning for this equation is presented in Section 4.E.2 of the SI. Then, we calculate the activation energy E_a for the growth step using the Arrhenius equation (Mersmann, 2001):

$$\frac{b}{\tau_g} = k_0 \exp[-E_a/RT] \quad (4.3.19)$$

where k_0 is the pre-exponential factor for the growth step. By rearranging Eq. (4.3.19), we obtain:

$$\ln\left(\frac{1}{\tau_g}\right) = \ln\left(\frac{k_0}{b}\right) - \frac{E_a}{RT} \quad (4.3.20)$$

Figure 4.3.3 shows the plot of $\ln(1/\tau_g)$ versus $1/T$, based on the experimental data of Polte et al. (2010). The value of the slope is $-6102.6\ K$. From this value:

$E_a = 5{,}010\ \ K \times 8.31\, J/(mol.K) = 41{,}633\ J/mol$

Given that $k_g(75\,^0C) = 2.00 \times 10^{-6}\, m^4/(mol.s)$, we can write:

$2.00 \times 10^{-6}\, m^4/(mol.s) = k_0 \exp(-41{,}633\ /(8.31 \times 348))\ m^4/(mol.s)$

whence:

$k_0 = 3.58\ m^4/(mol.s)$

and the value of k_g at 100 ^{0}C is:

$k_g(100\,^0C) = 3.58\ m^4/(mol.s) \exp[-41{,}633\ /(8.31 \times 373)] = 5.25 \times 10^{-6}\, m^4/(mol.s)$

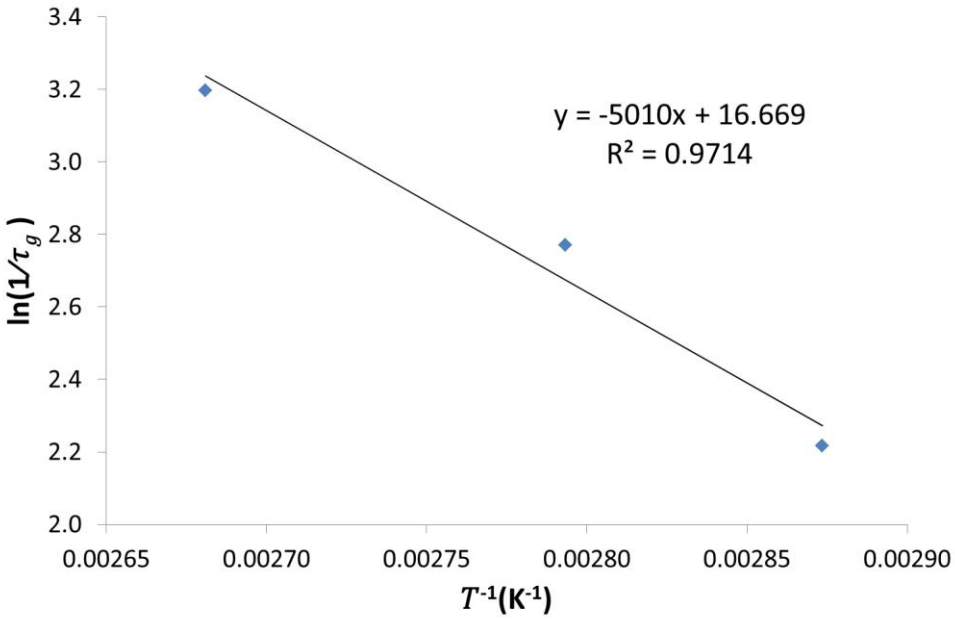

Figure 4.3.3. Plot of $y = \ln(1/\tau_g)$ vs $x = 1/T$ to determine the activation energy of the growth step. The experimental data, where the initial concentrations of the precursor and reducing agent in the synthesis solution are $0.25\ mol/m^3$ and $2.5\ mol/m^3$, respectively, are taken from Polte et al. (2010).

4.3.4 Seed formation step

The seed-mediated mechanism requires that the gold atoms, formed from the reduction step, aggregate into equal-sized “seed particles”. If the number concentration of gold atoms produced from the reduction step were approximately equal to the final number concentration of gold nanoparticles, each gold atom would coincide with a seed particle,

which would then “grow” into a final GNP (note that in this case the term “grow” is incorrect, since, at least initially, the particles are made up of few gold atoms; growth is possible solely when the particles comprise several atoms, so that the rate of change of their size caused by the attachment of additional atoms can be regarded as a continuous process). This is a limiting case for the seed particle size, not expected to be observed experimentally. The number concentration of gold atoms is expected to be far greater than the number concentration of the final GNPs, the seed size being consequently larger than the size of a gold atom, which is $0.272\ nm$ (Cordero et al. 2008). In this section, we propose a method for calculating the diameter of the seed particles; however, due to its complexity, we do not attempt to model the aggregation process or to determine its kinetics.

Because no further aggregation occurs after the seed formation step, the number concentration of the seed particles must be equal to the final number concentration of GNPs (Wuithschick et al., 2015). Assuming complete conversion of the precursor into GNPs and a monodisperse particle size distribution, we can estimate the final number concentration of GNPs as follows:

$$\frac{C_{HAuCl_4}}{\rho m_v {s_f}^3} \tag{4.3.21}$$

where C_{HAuCl_4} is the initial concentration of the precursor in the synthesis solution, and s_f is the final mean particle diameter.

The number concentration of seed particles, however, can also be calculated using the following equation:

$$\frac{C_s}{\rho m_v {s_s}^3} \tag{4.3.22}$$

where C_s is the amount of precursor that forms the seed particles per volume of synthesis solution and s_s is the seed diameter.

The value of C_{HAuCl_4} is known. To determine the value of C_s, we use the selectivity of the reduction step over the passivation step, defined as the ratio of the amount of precursor that forms gold atoms in the reduction step to the amount of precursor that becomes passivated. The amount of precursor that forms gold atoms and then seed particles is equal to VC_s and can be expressed as:

$$VC_s = V\int_0^{t_s} r_r dt \tag{4.3.23}$$

where V is the volume of synthesis solution, r_r is the reaction rate for the reduction step, t is the time, and t_s is the total synthesis time.

Similarly, the amount of precursor that becomes passivated can be expressed as:

$$V(C_{HAuCl_4} - C_s) = V\int_0^{t_s} r_p dt \tag{4.3.24}$$

where r_p is the rate of the passivation reaction. The selectivity S is defined as follows:

$$S = \frac{\int_0^{t_s} r_r dt}{\int_0^{t_s} r_p dt} \tag{4.3.25}$$

Using Eqs. (4.3.7) and (4.3.9), we thus have:

$$S = \frac{k_r}{k_p} \frac{\int_0^{t_s} \left[C_{AuCl_4^-}\right].\left[C_{CtH_2^-}\right]^{1.85} dt}{\int_0^{t_s} \left[C_{AuCl_4^-}\right][C_{OH^-}]\, dt} \tag{4.3.26}$$

To use this equation to obtain S, we need to know the time profiles of $C_{AuCl_4^-}$, $C_{CtH_2^-}$ and C_{OH^-}. For synthesis conditions where the molar ratio of initial concentrations of sodium citrate to tetrachloroauric acid in the synthesis solution is equal to or greater than five, we assume that the values of $C_{CtH_2^-}$ and C_{OH^-} do not change significantly from their values at quasi-equilibrium, denoted as $C_{CtH_2^-,0}$ and $C_{OH^-,0}$, respectively. The reasoning is discussed in Section 4.C of the SI. Thus, we can write:

$$S = \frac{k_r}{k_p} \frac{\left[C_{CtH_2^-,0}\right]^{1.85}}{[C_{OH^-,0}]} \frac{\int_0^{t_s} \left[C_{AuCl_4^-}\right] dt}{\int_0^{t_s} \left[C_{AuCl_4^-}\right] dt} = \frac{k_r}{k_p} \frac{\left[C_{CtH_2^-,0}\right]^{1.85}}{[C_{OH^-,0}]} \tag{4.3.27}$$

Writing a material balance equation over Au in the precursor, we have:

$$C_{HAuCl_4} = C_s + C_s/S \tag{4.3.28}$$

where C_s/S is the amount of precursor that becomes passivated. Solving Eq. (4.3.28) for C_s, substituting the resulting expression of C_s into Eq. (4.3.22) and then equating the quantity obtained to that reported in Eq. (4.3.21) yields:

$$s_s = s_f \left(\frac{S}{1+S}\right)^{1/3} \tag{4.3.29}$$

Note that the relation above applies to synthesis conditions where the molar ratios of the initial concentration of sodium citrate to tetrachloroauric acid in the synthesis solution are equal to or greater than five. As $S \to 0$, this limit being approached at high pH, $s_s \to 0$;.before reaching this extreme case, s_s will become equal to the size of a gold atom, as previously discussed.

Based on the criterion above, we simplify the balanced chemical equations for the reduction, passivation and growth steps, and present a model for the citrate synthesis method as follows.

4.3.5 Nanoparticle synthesis model

The proposed model is based on the seed-mediated mechanistic description of the synthesis describing how the gold nanoparticles evolve as they form. To simplify the kinetic equations, we restrict to initial molar ratios of citrate to gold to values greater than five. For this condition, as shown in Figure 4.C.2 in Section 4.C of the SI, the pH value at quasi-equilibrium is approximately equal to that at the end of the synthesis. This assumption has many implications. First, because the concentration of H^+ ions determines the pH, this concentration and that of OH^- ions do not change from their values at quasi-equilibrium. Second, the relative mole fractions among the four citrate species also do not change from the values present at quasi-equilibrium, even though the sum of their amounts decreases owing to the reduction reactions of CtH_2^- and CtH^{2-} with $AuCl_4^-$ and $AuCl_3(OH)^-$, respectively. This second implication is illustrated in Figure 4.C.1 in Section 4.C of the SI, where specifying the pH value of the reaction solution determines the relative mole fractions among the four citrate species. Here, to illustrate why, we consider the equilibrium equations for citrate speciation reactions in Eqs (4.2.4) – (4.2.6), which take place nearly instantly at a time scale of $\sim 10^{-11}\ s$ (Pines et al. 1997). For reaction (4.2.4), the equilibrium equation can be written as:

$$\frac{K_{R3}}{C_{H^+}} = \frac{C_{Ct^{3-}}}{C_{CtH^{2-}}} \tag{4.3.30}$$

Being an equilibrium constant, K_{R3} assumes a constant value which depends on the synthesis temperature. At a fixed synthesis temperature and once the pH value of the synthesis solution is determined at quasi-equilibrium, the ratio of $C_{Ct^{3-}}/C_{CtH^{2-}}$ in Eq. (4.3.30) assumes a constant value. Analogously, for Eqs (4.2.5) and (4.2.6), the ratios of $C_{CtH^{2-}}/C_{CtH_2^-}$ and $C_{CtH_2^-}/C_{CtH_3}$ are constant while the synthesis progresses, if one assumes that the mixture pH remains constant at the quasi-equilibrium value.

This assumption also implies that we cannot write the chemical equations in terms of the real reactants and products involved in the reduction, passivation and growth steps. For example, by keeping the concentration of OH^- constant, we cannot write that OH^- reacts with $AuCl_4^-$ to generate $AuCl_3(OH)^-$. We have to write instead that OH^- acts "as a catalyst", converting the precursor to another form, not available to produce the gold atoms in the seed particles, but available to grow them. In reality, since OH^- is consumed by the passivation step, this reaction shifts the equilibrium reaction in Eq. (4.2.1) to the right, so as to keep the concentration of OH^- constant. In the process, Eq. (4.2.1) yields an additional amount of H^+. This additional amount then shifts the speciation reactions of citrate in Eqs (4.2.2) – (4.2.4) to the right. To develop a model that accounts for the real reactants and products, apart from

the reaction rates so far considered, we need to know also the rates of the reactions involving H^+. We do not know these rates, but we know that they are extremely large. Accordingly, we use the quasi-equilibrium approximation instead. In doing so, we could still consider all the reactants and products, but we would have to solve the quasi-equilibrium at every time step of the simulation (that is, a time step of ~$10^{-11}\ s$), which is too demanding and costly. To avoid doing this, we opt for a simplified model that nevertheless is able to correctly predict the evolution of the particle size, ensuring that the amount of gold initially present in the precursor eventually turns into nanoparticles. As for the reactants, this simplified model cannot consider all the products of the reactions. Rather, it lumps a number of them into fictitious components.

Chemical reactions

For the reaction in Eqs. (4.3.2), we rewrite the chemical reaction as:

$$2T + 3(y_x \cdot Ct) \rightarrow 2Au + Pr1 \tag{4.3.31}$$

T represents the gold in $AuCl_4^-$, Ct represents the sum of all the species of citrate, y_x represents the relative mole fraction (among the four citrate species) of CtH_2^- at the quasi-equilibrium pH, Au represents the gold in the GNPs, and $Pr1$ represents all by-products from the reduction step, lumped together.

For the reaction in Eq. (4.3.8), we have:

$$T \overset{B}{\rightarrow} K \tag{4.3.32}$$

B represents OH^-, which is assumed to have a constant concentration, and acts as a catalyst; K represents the gold that becomes passive and that eventually grows the seed particles.

For the reaction in Eq. (4.3.14), we have:

$$2K + 3(y_y \cdot Ct) \xrightarrow{Particles} 2Au + Pr2 \tag{4.3.33}$$

y_y denotes the relative mole fraction of CtH^{2-} at the quasi-equilibrium pH, whilst $Pr2$ represents all by-products from the surface reduction, lumped together.

Mole balances

Assuming that the reaction solution is perfectly mixed (which implies that all intensive properties, such as temperature and concentrations, are uniform), we can select as control volume the region (of constant volume V) occupied by the mixture contained in the batch

reactor wherein the synthesis takes place. The balance equations of the mixture components are then those reported below.

Precursor

This is consumed by both the reduction and passivation steps. Considering Eqs (4.3.7) and (4.3.9), the material balance equation takes the form:

$$\frac{dC_T}{dt} = -k_r C_T (y_x C_{Ct})^{1.85} - k_p C_T C_B \tag{4.3.34}$$

Total citrate species

At any time, we consider the sum of the concentrations of all the citrate species (i.e., Ct^{3-}, CtH^{2-}, $CtH_2{}^-$ and CtH_3), which we denote as C_{Ct}, and model the time variation of this total concentration caused by the reduction and growth reactions. The reduction step consumes $CtH_2{}^-$, whose amount, at any time, is given by $y_x C_{Ct}$, whilst the growth step consumes CtH^{2-}, whose amount, at any time, is given by $y_y C_{Ct}$. Considering the stoichiometric ratios in Eqs (4.3.2) and (4.3.14) and the growth rate equation in Eq. (4.3.16), the material balance equation on the total citrate species is:

$$\frac{dC_{Ct}}{dt} = -\,(3/2)\, k_r C_T (y_x C_{Ct})^{1.85} - (3/2)\, m_a k_g C_K (\, y_y C_{Ct}) \int_{s_s}^{\infty} s^2 f(s,t) ds \tag{4.3.35}$$

Hydroxyl ions

Having assumed that the pH of the mixture is constant at the quasi-equilibrium value, we simply write that the concentration of hydroxyl ions is constant:

$$C_B = constant \tag{4.3.36}$$

Passive precursor

The precursor passive form is generated by the passivation step and consumed by the growth step. Considering Eqs (4.3.8) and (4.3.16), the material balance equation reads:

$$\frac{dC_K}{dt} = k_p C_T C_B - m_a k_g C_K (y_y C_{Ct}) \int_{s_s}^{\infty} s^2 f(s,t) ds \tag{4.3.37}$$

By-products

The reduction and growth reactions generate by-products such as CO_2, $(CH_3)_2C = O$ and Cl^-, as shown in Eqs (4.3.2) and (4.3.14). To ensure that total mass is conserved, we report the balance equations for these other by-products. To account for those generated in the reduction step, lumped into $Pr1$, we write:

$$\frac{dC_{Pr1}}{dt} = (1/2)\, k_r C_T (y_x C_{Ct})^{1.85} \tag{4.3.38}$$

To account for the by-products generated in the growth step, lumped in $Pr2$, we write the following material balance equation:

$$\frac{dC_{Pr2}}{dt} = (1/2)\, m_a k_g C_K (y_y C_{Ct}) \int_{s_s}^{\infty} s^2 f(s,t) ds \tag{4.3.39}$$

Eqs. (4.3.34) – (4.3.38) express Eq. (2.2.14) in detail, describing the evolution the aqueous components in the citrate synthesis method according to the seed-mediated mechanism.

Gold nanoparticles

In writing a continuity statement for the particle phase, one employs the population balance modelling approach (Ramkrisna, 2000; Marchisio and Fox, 2013; and see Chapter 2). This is based on the size distribution of the particles (PSD) and accounts for the processes that affect the particle population. In modelling the evolution of the GNPs, we do not model the nucleation process, and the subsequent aggregation process that yields the seed particles. Instead, we consider a nucleation term that accounts directly for the "nucleation" of the seed particles, whose size is determined using the method specified in Section 4.3.4. After the seed particles have "nucleated", they grow into the final GNPs. In the previous model by Kumar et al. (2007) and discussed in Chapter 3, the authors employed this modelling approach to describe the evolution of the GNPs by nucleation and growth, assuming that the nucleus had a known diameter of 2 nm. However, as illustrated in Section 4.3.4, the seed diameter does not have a constant value; this depends on the synthesis conditions.

As we have assumed that the reaction system is uniform, the PSD does not depend on the real-space coordinates. The PSD, which we denote as $f(s,t)$, depends solely on the particle size and on the time coordinate. As previously mentioned in Chapters 2 and 3, $f(s,t)ds$ represents the number of particles per unit volume of synthesis solution with size in the differential range ds about the size s at time t. For details about the derivation of the population balance equation, we refer to Ramkrishna (2000), Marchisio and Fox (2013), and Section 2.2.2 in Chapter 2. The equation in our case reads:

$$\partial_t f(s,t) = -\,\partial_s[f(s,t).\, G_s] + \left(\frac{1}{\rho m_v {s_s}^3}\right) k_r C_T (y_x C_{Ct})^{1.85} \delta(s - s_s) \tag{4.3.40}$$

where:

$$G_s = \left(\frac{m_a}{3\rho m_v}\right) k_g\, C_K (y_y C_{Ct}) \tag{4.3.41}$$

Here G_s is the particle growth rate, previously reported in Eq. (4.3.17). As shown, the model accounts for the reaction leading to the growth process according to the seed-mediated mechanism.

The term on the left-hand side of Eq. (4.3.40) represents accumulation, while the first term on the right-hand side accounts for the growth process due to surface reaction. The second and last term on the right-hand side accounts for the formation of the seed particles. In this term, $k_r C_T (y_x C_{Ct})^{1.85}$ gives the rate of formation of gold atoms in $mol/(m^3.s)$ which forms seed particles, and $\delta(s - s_s)$ indicates that all the seed particles have equal diameter s_s, given by Eq. (4.3.29). The term $\rho m_v {s_s}^3$ is the moles of gold present in one seed particle. We have assumed here that as soon as the gold atoms form, they immediately aggregate, turning into seed particles; we made this assumption, because, for the time being, we do not know the aggregation rate and do not have a model for the aggregation process. Developing one is quite complex, and doing so is part of future work.

4.4 Results and discussion

To solve the model, we used the numerical code Parsival, which is commercially available for solving population balance equations. For the computational details of Parsival, we refer the reader to Wuithschick et al. (2001). In this code, the equations are solved on a mass basis; therefore, we transformed the equations, which were derived on a mole basis, into a mass basis. Since the reaction system is uniform, we converted the mole into kg by writing:

$$m_i = C_i Y_i V \tag{4.4.1}$$

where m is the mass in kg, C is the concentration in mol/m^3, Y is the molar mass of species i in kg/mol and V is the volume of the synthesis solution. By differentiating Eq. (4.4.1) with respect to the time, one obtains:

$$\frac{dm_i}{dt} = Y_i V \frac{dC_i}{dt} + C_i Y_i \frac{dV}{dt} \tag{4.4.2}$$

In the synthesis, the reaction mixture is dilute, containing predominantly water. One can therefore assume that the volume of the mixture is constant. Therefore, Eq. (4.4.2) reduces to:

$$\frac{dm_i}{dt} = Y_i V \frac{dC_i}{dt} \tag{4.4.3}$$

The balance equations of the model can then be expressed as follows:

$$T: \frac{d[C_T Y_T V]}{dt} = \left[-k_r C_T (y_x C_{Ct})^{1.85} - k_p C_T C_B\right] Y_T V \tag{4.4.4}$$

$$Ct: \frac{d[C_{Ct} Y_{Ct} V]}{dt} = -1.5 \left[k_r C_T (y_x C_{Ct})^{1.85} + m_a k_g C_K (y_y C_{Ct}) \int_{s_s}^{\infty} s^2 f(s,t) ds\right] Y_{Ct} V \tag{4.4.5}$$

$$Pr1: \frac{d[C_{Pr1} Y_{Pr1} V]}{dt} = [0.5 \cdot k_r C_T (y_x C_{Ct})^{1.85}] Y_{Pr1} V \tag{4.4.6}$$

$$K\text{: } \frac{d[C_K Y_K V]}{dt} = \left[k_p C_T C_B - m_a k_g C_K (y_y C_{Ct}) \int_{s_s}^{\infty} s^2 f(s,t) ds\right] Y_K V \quad (4.4.7)$$

$$Pr2\text{: } \frac{d[C_{Pr2} Y_{Pr2} V]}{dt} = \left[0.5 \cdot m_a k_g C_K (y_y C_{Ct}) \int_{s_s}^{\infty} s^2 f(s,t) ds\right] Y_{Pr2} V \quad (4.4.8)$$

On the other hand, the population balance equation in Eq. (4.3.40) expresses how the particle size distribution evolves under the influence of the formation and growth of the seed particles. These are assumed to be formed at the seed size s_s, represented by the Dirac delta function. Because this function cannot be implemented in Parsival, we employed a similar but smooth function: a Gaussian distribution with mean equal to s_s (i.e., the size of the seed particles) and an extremely small standard deviation. In Chapter 3, we showed that assuming a narrow Gaussian distribution does not affect the final results. For reaction conditions in which the initial values of the citrate-to-gold molar ratio are equal to or greater than five, we followed the methodology presented in Section 4.3.4 to determine the values of y_x and y_y , which are the relative mole fractions of CtH_2^- and CtH^{2-}, respectively.

The values of the constants k_r, k_p and k_g also need to be specified. At $100\,^0C$, their values, as reported in Section 4.3, are:

$$k_r = 35.48\,[m^3/mol]^{1.85}\,1/s \;\; ; \;\; k_p = 6.1\,m^3/(mol.s) \;\; ; \;\; k_g = 5.25 \times 10^{-6}\,m^4/(mol.s)$$

Finally, in solving model equations in the synthesis model, we had to specify the initial conditions and the value of s_s. These initial conditions must satisfy the criterion that the initial value of the citrate-to-gold molar ratio in the synthesis solution be equal to or greater than five at a temperature of $100\,^0C$. In the literature, researchers such as Turkevich et al. (1951), Ji et al. (2007), Zabetakis et al. (2012) and Wuithschick et al. (2015) used experimental conditions that satisfy this condition. Albeit most of the experimental data reported by Turkevich et al. were for molar ratios below five, the authors reported a final mean size of 20 nm at an initial value of the citrate-to-gold molar ratio of 7.6, which can be regarded as the synthesis standard condition. Similarly, Zabetakis et al. (2012) investigated the synthesis at a single initial molar ratio of five. However, while keeping the molar ratio constant, they altered the initial pH of the precursor by changing the initial concentrations. Ji et al. (2007) and Wuithschick et al. (2015), on the other hand, investigated the synthesis at several initial molar ratios at or greater than five.

The value of the seed size s_s can be calculated employing Eq. (4.3.29). In the following section, we validate the predictions obtained from this equation using the synthesis conditions of Wuithschick et al. (2015), where the size of the seeds is reported. Once Eq. (4.3.29) has been validated, we use it to illustrate that the value of the seed size is not constant, but depends on the initial conditions of the synthesis.

4.4.1 Seed size validation and sensitivity analysis

To validate the value of the seed diameter obtained from Eq. (4.3.29), we employ the standard condition in the work of Wuithchick et al. (2015), where the molar ratio of citrate-to-gold is ten, the initial precursor concentration in the synthesis solution at $100\,^0C$ is $0.25\ mol/m^3$, and the final particle mean diameter is $18.6\,nm$. In this condition, the authors reported a value of the seed diameter of $\sim 3\,nm$. This value allows validating the predictions of Eq. (4.3.29).

To obtain the value of S, we use Eq. (4.3.27). At $100\,^0C$, $k_r = 35.48\,[m^3/mol]^{1.85}\,1/s$ and $k_p = 6.1\,m^3/(mol.s)$. To determine the values of $C_{CtH_2^-,0}$ and $C_{OH^-,0}$, we follow the procedure described in Section 4.A of the supporting information in Appendix E; these are $1.4 \times 10^{-3}\ mol/m^3$ and $7.44 \times 10^{-3}\ mol/m^3$, respectively, while the pH value is 6.06. Thus:

$$S = \frac{k_r}{k_p}\frac{\left[C_{CtH_2^-,0}\right]^{1.85}}{\left[C_{OH^-,0}\right]} = 4.11 \times 10^{-3} \quad ; \quad s_s = s_f\left(\frac{S}{1+S}\right)^{1/3} = 2.97\ nm$$

This value agrees with the measured seed size ($\sim 3\ nm$) measured by Wuithschick et al. (2015). We can therefore specify this value in the numerical code to implement the synthesis model for the standard condition of Wuithschick et al. (2015). Notice that changing the value of s_s, given the same synthesis conditions, does affect the model predictions. This indicates that the model is sensitive to the value assigned to the size of the seeds, and this value, therefore, has to be properly estimated. To illustrate this point, we changed the value of $2.97\ nm$ by $\pm 1\,\%$, $\pm 10\,\%$ and $\pm 50\,\%$ and then solved the model numerically using these new, incorrect values of the seed diameter. Table 4.4.1 shows the results.

Table 4.4.1. Sensitivity analysis of the model predictions (in terms of GNP final mean diameter) on the seed diameter. The value of the citrate-to-gold molar ratio is ten.

Deviation from the actual seed size	-50 %	-10 %	-1 %	0 %	1 %	10 %	50 %
Seed diameter (nm)	1.49	2.67	2.94	2.97	3.00	3.27	4.46
Final NP diameter (nm)	10.30	17.30	18.40	18.80	19.30	20.90	28.20

These results reveal that as the seed diameter increases from the actual size of 2.97 nm, the final mean diameter increases. Because the selectivity is determined by the initial reaction conditions, the amount of the precursor that forms the seed particles is fixed. Increasing the seed size, therefore, decreases the number density of seeds. These seeds then grow into final GNPs with a mean diameter larger than 18.8 nm. Hence, specifying the accurate value

of the seed diameter in the model is important to predict correctly the final mean diameter of the NPs.

In the calculations above, the model used as input the final size of the NPs, its output being the size of the seeds, which we were able to validate using the experimental information provided by Wuithschick et al. (2015). Nevertheless, one would like the model to be fully predictive and have as output also the final NP size. To this end, we need a submodel or an empirical correlation that can predict the seed size once the initial synthesis conditions are selected. Developing a submodel based on theoretical arguments is quite challenging and we regard it as part of future work. To render the model fully predictive, we opt for a correlation.

4.4.2 Seed size correlation

To derive a correlation able to predict the size of the seeds, we employ Eq. (4.3.29) to calculate the seed size for some syntheses for which experimental data are available and then relate the values obtained to the initial conditions adopted in the syntheses. We employ the experimental data of Ji et al. (2007), whose initial conditions satisfy the criterion for the synthesis model (i.e., the initial citrate-to-gold molar ratio must be equal to or greater than five). Ji et al. (2007) investigated the synthesis at $100\ ^0C$ *for a fixed initial value of precursor concentration,* equal to $0.25\ mol/m^3$, and an initial value of the citrate-to-gold molar ratio varying between 0.7 and 28 (values referred to the synthesis solution). To derive the correlation, we considered the syntheses in which the initial values of the citrate-to-gold molar ratio were 5.6, 7.7, 8.4, 14 and 27.8, whilst the final mean sizes of the GNPs were 19.79, 25.23, 25.87, 31.01, and $30.58\ nm$, respectively. From the initial conditions of these five syntheses and following the procedure described in Section 4.4.1, we could calculate the corresponding values of the selectivity S. Then, we calculated the seed diameters from Eq. (4.3.29). Figure 4.4.1A shows how the seed diameter varies with the initial value of the citrate-to-gold molar ratio.

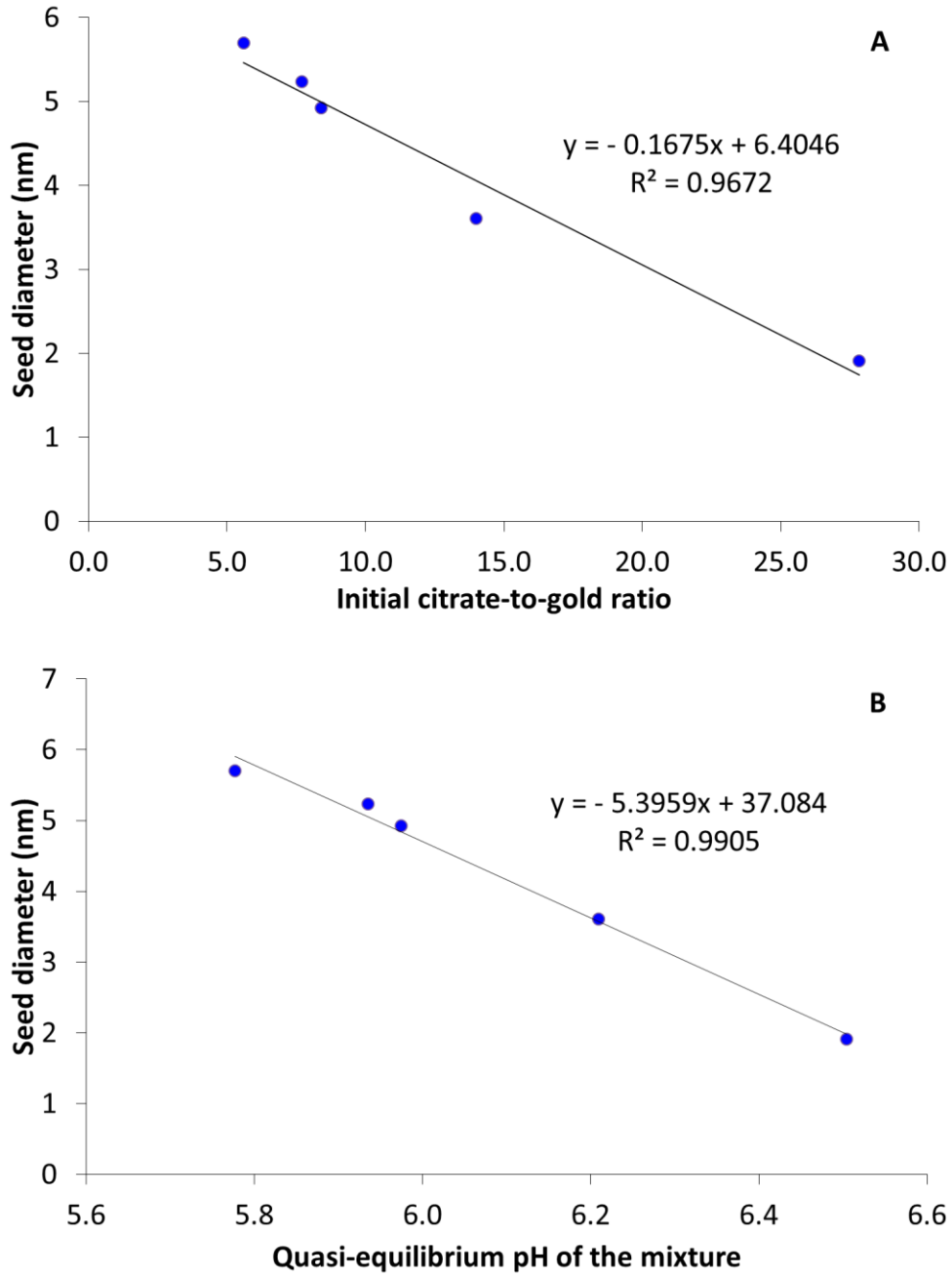

Figure 4.4.1. (A) Seed diameter predicted by Eq. (3.29) as a function of the initial value of the citrate-to-gold molar ratio. (B) Seed diameter predicted by Eq. (3.29) as a function of the quasi-equilibrium pH. The values refer to the syntheses studied experimentally by Ji et al. (2007) at 100 ^{0}C. The initial concentration of gold in the synthesis solution is equal to $0.25\ mol/m^3$ in all cases.

The figure shows that the seed size varies linearly with the citrate-to-gold molar ratio when the initial precursor concentration and temperature are constant (at 0.25 and $100\,^0C$, respectively). Once the initial conditions of the synthesis are assigned, the value of the quasi-equilibrium pH can be calculated using the method outlined in Section 4.A of the SI.

Once the value of the quasi-equilibrium pH is known for each value of the initial citrate-to-gold molar ratio, Figure 4.4.1B can be generated. This expresses the seed mean diameter of the NPs as a function of the quasi-equilibrium pH. Also in this case the functional relation is linear, the correlation fitting the data even better than in Figure 4.4.1A. Thus, letting pH_Q denote the quasi-equilibrium pH, we can write:

$$s_s = A_s \cdot pH_Q + B_s \tag{4.4.9}$$

where $A_s = -5.40$ and $B_s = 37.08\, nm$.

Notice that the quasi-equilibrium pH depends solely on the citrate-to-gold molar ratio, being independent of the initial precursor concentration. We verified this using the thermodynamic model presented in Section 4.A of the SI. We employed this model also to generate Figure 4.4.2, in which we report the values of the quasi-equilibrium pH against those of the citrate-to-gold molar ratio for syntheses investigated experimentally by various research groups. These syntheses had different initial values of precursor concentration, but, as the figure reveals, the experimental points fall on one curve; this implies that the only variable that affects the quasi-equilibrium pH is indeed the citrate-to-gold molar ratio.

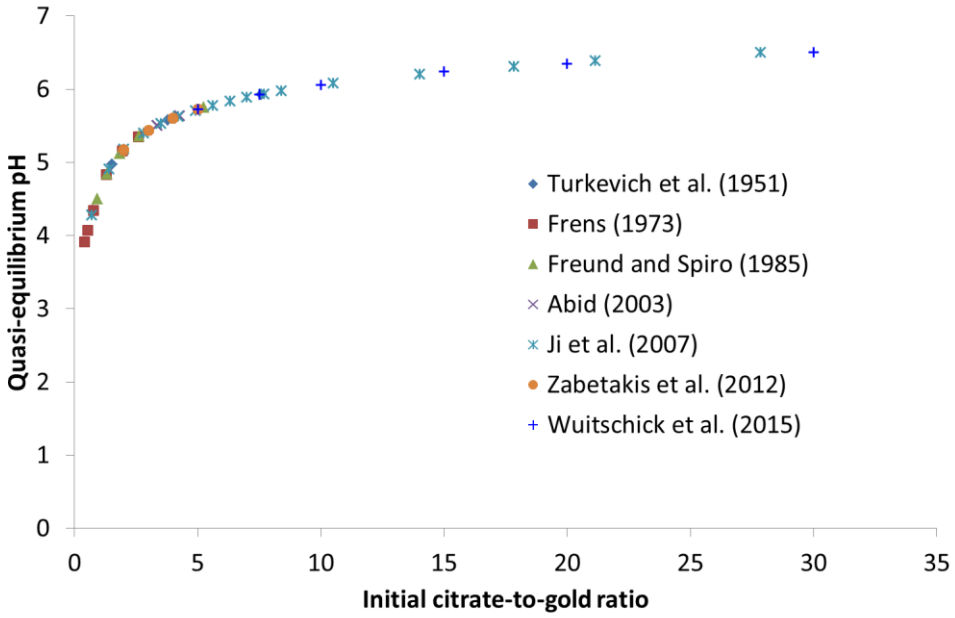

Figure 4.4.2. Relationship between the quasi-equilibrium pH and the initial value of the citrate-to-gold molar ratio. The data refer to syntheses conducted at 100 ^{0}C by various research groups [Turkevich et al. (1951), Frens (1973), Freund and Spiro (1983), Abid (2003), Ji et al. (2007), Zabetakis et al. (2012) and Wuithschick et al. (2015)].

The correlation (4.4.9) is valid at a temperature of $100\,^0C$ for a fixed value of precursor concentration. We now extend its range of validity by considering experimental data referring

to syntheses in which this concentration varies, while *the value of the initial citrate-to-gold molar ratio is kept fixed*. To this end, we employ the synthesis conditions of Zabetakis et al. (2012), who kept the molar ratio equal to 5 whilst considering the precursor concentrations $C_{T0} = 0.3,\ 0.6,\ 1.0,\ 1.2$, and $2.0\ mol/m^3$ in the synthesis solution. We use three out of these five initial conditions to obtain the dependence on the initial precursor concentration, while we use the remaining two in Section 4.4.3 to test the model predictions. These three initial conditions are $C_{T0} = 0.3,\ 1.0$, and $2.0\ mol/m^3$, which yielded GNPs with mean sizes of $18.70,\ 14.40$, and $16.00\ nm$, respectively. For these three initial conditions, we can calculate the selectivity S using the procedure in Section 4.4.1. Then, we calculate the seed diameter from Eq. (4.3.29). Figure 4.4.3 shows how the seed size varies with the initial precursor concentration. From this figure, the seed diameter linearly correlates with the initial concentration of precursor. To account for the dependence of the seed size on the initial precursor concentration in Eq. (4.4.9), we write:

$$s_s = A_s \cdot pH_Q + D_s \cdot C_{T0} + Q_s \tag{4.4.10}$$

where $D_s = 4.03$ and Q_s is a constant.

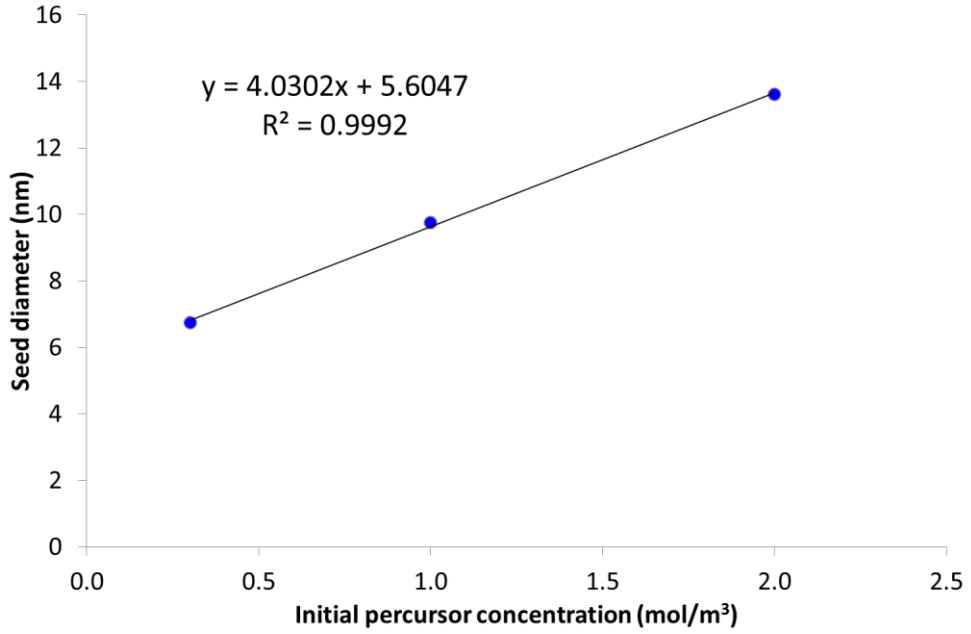

Figure 4.4.3. Seed diameter predicted by Eq.(4.3.29) as a function of the initial precursor concentration. The values refer to the syntheses studied experimentally by Zabetakis et al. (2012) at 100 ^{0}C. The initial citrate-to-gold molar ratio in the synthesis solution is equal to five in all cases.

Based on these figures, we take the values of A_s and D_s to be equal to -5.40 and 4.03, respectively. To obtain the value of Q_s, we equate the right-hand side of Eq. (4.4.10) to the

right-hand side of the linear correlation equation in Figure 4.4.1B, where the initial precursor concentration is $0.25\ mol/m^3$, thus writing:

$$4.03 \cdot C_{T0} + Q_s = 37.08 \qquad (4.4.11)$$

This yields $Q_s = 36.08\ nm$. Alternatively, one could equate the right-hand side of Eq. (4.4.10) to the right-hand side of the linear correlation equation in Figure 4.4.3, where the quasi-equilibrium pH is 5.72. This yields, $Q_s = 36.49\ nm$. This and the previous values are quite close; they would have been identical if the correlation coefficients in Figures 4.4.1B and 4.4.3 had been unity. As Figure 4.4.1B contains more data points than Figure 4.4.3, we opt for $Q_s = 36.08\ nm$. Thus, we write Eq. (4.4.10) as:

$$s_s = -5.40 \cdot pH_Q + 4.03 \cdot C_{T0} + 36.08 \qquad (4.4.12)$$

With this correlation for the seed diameter applicable at the synthesis temperature of 100 ^{0}C, the synthesis model is fully predictive. We test the model predictions in the following section.

4.4.3 Model validation

In this section, we test the model by comparing its predictions against experimental data. These data refer to syntheses whose initial conditions satisfy the criterion on which the model is based, namely that the initial citrate-to-gold molar ratio must be equal to or greater than five; furthermore, they refer to syntheses conducted at a temperature of 100 ^{0}C. Three data sets are taken from the work of Ji et al. (2007) and two from the work of Zabetakis et al. (2012). Ji et al. kept the initial precursor concentration constant at $0.25\ mol/m^3$ and varied the citrate-to-gold molar ratio considering the values of 7.0, 10.5 and 17.8. Zabetakis et al., conversely, kept the initial citrate-to-gold molar ratio constant at five and varied the initial precursor concentration, considering the values of 0.6 and $1.2\ mol/m^3$. From these initial conditions, following the procedure outlined in Section 4.A of the SI, we obtained the value of the quasi-equilibrium pH, and then calculated the corresponding values of seed diameter using Eq. (4.4.12). Notice that these data were not part of the data set employed to derive the seed size correlation in the previous section.

For the data of Ji et al. (2007), Figure 4.4.4A shows the particle sizes predicted by our model and by that of Kumar et al. (2007) against the experimental data. As shown, the predictions of our model are in very good agreement and follow the same trend as the experimental data. The values of the seed diameter calculated from Eq. (4.4.12) for the citrate-to-gold molar ratios of 7.0, 10.5 and 17.8 are 5.28, 4.26, and $2.99\ nm$, respectively. These values, also shown in Figure 4.4.4A, compare reasonably well with those of 5.63, 4.25, and $2.91\ nm$, calculated from Eq. (4.3.29). These good predictions of the seed diameter explain why the

model yields good predictions in terms of final particle size. As the quasi-equilibrium pH increases, indicating an increasing amount of OH^-, the amount of precursor that generates $AuCl_3(OH)^-$ increases, while the amount of precursor that forms gold atoms and then seed particles decreases. The latter trend is confirmed by the decreasing values of the seed diameter. Thereafter, the remaining precursor, in the form $AuCl_3(OH)^-$, grows the seed particles into the final GNPs. Since the initial precursor concentration in these three initial conditions was kept constant at $0.25\ mol/m^3$, the increasing amounts of $AuCl_3(OH)^-$ grow the seed particles to larger final sizes.

In Figure 4.4.4A, we also report the values predicted by the model developed by Kumar et al. (2007). To obtain these values, we implemented and solved their model numerically. In this model, Kumar et al. assumed the seed diameter to be constant at 2 nm for different reaction conditions. The description of how their model was solved numerically, and the checks carried out to verify that the implementation is correct, are discussed in Chapter 3. We see that the predictions from their model show an opposite trend: the predicted mean diameter decreases with increasing quasi-equilibrium pH; moreover, the model predictions are less accurate for two of the three conditions reported in Figure 4.4.4A. Their model is based on a mechanistic description which is completely different from that informed by the chemistry of precursor and reducing agent in the synthesis solution; accordingly, it does not account for the important role played by the pH in this synthesis method. The pH determines the relative mole fractions of the citrate species and the quantities of precursor that reduces to gold atoms and passivates into the hydroxylated form which is able to grow the seeds ($AuCl_3(OH)^-$). The concentration of gold atoms along with the balance of forces of attraction and repulsion determines the seed size. As discussed, this is not constant, contrary to the assumption used in the model of Kumar et al.

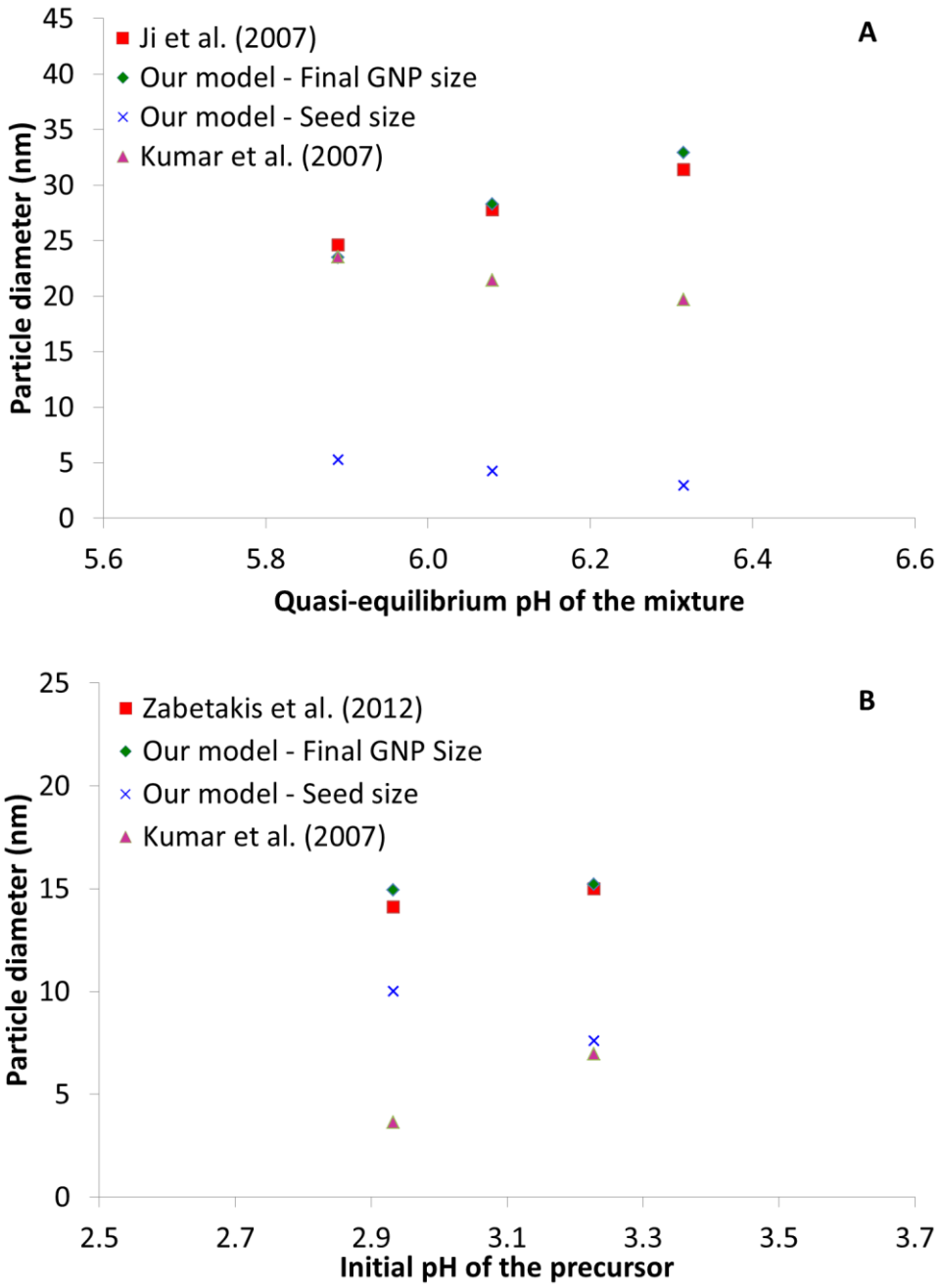

Figure 4.4.4. Final particle size predicted by our model and that of Kumar et al. (2007) against the experimental data obtained by Ji et al. (A) and Zabetakis et al. (B).

For the data of Zabetakis et al. (2012), Figure 4.4.4B shows the values of the final particle sizes predicted by our model and by that of Kumar et al. (2007) against the experimental data. Again, the predictions of our model are in very good agreement with the latter. The values of the seed diameter in this case are larger than those reported in Figure 4.4.4A for

the syntheses of Ji et al. This is because the seeds are formed via an aggregation process, whose effect decreases as the value of the pH of the mixture at quasi-equilibrium conditions increases. For both syntheses conducted by Zabetakis et al. the pH value is 5.72 (the value does not change because in both syntheses the value of the citrate-to-gold molar ratio is the same). This value is lower than all the pH values characterizing the syntheses conducted by Ji et al., as one can see from Figure 4.4.4A. Even if the quasi-equilibrium pH, which determines the selectivity, is identical for both conditions in Figure 4.4.4B, the initial precursor concentrations are different. The larger initial concentration of precursor increases the concentration of gold atoms. These atoms aggregate more significantly to produce larger seeds, and also a greater number concentration of seed particles. As shown in Figure 4.4.4B, the seed size for $C_{T0} = 1.2\, mol/m^3$ is $10.03\, nm$ while for $C_{T0} = 0.6\, mol/m^3$ is $7.61\, nm$. For the number concentration of seed particles, obtained by solving the synthesis model, $C_{T0} = 1.2\, mol/m^3$ yields about twice the value for $C_{T0} = 0.6\, mol/m^3$. For the growth process, although a larger amount of $AuCl_3(OH)^-$ is generated in the case of $C_{T0} = 1.2\, mol/m^3$, this amount grows the greater number of seed particles (per unit volume) to almost the same final size as in the case of $C_{T0} = 0.6\, mol/m^3$, as shown.

The predictions of the model by Kumar et al. (2007) deviate considerably from the experimental data, the NP final sizes being smaller than the size of the seeds yielded by our model. We have discussed in Chapter 3 why their model does not yield accurate predictions, and so here we do not comment on this at length. Although the model accounts for the reduction of the precursor, it does not account for the hydroxylation of the tetrachloroauric ions, a reaction that occurs in parallel with the reduction step when the precursor and reducing agent solutions are mixed.

In our model, the three most important synthesis parameters are the initial precursor concentration, equilibrium pH of the synthesis solution and synthesis temperature. From the seed correlation reported in Eq. (4.4.12), both the initial precursor concentration and equilibrium pH of the synthesis solution determine the seed size, and hence the final size of GNPs. The synthesis temperature, on the other hand, affects reaction rate constants and hence the selectivity of parallel reactions such as those of the precursor reduction and passivation steps. See Eq. (4.3.27). Notice that the seed correlation in Eq. (4.4.12) applies to the citrate synthesis method at 100 ^{0}C.

Also, the size distribution resulting from our model is monodisperse. This is because of some of the assumptions we employed in deriving the model. These assumptions include 1) the synthesis solution is perfectly mixed (since the synthesis is usually carried out in a well-mixed batch reactor), 2) the aggregation model is not modelled (the model is based on the

seed-mediated mechanism proposed by Wuithschick et al. (2015), where seed particles form and the grow), 3) the seed particles from the same synthesis condition have identical size i.e. they are monodisperse (see Eq. (4.3.40)), and 4) the seed formation step is fully decoupled from the growth step, where the growth rate is independent of size (see eq. (4.3.17)). Based on these assumptions, the predicted final size distribution is monodisperse as the seed size distribution.

4.6 Concluding remarks

This chapter presented a new mathematical model for the description of the synthesis of gold nanoparticles via the citrate synthesis method. This method involves reducing tetrachloroauric acid with sodium citrate in an aqueous medium. In this medium, the precursor and reducing agent can exist in various forms by reacting with OH^- and H^+, respectively. Furthermore, the system features several reactions and processes that occur in series and in parallel. Using the seed-mediated mechanism proposed by Wuithschick et al. (2015), we reported the steps describing the evolution of GNPs in the synthesis. Subsequently, we derived rate equations for the reactions involved in the reduction, passivation and growth steps, and proposed a method of calculating the seed diameter in the seed formation step. Then, we reported the synthesis model that describes how the components evolve with time, assuming that the pH value of the reaction mixture is constantly equal to its quasi-equilibrium value.

We solved the model for experimental conditions satisfying the criterion of initial values of the citrate-to-gold molar ratio equal to or greater than five. In this model, seed particles first form and then GNPs evolve from them. To determine the size of the seeds, we derived a correlation based on the initial conditions of the synthesis. We illustrated that the model predictions are sensitive to the value employed for the seed size. In the cases investigated, the model predictions agreed very well with the experimental data. In most of these cases, the growth process overrides the seed formation process in determining the final particle size; the more the amount of gold that passivates, the larger the final particle size is. At low pH values, nonetheless, we saw that seed sizes are larger, since the aggregation process is more vigorous.

Chapter 5

Modelling of the Aggregation Process

In this chapter, we present a modelling approach for the aggregation process in metal nanoparticles synthesis based on the theory proposed by Polte (2015). In the following introduction, we report the motivation and structure of the chapter.

5.1 Introduction

Metal nanoparticles (NPs) are investigated for several potential applications, in fields such as biomedicine, electronics, optics, energy and catalysis, because of their interesting thermal, electrical, optical, magnetic and chemical properties. These properties are determined by parameters such as size, shape, composition and crystalline structure. Although many techniques can be used to obtain them, researchers most commonly synthesize metal NPs in liquids, a mixture that is otherwise called a colloid (Polte, 2015). In colloids, the shape, composition and crystalline structure of the final NPs are usually pre-determined by selecting a synthesis method (Liveri, 2006). Size, on the other hand, varies from the nucleus size to the final size, resulting in a particle size distribution. The nucleus size corresponds to the smallest size of the particles. Understanding the evolution of NPs from the nucleus size to the final distribution therefore is essential.

Hypothetically, one can imagine the processes involved in the evolution of NPs to include nucleation, growth, aggregation, and possibly breakage and dissolution. Historically, however, colloidal NP syntheses have been described using a nucleation-growth mechanism. For many metal NPs, this mechanism follows the classical nucleation theory (CNT) first employed by LaMer and Dinegar (1950). For gold NPs synthesized by the citrate synthesis method, Turkevich et al. (1951) proposed another nucleation-growth mechanism called the Turkevich's organizer theory. While Finke and Watzy (1997) reported the failure of CNT in describing NP syntheses in general, in Chapter 3 we reported the failure of the Turkevich organizer theory for the citrate synthesis method. In a recent theory, Polte (2015) argued that metal atoms, in particular silver and gold atoms, formed from the precursor can exist in the particle phase as dimers and then as larger particles owing to the aggregation process. This process occurs because of the prevailing Van der Waal's forces of attraction at the atomic level, causing metal atoms to aggregate into bigger particles. In colloids, NP aggregation is stopped by either electrostatic repulsion or steric hindrance. In the former, ions called potential determining ions conjugate with the particles thereby making all

particles carry the same sign and quantity of charges. Because of the like charges, they repel one another. In the latter, the particles are shielded from contacting one another by macromolecules. In this work, we focus on electrostatically stabilized particles.

As discussed in Chapter 2, the interaction of colloidal particles due to the forces of attraction and repulsion is described in the popular DLVO theory, named after Derjaguin, Landau, Verwey and Overbreek (Derjaguin and Landau, 1941; Verwey and Overbreek, 1948). In this theory, the total interaction energy between two particles is the sum of the Van der Waal's energy of attraction and electrostatic energy of repulsion. Based on this theory, Fuch (1960) developed an expression for the stability of identical particles against aggregation in terms of the total interaction energy between a pair over the whole space of interaction. This interaction energy has a peak value at a separation between the particles equivalent to the electric double layer (Israelachvili, 2011). Subsequently, Reerink and Overbreek (1954) simplified the expression to a form in terms of the peak energy and then to another form in terms of concentration of the potential determining ions. For particles of different sizes, authors such as Marchisio and Fox (2013) and Bogush and Zukoski (1991) reported the equivalent expression of Fuch in terms of the total interaction energy and that of Reerink and Overbreek in terms of the peak energy. Using the expression of Reerink and Overbreek in terms of the concentration of the potential determining ions, on the other hand, Kumar et al. (2007) developed a model for the aggregation process and employed it as a submodel in predicting the evolution of particle size in the citrate synthesis method for gold nanoparticles. Unfortunately, the submodel failed to describe the synthesis as the aggregation process never stopped. For more details on this aspect, we refer the reader to Chapter 3.

To extend the expression of Reerink and Overbreek in terms of the peak energy, however, Bogush and Zukoski (1991) proposed that the peak energy linearly increases with the harmonic mean when particles of different sizes aggregate. On the profile of the peak energy with size, Polte (2015) proposed that it increases from a value of zero at the minimum particle size (that is a metal atom) to a maximum value in the final NP, thereby suggesting that aggregation should stop.

In this chapter, we develop a model for aggregation based on the theory proposed by Polte (2015). To test the behaviour of the model, we employ as case study the citrate reduction method of synthesizing gold nanoparticles for which in Chapter 4 we reported a synthesis model. This synthesis model describes the citrate synthesis method where the aggregation process is fully decoupled from other processes such the growth process. Using the synthesis model, we can calculate the particle size, called the seed size, resulting from the

aggregation process. Thus, we can investigate the behaviour of the aggregation submodel in the citrate synthesis method.

The chapter is structured as follows. Section 5.2 presents the new aggregation model while Section 5.3 briefly describes the case study along with the model describing the synthesis. This model comprises submodels for reactions, gold atoms formation, aggregation and growth. Section 5.4 presents the solutions of the model and discusses the results. Finally, Section 5.5 reports the concluding remarks.

5.2 The aggregation submodel

In writing a continuity statement for the particle phase, one employs the population balance modelling approach (Ramkrisna, 2000; Marchisio and Fox, 2013). This approach is based on the size distribution of the particles (PSD) and accounts for the processes that affect the particle population. In the particle phase, under the influence of only the aggregation process, new particles generate while consuming old particles. The generation and consumption terms owing to the aggregation process feature in the population balance modelling. For a colloidal system that is uniform in space, the PSD does not depend on the real-space coordinates. The PSD, which we denote as $f(s,t)$, depends solely on the particle size and on the time coordinate. By definition, $f(s,t)ds$ represents the number of particles per unit volume of synthesis solution with size in the differential range ds about the size s at time t. For details about the derivation of the population balance equation, we refer to Ramkrishna (2000), Marchisio and Fox (2013) and Chapter 2 of this thesis. Also in Chapter 2, Section 2.2.3.3, we have derived the source and death terms due to the aggregation process in the population balance equation. The equation reads:

$$\frac{\partial}{\partial t}f(s,t) = \left[(s^2/2)\int_0^s \frac{\widetilde{\omega}_A\left(\bar{s};\hat{s}(\bar{s},s)\right)}{W\left(\bar{s};\hat{s}(\bar{s},s)\right)} \times (s^3-\bar{s}^3)^{-2/3} f(\bar{s},t)\ * f(\hat{s},t)d\bar{s}\right]$$

$$-\left[f(s,t)\int_0^\infty \frac{\widetilde{\omega}_A(s,\bar{s})}{W(s,\bar{s})}\ f(\bar{s},t)\ d\bar{s}\right] \quad ; \quad \hat{s} \equiv (s^3-\bar{s}^3)^{1/3} \qquad (5.2.1)$$

The first and second terms on the right-hand-side account for the particles gained and lost due to the aggregation process, respectively. The first term gives the rate at which particles of sizes $\bar{s}$ and $\hat{s}$ aggregate to form particles of size s, while the second term gives the rate at which particles of size s aggregate with particles of size $\bar{s}$ to form larger particles. These terms involve the functions $\widetilde{\omega}_A(\bar{s},\hat{s})$ and $W(\bar{s},\hat{s})$. The former, measured in m^3/s, is the aggregation kernel and indicates the rate of aggregation; the latter is the stability factor, which accounts for the fact that not all collisions are successful at producing a new aggregate. This stability factor is a number between 1 and ∞. When $W = 1$, fast aggregation

is obtained, while when $W = \infty$, no aggregation occurs. There are many factors that can impede aggregation. As revealed in Section 2.2.3.3 in Chapter 2, in our case, we consider the effect of surface charges and their electric potential.

For colloidal systems, as the particle sizes are below $1\,\mu m$, the aggregation process is controlled by the Brownian motion and the aggregation kernel is expressed as (Elimelech et al., 1995):

$$\widetilde{\omega}_A(\bar{s},\hat{s}) = \frac{2k_BT}{3\mu}\left(\frac{1}{\bar{s}}+\frac{1}{\hat{s}}\right)(\bar{s}+\hat{s}) \tag{5.2.2}$$

where K_B, T and μ are the Boltzmann constant and the temperature and viscosity of the fluid, respectively, as presented in Eq. (2.2.106) in Chapter 2.

For the stability factor W, Fuch (1960) first developed an expression that accounts for the effect of the sum of the potential energies associated with the attractive and repulsive forces among monodisperse particles of diameter s_0. Subsequently, Bogush and Zukoski (1991) reported the expression for particles of different sizes $\bar{s}$ and $\hat{s}$, also previously reported in Chapter 2, as:

$$W(\bar{s},\hat{s}) = \frac{(\bar{s}+\hat{s})}{2}\int_{(\bar{s}+\hat{s})/2}^{\infty}\frac{\exp\left[{}^{E_T}/_{k_BT}\right]}{x^2}dx \tag{5.2.3}$$

Since binary aggregation is usually assumed (Ramkrishna, 2000), x is the distance away from the reference particle, which ranges from $(\bar{s}+\hat{s})/2$, when the two particles are in contact before aggregating, to infinity. E_T is the sum of the energy due to the Van der Waals force of attraction and that due the charge repulsion. E_T has a peak value E_{agg} at a separation between the particles equivalent to the electric double layer (Israelachvili, 2011). Reerink and Overbreek (1954) simplified the original expression of Fuch (for monodisperse particles) to a form in terms of E_{agg}. For particles of different sizes, however, as previously reported in Chapter 2, authors such as Marchisio and Fox (2013) and Bogush and Zukoski (1991) reported an expression in terms of E_{agg}. This expression, previously reported in Chapter 2, is:

$$W(\bar{s},\hat{s}) = \frac{2\kappa}{(\bar{s}+\hat{s})}\exp\left[{}^{E_{agg}(\bar{s},\hat{s})}\Big/_{k_BT}\right] \tag{5.2.4}$$

$1/\kappa$, with a dimension of L, is the thickness of the electric-double layer formed by the surface charges. It is expressed as (Israelachvili, 2011; also see Chapter 2):

$$1/\kappa = \left[\frac{\epsilon_0\epsilon_c k_BT}{\sum_i(p_i e^2 z_i{}^2)}\right]^{1/2} \tag{5.2.5}$$

ϵ_0 is the permittivity of free space, whose value is $8.85 \times 10^{-12}\, F/m$; ϵ_c is the dielectric constant of the solution; e is the charge on an electron, whose value is $1.6 \times 10^{-19} C$; p_i is the number concentration of the potential determining ions in the bulk of the solution measured in $1/m^3$; and z_i is the charge on the ion. In Appendix F, we present a calculation using Eq. (5.2.5).

In Chapter 2, Section 2.2.3.3, we have shown that Eq. (5.2.4) is dimensionally incorrect; it cannot yield $W(\bar{s}, \hat{s})$, a dimensionless number.

To correct this problem, instead of $2\kappa/(\bar{s} + \hat{s})$ as the coefficient in Eq. (5.2.4), we use $\kappa(\bar{s} + \hat{s})/2$. (The term $(\bar{s} + \hat{s})/2$ is the average size of the two particles aggregating.) Doing so yields a dimensionally correct expression as:

$$W(\bar{s}, \hat{s}) = \frac{\kappa(\bar{s}+\hat{s})}{2} \exp\left[{E_{agg}(\bar{s}, \hat{s})}/{k_B T} \right] \tag{5.2.6}$$

To test that Eq. (5.2.6) yields an approximate value as Eq. (5.2.3), we employ them in solving a problem investigated experimentally and reported by Israelachvili (2011). We refer the reader to Appendix G for this problem and its calculations. In these calculations, we solved Eq. (5.2.3) numerically and Eq. (5.2.6) at the double layer thickness. Table 5.2.1 shows the results from these expressions.

Table 5.2.1: Results for the experimental problem from Israelachvili (2011) using Eqs (5.2.3) and (5.2.6).

	Eq. (5.2.3)	Eq. (5.2.6)
$W(\bar{s}, \hat{s})$	8.32×10^{13}	1.27×10^{14}

As shown, the result from Eq. (5.2.6) has the same order of magnitude as that of the original expression (Eq. (5.2.3)). Thus, Eq. (5.2.6) is the approximate expression of Eq. (5.2.3).

Eq. (5.2.6) yields a value of the stability factor $W(\bar{s}, \hat{s})$ between any particle pair of sizes $\bar{s}$ and $\hat{s}$ in a colloidal system defined by the thickness of the electric double layer κ, aggregation barrier E_{agg} and temperature T of the colloidal system. Given Eq. (5.2.5), κ can be calculated. Similarly, since the system is usually isothermal, T is known. However, for any colloidal system, E_{agg} cannot be easily determined. In deriving a simplified expression for $(\bar{s}, \hat{s})$, Reerink and Overbreek (1954) assumed $E_{agg} = 0$ and reported an equation in terms

of the concentration of the potential determining ions. In Section 2.2.3, we showed that $E_{agg} = 0$ in the derivation of Reerink and Overbreek. This assumption may be reasonable for colloidal systems where there is no stabilization by electrostatic repulsion, only the Van der Waal's force of attraction. For these systems, the value of E_T varies from a large negative number to zero. Kumar et al. (2007) employed this simplified expression for the aggregation process in the citrate method of synthesizing gold nanoparticles. Because of the assumption that $E_{agg} = 0$, which is not applicable to colloidal systems (Polte, 2015), in the model developed by Kumar et al., particles aggregated indefinitely, in contrast to experimental evidence. We refer the reader to Chapter 3 for more details.

In nanoparticle synthesis, however, since electrostatic repulsion stabilizes nanoparticles, the maximum value of E_{agg} cannot be zero. This claim is based on a profile reported in Figure 4 (d) of the article of Polte (2015), which presents how E_{agg} varies with size. In deriving this profile, Polte proposed a thought experiment. In this experiment, he employed the DLVO theory, which we have reviewed in Chapter 2, Section 2.2.3. He imagined that the aggregating particles are identical in size, forming identical bigger particles, as the aggregation process progresses. In the following derivation, to obtain an expression for E_{agg} for particles of identical size $\bar{s}$ (($\hat{s} = \bar{s}$), we reason as Polte (2015) did. Then, we modify the expression for particles of different sizes.

For identical spherical particles, an expression for E_T from the DLVO theory can be written as (Polte, 2015):

$$E_T = -\frac{A_H \bar{s}}{24D} + \frac{\pi \bar{s}}{2} \frac{z^2 e^2 {\psi_0}^2 \rho_0}{k_B T \kappa^2} \exp(-\kappa D) \qquad (5.2.7)$$

The terms in this equation are as defined previously (see Section 2.2.3).

Based on this equation and his experimental investigations of metal nanoparticles, Polte claimed that E_T and hence E_{agg} increase with size according to Figure 4 (d) of the article of Polte (2015). We have reproduced this figure in Figure 5.2.1. In this figure, A, B, C, and D represent the profiles of E_{agg} for four colloidal systems. As shown, for each system, E_{agg} increases with size from zero to a maximum value. We can assume the value of E_{agg} to be zero at the smallest particle size, which is taken to be the size of a metal atom since the particle phase evolves from metal atoms (Polte, 2015). For any system to be stable to aggregation, the value of E_{agg} must be above the grey area. At the upper bound of the grey area, the value of E_{agg} of the colloidal system is sufficient to overcome the fluctuation energy of the aggregating particles. The fluctuation energy is equivalent to the thermal energy $k_B T$ as revealed in Eq. (5.2.6). In the grey area, the values of E_{agg} are insufficient to prevent

particle aggregation. (Particles aggregate significantly in colloidal systems whose values of E_{agg} are within the grey area.) Thus, while the colloidal systems described by A and B can be stabilized by electrostatic repulsion once their particle sizes correspond to values of E_{agg} that are above the grey area, systems described by C and D cannot be stabilized in the range of size shown. We refer the reader to the article of Polte (2015) for more details. Further, the initial steepness of the profile of E_{agg} with size relates to how small the stable size of the colloidal system is. The steeper the curve is initially, the smaller the stable size is. The stable size in Figure 5.2.1 is the size corresponding to the intersection of the E_{agg} curve and the upper bound of the grey area. This stable size is smaller for system A than for system B. In the same vein, we can conclude that system A is more stable than system B.

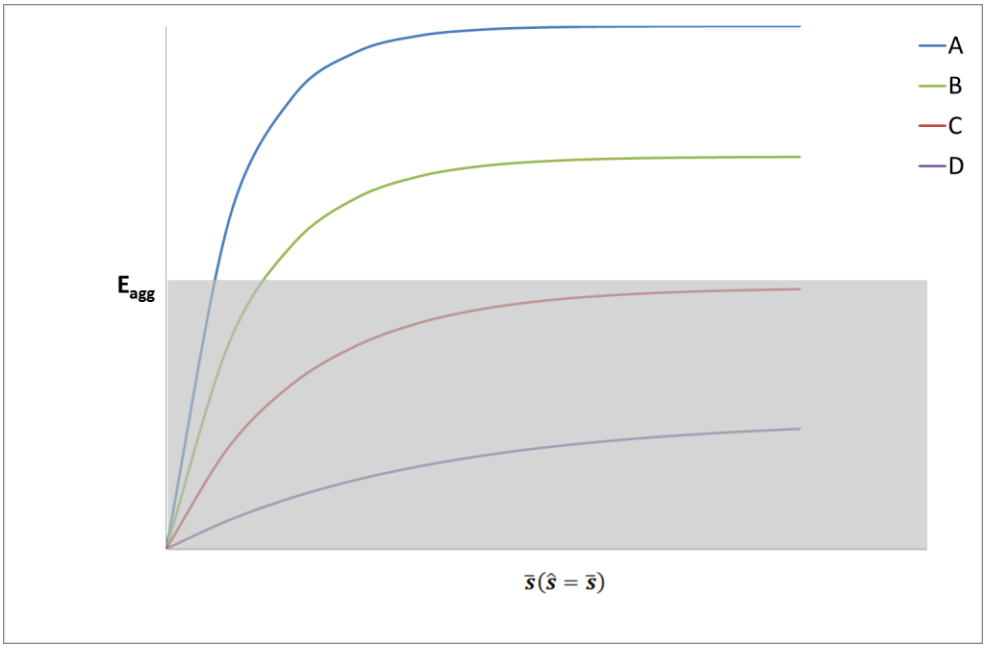

Figure 5.2.1: The profiles of the aggregation barrier E_{agg} with particle size for four different colloidal systems. Systems described by profiles A and B form stable particles while systems described by profiles C and D do not. Data derived from Polte (2015): Figure 2 (d).

From this figure, E_{agg} increases with size and attains a maximum value at an infinite size (the curve having an asymptote). We describe this asymptote as:

$$E_{agg} = E_{max} \tag{5.2.8}$$

where E_{max} is a maximum value of E_{agg} as illustrated in Figure 5.2.1 As shown, the value of E_{max} depends on the colloidal system. Furthermore, we can describe how the profile of E_{agg} approaches the asymptote quite well using an exponential function. The form of the exponential function should resemble that used to describe the dynamics of a first-order system. After a step change in an input variable, the output variable of a first-order system attains a new equilibrium value as time $t \to \infty$. At $t = 0$, however, the change in the output variable is zero. The dynamics of a first-order is given by:

$$\Delta u = \Delta u_{max}(1 - \exp[-t/\tau]) \tag{5.2.9}$$

where Δu is the change in the output variable, Δu_{max} is the maximum change of the output variable, which depends on the step change in input, and τ is the characteristic time for the system to reach equilibrium. While t has the value of zero, the smallest possible size of the particles is the diameter of a metal atom s_0. Therefore, to write Eq. (5.2.9) in terms of a colloidal system, we make the following transformations:

$$t = \left(\frac{\bar{s}}{s_0} - 1\right);\ \Delta u = E_{agg};\ \Delta u_{max} = E_{max};\ \tau = 1/h \tag{5.2.10}$$

where h is a constant value.

Thus, to describe the profile of E_{agg} with size, we propose the equation as:

$$E_{agg}((\bar{s}; \hat{s} = \bar{s})) = E_{max}\left(1 - \exp\left[-h\left(\frac{\bar{s}}{s_0} - 1\right)\right]\right) \tag{5.2.11}$$

Using Eq. (5.2.11), when $s_0 = \bar{s}$, $E_{agg} = 0$ as required from Figure 5.2.1. The value of E_{max}, as observed from Figure 5.2.1, depends on the colloidal system, decreasing in value as we move from system A to system D. Substituting Eq. (5.2.11) in Eq. (5.2.6), however, yields a more complex expression for W that can lead to numerical convergence problems (for example, a numerical overflow – that is, yielding values larger than the largest number that can be handled by a computer). To simplify it, we propose a linear approximation for Eq. (5.2.11). For curves A and B, this linear relationship is sufficient to describe how E_{agg} varies with size, because their colloidal systems become stable within the initial steepness of the curve. However, for the other two colloidal systems represented by curves C and D, this linear relationship would be inaccurate. Furthermore, as described in the Figure, aggregation in these later colloidal systems would never stop. Notice that Polte (2015) derived Figure 5.2.1, and in particular curves C and D, from a thought experiment. Experimentally, however, aggregation in all colloidal systems stops. In describing the profile of E_{agg} for their experimental investigations, Bogush and Zukoski (1991) employed a linear relationship between E_{agg} and size. Furthermore, they illustrated that the particles in their colloidal

systems were stable to the aggregation process. Thus, instead of the exponential relation in Eq. (5.2.11), we opt for a linear relationship. Using a Taylor's series expansion of the right-hand side Eq. (5.2.11) about the point $\bar{s} = s_0$, we write:

$$E_{agg}\big((\bar{s};\hat{s}=\bar{s})\big) = E_{agg}(s_0) + \frac{dE_{agg}}{ds}(s_0)(\bar{s}-s_0) \tag{5.2.12}$$

As previously shown, $E_{agg}(s_0) = 0$. From Eq. (5.2.11),

$$\frac{dE_{agg}}{ds}(s_0) = E_{max}\frac{h}{s_0} \tag{5.2.13}$$

Eq. (5.2.12) when rearranged becomes:

$$E_{agg}(\bar{s};\hat{s}=\bar{s}) = Z(\bar{s}/s_0 - 1);\ Z = E_{max}h \tag{5.2.14}$$

where Z is a gradient that is constant for a colloidal system. When divided by the thermal energy i.e. Z/k_BT, we call it the stability gradient.

In Eq. (5.2.14), when $s_0 = \bar{s}$, $E_{agg} = 0$ as required from Figure 5.2.1. Thereafter, E_{agg} increases linearly with size, describing quite well the colloidal systems represented by curves A and B in the grey area in Figure 5.2.1.

As shown, Eq. (5.2.14) holds for particles of identical size $\bar{s}$. To extend this equation to particles of different sizes, we employ an expression proposed by Bogush and Zukoski (1991). In this expression, Bogush and Zukoski (1991) used the harmonic mean of sizes $\bar{s}$ and $\hat{s}$ of the aggregating particles. We write the expression for the harmonic mean as (Bogush and Zukoski, 1991):

$$\frac{2\bar{s}\hat{s}}{(\bar{s}+\hat{s})} \tag{5.2.15}$$

Thus, instead of $\bar{s}$ in Eq. (5.2.14), we write:

$$E_{agg}(\bar{s};\hat{s}) = Z\left(\frac{2\bar{s}\hat{s}}{(\bar{s}+\hat{s})s_0} - 1\right) \tag{5.2.16}$$

In Eq. (5.2.16), when $\bar{s} = \hat{s} = s_0$, $E_{agg} = 0$ as required from Figure 5.2.1. Further, for identical size, when $\bar{s} = \hat{s} \neq s_0$, E_{agg} is finite and increases with size. Considering Eq. (5.2.15) for different sizes, as the size difference increases, the harmonic mean increases, thus increasing E_{agg} and W. Using Eq. (5.2.16), therefore, particles of different sizes should aggregate less than those of identical size. We can combine Eqs. (5.2.2), (5.2.6) and (5.2.16) as follows:

$$\frac{\tilde{\omega}_A}{W}(\bar{s};\hat{s}) = \frac{4k_BT}{3\mu\kappa} \times \frac{\left(\frac{1}{\bar{s}}+\frac{1}{\hat{s}}\right)}{\exp\left[\frac{Z}{k_BT}\left(\frac{2\bar{s}\hat{s}}{s_0(\bar{s}+\hat{s})}-1\right)\right]} \tag{5.2.17}$$

To use this equation, we need a value for Z. Employing the aggregation model (a combination of Eqs. (5.2.1) and Eq. (5.2.17)), this value can be obtained by fitting experimental data. As $Z \to \infty$, Eq. (5.2.17) approaches zero. Also, the stable size approaches the size of the metal atom. While as $Z \to 0$, the stable size approaches a size equivalent to the largest size obtained experimentally. For the particular value of Z for a colloidal system of aggregating particles, we investigate a synthesis method where the aggregation process occurs.

5.3 Case study: the citrate synthesis method

As a case study, we apply the developed aggregation model to describe the citrate synthesis method. In this method, tetrachloroauric reacts with sodium citrate in an aqueous solution to produce at the end of the synthesis gold nanoparticles (GNPs). In the evolution of GNPs, Polte et al. (2010) reported data illustrating the aggregation process. These data, reported in Figure 2(d) of their article, show particles aggregating in the first 20 minutes of the synthesis. Thereafter, this process stops while the particle mean size increases until the end of the synthesis. The latter size increase is due to the growth process. In Chapter 4, we showed that the aggregation process can be assumed as fully decoupled from the growth process, for conditions where the initial citrate-to-gold ratios are equal to or greater than five. Before particles begin to aggregate, however, they must be generated first from the aqueous solution via the nucleation process. For the nucleus size, as discussed in Chapter 2, Polte (2015) argued that it is the size of an atom (for metal nanoparticles such as GNPs). To form gold atoms, the gold in tetrachloroauric acid reduces from an oxidation state of +3 to zero, due to the reducing action of sodium citrate. In the reacting mixture as well, we illustrated in Chapter 4 that OH^- can react with the precursor in the passivation step, which occurs in parallel with the reduction of tetrachloroauric acid to gold atoms. For detailed information about the mechanism of the citrate synthesis method, we refer the reader to Chapter 4.

At the end of the aggregation process, for conditions where the initial citrate-to-gold ratios are equal to or greater than five, the particles are called seed particles. Thus, due to the aggregation process, the particles evolve from the size of a gold atom, which is $0.272\,nm$ (Cordero et al. 2008), to the seed size. The latter size is not constant but varies depending on the initial condition of the synthesis (see Chapter 4 for details). For the standard synthesis condition of Wuithschick et al. (2015), they reported the seed diameter as 3 nm. For other initial conditions, we reported an equation in Chapter 4 that can be used to calculate the seed size at the synthesis temperature of 100^0 C. As shown in the aggregation model in the previous section, the number concentration of particles affects the aggregation process. At the minimum size of a gold atom, we need to know the rate of formation of atoms from the

reduction step. Also, we need to know the rate of the passivation step since both this step and the reduction step competitively consume the precursor.

We therefore couple the aggregation model developed in the previous section with the synthesis model (excluding the growth submodel) developed in Chapter 4 in what we call Case A. We refer the reader to Chapter 4 for the details about the synthesis model. On the other hand, we assume the aggregation is fully decoupled from the reduction and passivation steps in what we call Case B. The latter case is justified considering Figure 2 (d) of the article of Polte et al. (2010), reproduced in Figure 4.B.1 in Section 4.B, where the number concentration of particles rapidly declines from a maximum value. To determine the case that closely describes the citrate reduction method, we test the two cases in Section 5.4. Herein, we discuss the models for the two cases as follows.

5.3.1 Case model A: coupled aggregation

In the synthesis model of this case, we do not account for the growth process since this process does not influence the seed formation step. However, we couple the aggregation model with the reduction and passivation steps. Furthermore, in the particle phase, we account for the formation of gold atoms and the aggregation process. We report the chemical reactions and the material and population balance equations as follows.

Chemical equations

For the reduction step, we write the chemical equation as:

$$2T + 3(y_x \cdot Ct) \rightarrow 2Au + Pr1 \tag{5.3.1}$$

T represents the gold in $AuCl_4^-$, Ct represents the sum of all the species of citrate, y_x represents the relative mole fraction (among the four citrate species) of CtH_2^- at the quasi-equilibrium pH, Au represents the gold in the GNPs, and $Pr1$ represents all by-products from the reduction step, lumped together.

For the passivation step, we have:

$$T \overset{B}{\rightarrow} K \tag{5.3.2}$$

B represents OH^-, which is assumed to have a constant concentration, and acts as a catalyst; K represents the gold that becomes passive and that eventually grows the seed particles.

Assuming that the reaction solution is perfectly mixed (which implies that all intensive properties, such as temperature and concentrations, are uniform), we can select as control

volume the region (of constant volume V) occupied by the mixture contained in the batch reactor wherein the synthesis takes place. The balance equations of the mixture components are then those reported below.

Balance equations

Precursor

This is consumed by both the reduction and passivation steps. The material balance equation takes the form:

$$\frac{dC_T}{dt} = -k_r C_T [y_x C_{Ct}]^{1.85} - k_p C_T C_B \tag{5.3.3}$$

This equation is identical to Eq. (4.3.34), reported in Chapter 4.

Total citrate species

At any time, we consider the sum of the concentrations of all the citrate species (i.e., Ct^{3-}, CtH^{2-}, $CtH_2{}^-$ and CtH_3), which we denote as C_{Ct}, and model the time variation of this total concentration caused by the reduction step. This step consumes $CtH_2{}^-$, whose amount, at any time, is given by $y_x C_{Ct}$. The material balance equation on the total citrate species thus is:

$$\frac{dC_{Ct}}{dt} = -\,(3/2)\; k_r C_T [y_x C_{Ct}]^{1.85} \tag{5.3.4}$$

This equation is a simplified version of Eq. (4.3.35) in Chapter 4, in which the growth term has been neglected in line with the modelling choice we have made.

Hydroxyl ions

Having assumed that the pH of the mixture is constant at the quasi-equilibrium value, we simply write that the concentration of hydroxyl ions is constant:

$$C_B = constant \tag{5.3.5}$$

Also, this equation is identical to Eq. (4.3.36), reported in Chapter 4.

Passive precursor

The precursor passive form is generated by the passivation step. The material balance equation reads:

$$\frac{dC_K}{dt} = k_p C_T C_B \tag{5.3.6}$$

This equation is a simplified version of Eq. (4.3.37) in Chapter 4, in which the growth term has been neglected in line with the modelling choice we have made.

By-products

The reduction step generates by-products such as CO_2, $(CH_3)_2C=O$ and Cl^-, as reported in Chapter 4. To ensure that total mass is conserved, we report the balance equation for these other by-products, lumped into Pr. We write the equation as:

$$\frac{dC_{Pr1}}{dt} = (1/2)\, k_r C_T [\, y_x C_{Ct}]^{1.85} \tag{5.3.7}$$

Also, this equation is identical to Eq. (4.3.38), reported in Chapter 4.

Particles

In modelling the evolution of the particle size distribution (PSD), we model the generation of gold atoms, the real nucleation process, and the subsequent aggregation process that yields the seed particles. As we have assumed that the reaction system is uniform, the PSD does not depend on the real-space coordinates. The PSD, which we denote as $f(s,t)$, depends solely on the particle size and on the time coordinate.

The evolution of the PSD, governed by the population balance equation, must reflect the effects of the nucleation and aggregation processes taking place in the mixture. The growth process is neglected. The nucleation rate is modelled as follows:

$$H_N(s) = \left(\frac{1}{\rho m_v {s_0}^3}\right) k_r C_T [\, y_x C_{Ct}]^{1.85} \delta(s - s_0) \tag{5.3.8}$$

In the nucleation term, $k_r C_T [\, y_x C_{Ct}]^{1.85}$ gives the rate of formation of gold atoms in $mol/(m^3.s)$, and $\delta(s-s_0)$ indicates that all the nuclei have equal size, given by s_0 (the size of one atom). The term $\rho m_v {s_0}^3$ is the amount of gold in moles present in one atom. ρ is molar density of gold.

For the aggregation process, from Section 5.2, we write the aggregation submodel as:

$$B(s) - D(s) = \left[(s^2/2)\int_0^s \frac{\tilde{\omega}_A(\bar{s};\hat{s}(\bar{s},s))}{W(\bar{s};\hat{s}(\bar{s},s))} \times (s^3 - \bar{s}^3)^{-2/3} f(\bar{s},t)\ * f(\hat{s},t) d\bar{s}\right] - \left[f(s,t)\int_0^\infty \frac{\tilde{\omega}_A(s,\bar{s})}{W(s,\bar{s})}\, f(\bar{s},t)\ d\bar{s}\right] \tag{5.3.9}$$

Eq. (5.2.17) gives the equation for $\tilde{\omega}_A/W$. To calculate the value of κ in Eq. (5.2.17), we need to know the potential determining ions (PDIs) and their concentrations. Briggs et al. (1993) assumed them to be CtH^{2-} and Ct^{3-}. The electrostatic charges on CtH_3 and $CtH_2{}^-$ are 0 and -1, respectively. Conversely, those on CtH^{2-} and Ct^{3-} are -2 and -3,

respectively. Furthermore, in the process conditions investigated by Briggs et al., the amounts of CtH_3 and CtH_2^- are insignificant. The combination of the charges and amounts of CtH^{2-} and Ct^{3-} makes them the PDIs. Similarly, in the process conditions satisfying the synthesis model, the amounts of CtH_3 and CtH_2^- are insignificant. Thus, we assume CtH^{2-} and Ct^{3-} to be the PDIs. Following Eq. (5.2.5), we write the expression for κ as:

$$1/\kappa = \left[\frac{\epsilon_0 \epsilon_c k_B T}{(4.p_{CtH^{2-}} e^2 + 9.p_{Ct^{3-}} e^2)}\right]^{1/2} \tag{5.3.10}$$

$p_{CtH^{2-}}$ and $p_{Ct^{3-}}$ are the number concentrations of CtH^{2-} and Ct^{3-}, respectively, in the bulk of the solution measured in $1/m^3$.

For the term Z in Eq. (5.2.17), we obtain its value by fitting experimental data. We discuss the fitting procedure in Section 5.4.

Finally, the population balance equation reads:

$$\partial_t f(s) = H_N(s) + B(s) - D(s) \tag{5.3.11}$$

The terms on the right-hand side represent generation owing to nucleation and aggregation.

5.3.2 Case model B: fully decoupled aggregation

In this case, we first calculate the amount of gold atoms formed from the precursor VC_s using the yield of the reduction step. Then in the population balance equation, we account for the aggregation process only, starting with the gold atoms calculated. The initial amount of gold in the precursor is equal to the sum of the amount of gold atoms formed from the reduction step and that of gold in the passive precursor from the passivation step. This statement reads:

$$VC_{T0} = V \int_0^{t_s} (r_r + r_p) dt \tag{5.3.12}$$

where V is the volume of synthesis solution, C_{T0} is the initial precursor concentration, r_r is the reaction rate for the reduction step, r_p is the rate of the passivation reaction, t is the time, and t_s is the total synthesis time. Notice that the synthesis solution is assumed to be uniform, so that r_r and r_p do not depend on space coordinates.

The yield L_d is defined as follows:

$$L_d = \frac{\int_0^{t_s} r_r dt}{C_{T0}} \tag{5.3.13}$$

Using Eqs. (5.3.12) and the equations for r_r and r_p, reported in Chapter 4, we thus have:

$$L_d = \frac{k_r \int_0^{t_s} C_{AuCl_4^-} . C_{CtH_2^-}{}^{1.85}\, dt}{k_r \int_0^{t_s} \left(C_{AuCl_4^-} . C_{CtH_2^-}{}^{1.85} \right) dt + k_p \int_0^{t_s} \left(C_{AuCl_4^-} C_{OH^-} \right) dt} \quad (5.3.14)$$

In this equation, the denominator on the right-hand side is equal to C_{T0} because all the precursor eventually reacts via the two reactions considered (reduction and passivation).

To use this equation to obtain L_d, we need to know the time profiles of $C_{AuCl_4^-}$, $C_{CtH_2^-}$ and C_{OH^-}. For synthesis conditions where the ratio of initial concentrations of sodium citrate to tetrachloroauric acid in the synthesis solution is equal to or greater than five, we assume that the values of $C_{CtH_2^-}$ and C_{OH^-} do not change significantly from their values at quasi-equilibrium, denoted as $C_{CtH_2^-,0}$ and $C_{OH^-,0}$, respectively. The reasoning is discussed in Chapter 4. Thus, we can write:

$$L_d = \frac{k_r . C_{CtH_2^-,0}{}^{1.85} \int_0^{t_s} C_{AuCl_4^-}\, dt}{k_r . C_{CtH_2^-,0}{}^{1.85} \int_0^{t_s} \left(C_{AuCl_4^-} \right) dt + k_p C_{OH^-,0} \int_0^{t_s} \left(C_{AuCl_4^-} \right) dt}$$

$$= \frac{k_r . C_{CtH_2^-,0}{}^{1.85} \int_0^{t_s} C_{AuCl_4^-}\, dt}{\left(k_r . C_{CtH_2^-,0}{}^{1.85} + k_p C_{OH^-,0} \right) \int_0^{t_s} \left(C_{AuCl_4^-} \right) dt}$$

$$L_d = \frac{k_r . C_{CtH_2^-,0}{}^{1.85}}{\left(k_r . C_{CtH_2^-,0}{}^{1.85} + k_p C_{OH^-,0} \right)} \quad (5.3.15)$$

Thus, the amount of gold atoms formed from the precursor VC_s is given as:

$$VC_s = L_d . VC_{T0} \quad (5.3.16)$$

From this equation, the number concentration of gold atoms before the aggregation process begins can be expressed as:

$$\left(\frac{1}{\rho m_v {s_0}^3} \right) . C_s \quad (5.3.17)$$

For the population balance equation, which in the present case accounts only for the aggregation process, we write:

$$\partial_t P(s) = B(s) - D(s) \quad (5.3.18)$$

The expressions for $B(s)$ and $D(s)$ (as well as those for the other implicit terms) have been reported in Case A.

To close the model for each case, one needs a value of Z, or $Z/k_B T$ (the stability gradient). However, this value or a correlation for finding it is not available in the literature. To overcome this problem, using the model, we fit experimental data to estimate the value of Z for a particular initial condition. While many authors have investigated the citrate synthesis method and reported the final mean diameter, only Wuithschick et al. (2015) reported the

particle size (called the seed size) at the end of the aggregation process as well as the final mean diameter at the end of the synthesis. However, they reported the seed size for only one initial condition. For other initial conditions, we use the correlation in Eq. (4.4.12) reported in Chapter 4 to calculate the actual seed size. Therefore in estimating the value of Z for a particular initial condition, we employ the seed size as the experimental data. By following this procedure, we can estimate the values of Z for different initial conditions. These values of Z, when related to their initial conditions, correlate linearly. Then, we derive a correlation for calculating Z. With this correlation, the models above are fully predictive. We describe how to estimate the value of Z, the derived correlation and the test for the fully predictive model in the following section.

5.4 Results and discussion

In solving the model (for both Case A and Case B), we use the commercial numerical code Parsival. For Case A, due to numerical convergence problems, we initialized the amount of particles with a vanishingly small mass (or number) of particles with a mean size equal to the diameter of a gold atom. The details of model implementation in Parsival, for example those of the synthesis model, have been provided in Chapters 3 and 4. For these details, we refer to these chapters. On the other hand, for Case B, we initialized with the mass of gold corresponding to the amount calculated from Eq. (5.3.16).

5.4.1 Parameter estimation and case model validation

To illustrate how to estimate the value of Z, we employ the standard condition in the work of Wuithchick et al. (2015), where the ratio of citrate-to-gold is 10, the initial precursor concentration in the synthesis solution at $100\,^0C$ is $0.25\ mol/m^3$, and the final particle mean diameter is $18.6\,nm$. In these conditions, the authors reported a value of the seed diameter of $3\,nm$ at about 40% polydispersity. This value allows estimating the value of Z. For each case model, we specified the initial condition and the final condition, which is the seed diameter of $3\,nm$ as reported by Wuithschick et al. (2015), to estimate the corresponding value of Z. The initial condition corresponds to $t = 0$. Similarly, the final condition at the end of the aggregation process corresponds to a particular time $t = t_a$, when the size of the aggregating particles reaches the seed diameter and remains constant thereafter. Wuithschick et al. (2015) reported this time to be between 3 and 7 mins for this synthesis solution at $100\,^0C$. Thereafter, the seed diameter should remain constant. In fitting the result from the model to a mean diameter of 3 nm, we initialised in the code the initial condition. Then, we specified the same value of 3 nm as the mean diameter at $t_a = 200\,s$. Furthermore, to ensure particle stability at the seed diameter, we specified 3 nm as the

mean diameter at times 300, 400, 500, 1000 and 10000 s. The latter time is sufficiently longer than the synthesis time of 1200 s observed experimentally by Wuithschick et al. (2015). Later, we check whether the model is stable to aggregation.

Table 5.4.1: Results from the parameter estimation

	Case A	Case B
Value of Z/k_BT	0.81	1.18
Particle number concentration ($1/m^3$)	3.85E+15	3.55E+17

Table 5.4.1 shows the results from the parameter estimation. The value of Z/k_BT in Case A is smaller than that in Case B. As the value of Z/k_BT decreases, the value of W (the stability factor) in Eq. (5.2.6) decreases, indicating that aggregation is more significant. In Case A, once the reduction step has yielded gold atoms in sufficient concentration, these begin to aggregate. This aggregation process continues until the particle mean size reaches the seed diameter. In Case B, on the other hand, all the gold atoms have been produced before the aggregation process begins. Because of this time delay, aggregation is more significant in Case A than in Case B. The particle number concentrations in Table 5.4.1 illustrate better this significant aggregation as the value of the number concentration in Case A is about two orders of magnitude smaller than that in Case B. To determine the case that closely applies to the citrate synthesis method, we estimate the seed particle concentration and then compare with the values in Table 5.4.1. To estimate this concentration, since particle aggregation is insignificant after the seed formation step, we equate the seed number concentration to the number concentration at the end of the synthesis. To calculate the latter, assuming that the GNP size distribution is monodisperse, one can use the expression $C_{T0}/\rho m_v {s_f}^3$, where s_f is the final mean diameter, ρ is the molar density of gold, taken as $10^5\ mol/m^3$ (Kumar et al., 2007) and m_v is the particle volume shape factor (which we set equal to $\pi/6$, assuming that the particles are spherical). From the data of Wuithschick et al. (2015), $C_{T0} = 0.25\ mol/m^3$ and $s_f = 18.6\,nm$. Thus, the seed concentration is estimated as:

$$\frac{0.25\ mol/m^3}{1 \times 10^5 \times \pi/6 \times (18.6 \times 10^{-9})^3} = 7.42 \times 10^{17}\ 1/m^3$$

This value compares with the value in Case B much better than that of Case A. See Table 5.4.1. Thus, we assume that the aggregation process is fully decoupled from the nucleation process (i.e. the formation of gold atoms) and adopt case model B for the citrate synthesis method.

Furthermore, we confirmed that in this case model, beyond the seed diameter, particles do not aggregate significantly. To do this, we simulated the aggregating system using the case model (for the standard synthesis condition of Wuithschick et al. (2015)) for $1 \times 10^5\ s$. Figure 5.4.1A shows how the mean size varies over this simulation time. Within the synthesis time of about 1,000 s, the particles aggregate to a mean diameter of about 3nm, the size experimentally observed by Wuithschick et al. (2015). Thereafter, the mean diameter continues to increase. However, this increase is barely significant. The mean size at 100,000 s is 3.5 nm. This size is smaller than the resulting value when two particles having identical sizes of 3 nm aggregate. To estimate this resulting value s_a of the aggregate, we assume that its volume equals the sum of the volumes of the two primary particles of 3 nm. Thus, we have:

$$s_a{}^3 = 2 \times 3^3 \quad \rightarrow \quad s_a = 3.78\ nm \tag{5.4.1}$$

By 1,000 s, in the citrate synthesis method, the growth step starts affecting the particle size significantly, doubling the size to about 6 nm. By this size, the effect of the aggregation process would be much less significant. Thus, the Case B model would be able to describe the evolution in size in the synthesis.

Figure 5.4.1B reports at 1,000 s the particle size distribution whose polydispersity is calculated as 38%. This value compares reasonably well with the polydispersity of 40% for seed particles experimentally observed by Wuithschick et al. (2015).

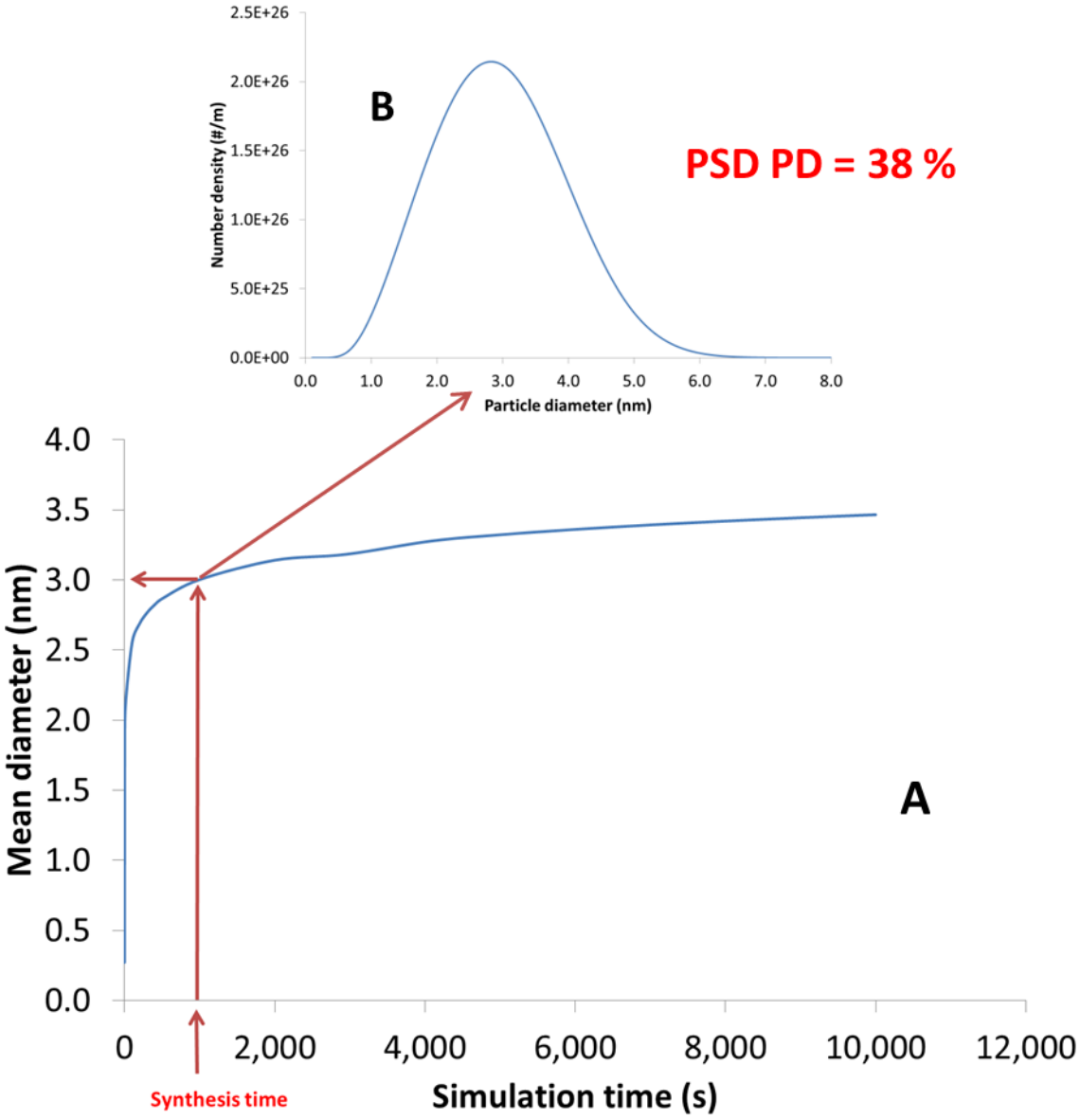

Figure 5.4.1 Time evolution of the particle phase from the modelling results using the experimental data of the work of Wuithchick et al. (2015), where the ratio of citrate-to-gold is 10, the initial precursor concentration in the synthesis solution at $100\,^0C$ is $0.25\ mol/m^3$. A: The profile of mean particle diameter with time, B: Particle size distribution at the synthesis time of 1200 s. PSD PD represents the polydispersity of the particle size distribution.

As shown, the value of Z/k_BT for the standard condition of Wuithschick et al. was estimated from the seed diameter. Nevertheless, one would like the case model to be fully predictive, yielding the particle size distribution comparable to experimental data. To this end, we need an empirical correlation that can predict the value of Z/k_BT once the initial synthesis conditions are selected.

5.4.2 Correlation for the stability gradient Z/k_BT

As shown, Z/k_BT depends on the process conditions in the synthesis mixture (i.e. the colloidal system). These process conditions vary with time from the initial conditions to the final conditions. However, past authors such as Wuithschick et al. (2015) and Bogush and Zukoski (1991) assumed the value of Z/k_BT to be constant for an initial condition of a system of aggregating particles. Thus, in deriving a correlation for Z/k_BT, we use only the initial conditions, i.e. the initial precursor concentration, initial citrate-to-gold ratio and synthesis temperature. To relate Z/k_BT to the initial precursor concentration, we employ the synthesis conditions of Zabetakis et al. (2012), who kept the ratio equal to 5 whilst considering the precursor concentrations $C_{T0} = 0.3,\ 0.6,\ 1.0,\ 1.2,$ and $2.0\ mol/m^3$ in the synthesis solution. These synthesis conditions satisfy the criteria for the synthesis model. We use three out of these five initial conditions to obtain the dependence on the initial precursor concentration, while we use the remaining two in Section 5.4.3 to test the model predictions. These three initial conditions are $C_{T0} = 0.3,\ 1.0,$ and $2.0\ mol/m^3$, which yielded seed diameters of $6.74,\ 9.75,$ and $13.62\ nm$, respectively (see Chapter 4, Section 4.4.2). From these seed diameters and the corresponding initial conditions, following the procedure described in Section 5.4.1, we estimated the values of Z/k_BT. Figure 5.4.2 shows how Z/k_BT varies with the initial precursor concentration.

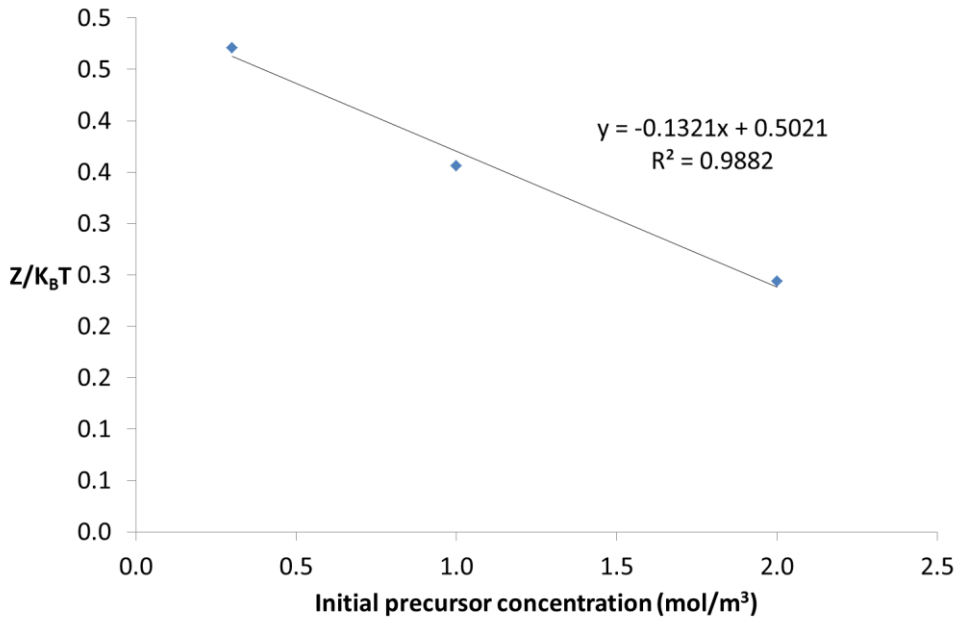

Figure 5.4.2: The value of Z/k_BT estimated as a function of the initial precursor concentration. The experimental data are from Zabetakis et al. (2012).

Based on this figure, we propose a linear function of Z/k_BT on the initial precursor concentration as:

$$Z/k_BT = F_z \cdot C_{T0} + D_z \quad (5.4.1)$$

where $F_z = -0.1321$ and $D_z = 0.5021$.

To relate Z/k_BT to the initial citrate-to-gold ratio, we employ the synthesis conditions of Ji et al. (2012), who investigated the synthesis at $100\,^0C$ *for a fixed initial value of precursor concentration,* equal to $0.25\,mol/m^3$, and an initial value of the citrate-to-gold ratio varying between 0.7 and 28 (values referred to the synthesis solution). To derive the correlation, we considered the syntheses in which the initial values of the citrate-to-gold ratio (R^a) are 7.0, 8.4, 14 and 27.8, whilst the seed diameters are 5.63, 4.92, 3.61, and $1.91\,nm$, respectively (see Chapter 4, Section 4.4.2). These ratio values are greater than five, satisfying the criterion for the synthesis model. From these seed diameters and the corresponding initial conditions, following the procedure in Section 5.4.1, we estimated the values of Z/k_BT. Figure 5.4.3 shows how Z/k_BT varies with the initial citrate-to-gold ratio.

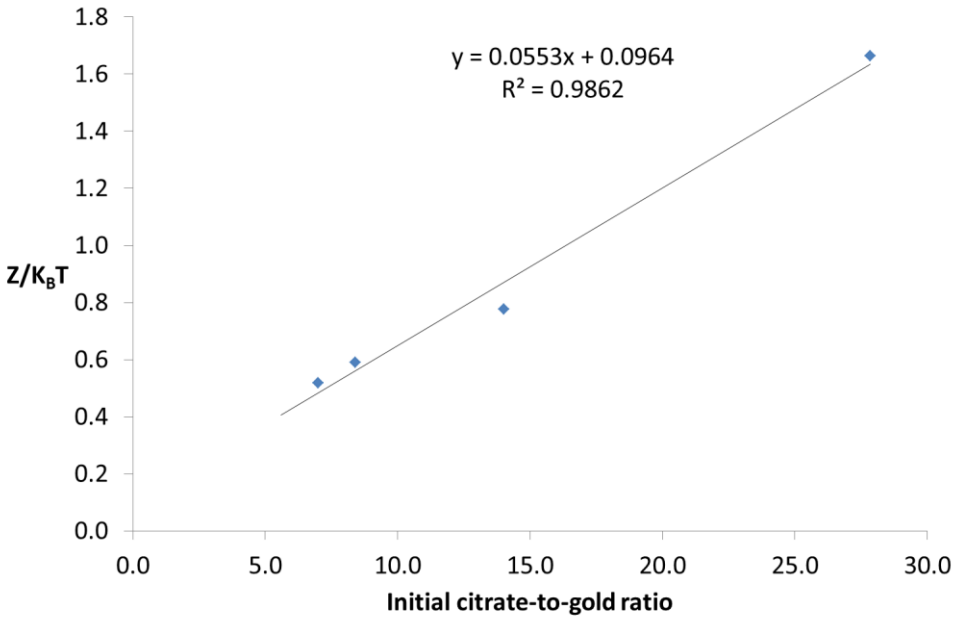

Figure 5.4.3: The value of Z/k_BT estimated as a function of the initial precursor concentration. The experimental data are from Ji et al. (2007).

Based on this figure, we propose a linear function of Z/k_BT on R^a as:

$$Z/k_BT = Q_z \cdot R^a + L_z \quad (5.4.2)$$

where $Q_z = 0.0553$ and $L_z = 0.0964$.

To relate Z/k_BT to the synthesis temperature, we do not have data from the literature. However, because the synthesis is usually carried out at $100\ ^0C$, we focus only on this temperature. We therefore combine Eqs. (5.4.1) and (5.4.2) to derive an overall correlation of Z/k_BT on the initial conditions at the synthesis temperature of $100\ ^0C$ as:

$$Z/k_BT = F_z \cdot C_{T0} + Q_z \cdot R^a + P_z \quad (5.4.3)$$

Based on these figures, we take the values of F_z and Q_z to be equal to -0.1321 and 0.0553, respectively. To obtain the value of P_z, we equate the right-hand side of Eq. (5.4.3) to the right-hand side of the linear correlation equation in Figure 5.4.2, where the ratio is 5, thus writing:

$$0.0553 \cdot R^a + P_z = 0.5021 \quad (5.4.4)$$

This yields $P_z = 0.2256$.

Alternatively, one could equate the right-hand side of Eq. (5.4.3) to the right-hand side of the linear correlation equation in Figure 5.4.3, where the initial precursor concentration is $0.25\ mol/m^3$, thus writing:

$$-0.1321 \cdot C_{T0} + P_z = 0.0964 \quad (5.4.5)$$

This yields $P_z = 0.129$. The two values obtained for P_z are different; this is because of the slight difference in the correlation coefficients in Figures 5.4.2 and 5.4.3. The values would have been identical if the correlation coefficients in both figures had been unity. Based on the correlation coefficients, Eq. (5.4.4) should be selected. However, Figure 5.4.3, which yields Eq. (5.4.5), contains one data point more than Figure 5.4.2, which yields Eq. (5.4.4). Thus, in correlating the stability gradient, we will consider both values of P_z, employing these two correlations:

1: $Z/k_BT = -0.1321 \cdot C_{T0} + 0.0553 \cdot R^a + 0.129$ (5.4.6)

2: $Z/k_BT = -0.1321 \cdot C_{T0} + 0.0553 \cdot R^a + 0.2256$ (5.4.7)

With either of these correlations for the value of Z/k_BT, at the synthesis temperature of 100 ^{0}C, the Case B model is fully predictive. We test the predictions of this model based on these two correlations in the following section.

5.4.3 Model validation

In this section, we test the model (Case B model) by comparing its predictions against the seed diameters resulting from the reaction conditions. Furthermore, we couple the model

with the growth process and test the predictions from the resulting model against the final diameters from the same reaction conditions. By the calculations relating to Figure 4.B.1 in Chapter 4, we observed that the growth process is absent at the beginning of the aggregation process. Furthermore in Chapter 4, we showed that the model predictions of the final mean diameter is sensitive to the value of the seed diameter. No matter how small the effect of growth is on particle size, coupling the aggregation process to the growth process at the beginning of the synthesis would yield poor predictions of the final mean diameter. To obtain good predictions of the latter, we couple the aggregation process to the growth process at a particular time. To determine this coupling time, we also report the characteristic times of the processes in the citrate synthesis method.

5.4.3.1 Seed size validation

For this model validation, we employ three initial conditions from the work of Ji et al. (2007) and two from the work of Zabatakis et al. (2012). For these experimental conditions, the initial citrate-to-gold molar ratios are equal to or greater than five, thereby satisfying the criterion for the synthesis model reported in Chapter 4. Thus, by an alternative method, that is, using the seed correlation reported in Chapter 4, we can calculate the seed diameter resulting from the aggregation process. These calculated seed diameters can then be employed to validate the fully predictive models (based on the two correlations for Z/k_BT) reported in the previous section. In the work of Ji et al. (2007), who kept the initial precursor concentration constant at $0.25\,mol/m^3$ and varied the citrate-to-gold ratio at the synthesis temperature 100 ^{0}C, we employ the ratios of 7.7, 10.5 and 17.8. On the other hand, in the work of Zabetakis et al. (2012), who kept the initial citrate-to-gold ratio constant at 5 and varied the initial precursor concentration at the synthesis temperature 100 ^{0}C, we employ the initial precursor concentrations of 0.6 and $1.2\,mol/m^3$. Using these initial conditions, we calculated the corresponding value of Z/k_BT from either correlation 1 (i.e. Eq. (5.4.6)) or correlation 2 (i.e. Eq. (5.4.7)), and then simulated the synthesis using case model B. Notice that these data were not part of the data set employed to derive the correlation for Z/k_BT in the previous section.

For the data of Zabetakis et al. (2012), Figure 5.4.4 shows how the mean diameter of the aggregating particles compares with the actual seed diameter reported previously in Chapter 4. For correlation 1 (see Figure 5.4.4A), by 500 s, the predicted mean sizes for the two data points have exceeded the actual sizes of the seed particles. The results also show the predicted mean sizes increase over time. By $10^5\,s$, the predicted mean sizes are about twice the values at 500 s. For the higher initial precursor concentration, where $C_{T0} = 1.2\,mol/m^3$,

Zabetakis et al. (2012) reported a final particle diameter (not the seed diameter) of $14.1\ nm$. By $10^4\ s$, the seed diameter in Figure 5.4.4A has exceeded the final particle diameter.

For the results from correlation 2 shown in Figure 5.4.4B, on the other hand, the predicted seed diameters are slightly smaller than the actual sizes by 500 s. Similar to Figure 5.4.4A, the results in Figure 5.4.4 B increase with time. However, the predicted seed mean diameters are smaller than those of Figure 5.4.4A. Furthermore, by $10^5\ s$, the predicted seed diameter for the higher initial precursor concentration is smaller than the final mean size of $14.1\ nm$. The constant value in calculating the stability gradient in correlation 1 (Eq. (5.4.6) is 0.129 while the constant value in correlation 2 (Eq. 5.4.7) is 0.2256. As the value of the stability gradient increases, the stable size decreases (as previously illustrated in Section 5.2).

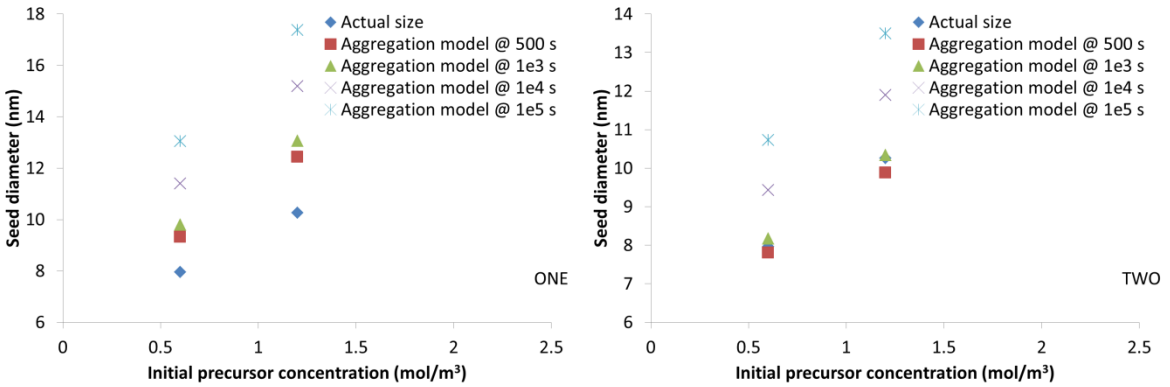

Figure 5.4.4 The model predictions of the seed diameter using Case B model. A: The predictions from correlation 1 in Eq. (5.4.6); B: The predictions from correlation 2 in Eq. (5.4.7). Two data sets are taken from the work of Zabetakis et al. (2012).

For the data of Ji et al. (2007), on the other hand, Figure 5.4.5 shows how the mean diameter of the aggregating particles compares with the actual seed diameter reported previously in Chapter 4 (Section 4.4.3). The behaviour of the model based on the correlations is similar to that discussed for Zabetakis et al. (2012). For the data of Zabetakis et al. (2012) and those of Ji et al. (2007), however, the predicted seed diameters from the model based on correlation 2 compare to the actual sizes better than those predicted from the model based on correlation 1.

One may conclude that correlation 2 in case model two yields better predictions than correlation 1, as the seed size predictions from the latter yielded sizes larger than the final mean diameter within the time considered. Nevertheless, we can observe that the predicted mean sizes from both correlations increase with time. Thus, it is possible that the predicted sizes of the model with either correlation could be larger than the final mean diameters as the synthesis time approaches infinity. However, in the citrate synthesis method, the growth process also affects the particle size distribution, increasing the size significantly in a time scale of about $10^3\ s$. To obtain this value, we calculated the characteristic times of the growth process. We also calculated those for the other processes. These calculations are presented in the following section.

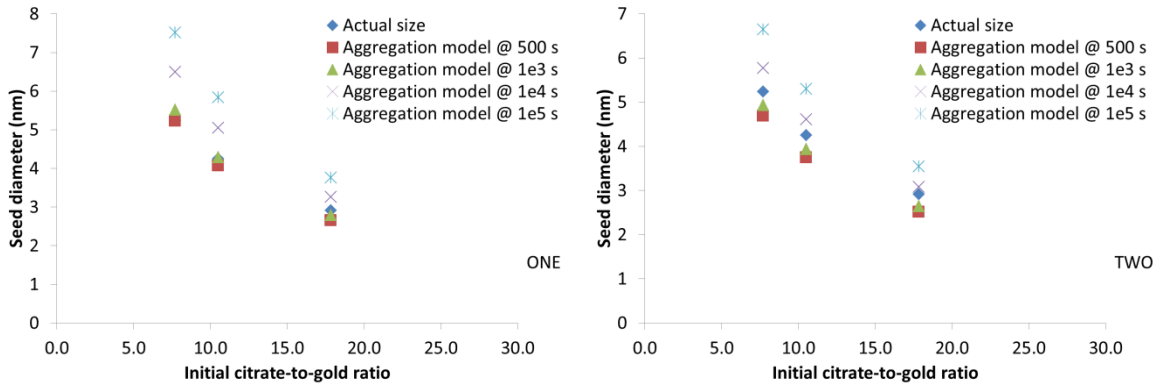

Figure 5.4.5 The model predictions of the seed diameter using case model B. A: the predictions from correlation 1 in Eq. (5.4.6); B: the predictions from correlation 2 in Eq. (5.4.7). Three data sets are taken from the work of Ji et al. (2007).

5.4.3.2 Characteristic times of the synthesis processes

We estimate the characteristic time for each of the reactions in the nanoparticles synthesis model for the citrate synthesis method to determine how the reactions progress relative to each other. We refer to Section 4.4.5 for these reactions. Also, we determine the characteristic time for the aggregation process. The characteristic time of a reaction indicates how long the reaction requires to convert a significant amount of the limiting reactant.

Precursor reduction reaction

After the synthesis solution has reached quasi-equilibrium, this reaction occurs between the precursor and CtH_2^-, producing gold atoms.

Considering the threshold initial molar ratio of citrate-to-gold of five, and assuming that $C_{T_0} = 0.3\ mol/m^3$, then $C_{C_0} = 1.5\ mol/m^3$. We can write:

$$\frac{dC_T}{dt} = -k_r C_T (y_x C_{Ct})^{1.85} = \{-k_r (y_x C_{Ct})^{1.85}\} C_T \tag{5.4.8}$$

The term in the parenthesis in Eq. (5.4.8) is approximately constant because citrate is in excess. For more details, we refer to Chapter 4. Thus, the characteristic time is equal to:

$$\tau_r \sim \frac{1}{k_r (y_x C_{Ct})^{1.85}} \tag{5.4.9}$$

At quasi-equilibrium, following the reasoning in Section 4.A.3 in Appendix E, this reaction condition yields $y_x = 2.353 \times 10^{-3}$. With $k_r = 35.48\ [m^3/mol]^{1.85}\ 1/s$. Thus, we have:

$$\tau_r \sim \frac{1}{35.48\ (2.353 \times 10^{-3} \times 1.5\ mol/m^3)^{1.85}} \sim 970\ s$$

This is the characteristic time for this reaction to convert the precursor by about 63 %. Experimentally, however, this reaction only consumes about 4.7 % of the precursor. To obtain this value, we used the ratio of the amount of the precursor in the seed particles to the amount of precursor in the final particles. In Section 4.5.2, we reported for this reaction condition the seed and final diameters as 6.75 and $18.70\ nm$, respectively. The percentage consumed in the reduction step would be $6.75^3/18.7^3\ \% = 4.7\%$.

We can therefore estimate the time for the reduction reaction to complete as

$$\frac{4.7\ \%}{63\ \%} \times 970\ s = 72.4\ s$$

This time is 2.4 times the time scale of $\sim 30\ s$ at 100 ^{0}C reported by Wuithschick et al. (2015) for this reaction. However, in the reaction condition of Wuithschick et al. (2015), only about 2 % of the precursor was consumed in the reduction step.

Precursor passivation reaction

This reaction converts the precursor to the passive form and occurs in parallel with the reduction reaction.

$$\frac{dC_T}{dt} = -k_p C_T C_B \tag{5.4.10}$$

Since the concentration of B (OH^-) remains almost constant in the course of the synthesis, we can write:

$$\tau_p \sim \frac{1}{k_p C_B} \tag{5.4.11}$$

Using the same reaction condition as above and following the reasoning in Section 4.2.4, $C_B = 3.43 \times 10^{-3}\ mol/m^3$ and $k_p = 6.1\, m^3/(mol.s)$. Thus:

$$\tau_p \sim \frac{1}{6.1 \times 3.43 \times 10^{-3}} \sim 48\ s \qquad (5.4.12)$$

This is the characteristic time for about 63 % of the precursor to convert to the passive form. Considering that 95.3 % of the precursor converts in this reaction, we can estimate the time for this reaction to complete as:

$$\frac{95.3\ \%}{63\ \%} \times 48\ s = 73\ s$$

This time is approximately equal to the characteristic time for the reduction step calculated above.

Seed growth step

We calculate the seed number density as:

$$\frac{C_{T0}}{\rho m_v {s_f}^3} = \frac{0.3}{10^5(\pi/6)(18.7 \times 10^{-9})^3} = 8.76 \times 10^{17}\ 1/m^3$$

Assuming that the seed formation and growth steps are fully decoupled, the particle number density can be taken equal to $8.76 \times 10^{17}\ 1/m^3$. So, we can estimate the order of magnitude of the particle surface per unit volume of physical space as follows:

$$\int_{s_s}^{\infty} s^2 f(s,t) ds \sim (6.75 \times 10^{-9})^2 \times 8.76 \times 10^{17} = 39.91\, m^2/m^3$$

We can then write:

$$\frac{dC_K}{dt} = -\left[m_a k_g (y_y C_{Ct}) \int_{s_s}^{\infty} s^2 f(s,t) ds\right] C_K \qquad (5.4.13)$$

As previously mentioned, since citrate is in excess, all the terms in bracket are approximately constant. In the reaction condition, $k_g = 5.25 \times 10^{-6}\, m^4/(mol.s)$, $y_y = 0.196$, $C_{Ct} = 1.5\ mol/m^3$.

Therefore, the reaction is first-order and the characteristic time is:

$$\tau_{h1} \sim \frac{1}{m_a k_g (y_y C_{Ct}) \int_{s_s}^{\infty} s^2 f(s,t) ds} = \frac{1}{\pi \times 5.25 \times 10^{-6} \times 0.196 \times 1.5\ \times 39.91} s = \ 5{,}167\ s$$

In the above, we assumed the total surface area as that of the seed particles. However, with time, this total surface area increases and would reduce τ_{h1}. If we calculate the time scale based on the final size, which is 18.70 nm, we have:

$$\int_{s_s}^{\infty} s^2 f(s,t) ds \sim (18.70 \times 10^{-9})^2 \times 8.76 \times 10^{17} = 306.33\, m^2/m^3$$

so that $\tau_{h2} = 673\, s$. Thus, the growth process starts slowly with a time constant of $5167\, s$ and ends with a time constant of $673\, s$. These orders of characteristic times of the growth process explain why the citrate synthesis method completes in a synthesis time of about $10^3\, s$.

Aggregation characteristic time

NPs are most likely to aggregate when their concentration is the highest. To estimate the characteristic time of the aggregation process, we consider the scenario where the aggregation rate is at its maximum value. In this scenario, all the gold atoms form before aggregating.

According to Marchisio & Fox (2013) and as reported in Chapter 3, the aggregation characteristic time is given by:

$$\tau_a \sim \frac{W}{\tilde{\omega}_A(s_0,s_0) N_c} \tag{5.4.14}$$

Here N_c is the number of gold atoms of size s_0 in the system. At this size, $E_{agg} = 0$ and W is the minimum, calculated using Eq. (5.2.6) as:

$$W(\bar{s},\hat{s}) = \frac{\kappa(\bar{s}+\hat{s})}{2} \exp\left[{E_{agg}(\bar{s},\hat{s})}\Big/{k_B T} \right] = \kappa \times 2.72 \times 10^{-10}$$

where:

$$1/\kappa = \left[\frac{\epsilon_0 \epsilon_c k_B T}{(4.p_{CtH^{2-}} e^2 + 9.p_{Ct^{3-}} e^2)}\right]^{1/2} = \frac{1}{e}\left[\frac{\epsilon_0 \epsilon_c k_B T}{(4.p_{CtH^{2-}} + 9.p_{Ct^{3-}})}\right]^{1/2}$$

$$= \frac{1}{1.6 \times 10^{-19}}\left[\frac{8.85 \times 10^{-12} \times 55.3 \times 1.38 \times 10^{-23} \times 373}{(4 \times 1.26 \times 10^{23} + 9 \times 5.06 \times 10^{23})}\right]^{1/2}$$

$$= 4.41 \times 10^{-9}\, nm$$

Thus:

$$W(\bar{s},\hat{s}) = \frac{2.72\times10^{-10}}{4.41\times10^{-9}} = 0.06$$

This number is below 1, the value of W for fast aggregation. At the atomic level, in addition to the Brownian motion, the Van der Waals' forces of attraction cause aggregation.

At the conditions at which the synthesis is conducted, $T = 373\,K$, $\rho = 10^5\,mol/m^3$ and $\mu = 2.74\times10^{-4}\ kg/(m.s)$. Since $K_B = 1.38\times10^{-23}\ J/K$, Eq. (5.2.2) gives:

$$\widetilde{\omega}_A(\bar{s},\hat{s}) = \frac{2k_BT}{3\mu}\left(\frac{1}{\bar{s}}+\frac{1}{\hat{s}}\right)(\bar{s}+\hat{s}) = \frac{8K_BT}{3\mu} = 5\times10^{-17}\ m^3/s$$

The number of atoms per unit volume of physical space that would form before aggregation starts taking place if the precursor reduction reaction went to completion is equal to:

$$N_{c,max} = 4.7\ \%\ \frac{C_{T_0}}{\rho m_v {s_0}^3} \qquad (5.4.15)$$

As seen above, we have included the percentage yield of the precursor reduction step. Therefore, it is:

$$4.7\ \%\ \frac{0.3}{10^5(\pi/6)(2.72\times10^{-10})^3} = 1.34\times10^{22}\,1/m^3$$

Thus, replacing these results in Eq. (5.4.14), we obtain:

$$\tau_a \sim \frac{0.06}{5\times10^{-17}\times1.34\times10^{22}} = 8.96\times10^{-8}\,s\ \approx\ 10^{-9}\,s$$

This is the characteristic time of the aggregation process for the initial conditions used in the synthesis. It gives an estimate of the time required by aggregation to take place significantly. In the simulation in Parsival for this reaction condition, we noticed the number concentration decreased from $1.34\times10^{22}\,1/m^3$ to $7.72\times10^{21}\,1/m^3$ in $2.35\times10^{-7}\,s$.

5.4.3.3 Coupling aggregation and growth

With the significant size increase from growth at about $10^3\,s$, the effect of aggregation would decrease significantly because $E_{agg}(\bar{s};\hat{s})$ in Eq. (5.2.16) increases with size. Then, the value of W diverges thus stabilizing the particles from further aggregation.

To illustrate this decreasing effect of aggregation with time, we simulate only the aggregation model for a simulation time of $t = 500\,s$. Thereafter, we couple the aggregation and growth process. By this coupling at $t = 500\,s$, we allow both the aggregation and growth processes to influence the PSD. We do not couple the two processes at $t = 0\,s$ because in deriving the

synthesis model in Section 4.4, we assumed that the growth is absent in the seed formation step, that is in the early part of the aggregation process.

In the growth process, the passive precursor $AuCl_3(OH)^-$ reacts on the surface, growing the particles and changing the particle size distribution (see Chapter 4). Following the reasoning in Section 5.3 (Case B model), we calculate the amount of $AuCl_3(OH)^-$ that grows the particles as:

$$C_{T0}(1 - L_d).V \tag{5.4.16}$$

This amount affects the PSD as the growth process according to:

$$-\partial_s[f(s,t).G_s] \tag{5.4.17}$$

where:

$$G_s = \left(\frac{m_a}{3\rho m_v}\right) k_g \, C_K(y_y C_{Ct}) \tag{5.4.18}$$

Here G_s is the particle growth rate, previously reported in Chapter 4.

$k_g = 5.25 \times 10^{-6}\, m^4/(mol.s)$ and y_y is the relative mole fraction of CtH^{2-} in the citrate species.

Also, m_a is the particle area shape factor (which we set equal to π, assuming that the particles are spherical), ρ is the molar density of gold, taken to be $10^5\ mol/m^3$ (Kumar et al., 2007) and m_v is the particle volume shape factor (which we set equal to $\pi/6$, assuming that the particles are spherical). See Section 4.4.3 for the derivation of Eqs (5.4.17) and (5.4.18).

After simulating Case B model (based on either correlation 1 or 2) for $t = 500$, we couple the growth model with the case model so that at $t \geq 500\, s$ both the aggregation and growth processes influence the particles size distribution. We then simulate for total times of 10^4 and $10^5\ s$, that is simulating the coupled model for $9500\ s$ and $99500\ s$, respectively.

For the data of Zabetakis et al. (2012), Figure 5.4.6 shows how the mean diameter of the particles compares with the final mean diameter obtained experimentally. This figure shows that the sizes at 10^4 and $10^5\ s$ are identical. By $10^4\ s$, the growth process has vanished as the driving force (that is, the concentration of $AuCl_3(OH)^-$) is depleted. Also, beyond $10^4\ s$, we can conclude that the aggregation process is absent in the model (for both correlations).

Similarly, we can observe that the predictions agree excellently (that is, they overlap) with the experimental data.

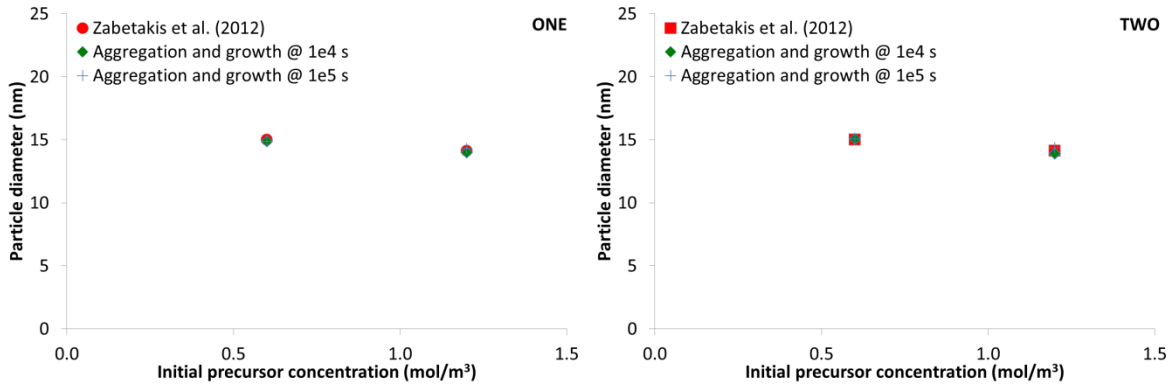

Figure 5.4.6 The predictions of the final diameter using case model B. A represents correlation 1 in Eq. (5.4.6) while B represents correlation 2 in Eq. (5.4.7). Two data sets are taken from the work of Zabetakis et al. (2012).

For the data of Ji et al. (2007), Figure 5.4.7 shows how the mean diameter of the particles compares with the final mean diameter obtained experimentally. As above, beyond the simulation time of $10^4\ s$ both the aggregation and growth processes are absent. However, it is only in the model based on correlation 1 that the predicted mean diameters overlap those obtained experimentally although the predicted diameters from the model based on correlation 2 are also good. The slight deviation in the latter is due to the value of the constant in calculating the stability gradient in Eq. (5.4.7), which is 0.2256 compared to 0.129 in Eq. (5.4.6) for the former. As the stability gradient increases, the particle size resulting from the aggregation process decreases (Eq. (5.2.17) when combined with Eq. (5.2.1) illustrates this relationship). Particles do not aggregate significantly, resulting in a large number of particles. Since the same amount of $AuCl_3(OH)^-$) is available in the model for both correlations, the particles from correlation 1 grow to slightly smaller size than those correlation 2.

This figure shows that the sizes at 10^4 and $10^5\ s$ are identical. By $10^4\ s$, the growth process has vanished as the driving force (that is, the concentration of $AuCl_3(OH)^-$) is depleted. Also, beyond $10^4\ s$, we can conclude that the aggregation process is absent in the model (for both correlations). Similarly, we can observe that the predictions agree excellently with the experimental data.

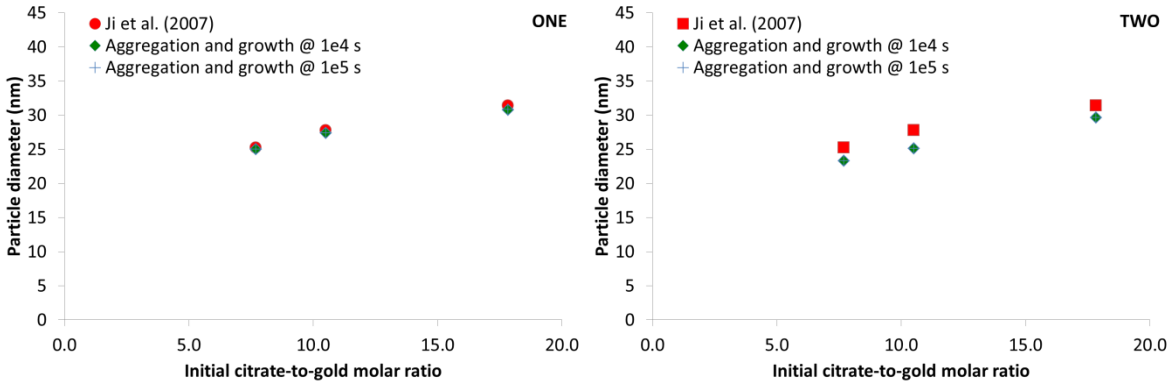

Figure 5.4.7 The predictions of the final diameter using case model B. A represents correlation 1 in Eq. (5.4.6) while B represents correlation 2 in Eq. (5.4.7). Three data sets are taken from the work of Ji et al. (2007).

5.5 Concluding remarks

In this chapter, we presented a new mathematical model for the aggregation process in nanoparticle synthesis. This model accounts for the stabilization of the colloidal system by electrostatic repulsion and is based on the theory proposed by Polte (2015) that the energy barrier increases with size. To investigate the model, because the aggregation process occurs alongside other processes, we employ the citrate synthesis method. This synthesis method involves reactions, nucleation, aggregation and growth. In addition, the seed size resulting from the aggregation process in this synthesis method has been previously reported.

In this chapter, we described the synthesis model using two case models: 1) case model A assumes the aggregation process is coupled with the reactions and nucleation and 2) case model B assumes the aggregation process is fully decoupled from other processes. From the model validation, we showed that the citrate synthesis method evolves by decoupling the aggregation process that forms the seed particles from other processes.

Furthermore, we developed two correlations for the profile of energy barrier with size, reported as the stability gradient, to make case model B fully predictive and then validated the predictions using the seed size reported previously. At a particular time, the model predictions agree with the seed size. However, the predicted seed size increases thereafter with time.

To test the stability of the particles to aggregation, we coupled it with the growth process. We found that the particles are stable to aggregation within the characteristic time of the synthesis. Furthermore, Case B model (based on either correlation 1 or correlation 2) yielded excellent results. Thus, either correlation may be used in describing the citrate synthesis method.

Chapter 6

Conclusions and future work

This Ph.D. work presented the mathematical modelling of the formation of gold nanoparticles by the citrate synthesis method. After reviewing the literature for various experimental investigations of this synthesis method, we adopted the population balance approach to model it. Then, we investigated the mathematical model developed by Kumar et al. (2007) for the synthesis of gold nanoparticles by means of the citrate method. This is the only model, based on any mechanistic theory (that is, the Turkevich organizer theory), available in the literature. The model accounts for five reaction steps, one of which produces dicarboxy acetone, which organizes gold in the nucleation step. While DCA decomposes, the particles grow by the deposition of the residual precursor on their surfaces. GNPs evolve by the nucleation-growth mechanism, as proposed by Turkevich et al. (1951). Although Kumar et al. (2007) included a submodel for aggregation, this submodel does not play a significant role over the synthesis time.

Furthermore, we tested the model developed by Kumar et al. for different conditions of temperature, concentrations and pH using various experimental data from the literature. The model performed poorly in describing the synthesis. We believe that this is because the five chemical steps over which the model of Kumar et al. is built do not reflect the chemistry of the synthesis accurately. Because the precursor and reducing agent are a strong acid and a weak base, respectively, their acid-base properties cover an important role in the synthesis. As a weak base, the reducing agent releases OH^- in water. The precursor, on the other hand, can be reduced and/or hydroxylated. Kumar et al. only modelled the reduction step that produces the nuclei but did not consider the hydroxylation step. Subsequently, these nuclei aggregate into seeds, which then grow by reacting with the hydroxylated precursor. Using the seed-mediated mechanism proposed by Wuithschick et al. (2015), we were able to qualitatively explain the experimental data reported by the researchers.

Thereafter, we presented a new mathematical model for the description of the synthesis of gold nanoparticles via the citrate synthesis method. This method involves reducing tetrachloroauric acid with sodium citrate in an aqueous medium. In this medium, the precursor and reducing agent can exist in various forms by reacting with OH^- and H^+, respectively. Furthermore, the system features several reactions and processes that occur in series and in parallel. Using the seed-mediated mechanism proposed by Wuithschick et al.

(2015), we reported the steps describing the evolution of GNPs in the synthesis. Subsequently, we derived rate equations for the reactions involved in the reduction, passivation and growth steps, and proposed a method of calculating the seed diameter in the seed formation step. Then, we reported the synthesis model that describes how the components evolve with time, assuming that the pH value of the reaction mixture is constantly equal to its quasi-equilibrium value.

Then, we solved the model for experimental conditions satisfying the criterion of initial values of the citrate-to-gold molar ratio equal to or greater than five. In this model, seed particles first form and then GNPs evolve from them. To determine the size of the seeds, we derived a correlation based on the initial conditions of the synthesis. We illustrated that the model predictions are sensitive to the value employed for the seed size. In the cases investigated, the model predictions agreed very well with the experimental data. In most of these cases, the growth process overrides the seed formation process in determining the final particle size; the more the amount of gold that passivates, the larger the final particle size is. At low pH values, nonetheless, we saw that seed sizes are larger, since the aggregation process is more vigorous.

This work also, in Chapter 5, presented a new mathematical model for the aggregation process in nanoparticle synthesis. This model accounts for the stabilization of the colloidal system by electrostatic repulsion and is based on the theory proposed by Polte (2015) that the energy barrier increases with size. To close the model, we require a value for the initial steepness of the profile of energy barrier and size. To investigate the model, because the aggregation process occurs alongside other processes, we employ the citrate synthesis method. This synthesis method involves reactions, nucleation, aggregation and growth. In addition, the size resulting from the aggregation process in this synthesis method has been previously reported.

Also in Chapter 5, we described the synthesis using two case models: 1) case model A assumes the aggregation process is coupled with the reactions and nucleation and 2) case model B assumes the aggregation process is fully decoupled from other processes. From the model validation, we showed that the citrate synthesis method evolves by decoupling the aggregation process from other processes (case model B).

Furthermore, we developed a correlation for the stability gradient to make case model B fully predictive and then validated it using experimental data. The model predictions agree reasonably with the experimental data.

With this aggregation model, we will be able to investigate the citrate synthesis method for initial citrate-to-gold ratios smaller than five at the synthesis temperature of 100 ^{0}C and other synthesis temperatures.

6.1 Future work

In Chapter 4, in order to make the nanoparticle synthesis model fully predictive, we derived a correlation for the seed diameter in the seed-mediated mechanism. The correlation, however, is only valid at the synthesis temperature of 100 ^{0}C. We would like to extend its validity and that of the whole synthesis model to other temperatures. To do this, we would need the rate constants of the reactions in the synthesis model (that is, the precursor reduction and passivation steps, and the seed growth step). For both the precursor passivation and seed growth steps, we have calculated their Arrhenius parameters (that is, activation energies and pre-exponential factors) in Chapter 4. Thus, we can calculate their rate constants at other temperatures. However, for the precursor reduction step, we need kinetic data such as those presented in Section 4.3.1 at other temperatures (at least at two other temperatures). Then, we follow the procedure in Section 4.3.1 to calculate the rate constant at these temperatures. Along with the value of the rate constant calculated in this Ph.D. work, we will calculate the Arrhenius parameters for the reduction step and hence its rate constant at any other temperature. Thereafter, we follow the procedure discussed in Section 4.4.2 to obtain the seed correlation and hence a predictive synthesis model for gold nanoparticles in the citrate synthesis conducted at other temperatures.

In developing the nanoparticle synthesis model in Section 4.3.5, we focused on experimental data whose initial molar citrate-to-gold ratios are greater than or equal to five. For these ratios, we assumed the pH value of the synthesis mixture at quasi-equilibrium is equal to the pH value at final equilibrium. Thus, we did not account for the reactions involving H^+. Past authors such as Turkevich et al. (1951) and Frens (1973) have investigated the synthesis at citrate-to-gold ratios below five. For these ratios, however, we need to account for the reactions involving H^+ because the pH value of the synthesis mixture at quasi-equilibrium is not equal to the pH value at final equilibrium. For these ratios as well, the final synthesis mixture contains considerably polydisperse gold nanoparticles, reported in the literature to follow a mechanism different from the seed-mediated mechanism. Nevertheless, the various reactions and processes such as nucleation (formation of gold atoms), aggregation, and growth described in the thesis influence the dynamics of the synthesis mixture and that of gold nanoparticles. For the reactions involving H^+, in the forward step, we would base their rates on the time scale of $\sim 10^{-11}\ s$, reported by Pines et al. (1997) for reactions involving H^+ ions to reach completion at 23 ^{0}C. In the backward step, we would use their equilibrium

constants to obtain the kinetic rate constants. Then, we derive rate models for these reactions. These rate models along with the synthesis and aggregation models developed in the work would be able to describe the synthesis at all ratios.

We would also like to improve the aggregation sub-model. As revealed in Chapter 5, we derived a correlation for the stability gradient based on the initial condition of the synthesis. However, it should be based on the prevailing process condition, which changes with time as the concentrations of particles and reactants change. We would like to account for the effect of the changing dynamics on the stability gradient.

Finally, we hope to integrate the synthesis model with fluid dynamics. We aim to derive, implement and validate a more advanced model able to account for the fluid dynamics. This would no longer be based on the assumption that the system is perfectly mixed.

References

1. Abid, J. P., 2003. Laser Induced Synthesis and Nonlinear Optical Properties of Metal Nanoparticles, Ph.D. Thesis, Ecole Polytechnique Federale de Lausanne, Lausanne, Switzerland.
2. Agunloye, E., Gavriilidis, A., Mazzei, L., 2017. A Mathematical Investigation of the Turkevich Organizer Theory in the Citrate Method for the Synthesis of Gold Nanoparticles, Chemical Engineering Science. http://dx.doi.org/10.1016/j.ces.2017.07.032.
3. Agunloye, E., Panariello, L., Gavriilidis, A., Mazzei, L., 2018. A Model for the Formation of Gold Nanoparticles in the Citrate Method, Chemical Engineering Science, *Chemical Engineering Science, 173*, 275-286. doi:10.1016/j.ces.2018.06.046
4. Agunloye, E., Gavriilidis, A., & Mazzei, L., 2017. A mathematical investigation of the Turkevich organizer theory in the citrate method for the synthesis of gold nanoparticles. *19th International Conference on Nanoparticles*.
5. Alkilany, A. M., and Murphy, C. J., 2010. Toxicity and cellular uptake of gold nanoparticles: what we have learned so far?, J Nanopart Res, 12(7): 2313–2333, doi: 10.1007/s11051-010-9911-8.
6. ANUI (2012) Apply nanotech to up industrial, agri output. The Daily Star (Bangladesh). http://www.thedailystar.net/newDesign/news-details.php?nid=230436
7. Barron, J. J., Ashton, C., Geary, L., 2006. The Effects of Temperature on pH Measurement, County Clare, Ireland. https://reagecon.com.
8. Belloni, J.; Mostafavi, M.; Remita, H.; Marignier, J. L.; Delcourt, A. M. O. (1998). "Radiation-induced synthesis of mono- and multi-metallic clusters and nanocolloids". New Journal of Chemistry. 22 (11): 1239–1255. doi:10.1039/A801445K
9. Biggs, S., Chow, M. K., Zukoski, C. F., and Grieser, F., 1993. The Role of Colloidal Stability in the Formation of Gold Sols, *J. Colloid Interface Sci.* 160, 511.
10. Bogush, G.H., Zukoski IV, C.F., 1991. Uniform silica particle precipitation: An aggregative growth model, J. Colloid Interface Sci. 142 19–34. doi:10.1016/0021-9797(91)90030-C.
11. Boulos, M., I., 1991. Thermal plasma processing; Plasma Sci IEEE Trans, 19 (6) pp. 1078–1089
12. Chakraborty, A., Chakraborty, S., Chaudhuri, B., Bhattacharjee, S., 2016. Process Engineering Studies on Gold Nanoparticle Formation via Dynamic Spectroscopic Approach, Gold Bull, 49: 75. doi:10.1007/s13404-016-0183-7.
13. Chow, M.; Zukoski, C., 1994. Gold Sol Formation Mechanisms: Role of Colloidal Stability. J. Colloid Interface Sci., 165, 97 -109.
14. Clarence S. Yah., 2013. The toxicity of Gold Nanoparticles in relation to their physiochemical properties, Biomedical Research, Volume 24, Issue 3
15. Cordero, B.; Gómez, V.; Ana E. Platero-Prats; Marc Revés; Jorge Echeverría; Eduard Cremades; Flavia Barragán; Santiago Alvarez (2008). "Covalent Radii Revisited". Dalton Trans. (21): 2832–2838. doi:10.1039/b801115j.
16. Corma, A., and Garcia, H., 2008. Supported Gold Nanoparticles as Catalysts for Organic Reactions, *Chem. Soc. Rev.***,** 37, 2096-2126 doi: 10.1039/B707314N.
17. Cussler, E.L., 2009. *Diffusion: Mass Transfer in Fluid Systems,* 3rd ed., Cambridge University Press. doi:10.1017/CBO9780511805134.010. ISBN 9780521871211
18. Daniel, M., and Astruc, D., 2004. Gold Nanoparticles: Assembly, Supramolecular Chemistry, Quantum-Size-Related Properties, and Applications toward Biology, Catalysis, and Nanotechnology; *Chem. Rev. 104,* 293-346.
19. Davies, A. The Kinetics of the Coagulation of Gold Sols. *J. Phys.Chem.* **1929**, *33*, 274.

20. Derjaguin, B., and Landau, L., 1941. Theory of the stability of strongly charged lyophobic sols and of the adhesion of strongly charged particles in solutions of electrolytes, Prog. Surf. Sci., 43, 30–59, DOI: 10.1016/0079-6816(93)90013-L.
21. Debye, P., J., W., 1954. The Collected Papers of Peter J. W. Debye. New York, New York: Interscience Publishers, Inc.
22. Dreaden, E. C., Austin, L. A., Mackey, M. A., El-Sayed, M. A., 2012. Size Matters: Gold Nanoparticles in Targeted Cancer Drug Delivery, Ther Deliv., 3:457–478. doi: 10.4155/tde.12.21.
23. Dreifuss, T., Betzer, O., Shilo, M., Popovtzer, A., Motieia, M. and Popovtzer, R. 2015. A challenge for theranostics: is the optimal particle for therapy also optimal for diagnostics? Nanoscale, 7, 15175.
24. Elimelech, M. Gregory, J. Jia, X. Williams. R.A., 1995. Particle Deposition and Aggregation - Measurement, Modelling and Simulation. Elsevier. Online version available at: http://app.knovel.com/hotlink/toc/id:kpPDAMMS01/particle-deposition-aggregation/particle-deposition-aggregation
25. Evans, W. L., and Sefton, L. B 1922. The Oxidation Of Isopropyl Alcohol With Potassium Permanganate, *J. Am. Chem. Soc.*, 1922, *44* (10), pp 2271–2276 DOI: 10.1021/ja01431a024
26. Faraday, M., 1857. Philosophical Transactions of the Royal Society, London.
27. Faraday, M., 1857. "Experimental Relations of Gold (and Other Metals) to Light,". Philosophical Transactions of the Royal Society. 147: 145. doi:10.1098/rstl.1857.0011.
28. Feynman, R. P., 1959. "Plenty of Room at the Bottom", web.pa.msu.edu/people/yang/RFeynman_plentySpace. Retrieved 2018-05-30.
29. Fogler, H. S., 2004. Elements of Chemical Reaction Engineering, Prentice -Hall, Upper Saddle, New Jersey.
30. Freestone, I., Meeks, N., Sax, M., Higgitt, C., 2007. "The Lycurgus Cup — A Roman nanotechnology". Gold Bulletin. 40 (4): 270–277. doi:10.1007/BF03215599. ISSN 0017-1557.
31. Frens, G., 1973. Controlled Nucleation for the Regulation of the Particle Size in Monodisperse Gold Suspensions. *Nature*, *241*, 20.
32. Freund, P.; Spiro, M., 1985 Colloidal Catalysis: The Effect of Sol Sizeand concentration. *J. Phys. Chem. 89*, 1074.
33. Fuchs, N. A., 1964, “The Mechanics of Aerosols”, Pergamon, New York.
34. Giasuddin, A.S.M., Jhuma, K. A., Mujibul Haq, A. M., 2012. Use of Gold Nanoparticles in Diagnostics, Surgery and Medicine: A Review ASM Bangladesh Journal of Medical Biochemistry ISS N: 2073-9915
35. Gimeno, M. C. 2008. The Chemistry of Gold. In: Laguna, A. ed. Modern Supramolecular Gold Chemistry: Gold-Metal Interactions and Applications. Wienheim Wiley pp 1-50
36. Goia, D. V.; Matijevic, E., 1999. Tailoring the particle size of monodispersed colloidal gold, *Colloids Surf. A*, 146, 139– 152
37. Grosch, R; Briesen, H; Getting Started with Parsival – A Tutorial Introduction; CiT GmbH, **2005**.
38. Gutierrez, C., 2005. The Commerce Department’s Fiscal Year 2006 Budget, Department of Commerce, United States of America, https://www.legislative.noaa.gov/Testimony/gutierrez052605.pdf
39. Haiss, W., Thanh, N. T. K., Aveyard, J., and Fernig, D. G., 2007. Determination of Size and Concentration of Gold Nanoparticles from UV-Vis Spectra, Anal. Chem., 79, 4215-4221, 10.1021/ac0702084

40. Hanes, G., Koeber, K., Kreuzbichler, I. Neu-Becker, U., Schwager, B., 1992. Gmelin Handbook of Inorganic and Organometalic Chemistry (8 ed.) Au Gold Supplement Vol. B1, Springer-Verlag, Berlin.
41. Hashmi, A. S. K., and Hutchings, G. J., 2006. Gold Catalysis; Angew. Chem. Int. Ed., 45, 7896 – 7936; DOI: 10.1002/anie.200602454
42. Hauser, E., A., Lynn, J., E., 1940. Experiments in Colloid Chemistry; McGraw-Hill: New York.
43. Hendel, T.; Wuithschick, M.; Kettemann, F.; Birnbaum, A.; Rademann, K.; Polte, J., 2014. In Situ Determination of Colloidal Gold Concentrations with UV-Vis Spectroscopy: Limitations and Perspectives. Anal. Chem., 86 (22), 11115−11124.
44. Himmel, D., Goll S. K., Leito, I., Krosing, I., 2010. A Unified pH Scale for All Phases, *Angew. Chem. Int. Ed.* **49** (38): 6885-6888. doi: 10.1002/anie.201000252.
45. Hornberger, G. and Wiberg, P., 2005. Numerical Methods in the Hydrological Sciences-Numerical Methods for Solving First-Order Ordinary Differential Equations, the American Geophysical Union, Washington DC.
46. Huang, H., Du Toit, H., Panariello, L., Mazzei, L., & Gavriilidis, A. (2018). Continuous Synthesis of Gold Nanoparticles in Micro- and Milli-fluidic Systems. In C. Kumar (Ed.), *Chemistry of Nanomaterials - A Practical Guide* (pp. 1-60). De Gruyter.
47. Hunter, R., 1995. *Foundations of colloid science, Vol. 1*; Clarendon Press: Oxford, U.K., Chapter 7, pp 441-447
48. Hvolbæk, B., Janssens, T. V., Clausen, B. S., Falsig, H., Christensen, C. H., Nørskov, J. K., 2007. Catalytic activity of Au nanoparticles, Nano Today 2, 14–18.
49. Israelachvili, J. N., 2011. Intermolecular *and* surface forces, 3rd edition, Academic Press, Burlinton, MA.
50. Ji, X. H., Song, X. N., Li, J., Bai, Y. B., Yang, W. S., Peng, X. G., 2007. Size Control of Gold Nanocrystals in Citrate Reduction: The Third Role of Citrate, J. Am. Chem. Soc., 129, 13939.
51. Jones, A. G., 2002. Crystallization Process Systems, Butterworth-Heinemann, Oxford.
52. Jones, A.G., and Mullin, J.W., 1974. Programmed cooling crystallization of potassium sulphate solutions Chem. Eng. Sci., 29, pp. 105–118
53. Kettemann, F., Birnbaum, A., Witte, S., Wuithschick, M., Pinna, N., Kraehnert, R., Rademann, K., Polte, J., 2016. Missing Piece of the Mechanism of the Turkevich Method: The Critical Role of Citrate Protonation, Chem. Mater. (11), 4072-4081, DOI: 10.1021/acs.chemmater.6b01796.
54. Kreyzig, E., 1999. Advanced Engineering Mathematics, 8th edition, Wiley, London.
55. Kumar, S., Kumar, R., Gandhi, K. S., 2007. Modeling of Formation of Gold Nanoparticles by Citrate Method. Ind. Eng. Chem. Res., 46, 3128-3136, DOI: 10.1021/ie060672j
56. Lane, L. A., Qian, X., and Nie, S., 2015. SERS Nanoparticles in Medicine: From Label-Free Detection to Spectroscopic Tagging *Chem. Rev.*, 115 (19), pp 10489–10529 DOI: 10.1021/acs.chemrev.5b00265
57. Lazzari, S., Abolhasani, M., Jensen, K.F., 2017. Modeling of the formation kinetics and size distribution evolution of II-VI Quantum Dots, React. Chem. Eng. doi:10.1039/C7RE00068E.
58. Leonhardt, U., 2007. Invisibility Cup, Optical Metalmaterials, Nature Photonics, Vol 1, www.nature.com/naturephotonics
59. Li, C., Li, D., Wan, G., Xu, J., and Hou, W., 2011. “Facile synthesis of concentrated gold nanoparticles with low size-distribution in water: temperature and pH control”, Nanoscale Research Letters, vol. 6, p.440
60. Liu, H., Li, J., Sun, D., Odoom-Wubah, T., Huang, J., Li, Q, 2014. Modeling of Silver Nanoparticle Formation in a Microreactor: Reaction Kinetics Coupled with Population Balance Model Fluid Dynamics. Ind. Eng. Chem. Res. 53, 4263.
61. Liveri, V. T., 2006. Controlled Synthesis of Nanoparticles in Microheterogeneous Systems, Nanostructure Science and Technology, Springer Science.

62. Majumder, D., D., Banerjee, R., Ch Ulrichs, I. M., Goswami, A., 2007. Nano-materials: Science of bottom-up and top-down, IETE Technical Review, Vol 24, No 1, January-February, pp 9-25
63. Marchisio, D. L., Fox, R. O., 2013. Computational Models for Polydisperse Particulate and Multiphase Systems, Cambridge University Press, New York.
64. Matias, A.S., Carlos, F.F., Pedrosa, P., Fernandes, A.R., Baptista, P.V., 2017. Gold Nanoparticles in Molecular Diagnostics and Molecular Therapeutics, in: Rai, M., Shegokar, R. (Eds), Metal Nanoparticles in Pharma, Springer, New York, pp. 365 – 387.
65. Mellor J. W., 1946. A comprehensive treatise on inorganic and theoretical chemistry. Vol. 3, pp. 593.
66. Mersmann, A., 2001. Crystallization Technology Handbook, second ed., Dekker, New York.
67. Mironov I.V., Makotchenko E.V., 2009. The Hydrolysis of AuCl4 and the stability of aquachloro hydroxo complexes of gold(III) in aqueous solution, J. Solution. Chem. 38, 725–737
68. Mullin, J. W., 2001. Crystallization, 4th Edition, Butterworth-Heinemann, Oxford.
69. Ojea-Jiménez, I., Campanera, J. M., 2012. Molecular Modeling of the Reduction Mechanism in the Citrate-Mediated Synthesis of Gold Nanoparticles. J. Phys. Chem. C, 116, 23682–23691. dx.doi.org/10.1021/jp305830p
70. Pacławski, K., Streszewski, B., Jaworski, W., Luty-Błocho, M., Fitzner, K., 2012, Gold Nanoparticles Formation via Gold(III) Chloride Complex Ions Reduction with Glucose in the Batch and in the Flow Microreactor Systems; Colloids and Surfaces A: Physicochem. Eng. Aspects 413, 208– 215, doi:10.1016/j.colsurfa.2012.02.050
71. Peck, J. A., Tait, C. D., Swanson, B. I., Brown, G. E., 1991. Speciation of Aqueous Gold(III) Chlorides from Ultraviolet/Visible Absorption and Raman/Resonance Raman spectroscopies, Jr. Geochim. Cosmochim. Acta, 55, 671-676.
72. Pines, E., Magnes, B.-Z., Lang, M.J., Fleming, G.R., 1997. Direct Measurement of Intrinsic Proton Transfer Rates in Diffusion-controlled Reactions. Chem. Phys. Lett. 281 (4–6), 413–420.
73. Polte, J., Ahner, T. T., Delissen, F., Sokolov, S., Emmerling, F.; Thünemann, A. F.; Kraehnert, R., 2010. Mechanism of Gold Nanoparticle Formation in the Classical Citrate Synthesis Method Derived from Coupled In Situ XANES and SAXS Evaluation. J. Am. Chem. Soc., 132, 1296–1301
74. Pong, B-K, Elim, H., I., Chong, J-X, Ji, W., Trout, B., L., and Lee, J-Y, 2007. New Insights on the Nanoparticle Growth Mechanism in the Citrate Reduction of Gold(III) Salt: Formation of the Au Nanowire Intermediate and Its Nonlinear Optical Properties, J. Phys. Chem. C 2007, 111, 6281-6287 DOI: 10.1021/jp068666o
75. Porter, A. L., and Youtie, J., 2009. How interdisciplinary is nanotechnology? J Nanopart Res 11:1023–1041 DOI 10.1007/s11051-009-9607-0
76. Ramkrishna, D., 2000. Population Balances. Academic Press, New York.
77. Ranade, V. V., 2002. Computational Flow Modeling for Chemical Reactor Engineering, Academic Press, London.
78. Randolph, A. D. and Larson, M. A. 2001. Theory of particulate processes. Academic Press
79. Reddy, V. R., 2006. Gold Nanoparticles: Synthesis and Applications, Thieme eJournals, Vol., No. 11, pp. *1791*-1792.
80. Reerink, H., and Overbeek, J. T. G., 1954. The rate of coagulation as a measure of the stability of silver iodide sols, Discuss. Faraday Soc., 18, 74–84, DOI: 10.1039/DF9541800074.
81. Robb, D. T.; Privman, V., 2008. Model of Nanocrystal Formation in Solution by Burst Nucleation and Diffusional Growth. Langmuir, 24, 26−35

82. Roco, M. C. and Bainbridge, W. S., 2002. Converging Technologies for Improving Human Performance: NANOTECHNOLOGY, BIOTECHNOLOGY, INFORMATION TECHNOLOGY AND COGNITIVE SCIENCE, National Science Foundation, https://www.wtec.org/ConvergingTechnologies/Report/NBIC_report.pdf
83. Sandler, S. I., 2006. Chemical, Biochemical, and Engineering Thermodynamics, fourth ed., John Wiley and Sons, New Jersey.
84. Schwerdtfeger, P. and Lein, M., 2009. Theoretical Chemistry of Gold. In Mohr, F. ed. Gold Chemistry: Applications and Future Directions in the Life Sciences Wienheim Wiley pp 183-221
85. Serjeant, E.P., Dempsey B., 1979. Ionisation Constants of Organic Acids in Aqueous Solution. International Union of Pure and Applied Chemistry (IUPAC). IUPAC Chemical Data Series No. 23, Pergamon Press, New York.
86. Shapira, P., Youtie, J., Porter, A. L., 2010. The emergence of social science research on nanotechnology, Scientometrics DOI 10.1007/s11192-010-0204-x
87. Shapira, P., and Youtie, J., 2012. The Economic Contributions of Nanotechnology to Green and Sustainable Growth, Prepared for the International Symposium on Assessing the Economic Impact of Nanotechnology, Organisation for Economic Cooperation and Development and the US National Nanotechnology Initiative, Washington DC, 27-28 March 2012.
88. Smoluchowski, M. v., 1917. Mathematical Theory of the Kinetics of the Coagulation of Colloidal Solutions *Z. Phys. Chem. 92 129-68*
89. Sohnel, O and Garside, J., 1992. Precipitation, Basic Principles and Industrial Applications, Butterworth-Heinemann, Oxford.
90. Stratakis, M., Garcia, H., 2012. Catalysis by Supported Gold Nanoparticles: Beyond Aerobic Oxidative Processes *Chemical Reviews 112* (8), 4469-4506 DOI: 10.1021/cr3000785
91. Stroud, K. A., and Booth, D. J., 2003. Advanced Engineering Mathematics, Palgrave MacMillan, London
92. Takiyama, K. 1958. Formation and Aging of Precipitates. VIII. Formation of Monodisperse Particles (1) Gold Sol Particles by Sodium Citrate Method. Bull. Chem. Soc. Jpn. 31, 944–950.
93. Tung, H., Paul, E. L., Midler, M., McCauley, J. A., 2009. Crystallization of Organic Compounds: An Industrial Perspective, A John Wiley and Sons, New Jersey.
94. Turkevich, J., Stevenson, P., Hillier, J., 1951. A Study of the Nucleation and Growth Process in the Synthesis of Colloidal Gold. Discuss. Faraday Soc., 11, 55.
95. Urban, A., S., Lutich, A., A., Stefani, F., D., and Feldmann, J., 2010. "Laser Printing Single Gold Nanoparticles", Nano Letters, VOL. 10, NO. 12.
96. Vance, M. E., Kuiken, T., Vejerano, E. P., McGinnis, S. P., Hochella Jr, M. F., Rejeski, D., Hull, M. S., 2015. Nanotechnology in the real world: Redeveloping the nanomaterial consumer products inventory, Beilstein J Nanotechnol. 2015 Aug 21;6:1769-80. doi: 10.3762/bjnano.6.181. eCollection.
97. Vazquez-Muñoz, R., Borrego, B., Juárez-Moreno, K., García-García, M., Mota Morales, J. D., Bogdanchikova, N., Huerta-Saquero, A., 2017. Toxicity of silver nanoparticles in biological systems: Does the complexity of biological systems matter? Toxicology Letters Volume 276, https://doi.org/10.1016/j.toxlet.2017.05.007
98. Verwey, E. J. W., and Overbeek, J. T. G., 1948. Theory of the Stability of Lyophobic Colloids, Elsevier, Amsterdam.
99. Viswanatha, R., Sarma, A. A., 2007. Growth of Nanocrystals in Solution, In: Rao, C. N. R.,Müller, A., Cheetham, A. K. (Eds.), *Nanomaterials Chemistry: recent developments and new directions*; Wiley, pp. 139-170.
100. Wang, W., Li, N., and Speaker, S., 2010. External Factors Affecting Protein Aggregation, Hoboken, NJ, USA: John Wiley & Sons, Inc.
101. Watzky, M.A., Finke, R.G., 1997. Nanocluster Size-Control and “Magic Number Investigations.Chem. Mater. 9, 3083.

102. Wuithschick, M., Witte, S., Kettemann, F., Rademann, K., Polte, J., 2015. Turkevich in New Robes: Key Questions Answered for the Most Common Gold Nanoparticle Synthesis, Phys. Chem. Chem. Phys., *17*, 19895-19900, DOI: 10.1021/acsnano.5b01579
103. Wulkow, M., Gerstlauer, A., Nieken, U., 2001. Modeling and simulation of crystallization processes using parsival, Chem. Eng. Sci., 56, 2575 -2586, DOI: 10.1016/S0009-2509(00)00432-2
104. Yang, X., Yang, M., Pang, B., Vara, M., and Xia, Y., 2015. Gold Nanomaterials at Work in Biomedicine, *Chem. Rev.*, *115* (19), pp 10410–10488, DOI: 10.1021/acs.chemrev.5b00193
105. Zabetakis, K., Ghann, W.E., Kumar, S., Daniel, M.-C. , 2012. Gold Bull. 45, 203, DOI 10.1007/s13404-012-0069-2
106. Zaidi, S. A. N., 2017. Nanotechnology, A Paradigm Shift Towards Scientific Revolution, Law and Regulations: An Overview, J. Biol. Chem. Research. Vol. 34, No. 2: 938-947, 2017
107. Zhang, L., Wang, Y., Tong, L., Xia, Y. 2014. Synthesis of Colloidal Metal Nanocrystals in Droplet Reactors: The Pros and Cons of Interfacial Adsorption, Nano Letters, dx.doi.org/10.1021/nl501994q
108. Zheng, K., Setyawati, M. I., Leong, D. T., and Xie, J., 2017. Antimicrobial Gold Nanoclusters, *ACS Nano* 11, 7, 6904-6910, DOI: 10.1021/acsnano.7b02035
109. Zhou, W., Gao, X., Liu, D., and Chen, X., 2015. Gold Nanoparticles for In Vitro Diagnostics *Chemical Reviews, 115* (19), 10575-10636 DOI: 10.1021/acs.chemrev.5b00100.
110. Anonymous author, 2014. "Michael Faraday's gold colloids | The Royal Institution: Science Lives Here". www.rigb.org. Retrieved 2015-12-04.

Appendix A

In this appendix, using the averaging theory, we derive the material balance for the continuous phase. This is an alternative method to the method presented in the thesis. For the material balance, we write:

$$\partial_t C_i = -\nabla_{\boldsymbol{x}} \bar{\boldsymbol{J}}_{\boldsymbol{i}} + r_i \tag{A.1}$$

This equation is identical to Eq. (2.2.13) in the thesis. The term on the left-hand side represents the accumulation term as Eq. (2.2.13). The first term on the right-hand side is the total molar flux $\bar{\boldsymbol{J}}_{\boldsymbol{i}}$, combining both the convective and diffusive terms in Eq. (2.2.13). The last term on the right-hand side is identical to the last term of Eq. (2.2.13).

By the averaging theory, we integrate Eq. (A.1) over the physical volume V, which is assumed to be fixed and constant. This strategy would produce a mean concentration $\langle C_i \rangle$, which is no longer dependent on the physical space. We implement this integral transform as follows:

$$\int_V \left[\partial_t C_i + \nabla_{\boldsymbol{x}} \bar{\boldsymbol{J}}_{\boldsymbol{i}} - r_i\right] dV = 0 \tag{A.2}$$

The first term on the left-hand side in eq. (A.2) is transformed as:

$$\int_V \partial_t C_i \, dV = \frac{d}{dt} \int_V C_i \, dV = \frac{d}{dt} [\langle C_i \rangle . V] = V \frac{d\langle C_i \rangle}{dt} \tag{A.3}$$

Using the Gauss theorem, the second term on the left-hand side of eq. (A.2) is transformed as:

$$-\int_V \nabla_{\boldsymbol{x}} \bar{\boldsymbol{J}}_{\boldsymbol{i}} \, dV = -\int_S \bar{\boldsymbol{J}}_{\boldsymbol{i}} . d\boldsymbol{S} \tag{A.4}$$

For a batch reactor, Eq. (A.4) is zero. That is:

$$\int_S \bar{\boldsymbol{J}}_{\boldsymbol{i}} . d\boldsymbol{S} = 0 \tag{A.5}$$

The last term on the left-hand side of Eq. (A.2) is transformed as:

$$\int_V r_i \, dV = V \langle r_i \rangle \tag{A.6}$$

where $\langle r_i \rangle$ is the mean rate of generation of component i per unit volume from various reactions and it is only a function of time.

Putting all the terms together, Eq. (A.2) becomes:

$$V\frac{d\langle C_i\rangle}{dt} = V\langle r_i\rangle; \frac{d\langle C_i\rangle}{dt} = \langle r_i\rangle \quad \text{(A.7)}$$

Notice that we obtained Eq. (A.7) without imposing the condition of perfect mixing in the reactor. By imposing this condition,

$$\langle C_i\rangle = C_i \text{ and } \langle r_i\rangle = r_i \quad \text{(A.8)}$$

Thus, Eq. (A.7) becomes:

$$\frac{dC_i}{dt} = r_i \quad \text{(A.9)}$$

Eq. (A.9) is identical to Eq. (2.2.14) reported in the thesis for a perfectly mixed batch reactor.

Appendix B

In this appendix, we provide qualitative criteria to determine the controlling mechanism for the growth process. As discussed in the thesis using Figure 2.2.3, the growth process can be controlled by mass transfer or by surface integration or by both mechanisms. In Figure 2.2.3, the total mass flux $\bar{J}$ due to mass transfer can be written as:

$$\bar{J} = k_{MT}(c - c') = \frac{(c-c')}{R_{MT}} \tag{B.1}$$

where c is the bulk concentration, c' is the concentration of the solute at the particle surface, as shown in Figure 2.2.3, k_{MT} is the mass transfer coefficient, and R_{MT} is the mass transfer resistance. For a well-mixed reactor, the mass transfer coefficient is given by Eq. (2.2.89) as:

$$k_{MT} = \frac{D_0}{r_c}\left(1 + \frac{r_c}{\delta}\right) \tag{B.2}$$

Similarly, in terms of surface integration, the total mass flux can be written as:

$$\bar{J} = k_{SI}(c' - c_{eq}) = \frac{(c'-c_{eq})}{R_{SI}} \tag{B.3}$$

where R_{SI} is the surface integration resistance.

In this equation, we have assumed the order of reaction to be one, following the work Turkevich et al. (1951).

From Eq. (B.1), we have:

$$c' = c - \bar{J}R_{MT} \tag{B.4}$$

And from Eq. (B.3), we have:

$$c' = \bar{J}R_{SI} + c_{eq} \tag{B.5}$$

Thus,

$$\bar{J} = \frac{(c-c_{eq})}{R_{MT}+R_{SI}} \tag{B.6}$$

When $R_{MT} \gg R_{SI}$, Eq. (B.6) becomes:

$$\bar{J} = \frac{(c-c_{eq})}{R_{MT}} \tag{B.7}$$

This is the expression for growth controlled by mass transfer.

When $R_{SI} \gg R_{MT}$, Eq. (B.6) becomes:

$$\bar{J} = \frac{(c - c_{eq})}{R_{SI}} \qquad \text{(B.8)}$$

This is the expression for growth controlled by surface integration.

When $R_{SI} \approx R_{MT}$, then both mechanisms control the growth process.

Appendix C

In population balance equations, we theoretically solve for the number density function, $f(s,t)$. However, experimental data like the sieve analysis can be described using some analytical distribution functions. We fit the experimental data and compare the resulting profile with any of the distribution functions, to determine which one describes the data. Sometimes, however, none of the functions may be suitable to describe the data. These distribution functions are (Randolph and Larson, 2001):

1. Normal distribution
2. Log-normal distribution
3. Gamma distribution
4. Rosin-Rammler distribution
5. Guadin-Melloy distribution

We discuss the function of each distribution as follows.

C.1 Normal distribution

Normal distribution suggests that the distribution is evenly distributed about the mean size, $\langle s \rangle$, i.e. exactly half the number are on either side of the mean and extends from $-\infty$ to $+\infty$. Its expression is:

$$f(s) = \frac{n(s)}{N_T} = \frac{1}{\sigma\sqrt{2\pi}} \exp\left(-\frac{(s-\langle s \rangle)^2}{2\sigma^2}\right) \quad \text{(C.1)}$$

where $n(s)$ is the number of particles having size s, and N_T is the total number of particles.

Since it is normalized, the number fraction is given as

$$F(s) = \int_{-\infty}^{s} f(s)ds = \int_{-\infty}^{s} \frac{1}{\sigma\sqrt{2\pi}} \exp\left(-\frac{(s-\langle s \rangle)^2}{2\sigma^2}\right) ds \quad \text{(C.2)}$$

and

$$F(s) = \int_{-\infty}^{\infty} f(s)ds = 1 \quad \text{(C.3)}$$

Equation (C.2) can be expressed in a reduced form by making the following substitution:

$$p = \frac{s-\langle s \rangle}{\sigma\sqrt{2}} \quad \text{(C.4)}$$

So it becomes:

$$F(p) = \frac{1}{\sqrt{\pi}} \int_{-\infty}^{p} \exp(-p^2)\, dp \quad \text{(C.5)}$$

Equation (C.5) can be re-expressed as:

$$F(p)\sqrt{\pi} = \int_{-\infty}^{0} \exp(-p^2)\, dp + \int_{0}^{p} \exp(-p^2)\, dp \qquad \text{(C.6)}$$

Assuming that the integrand is an even function of p, the first term on the right-hand side of Eq. (C.6) can be expressed as (Randolph and Larson, 2001):

$$\int_{-\infty}^{0} \exp(-p^2)\, dp = \frac{\sqrt{\pi}}{2} \qquad \text{(C.7)}$$

Eq. (C.6) then becomes:

$$F(p)\sqrt{\pi} = \frac{\sqrt{\pi}}{2} + \int_{0}^{p} \exp(-p^2)\, dp; \qquad F(p) = \frac{1}{2} + \frac{1}{\sqrt{\pi}} \int_{0}^{p} \exp(-p^2)\, dp \qquad \text{(C.8)}$$

Alternatively, we can express Eq. (C.8) as:

$$F(p) = 0.5(1 + \operatorname{erf} p) \qquad \text{(C.9)}$$

Where $\operatorname{erf} p = \frac{2}{\sqrt{\pi}} \int_{0}^{p} \exp -y^2\, dy$ (C.10)

When $F(p) = 0.5$, $p = 0$ and the corresponding value of s can be read off from the cumulative distribution F vs s, that is $\langle s \rangle$.

At $s = \langle s \rangle + \sigma$, $p = \frac{1}{\sqrt{2}}$, so $F(p) = 0.84$ from equation (C.9). As above, the corresponding value of s can be read off from F vs s. Therefore, $\sigma = s - \langle s \rangle$.

We insert $\langle s \rangle$ and σ into equation (C.1) and generate $f(s)$ for all values of s from $-\infty$ to $+\infty$.

C.2 Log-normal distribution

Log-normal distribution ensures that the range of s is from 0 to $+\infty$. $\log s$, $\log\langle s \rangle$ and $\log \sigma$ replace s, $\langle s \rangle$ and σ respectively in equation (C.1). For a number of sizes, $\langle s \rangle$ is the geometric mean which is found as:

$$\langle s \rangle = \sqrt[n]{\prod_{1}^{n} s_i} \qquad \text{(C.11)}$$

The expression for the log-normal is given as;

$$f(\log s) = \frac{1}{\log \sigma \sqrt{2\pi}} \exp - \frac{(\log s - \log\langle s \rangle)^2}{2(\log \sigma)^2} \qquad \text{(C.12)}$$

And

$$F(\log s) = \int_{0}^{\log s} f(\log s) d(\log s) \qquad \text{(C.13)}$$

where $F(\infty) = 1$

The reduced form log-normal distribution is obtained by

$$p = \frac{\log s - \log\langle s\rangle}{\sqrt{2}\log\sigma} \tag{C.14}$$

Then equation (C.13) can be expressed as equation (C.9). We obtain $\langle s\rangle$ and σ exactly as in the case of normal distribution and plot $f(s)$.

C.3 Gamma distribution

Like $\langle s\rangle$ and σ in the previous density functions, parameters a and b are required in the density function to plot the gamma distribution. The expression is:

$$f(s) = \left[\lceil(a+1)\left({}^{b}/_{a}\right)^{a+1}\right]^{-1} s^{a}\exp\left(-\frac{as}{b}\right) \tag{C.15}$$

Where $\lceil(a+1) = a!$

$$F(s) = \int_0^s \left[\lceil(a+1)\left({}^{b}/_{a}\right)^{a+1}\right]^{-1} s^{a}\exp\left(-\frac{as}{b}\right) ds \tag{C.16}$$

Randolph and Larson (2001) suggested that b is the mode of the distribution while a is the wideness of the distribution; a and b resemble $\langle s\rangle$ and σ respectively. The parameters in normal, log-normal and gamma distributions are similar. Figure C.1 shows their resemblance.

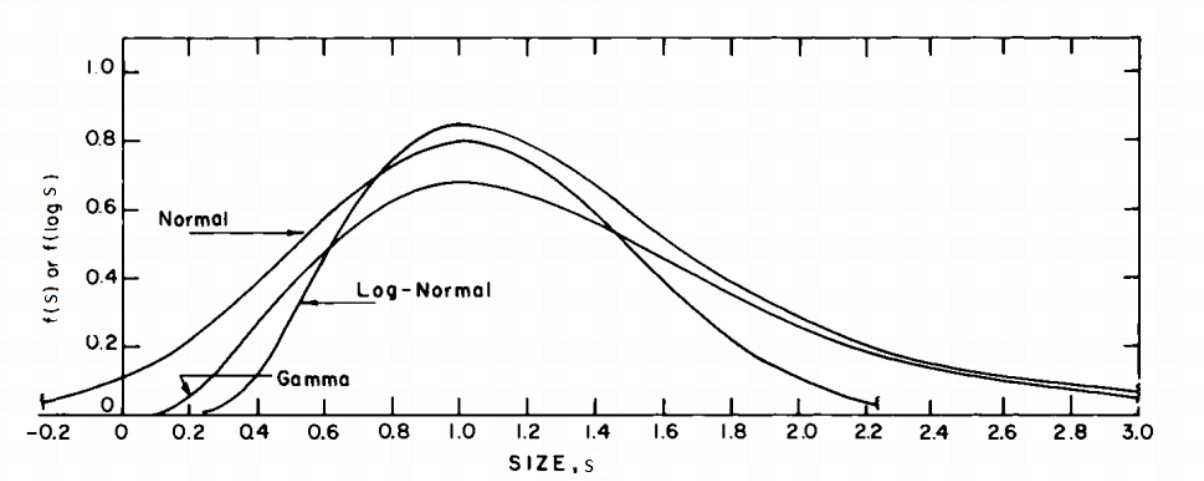

Figure C.1 Profiles of normal, log-normal and gamma distributions over size, s, obtained from Randolph and Larson (2001).

Equation (C.16) can be expressed in its reduced form by substituting: $z = {}^{as}/_{b}$ as:

$$F(z) = [\lceil(a+1)]^{-1}\int_0^z z^{a}e^{-z}dz \tag{C.17}$$

Integrating equation (C.17) becomes:

$$F(z) = 1 - e^{-z}\left[1 + z + \frac{z^2}{2!} + \frac{z^3}{3!} + \cdots + \frac{z^a}{a!}\right] \quad \text{(C.18)}$$

In mixed-suspension mixed-product removal, z expresses $\frac{s}{G_s\tau}$, where G_s and τ are the growth rate and the residence time respectively.

C.4 Rosin-Rammler distribution

Rosin-Rammler distribution is given as

$$f(s) = nbs^{n-1}\exp(-bs^n) \quad \text{(C.19)}$$

Then, the cumulative fraction will be:

$$F(s) = \int_0^s nbs^{n-1}\exp(-bs^n)\ ds \quad \text{(C.20)}$$

Say $x = bs^n$

Equation (C.20) becomes

$$F(x) = \int_0^x \exp(-x)\ dx \quad \text{(C.21)}$$

Integrating equation (C.21) gives

$$F(x) = 1 - \exp(-x) \quad \text{(C.22)}$$

Equation (C.22) can subsequently be rearranged by taking log of both sides and substituting $x = bs^n$ as

$$\log(\log(1-F)^{-1}) = \log b + n\log s \quad \text{(C.23)}$$

If the plot of $\log(\log(1-F)^{-1})$ vs $\log s$ is linear, then the experimental data obeys Rosin-Rammler distribution.

C.5 Gaudin-Melloy distribution

The expression for the number density function of Gaudin-Melloy distribution is given as

$$f(s) = \frac{m}{s_m}\left[1 - \frac{s}{s_m}\right]^{n-1} \quad \text{(C.24)}$$

Then, the cumulative fraction is:

$$F(s) = \int_0^s \frac{m}{s_m}\left[1 - \frac{s}{s_m}\right]^{m-1}\ ds \quad \text{(C.25)}$$

Equation (C.25) can be reduced to:

$F(p) = \int_0^p m[1-p]^{m-1}\, dp$ where $p = {}^{s}/_{s_m}$ (C.26)

Integrating equation (C.26) gives:

$F(p) = 1 - (1-p)^m$ (C.27)

Eq. (C.27) can be re-expressed as:

$\log(1-F) = m\log(1-p)$ (C.28)

If the plot of $\log(1-F)$ vs $\log(1-p)$ is linear, then the experimental data obeys Gaudin-Melloy distribution.

In most cases, mean size $\langle s \rangle$ and the coefficient of variation describe the quality of particle size distribution; the mean describes the average of the distribution while the coefficient of distribution describes how far the size distribution is from the mean. They are mathematically expressed as:

$\langle s \rangle = \int_0^s sf(s)ds$ (C.29)

$c.v. = {}^{\sigma}/_{\langle s \rangle}$ (C.30)

These properties of a distribution and others are obtained from the calculation and manipulation of the moments of particle size distribution.

C.6 Moments of particle size distribution

Moments of distribution are used to obtain representative numbers of a distribution like the total number of particles, the total length of particles etc. Once these moments are known, the quality of the distribution like mean size, coefficient of variation, skewness and kurtosis can be determined.

The definition of the moment for the particle size distribution is given as:

$m_j = \int_0^\infty s^j n(s)ds$ (C.31)

The first four moments and their meanings are:

- Total number of particles : $N_T = m_0 = \int_0^\infty n(s)ds$ (C.32)
- Total length of particles :$s_T = m_1 = \int_0^\infty sn(s)ds$ (C.33)
- Total area of particles :$A_T = m_2 = \int_0^\infty s^2 n(s)ds$ (C.34)
- Total mass of particles:$M_T = k_V \rho m_3 = k_V \rho \int_0^\infty s^3 n(s)ds$ (C.35)

The general expression for the mean size in terms of the moments is:

Mean size, $s_{j+1,j} = \frac{m_{j+1}}{m_j}$ (C.36)

The value of j determines the type of mean size. The first four mean sizes are:

Number mean size, $s_{1,0} = \frac{m_1}{m_0}$ (C.37)

Length mean size, $s_{2,1} = \frac{m_2}{m_1}$ (C.38)

Area mean size, $s_{3,2} = \frac{m_3}{m_2}$ (C.39)

Weight mean size, $s_{4,3} = \frac{m_4}{m_3}$ (C.40)

Appendix D

In this appendix, to test the numerical accuracy in Parsival, we consider solving another problem using the code and later analyse the convergence of its results. Also, we describe the procedures for model implementation using the Parsival interface.

D.1 Validation of PBM in Parsival

The model developed by Kumar et al. (2007) is centred on the nucleation-growth mechanism of Turkevich et al. (1951). Aggregation plays a secondary role. Thus, to investigate how accurate the solution of population balance equations is in Parsival, we consider a crystallization problem that involves nucleation and growth only. The crystallizer is a batch vessel operated on the natural and linear cooling mechanisms (these mechanisms are defined below). This problem was solved by means of another numerical technique (Runge-Kunta method) and the results are available in the literature (Jones and Mullin, 1973). We now use Parsival to solve the model.

Crystallization occurs by mass transfer from the liquid phase to the solid phase (the crystals). The mass transfer can occur by nucleation or growth or both. The liquid phase, which is largely the solvent, contains the solute forming a homogeneous solution. This homogeneous solution can only be formed if the solvent contains an amount of solute that is below its solubility. The solubility of a solute in a solvent is the maximum amount of solute that can dissolve in a certain amount of solvent forming a homogeneous solution. The solubility of a solute depends on the temperature of the solution, usually increasing with temperature. If a homogeneous solution is therefore cooled, some of the mass in the liquid phase will transfer into the solid phase through the nucleation and growth processes forming crystals. Apart from cooling, crystallization can be caused by evaporating the solvent, precipitating the solute, or adding another solvent. We consider the crystallization of potassium sulphate/water solution by cooling in a batch crystallizer. First, we derive the material balance equation and the population balance equation. Then we apply the cooling mechanisms: natural cooling and linear cooling (for more details, see Jones and Mullin (1973)).

Material balance

Taking the aqueous phase as the system, the material balance for the solute is:

$$Acc = In - Out + Generation \tag{D.1}$$

where Acc is the rate of accumulation of the solute in the liquid phase, given as

$$Acc = \frac{d(cM)}{dt} = M\frac{dc}{dt} \quad \text{(D.2)}$$

in which c is kg solute per kg water and M is kg of water. M does not vary with time.

In is the mass flow rate of solute that enters the liquid phase. For a batch system, in the absence of crystal dissolution, it is:

$$In = 0 \quad \text{(D.3)}$$

Out is the mass flow rate of solute leaving the aqueous phase. The solute can leave the aqueous phase by nucleation and growth. The nucleation rate is defined as the number of nuclei formed per unit volume of solution per unit time. The nucleation mass flow rate, on the other hand, is the mass of solute in the form of nuclei produced per unit time, denoted as $R_n.M$, where R_n is the mass of solute in the form of nuclei produced per kg of water per unit time. R_n can be expressed as (Jones and Mullin, 1973):

$$R_n = k_n \Delta c^n(t) \quad \text{(D.4)}$$

where k_n is the nucleation rate constant, Δc is the supersaturation and n is the order of the nucleation rate equation. The mass of solute that leaves the liquid phase by nucleation therefore is:

$$k_n \Delta c^n(t) M \quad \text{(D.5)}$$

Growth also causes the solute to leave the aqueous phase. The growth process depends on the supersaturation and the area of the particles according to:

$$k_g A(t) \Delta c^g(t) M \quad \text{(D.6)}$$

where k_g is the growth rate constant, $A(t)$ is the total surface area of particles per kg of water, and g is the order of the growth equation. $A(t)$ can be expressed as:

$$A(t) = \frac{m_a V}{M} \int_{s_0}^{\infty} s^2 f(s,t) ds \quad \text{(D.7)}$$

where m_a is the area shape factor, V is the volume of the solution, and $\int_{s_0}^{\infty} s^2 f(s,t) ds$ is the second moment of the particle size distribution per unit volume of solution. s is the particle diameter, $f(s,t)$ is the number density function, such that $f(s,t)ds$ is the number of particles at time t present in a differential size ds per unit volume of solution. s_0 is the size of a nucleus.

In the aqueous system, $Generation = 0$.

Putting Eqs. (D.2), (D.5), (D.6) and (D.7) together:

$$M\frac{dc}{dt} = -\left[k_n \Delta c^n M + m_a k_g \Delta c^g(t) V \int_{s_0}^{\infty} s^2 f(s,t) ds\right] \quad \text{(D.8)}$$

Another way to express growth is by considering a single crystal. The rate of change of mass on the crystal is

$$\frac{d(\,mass\ of\ a\ crystal)}{dt} = \frac{d(\rho_c . v_c)}{dt} = \rho_c \frac{dv_c}{dt} \quad \text{(D.9)}$$

where ρ_c is the mass density of the crystal; v_c is the volume of a crystal, which can be expressed as

$$v_c = m_v s^3 \quad \text{(D.10)}$$

where m_v is the volume shape factor. Thus:

$$\frac{dv_c}{dt} = 3 m_v s^2 \frac{ds}{dt} \quad \text{(D.11)}$$

ds/dt is the crystal growth rate $G_s(s)$.

Also, from the area of this crystal $m_a s^2$, we can calculate the rate of change of mass as:

$$m_a k_g \Delta c^g(t) s^2 \quad \text{(D.12)}$$

Eqs. (D.9) and (D.12) are equivalent. By substituting for dv_c/dt, we have:

$$\rho_c 3 m_v s^2 G_s = m_a k_g \Delta c^g(t) s^2$$

Then:

$$k_g \Delta c^g = \frac{3 m_v \rho_c G_s(s)}{m_a} \quad \text{(D.13)}$$

Substituting for $k_g \Delta c^g$ in Eq. (E.8), we have:

$$M\frac{dc}{dt} = -\left[k_n \Delta c^n M + 3 m_v \rho_c G_s(t) V \int_{s_0}^{\infty} s^2 f(s,t) ds\right] \quad \text{(D.14)}$$

But:

$$c = c^* + \Delta c \quad \text{(D.15)}$$

where c^* and Δc are the solubility and supersaturation, respectively. Then:

$$M\frac{d(\Delta c)}{dt} = -M\frac{dc^*}{dt} - \left[k_n \Delta c^n M + 3 m_v \rho_c G(t) V \int_{s_0}^{\infty} s^2 f(s,t) ds\right] \quad \text{(D.16)}$$

Also, we can write:

$$\frac{dc^*}{dt} = \frac{dc^*}{d\theta} . \frac{d\theta}{dt} \quad \text{(D.17)}$$

where θ denotes the temperature of the solution.

$dc^*/d\theta$ is the gradient of the solubility curve, expressed as:

$$\frac{d(c^*)}{d\theta} = \beta_1 + 2\beta_2\theta \quad \text{(D.18)}$$

β_1 and β_2 are constants of the solubility curve.

$d\theta/dt$ is the rate of change of temperature with time and accounts for the cooling mechanism.

Thus:

$$M\frac{d(\Delta c)}{dt} = -M\left(\frac{dc^*}{d\theta}.\frac{d\theta}{dt}\right) - \left[k_n\Delta c^n M + 3m_v\rho_c G_s(s)V\int_{s_0}^{\infty} s^2 f(s,t)ds\right] \quad \text{(D.19)}$$

Eq. (D.19) describes the changes in mass of the solute in the aqueous phase. Next, we consider the solid phase using the population balance equation.

A batch crystallizer is assumed to be well-mixed and the crystals are described by only the particle diameter s. Thus, we will use the simplified population balance equation discussed in the main thesis as:

$$\frac{\partial f(s,t)}{\partial t} = -\frac{\partial[G_s(s)f(s,t)]}{\partial s} + H_N(s_0) \quad \text{(D.20)}$$

Eq. (D.20) describes how the NDF ($f(s,t)$) changes with time under the influence of nucleation ($H_N(s_0)$) and particle growth ($-\partial[G_s(s)f(s,t)]/\partial s$). $H_N(s_0)$ is the nucleation term, related to the mass nucleation rate as:

$$\int H_N(s_0)ds = \frac{R_n.M}{m_v\rho_c {s_0}^3 V} = \frac{k_n\Delta c^n(t).M}{m_v\rho_c {s_0}^3 V} \quad \text{(D.21)}$$

The growth rate, on the other hand, is expressed as (Jones and Mullin (1973)):

$$G_s = as^b \exp[-E/R(\theta+273)]\,\Delta c^g \quad \text{(D.22)}$$

To solve the population balance equation, apart from the temperature θ, we need the initial particle size distribution, and the supersaturation Δc at time t. The former is given by the mass of seeds per kg water ($W_{s_{initial}}$) and the seed size ($s_{initial}$). The latter is given by Eq. (D.19), which can only be solved if we know $d\theta/dt$ and the initial supersaturation $\Delta c(0)$. We consider the two cooling mechanisms of natural cooling and linear cooling as follows.

For natural cooling, the heat loss Q is proportional to the temperature difference between the temperature of the system θ and the temperature of the surrounding θ_w. Assuming that the

heat capacity ϑ_p for the system is constant in the temperature range of interest, considering also that for a batch system the total mass M_T is constant, we can write:

$$\frac{d(\vartheta_p M_T \theta)}{dt} = -Q = -p_n(\theta - \theta_w) \quad \text{(D.23)}$$

p_n is the proportionality constant for how the temperature of the solution changes with the temperature difference between the solution and the surrounding.

$$\frac{d\theta}{dt} = -\frac{p_n}{\vartheta_p M_T}(\theta - \theta_w) = K_1(\theta - \theta_w) \quad \text{(D.24)}$$

If we know the batch time for the crystallization process τ, the initial solution temperature θ_0 and the final solution temperature θ_f, we can obtain K_1 as:

$$\int_{\theta_0}^{\theta_f} \frac{d\theta}{(\theta - \theta_w)} = \int_0^{\tau} K_1 dt \quad \text{(D.25)}$$

$$K_1 = \frac{1}{\tau} \ln \frac{(\theta_f - \theta_w)}{(\theta_0 - \theta_w)} \quad \text{(D.26)}$$

Thus:

$$\theta = \theta_w + (\theta_0 - \theta_w)\left[\frac{(\theta_f - \theta_w)}{(\theta_0 - \theta_w)}\right]^{\frac{t}{\tau}} \quad \text{(D.27)}$$

For linear cooling, however, the heat loss is constant:

$$\vartheta_p M_T \frac{d(\theta)}{dt} = p_l; \qquad \frac{d\theta}{dt} = K_2 \quad \text{(D.28)}$$

p_l is the constant for linear cooling while $K_2 = p_l / \vartheta_p M_T$.

Similarly, if we know the batch time τ for the crystallization process, the initial system temperature θ_0 and the final system temperature θ_f, we can obtain K_2 as:

$$\int_{\theta_0}^{\theta_f} d\theta = \int_0^{\tau} K_2 dt \quad \text{(D.29)}$$

Thus:

$$K_2 = \frac{(\theta_f - \theta_0)}{\tau} \quad \text{(D.30)}$$

So that:

$$\theta = \theta_0 + \frac{(\theta_f - \theta_0)}{\tau} t \quad \text{(D.31)}$$

In Parsival, we used the initial conditions, and the parameters employed by Jones and Mullin (1973) as follows:

$a = 100;\ b = 0.5;\ E/R = 2.4 \times 10^3\ ;\ k_n = 2 \times 10^8\ ;\ n = 7.63\ ;\ g = 2\ ;\ s_0 = 6 \times 10^{-5}\, m;$ $s_{initial} = 5.5 \times 10^{-4}\, m;\ \beta_0 = 6.66 \times 10^{-2}\ ;\ \beta_1 = 2.3 \times 10^{-3}\ ;\ \beta_2 = 6 \times 10^{-6};\ m_v = 0.47;$ $W_{s_{initial}} = 2.36 \times 10^{-3}\, kg\ particles/kg\ water; \theta_0 = 60^0 C\ ;\ \theta_f = 25^0 C\ ;\ \theta_w = 15^0 C\ ;\ \Delta c(0) =$ $7.32 \times 10^{-3}\, kg\ solute/kg\ water; \tau = 10800\, s.$

After simulating, Parsival solved the problem for the two mechanisms.

For the natural cooling, we obtained a mean size of $591\ \mu m$ compared to $594\ \mu m$ reported by Jones and Mullin, representing a relative deviation of 0.5%. While for the linear cooling, we obtained $845\ \mu m$ compared to $831\ \mu m$ reported by Mullin and Jones, representing a relative deviation of 1.7%. Further, we analysed how the calculations in Parsival converge.

D.2 Convergence analysis in Parsival

In solving the population balance equation, an integro-differential equation, Parsival uses the adaptive h-p Galerkin method. The h-p Galerkin method is a finite element scheme that divides the size space into a number of nodes h and represents each node with an algebraic equation of order p, hence the name h-p. The nodes and the equations, when brought together, yield the particle size distribution. The method solves the population balance equation within a time step that guarantees the specified accuracy. The accuracy refers to the difference between the solutions (the concentrations of the fluid components and PSD) at time t and time $t + \Delta t$. For all cases in our simulations, because of the simulation time, we specified an accuracy of 0.1%. The time step, called the actual time step Δt_a, is obtained using the Rothe method (see Wulkow et al. (2001) for details). We do not specify it. However, we specify the maximum time step Δt_m. Parsival uses Δt_a when $\Delta t_a < \Delta t_m$; otherwise, it uses Δt_m. In this analysis, we check the impact of using $\Delta t_m = 0.1,\ 1$ and $10\ s$.

On the size step Δs, the h-p Galerkin method adapts to the particle size distribution and refines the number of nodes as the simulation progresses. We fixed the initial minimum size $s_{min} = 0.1\ nm$, the first node; Parsival generates the number of subsequent nodes and their locations by searching the semi-infinite size space (i.e. from s_{min} to ∞) for particles.

However, when a very narrow distribution is used, as in our case, where we simulated a Dirac delta distribution in the model developed by Kumar et al. (2007), the search may omit the particles within the distribution. In order to capture this distribution, we instructed Parsival to search at and around the mean size ($s_0 = 2\ nm$) by adding specific nodes. The node step is represented by Δx. Once Parsival has captured particles in one time step Δt_a, it is able to refine and propagate the nodes for later time steps by taking note of the processes such as

growth and aggregation until the final simulation time. For this analysis therefore, we added nodes at $2\ nm$ and $-\Delta x$ from $2\ nm$ down to $1\ nm$, and $+\Delta x$ from $2\ nm$ up to $3\ nm$.

We simulated the implemented model of Kumar et al. (2007) using the initial conditions of $0.3\ mol/m^3$ for both chloroauric acid and sodium citrate.

Table D.1: Mean particle diameters for a combination Δt_m and Δx

Δt_m (s)	0.1	1.0	10.0
Δx (nm)		(nm)	
0.01	38.1	37.6	37.6
0.10	38.1	37.6	37.6
1.00	38.1	37.6	37.6

Table D.1 shows the results of the mean size for simulating the model by Kumar et al. for the case $C_{T_0} = C_{C_0} = 0.3\ mol/m^3$ using a combination of Δt_m and Δx. Changing the node steps does not affect the results. Also, time steps of 1 and $10\ s$ produce identical results but reducing the time step to $0.1\ s$ changes the results by $\sim 1\%$.

As we said before, the specified value of accuracy determines Δt_a. Further, we check the impact of changing this value on the numerical solution in Parsival. Using the same initial conditions as above, for values of accuracy: $0.01, 0.1\ and\ 1\%$ in diiferent time steps $\Delta t_m =$ 0.1, 1 and $10\ s$, Table D.2 shows the results of the mean size.

Table D.2: Mean particle diameters for a combination accuracy and Δt_m

Δt_m (s)	0.1	1	10
Accuracy		(nm)	
0.01%	38.1	38.1	38.1
0.10%	37.6	37.6	37.1
1.00%	37.6	37.6	37.1

The table illustrates that both the values of accuracy and Δt_m affect the results. When the accuracy is 0.01%, Δt_a calculated from the Rothe method (for the whole simulation time) is less than Δt_m so that the latter does not affect the results. By relaxing the accuracy to 0.1,and 1%, Δt_m begins to affect the results, giving the least accurate result of $37.1\ nm$ when $\Delta t_m = 10\ s$. In the main thesis, for these initial conditions, we used accuracy of 0.1% and Δt_m of $1\ s$, and reported the mean particle diameter $37.6\ nm$. Thus, our values were reasonably accurate.

Based on the foregoing, we can conclude that the numerical calculations in Parsival for high accuracy converge to nearly the same final results regardless of the time and size steps specified.

D.3 Procedures for model implementation using the Parsival interface

In this section, we discuss the procedures for implementing and solving a system of equations (i.e., a combination of population balance equation and material balance equations) describing a nanoparticles synthesis. To illustrate these procedures, we employ the model developed by Kumar et al. (2007) discussed in Chapter 3 because it is simpler than the synthesis model developed by Chapter 4, yet it covers key processes such as reactions, nucleation, growth and aggregation.

Figure D.1A shows the home page of Parsival, appearing after clicking the software from the windows start menus.

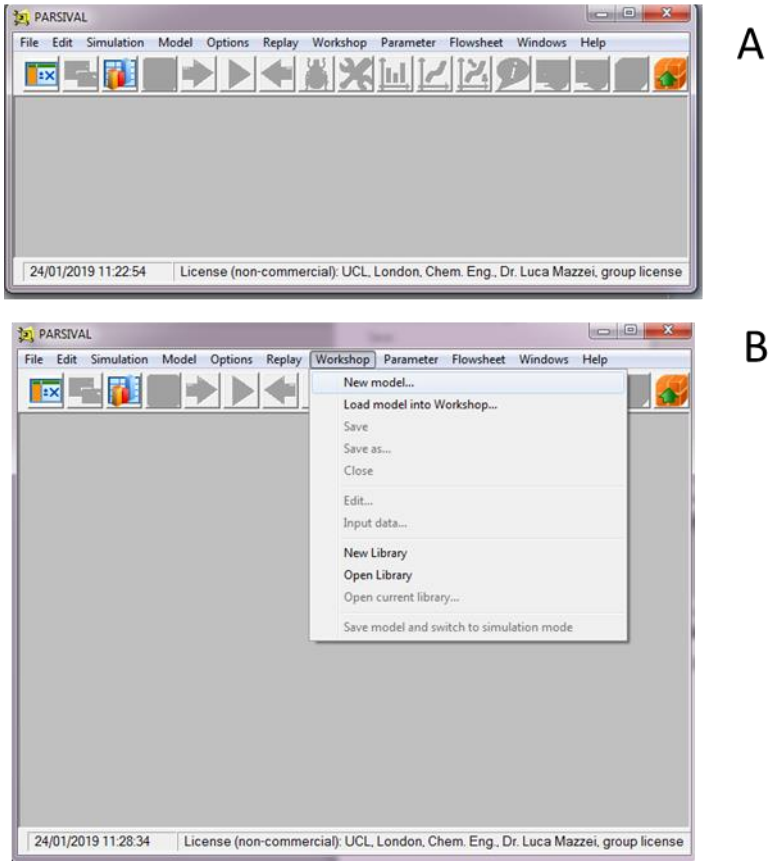

Figure D.1 - A: Showing the home page of Parsival; and, B: Showing where to click for new model.

To build a model, we left-click the workshop tab and select new model from the drop-down list, as illustrated in Figure D.1B. Doing so yields the interface in Figure D.2 called Parsival workshop. This interface comprises seven menu bars: 1) Settings, 2) Reactors, 3) Fluids, 4) Distributions, 5) Streams, 6) Coefficients, and 7) Modules. We describe the details that go into each bar as follows.

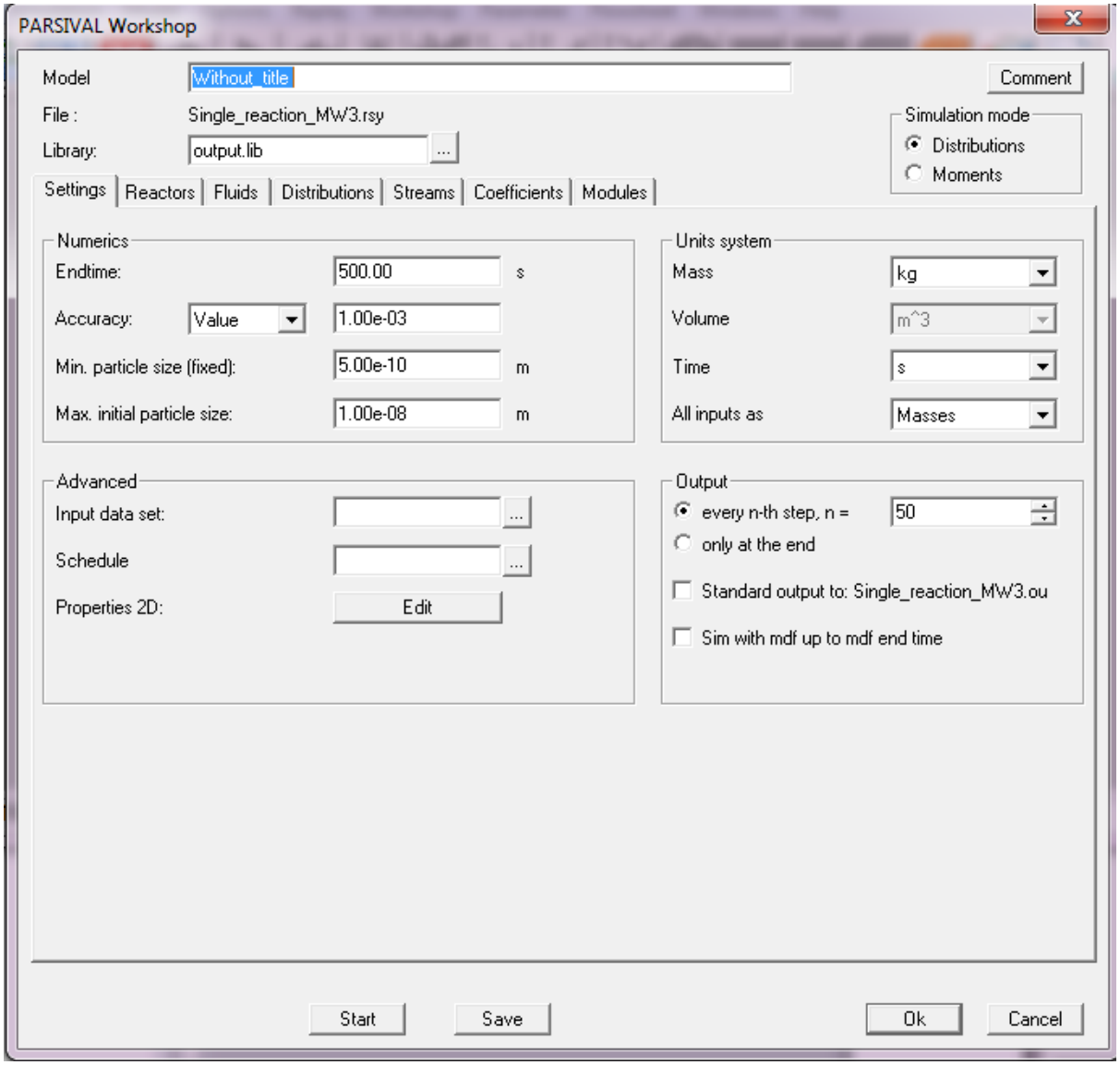

Figure D.2: Showing the Parsival workshop interface comprising seven menu bars: 1) Settings, 2) Reactors, 3) Fluids, 4) Distributions, 5) Streams, 6) Coefficients, and 7) Modules.

In the settings, we specify the simulation time in seconds in the 'Endtime' box and the numerical accuracy. For this model, as shown in Figure D.2, we have specified a simulation time of 500 s and an accuracy of 10^{-3}. Also, in the settings bar, we specify the minimum and maximum particle size, and the units system.

The second bar is for reactors, where we choose the type of reactor (batch or continuous reactor) as well as the condition of temperature. In our case, we employed a batch reactor and a synthesis temperature of 100 ^{0}C. Figure D.3A show the specifications in this bar.

The third bar is for fluids, where the components of the aqueous solution and their properties such as density and parameters such as molar masses and the initial amounts of the component in kg mass are specified. Figure D.3B shows the specifications in the third bar.

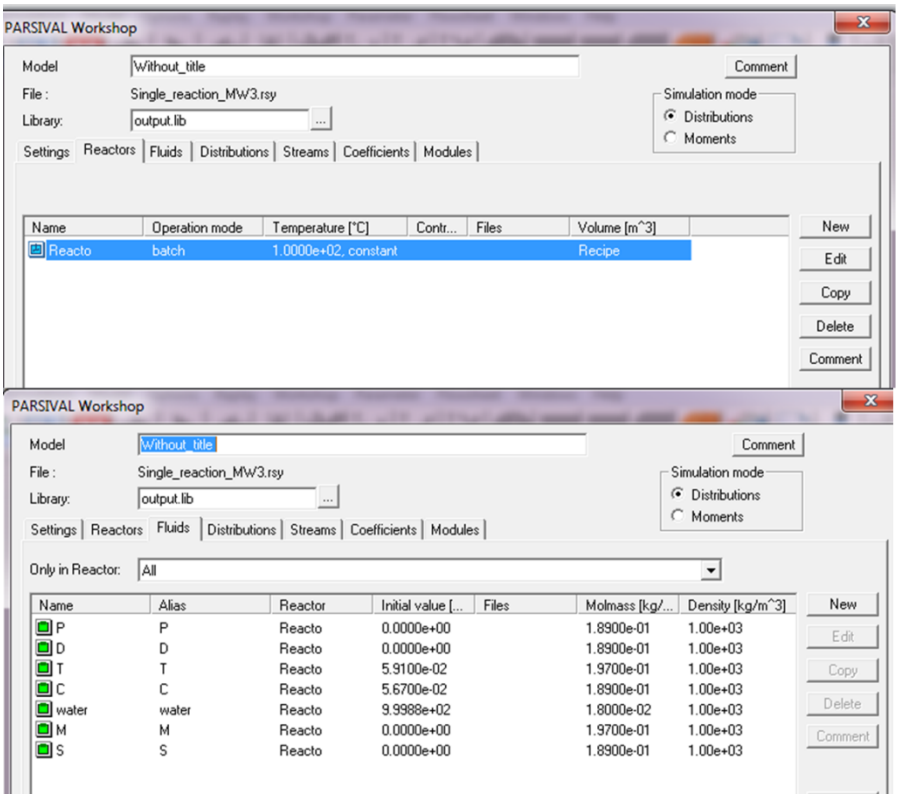

Figure D.3 - A: Showing the specifications in the second bar; and, B: Showing those in the third bar.

The fourth button is called distributions, where we specify the properties of the particle size distribution such as the mean size and standard deviation. From these parameters, Parsival constructs a Gaussian distribution of sizes. We can create more than one distribution, for example one representing particles initially present in the reactor and another representing nucleation. We also need to specify the mass of particles initial present (in our case, a negligible mass of $10^{-20}\,kg$), particle density an volume shape factor of $\pi/6 = 0.5238$. Figure D.4A shows the sub-interface of the fourth bar.

The fifth bar is specifying the inlet and outlet streams from the reactor. In our case, it is the batch reactor: no streams.

The sixth bar, called coefficients, is for specifying values of the parameters such as the rate constants. The sub-interface is shown in Figure D.4B.

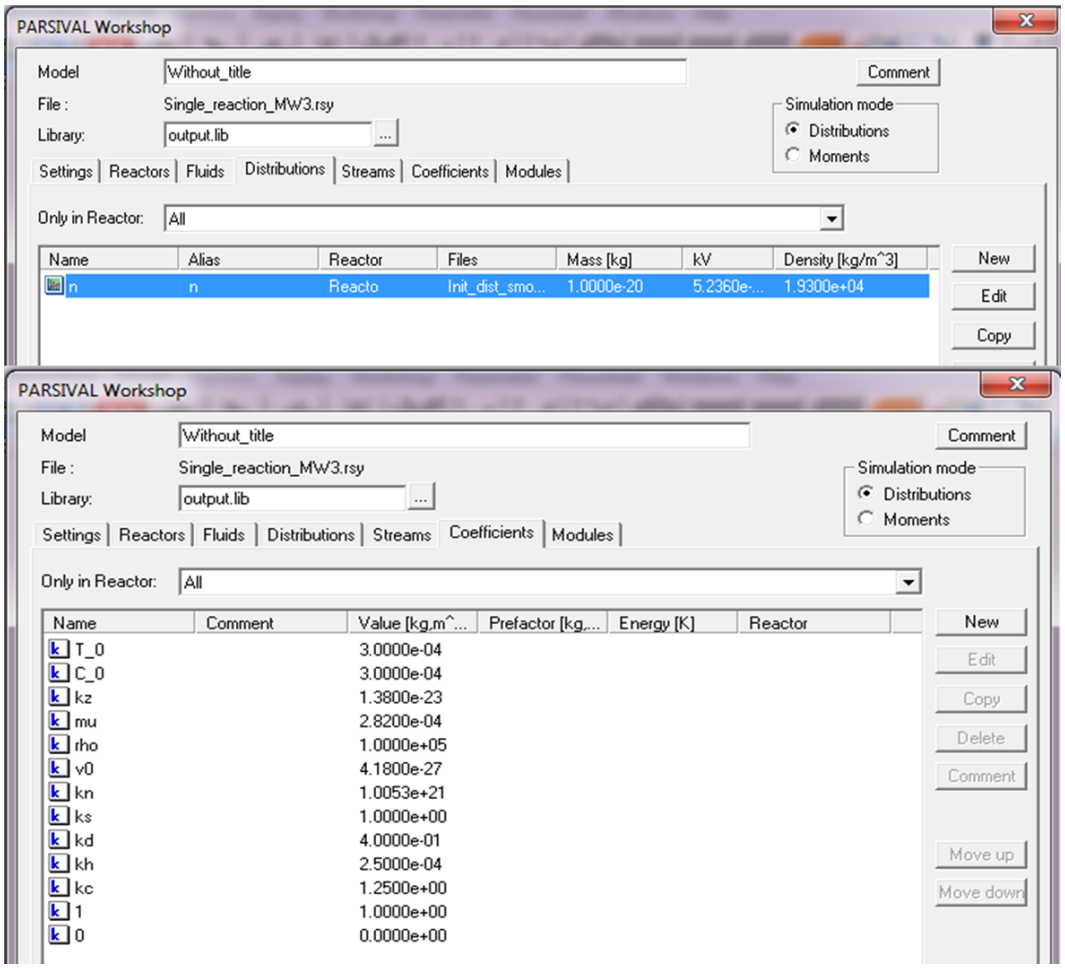

Figure D.4 – A: Showing the specifications in the fourth bar (distributions); and, B: Showing the specifications in the sixth bar (coefficients).

The seventh bar is called modules, where we build models for the processes. The required modules for our system of equations (see Section 3.3, Eqs (3.3.18) – (3.3.29) for these equations) are ODE-system for the material balance equations (describing the evolution of the fluid components); nucleation with form distribution for the expression describing the nucleation process; growth by supersaturation for the expression describing the growth process; and agglomeration (by diameter) for the expressions describing the aggregation process. Notice that the expressions describing the nucleation, growth and aggregation processes make up the population balance equation.

For the implementation of the material balance equations in the ODE-system, see Figure D.5 for the details included. First, we declare the fluid components (evolving with time). By this declaration, at each time step, Parsival feeds the amount in kg mass of each declared component into the sub-program (ODE-system). Second, we call the molecular weights of

the declared components as well as the total volume of the reaction volume. The ODE-system sub-program can now calculate the concentration of each fluid component in mol/m^3. Third, we call other parameters such as the rate constants. We can therefore build the material balance equations (describing how each component evolves with time) in the ODE-system sub-program. Notice that we have created some comments in the program for clarity.

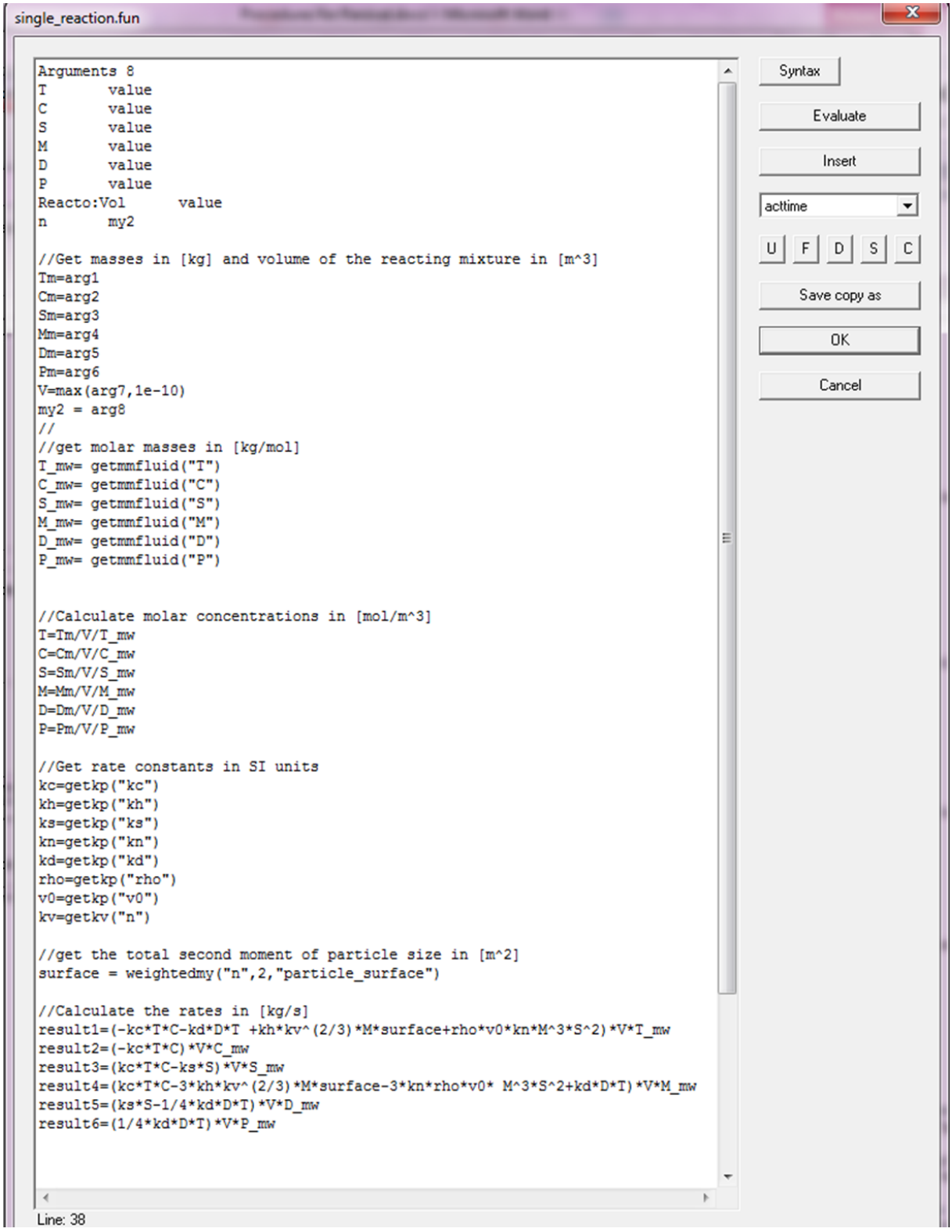

Figure D.5: Showing the details included in the ODE-system sub-program for solving the material balance equations.

For the implementation of the nucleation model in the nucleation with form distribution module, five inputs are required: the current particle size distribution (box 1), the fluid component consumed in the nucleation step (box 2), the sub-program for calculating the

nucleation rate, the particle size distribution of the nuclei (box 4), and the nucleation rate constant (box 5). Figure D.6A shows the sub-interface for the nucleation module. Of interest is the nucleation rate sub-program. Figure D.6B shows this sub-program for the model developed by Kumar et al. (2007). Other than the Dirac delta function, which is represented by a Gaussian distribution in box 4, the final expression in this sub-program is identical to Eq. (3.3.25). Before the final expression, we must declare and feed in the quantities in the expression every time step.

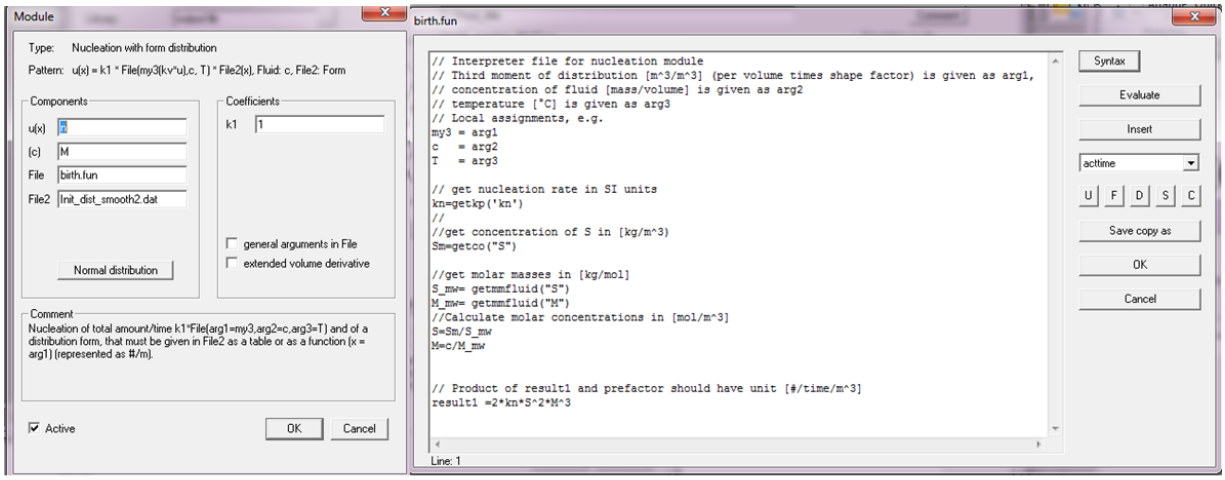

A B

Figure D.6 – A: Showing the sub-interface for the nucleation module; and, B: Showing the nucleation rate sub-program.

For the implementation of the growth sub-model in the module of growth by supersaturation, like for the nucleation module, five inputs are required: the current particle size distribution (box 1), the fluid component consumed in the growth process (box 2), the sub-program for calculating the concentration sub-program (box 3), the length sub-program (box 4), and the growth rate constant (box 5). For the growth rate expression such as Eq. (3.3.26) in Chapter 3, Parsival separates the function of size (the length sub-program) from the function of concentration (the concentration sub-program). However, this equation does not depend on size as the growth process surface-reaction controlled. Figure D.7 shows the sub-interface for the growth module, the concentration and length sub-programs. The final expression in the concentration sub-program is identical to Eq. (3.3.26) while final expression in the length sub-program is unity.

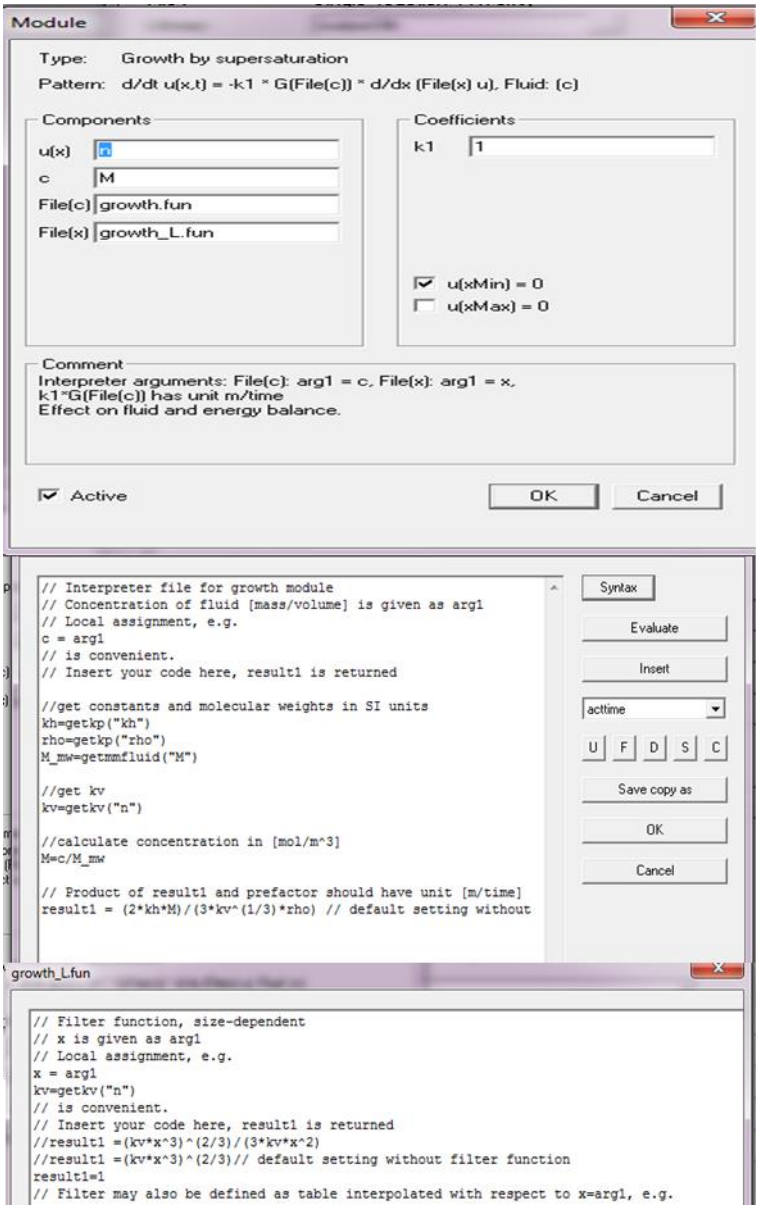

Figure D.7 – A: Showing the sub-interface for the growth module; B: Showing the concentration sub-program; and, C: Showing the length sub-program.

For the implementation of the aggregation sub-model in the module of agglomeration, four inputs are required: five inputs are also required: the two aggregating particle size distributions (basically specifying the current particle size distribution twice in boxes 1 and 2 since binary aggregation is assumed), the two sub-programs for the aggregation kernel (box 3) and the stability factor (box 4), and a constant (box 5). The multiplication product of the final expressions in these two sub-programs must yield the value of $\widetilde{\omega}_A(s,s')/W$. As in the growth module, Parsival separates the function of size from other quantities: the function of size in box 3 and other quantities in box 4. Figure D.8 shows the sub-interface for the aggregation module, the size sub-program and the subprogram for other quantities.

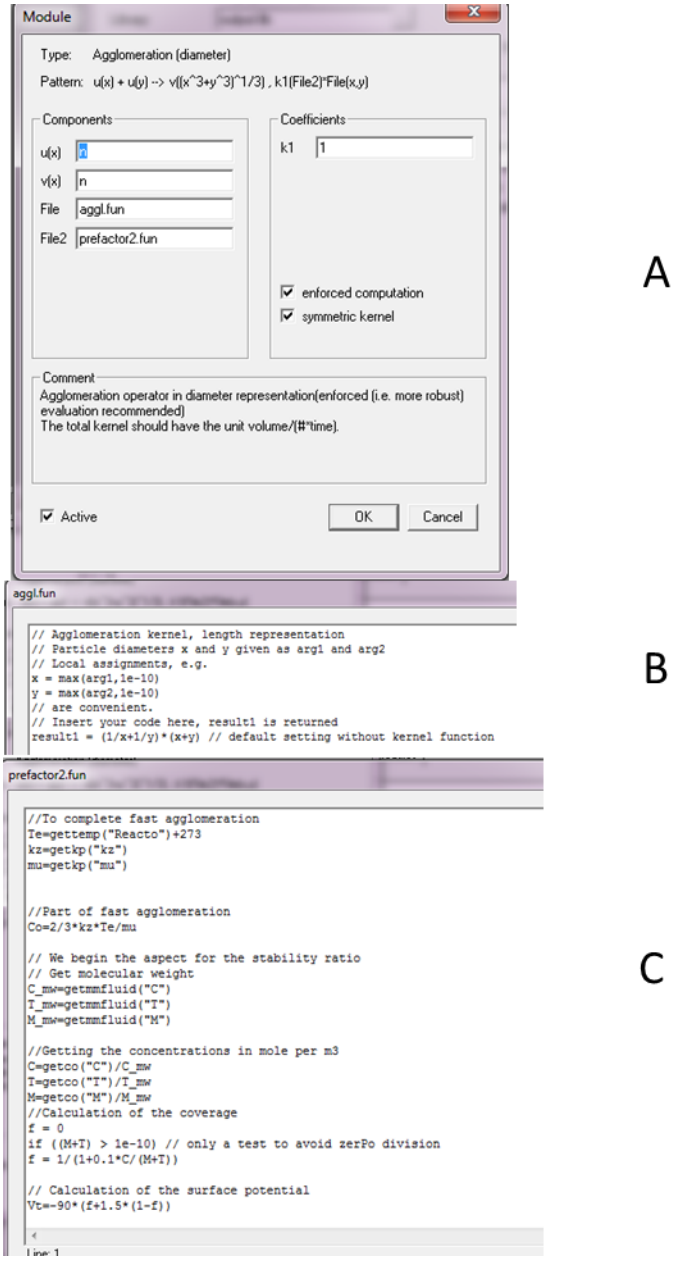

Figure D.8 – A: Showing the sub-interface for the aggregation module; B: Showing the size sub-program; and, C: Showing the subprogram for other quantities.

The implementation of the aggregation completes the procedures for building the model of Kumar et al. (2007). Therefore, the model can be solved in Parsival by clicking on the start button in Figure D.2. Similar procedures apply in implementing other model in Parsival.

D.4 Concluding remarks

Thus, from the PBM validation and convergence analysis, we can conclude that the numerical calculations in Parsival are reasonably accurate.

Appendix E

Supporting Information to Chapter 4

4.A Thermodynamics of the citrate synthesis method

In this section, we discuss the thermodynamics of the precursor and reducing agent solutions, separately; then, we discuss the thermodynamics of their mixture.

4.A.1 Thermodynamics of tetrachloroauric acid in water

Being an acid, $HAuCl_4$ shifts the equilibrium position of Eq. (4.2.1) (in the main contribution) to the left. In addition to the amounts of the components featuring in Eq. (4.2.1), we intend to determine the amounts of the other components present in the precursor solution at equilibrium; these amounts, of course, depend on the temperature of the solution. As the system evolves toward equilibrium, several reactions take place, some reactions being faster than others. While the dissociation reactions of water and acid occur nearly instantaneously (Pines et al., 1997, reported $\sim 10^{-11}\ s$ as the time scale of the dissociation reactions), the hydroxylation reactions of $AuCl_4^-$ occur much more slowly (Wuithschick et al., 2015, reported $\sim 30\ s$ as the time scale of these reactions). We assume that the precursor solution is allowed to reach the final equilibrium state at 25 ^{0}C. To synthesize the gold nanoparticles, a portion of this stock solution is subsequently heated to 100 ^{0}C. Therefore, we consider the precursor solution at 25 ^{0}C, which reaches very quickly a quasi-equilibrium state due to the dissociation reactions. Once this state has been reached, we account for the hydroxylation reactions, which occur before the solution reaches the final equilibrium state. Then, we account for the heating of the solution by considering its final equilibrium state at 100 ^{0}C.

Step 1: Quasi-equilibrium of tetrachloroauric acid in water at 25 ^{0}C

Tetrachloroauric acid completely ionizes in water according to:

$$HAuCl_4 \rightarrow H^+ + AuCl_4^- \qquad (4.A.1)$$

Based on Eqs. (4.2.1) and (4.A.1), the mixture contains H^+, $AuCl_4^-$, H_2O, and OH^-. We write the mass balance equations for these components using the following table:

Components:	H^+	OH^-	H_2O	$HAuCl_4$	$AuCl_4^-$
Symbols	A	B	C	D	E
Initial moles:	0	0	n_C^0	n_D^0	0
Moles at equilibrium:	n_A	n_B	n_C	0	n_E

The unknowns are n_A, n_B, n_C and n_E. We obtain their values by solving the mass balance equations and the equilibrium equation reported below.

Balance over the atoms:

$$H\text{: } 2n_C^0 + n_D^0 = n_A + n_B + 2n_C \qquad (4.A.2)$$

$$O\text{: } n_C^0 = n_B + n_C \qquad (4.A.3)$$

$$Au\text{: } n_D^0 = n_E \qquad (4.A.4)$$

At the quasi-equilibrium state, the amounts of Au and Cl are related; accordingly, an additional balance equation for Cl is not needed.

The equation for the equilibrium constant of the water dissociation reaction provides the last equation required to solve the problem; this reads:

$$K_{a,w} = \left(\frac{n_A}{V}\right)\left(\frac{n_B}{V}\right) \qquad (4.A.5)$$

where V denotes the volume of the solution in dm^3.

For the case of the preparation of the standard solution at 25 ^{0}C in which $C_{HAuCl_4} = 2.5 \times 10^{-4}\, M$, if we assume that $V = 1\, dm^3$, it is $n_D^0 = 2.5 \times 10^{-4}\, mol$. Also, since the molecular weight of $HAuCl_4$ is $340\ g/mol$, the mass concentration of $HAuCl_4$ is $0.085\ g/dm^3$. With $V = 1\, dm^3$, if the solution density ρ_{sol} is equal to $10^3\ g/dm^3$, the total mass of the solution is $1000\, g$; so, the mass of water is $999.915\, g$. Because the molecular weight of water is $18\, g/mol$, we obtain $n_C^0 = 55.55\, mol$.

At 25 ^{0}C, $K_{a,w} = 1 \times 10^{-14}$. Solving Eqs. (4.A.2) – (4.A.5) yields the values in Table 5.A.1.

Table 5.A.1. Mole numbers of the components present at quasi-equilibrium conditions in $1\,dm^3$ of aqueous solution of $HAuCl_4$. The initial precursor concentration is equal to $C_{HAuCl_4} = 2.5 \times 10^{-4} mol/dm^3$ in water at 25 ^{0}C.

$n_A\ (H^+)$	$2.50 \times 10^{-4}\ mol$
$n_B\ (OH^-)$	$4.00 \times 10^{-11}\ mol$
$n_C\ (H_2O)$	$55.55\ mol$
$n_E\ (AuCl_4^-)$	$2.50 \times 10^{-4}\ mol$
pH	3.60

Having taken the total mixture volume equal to $1\ dm^3$, one finds that the numerical values of the component amounts in moles and of the component concentrations in mol/dm^3 are the same. Thus, at quasi-equilibrium, $C_{OH^-} \ll C_{AuCl_4^-} \cong C_{HAuCl_4} \cong C_{H^+}$. We conclude that the amount of OH^- is insufficient to cause significant hydroxylation of $AuCl_4^-$. Nonetheless, because of the sensitivity of the synthesis to small amounts of either H^+ or OH^-, we consider these reactions in the following section.

Step 2: Final equilibrium of tetrachloroauric acid in water at 25 ^{0}C

According to the literature, the speciation of the tetrachloroauric acid is given by the reactions:

$$AuCl_4^- + OH^- \rightleftarrows AuCl_3(OH)^- + Cl^- \qquad K_{P1} \qquad (4.A.6)$$

$$AuCl_3(OH)^- + OH^- \rightleftarrows AuCl_2(OH)_2^- + Cl^- \qquad K_{P2} \qquad (4.A.7)$$

$$AuCl_2(OH)_2^- + OH^- \rightleftarrows AuCl(OH)_3^- + Cl^- \qquad K_{P3} \qquad (4.A.8)$$

$$AuCl(OH)_3^- + OH^- \rightleftarrows Au(OH)_4^- + Cl^- \qquad K_{P4} \qquad (4.A.9)$$

where the K_{Pi}'s are the equilibrium constants of the reactions. The values of these four constants at 20 ^{0}C are $3.98 \times 10^{-6}, 3.98 \times 10^{-7}$, 3.16×10^{-8} and 5.01×10^{-9}, respectively (Ojea-Jiménez and Campanera, 2012; Goai and Matijevic, 1999). To obtain their values at 25 ^{0}C, we use the following equation (Sandler, 2006):

$$K_a = \exp\left(-\frac{\Delta G^0}{RT}\right) \quad \rightarrow \quad \Delta G^0 = -RT \ln K_a \qquad (4.A.10)$$

where K_a is the equilibrium constant of a generic reaction, ΔG^0 is the Gibbs free energy change for the reaction at the standard state of both reactants and products, T is the temperature in Kelvin and R is the universal gas constant.

From this equation, we obtain ΔG^0 for reactions (4.A.6) – (4.A.9) as $(3.02,\ 3.59,\ 4.20$ and $4.65) \times 10^4\ J/mol$, respectively. Thus, at 25 ^{0}C, the values of the K_{Pi} are 4.90×10^{-6}, 5.13×10^{-7}, 4.57×10^{-8} and 6.92×10^{-9}, respectively.

Solving the mass balance equations for the atoms involved in the reactions and the equilibrium equations for the reactions yields the results reported in Table 4.A.2.

Table 4.A.2. Mole numbers of the components present at final equilibrium conditions in 1 dm^3 of aqueous solution of $HAuCl_4$. The initial precursor concentration is equal to $C_{HAuCl_4} = 2.5 \times 10^{-4} mol/dm^3$ in water at $25\,^0C$.

$n_A\ (H^+)$	$2.50 \times 10^{-4}\ mol$
$n_B\ (OH^-)$	$4.00 \times 10^{-11}\ mol$
$n_C\ (H_2O)$	$55.55\ mol$
$n_E\ (AuCl_4^-)$	$2.50 \times 10^{-4}\ mol$
$n_F\ (AuCl_3(OH)^-)$	$2.21 \times 10^{-10}\ mol$
$n_G\ (AuCl_2(OH)_2^-)$	$2.06 \times 10^{-17}\ mol$
$n_H\ (AuCl(OH)_3^-)$	$1.69 \times 10^{-25}\ mol$
$n_I\ (Au(OH)_4^-)$	$1.56 \times 10^{-34}\ mol$
$n_J\ (Cl^-)$	$2.21 \times 10^{-10}\ mol$
pH	3.60

The results indicate that $HAuCl_4$ exists almost entirely as $AuCl_4^-$ ion in water at 25 ^{0}C as the hydroxylated species of the precursor are present in negligible amounts, and the final pH remains unchanged from the value reported in Table 4.A.1.

As the synthesis is usually carried out at 100 ^{0}C, we now consider how the amounts of the components in Table 4.A.2 change on heating the solution.

Step 3: Final equilibrium of tetrachloroauric acid in water at 100 ^{0}C

To determine the equilibrium amounts at 100 ^{0}C, we write and solve again material balance equations for the atoms involved in the reactions and equilibrium equations for the reactions with the values of the equilibrium constants at 100 ^{0}C. Using Eq. (4.A.10), we find that $K_{a,w} = 6.46 \times 10^{-12}$ and the values of the K_{Pi}'s are 5.75×10^{-5}, 9.33×10^{-6}, 1.29×10^{-6}

and 3.02×10^{-7}, respectively. With the previous initial data ($n_D^0 = 2.5 \times 10^{-4}\, mol$ and $n_C^0 = 55.55\, mol$ contained in $1\ dm^3$ of solution), the results are shown in Table 4.A.3.

Table 4.A.3. Mole numbers of the components present at final equilibrium conditions in 1 dm^3 of aqueous solution of $HAuCl_4$. The initial precursor concentration is equal to $C_{HAuCl_4} = 2.5 \times 10^{-4} mol/dm^3$ in water at $100\ ^0$C.

$n_A\ (H^+)$	$2.50 \times 10^{-4}\ mol$
$n_B\ (OH^-)$	$2.61 \times 10^{-8}\ mol$
$n_C\ (H_2O)$	$55.55\ mol$
$n_E\ (AuCl_4^-)$	$2.50 \times 10^{-4}\ mol$
$n_F\ (AuCl_3(OH)^-)$	$1.94 \times 10^{-8}\ mol$
$n_G\ (AuCl_2(OH)_2^-)$	$2.44 \times 10^{-13}\ mol$
$n_H\ (AuCl(OH)_3^-)$	$4.20 \times 10^{-19}\ mol$
$n_I\ (Au(OH)_4^-)$	$1.01 \times 10^{-25}\ mol$
$n_J\ (Cl^-)$	$1.94 \times 10^{-8}\ mol$
pH	3.60

The amounts of the hydroxylated species of the precursor have increased from those in Table 4.A.2. For instance, the amount of $Au(OH)_4^-$ has increased by nine orders of magnitude. Nevertheless, the sum of the amounts of the four hydroxylated species is negligible as the precursor exists almost entirely as $AuCl_4^-$. Similarly, although the amount of OH^- has increased by three orders of magnitude, the value of the mixture pH remains unchanged. To increase the amount of OH^-, we need to add a base to the solution. In the Turkevich synthesis, an aqueous solution of sodium citrate, which is a weak base, is added to the precursor solution. The primary purpose of adding (tri)sodium citrate is to reduce the gold (in $AuCl_4^-$, $AuCl_3(OH)^-$, $AuCl_2(OH)_2^-$, $AuCl(OH)_3^-$ and $Au(OH)_4^-$) existing at $+3$ oxidation state to atomic gold, whose oxidation state is zero. To simplify our analysis, in the main contribution we consider only $AuCl_4^-$ and $AuCl_3(OH)^-$ as the existing forms of the precursor. We neglect higher hydroxylated forms, because, as shown in Tables 4.A.2 and 4.A.3 and as reported by Peck et al. (1991), they are present in negligible amounts within the range of pH of interest for the synthesis. In the next section, we consider the thermodynamics of the reducing agent solution (sodium citrate dissolved in water).

4.A.2 Thermodynamics of sodium citrate in water

Apart from being the synthesis reducing agent, an aqueous solution of sodium citrate is a weak base. To illustrate this, in this section we determine the components of the solution and their amounts at equilibrium. Wuithschick et al. (2015) observed that the solution reaches a final equilibrium state in less than $2\,s$. Consequently, unlike in the previous section, we only consider the final equilibrium state of the solution at the preparation and synthesis temperatures of 25 and 100 ^{0}C, respectively.

Step 1: Final equilibrium of sodium citrate in water at 25 ^{0}C

Sodium citrate first ionises completely as:

$$Na_3Ct \rightarrow 3Na^+ + Ct^{3-} \qquad (4.A.11)$$

Citrate subsequently interacts with H^+, produced due to the reaction in Eq. (4.2.1), as:

$$Ct^{3-} + H^+ \rightleftarrows CtH^{2-} \qquad 1/K_{R3} \qquad (4.A.12)$$

$$CtH^{2-} + H^+ \rightleftarrows CtH_2^- \qquad 1/K_{R2} \qquad (4.A.13)$$

$$CtH_2^- + H^+ \rightleftarrows CtH_3 \qquad 1/K_{R1} \qquad (4.A.14)$$

where the K_{Ri}'s are the equilibrium constants, whose values at 25 ^{0}C are 7.41×10^{-4}, 1.74×10^{-5} and 3.98×10^{-7}, respectively (Serjeant and Dempsey, 1979).

The reactions in Eqs. (4.A.12) – (4.A.14) occur significantly in less than $2\,s$ (Wuithschick et al., 2015). Solving the material balance equations for the atoms involved in the reactions and the equilibrium equations for the reactions yields the results in Table 4.A.4 if the initial concentration of Na_3Ct is $C_{Na_3Ct} = 0.194\,mol/dm^3$. This is the initial concentration of the reducing agent solution employed by Ji et al. (2007). When compared to the precursor solution, it is three orders of magnitude more concentrated. As we see in Section 4.A.3, however, only a small volume of this solution is added to the precursor solution to form the synthesis solution. With such a small addition of reducing agent solution, the initial concentrations of tetrachlorauric acid in the precursor solution and in the synthesis solution are essentially equal.

Table 4.A.4. Mole numbers of the components present at equilibrium conditions in 1 dm^3 of aqueous solution of Na_3Ct. The initial reducing agent concentration is equal to $C_{Na_3Ct} = 0.194\ mol/dm^3$ in water at 25 ^{0}C.

$n_A\ (H^+)$	$1.18 \times 10^{-10}\ mol$
$n_B\ (OH^-)$	$8.46 \times 10^{-5}\ mol$
$n_C\ (H_2O)$	$52.78\ mol$
$n_D\ (CtH_3)$	$9.07 \times 10^{-17}\ mol$
$n_E\ (CtH_2^-)$	$5.77 \times 10^{-10}\ mol$
$n_F\ (CtH^{2-})$	$8.46 \times 10^{-5}\ mol$
$n_G\ (Ct^{3-})$	$0.1939\ mol$
$n_I\ (Na^+)$	$0.5820\ mol$
pH	9.93

The results indicate that at 25 ^{0}C the solution is alkaline, because the value of the pH is higher than the neutral pH of 7. In comparison with Table 4.A.2, the amount of OH^- in the aqueous solution of sodium citrate is larger than that in the aqueous solution of tetrachloroauric acid by six orders of magnitude. Thus, this amount can hydroxylate $AuCl_4^-$ into $AuCl_3(OH)^-$.

The results also indicate that citrate exists almost entirely as Ct^{3-} ion in water at this condition of pH and temperature. To analyse the effect of heating, we consider the solution at $100\,^0C$.

Step 2: Final equilibrium of sodium citrate in water at 100 ^{0}C

To determine the equilibrium amounts of the components at 100 ^{0}C, we solve again the material balance equations and the equilibrium equations using the values of the equilibrium constants at this temperature. Using Eq. (4.A.10), at 100 ^{0}C, $K_{a,w} = 6.46 \times 10^{-12}$, while the values of the K_{Ri}'s are 3.16×10^{-3}, 1.58×10^{-4} and 7.76×10^{-6}, respectively. With the previous initial data, $n^0_{Na_3Ct} = 0.194\ mol$ and $n^0_C = 52.78\ mol$ in 1 dm^3 of solution, the results are shown in Table 4.A.5.

Table 4.A.5. Mole numbers of the components present at equilibrium conditions in 1 dm^3 of aqueous solution of Na_3Ct. The initial reducing agent concentration is equal to $C_{Na_3Ct} = 0.194\ mol/dm^3$ in water at $100\ ^0C$.

$n_A\ (H^+)$	$1.52 \times 10^{-8}\ mol$
$n_B\ (OH^-)$	$4.24 \times 10^{-4}\ mol$
$n_C\ (H_2O)$	$52.78\ mol$
$n_D\ (CtH_3)$	$1.89 \times 10^{-13}\ mol$
$n_E\ (CtH_2^-)$	$4.27 \times 10^{-8}\ mol$
$n_F\ (CtH^{2-})$	$4.24 \times 10^{-4}\ mol$
$n_G\ (Ct^{3-})$	$0.1936\ mol$
$n_I\ (Na^+)$	$0.5820\ mol$
pH	7.82

Note that the neutral pH at $100\ ^0C$ is 5.59. Thus, from the results, because the pH value is higher than this value, the aqueous solution of Na_3Ct is still alkaline. The amount of OH^- has increased by about an order of magnitude from the value at $25\ ^0C$ to $4.24 \times 10^{-4}\ mol$. Consequently, OH^- can significantly hydroxylate $AuCl_4^-$ to $AuCl_3(OH)^-$ when the solutions of the precursor and reducing agent are mixed.

4.A.3 Mixture of precursor and reducing agent solutions

In this section, we determine the amounts at quasi-equilibrium of the components in the solution obtained by mixing the precursor and reducing agent solutions. Here, by quasi-equilibrium we mean the state that the resulting solution reaches after mixing the precursor and reducing agent solutions and after the fast reactions involving H^+ in Eq. (4.A.12) – (4.A.14) have reached equilibrium, but before the synthesis reactions of $AuCl_4^-$ (hydroxylation and reduction reactions) have started occurring significantly. When the two solutions are mixed, in less than 2 s the following reactions reach equilibrium:

$H_2O \rightleftarrows H^+ + OH^-$ $K_{a,w}$ (reaction 1)

$CtH_3 \rightleftarrows CtH_2^- + H^+$ K_{R1} (reaction 2)

$CtH_2^- \rightleftarrows CtH^{2-} + H^+$ K_{R2} (reaction 3)

$CtH^{2-} \rightleftarrows Ct^{3-} + H^{+}$ K_{R3} (reaction 4)

At 100 ^{0}C, the value of $K_{a,w}$ is 6.46×10^{-12} and those of the K_{Ri}'s are 3.16×10^{-3}, 1.58×10^{-4} and 7.76×10^{-6}, respectively.

In preparing the synthesis solution, previous authors such as Turkevich et al. (1951), Frens (1973), Ji et al. (2007) and Wuithschick et al. (2015) kept the initial concentration of tetrachloroauric acid constant at about $0.25 \times 10^{-3}\ mol/dm^3$ by adding a small volume of the reducing agent solution to a large volume of the precursor solution. For example, in preparing the standard synthesis solution, Wuithschick et al. (2015) mixed $199\ cm^3$ of $0.25 \times 10^{-3}\ mol/dm^3$ precursor solution with $1\ cm^3$ of $0.5\ mol/dm^3$ reducing agent solution. In preparing other synthesis solutions, however, the previous authors did not report the volumes of the precursor and reducing agent solutions combined. Instead, they reported the concentrations of the precursor and reducing agent in the synthesis solution. These concentrations are what we need for the present analysis.

To determine the amounts of the components at quasi-equilibrium, we employ the smallest initial molar ratio of citrate to gold with a value of 0.7 in the data of Ji et al., who reported the initial concentrations of the precursor and reducing agent in the synthesis solution as $C_{HAuCl_4,0} = 0.25 \times 10^{-3}\ mol/dm^3$ and $C_{Na_3Ct,0} = 0.175 \times 10^{-3}\ mol/dm^3$, respectively. (Notice that the concentration of the reducing agent solution in Section 4.A.2 was $0.194\ mol/dm^3$, which is about three orders of magnitude larger than that in the synthesis solution. Ji et al. obtained this synthesis solution by mixing $100\ cm^3$ of $0.25 \times 10^{-3}\ mol/dm^3$ precursor solution with $0.09\ cm^3$ of $0.194\ mol/dm^3$ reducing agent solution). With these initial concentrations, assuming that amounts of the order of $10^{-8}\ mol$ (or smaller) in the volume of the resulting mixture are negligible, solving the material balance equations for the atoms and the equilibrium equations for the reactions, yields the results given in Table 4.A.6.

Table 4.A.6. Mole numbers of the components present at quasi-equilibrium conditions following the speciation of citrate for $C_{HAuCl_4,0} = 0.25 \times 10^{-3}\ mol/dm^3$ and $C_{Na_3Ct,0} = 0.175 \times 10^{-3}\ mol/dm^3$ at $100\ ^{0}C$ in $1\ dm^3$ of synthesis solution.

$n_A(H^+)$	$5.24 \times 10^{-5}\ mol$
$n_B(OH^-)$	$1.23 \times 10^{-7}\ mol$
$n_C\ (H_2O)$	$55.55\ mol$
$n_D(CtH_3)$	$6.45 \times 10^{-7}\ mol$

$n_E(CtH_2^-)$	$3.90 \times 10^{-5}\ mol$
$n_F(CtH^{2-})$	$1.18 \times 10^{-4}\ mol$
$n_G(Ct^{3-})$	$1.75 \times 10^{-5}\ mol$
$n_H(Na^+)$	5.25×10^{-4}
$n_I(AuCl_4^-)$	2.50×10^{-4}
pH	4.28

We see that all the citrate species, but CtH_3, are in significant amounts. Similarly, as expected, because the molar ratio of the initial concentration of sodium citrate to tetrachloroauric acid is 0.7, the mixture at quasi-equilibrium is still acidic, but less than the initial precursor solution. In the synthesis solution, keeping the initial amount of tetrachloroauric acid constant at $C_{HAuCl_4,0} = 0.25 \times 10^{-3}\ mol/dm^3$ and increasing the initial amount of sodium citrate $C_{Na_3Ct,0}$ would make the quasi-equilibrium pH increase. At a certain point, the quasi-equilibrium pH would exceed the neutral pH of 5.59, making the solution basic.

4.B Experimental evidence for the seed-mediated mechanism

In this section, we first show that the growth step in the citrate method is controlled by surface reaction and then we calculate the value of the rate constant k_g.

4.B.1 Growth step controlling mechanism

In Figure 2(d) of the article of Polte et al. (2010), reproduced in Figure 4.B.1, over the first 20 min of the synthesis the mean particle radius increases from about $2\ nm$ to about $3.6\ nm$, while the number of particles decreases to roughly 20% of the initial value measured at t~0 min. This decrease in the particle number indicates that on average five primary nanoparticles aggregate into one nanoparticle. To estimate the mean radius r_a of the aggregate, we assume that its volume equals the sum of the volumes of the five primary particles. Thus, we have:

$$r_a{}^3 = 5 \times 2^3 \quad \rightarrow \quad r_a = 3.42\ nm \qquad (4.B.1)$$

This value is approximately equal to the mean radius of about $3.6\ nm$ measured at 20 min. After this time, we can observe that the number of particles is almost constant at 20% of the initial value. We can therefore conclude that the time scale of the aggregation process at

$75\ ^0C$ is about 20 min. Within this time interval, the size increase owing to particle growth is negligible; growth occurs significantly only after, increasing the mean radius from $3.6\ nm$ to $\sim 7\ nm$ in ~ 40 mins. The length of this time interval coincides with the time scale of the growth step. Therefore, the processes of aggregation and growth are decoupled in time, consistently with the seed-mediated mechanistic description of Wuithschick et al. (2015).

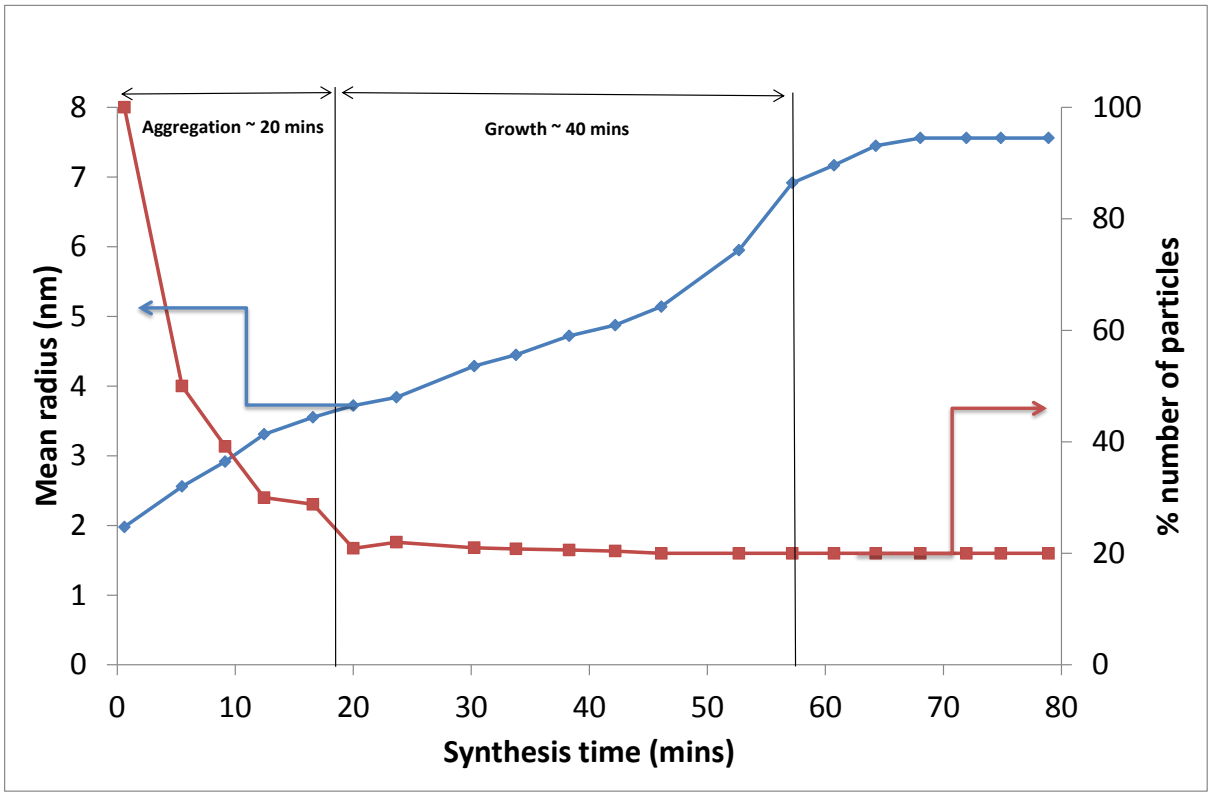

Figure 4.B.1. Evolution of the mean radius and of the percentage number of particles in the citrate synthesis method. The values of the initial concentrations of $HAuCl_4$ and Na_3Ct in the synthesis solution are $0.25\ mol/m^3$ and $2.5\ mol/m^3$, respectively. The mixture temperature is $75\ ^0C$. Data reproduced from Figure 2(d) of Polte et al. (2010).

Furthermore, this figure reveals that, between 20 and 60 min, the slope of the curve is almost constant over a large period of time, increasing slightly around the time of 60 min. For growth controlled by mass transfer, the slope, which is the growth rate, should decrease with size (Viswanatha and Sarma, 2007). However, because the growth rate is constant with the particle size over a large time interval, we assume the surface reaction process controls particle growth in the citrate synthesis method. After about 60 min from the start of the synthesis, the growth rate declines because of the depletion of the driving force (that is, of the concentration of $AuCl_3(OH)^-$).

4.B.2 Calculation of the growth rate k_g

To determine the value of k_g at 75 ^{0}C, we consider in Figure 4.B.1 the time interval between 20 and 45 min. In this region only particle growth is present; the particle number density is constant, since particles have stopped aggregating. Furthermore, the growth rate is constant, indicating growth is controlled by surface reaction. The number of particles is equal to the final number of GNPs per unit volume, which we denote as N_P. Within this time interval, we can express C_{Au}, that is, the amount of gold atoms present in the particle phase per unit volume of synthesis solution, as follows:

$$C_{Au} = N_P \rho m_v {s_m}^3 \quad (4.B.2)$$

where ρ is the molar density of gold, taken as $10^5\ mol/m^3$, m_v is the particle volume shape factor (which we set equal to $\pi/6$, assuming that the particles are spherical), and s_m is the (time-dependent) mean particle diameter. Also, it is:

$$A = N_P m_a {s_m}^2 \quad (4.B.3)$$

where m_a is the particle area shape factor (which we set equal to π, assuming that the particles are spherical). Substituting for C_{Au} and A in Eq. (4.3.16), we have:

$$3N_P \rho m_v {s_m}^2 \frac{ds_m}{dt} = N_P m_a {s_m}^2 k_g\ C_{AuCl_3(OH)^-}\ C_{CtH^{2-}}$$

This reduces to:

$$\frac{ds_m}{dt} = \left(\frac{m_a}{3\rho m_v}\right) k_g C_{AuCl_3(OH)^-}\ C_{CtH^{2-}} \quad (4.B.4)$$

Within the time interval between 20 and 45 min in Figure 4.B.1, we consider four points from the radius-time curve, specifically those at 25, 30, 35 and 40 min. At these times, we can calculate the corresponding values of ds_m/dt, which is equal to twice the slope of the curve; the results are $1.13 \times 10^{-3}, 1.13 \times 10^{-3}, 1.01\ \times 10^{-3}$ and $6.57 \times 10^{-4}\ nm/s$, respectively.

To obtain the corresponding values of $C_{AuCl_3(OH)^-}$, we operated as follows. We first calculated N_P using the values of the initial precursor concentration in the synthesis solution (equal to $0.25\ mol/m^3$) and of the final mean particle diameter s_f (equal to $15\ nm$). Because all the gold contained in the precursor eventually forms gold nanoparticles, we can write:

$$N_P = \frac{0.25\ mol/m^3}{\rho m_v {s_f}^3} = \frac{0.25\ mol/m^3}{1 \times 10^5\ mol/m^3 \times \pi/6 \times (15 \times 10^{-9})^3} = 1.41 \times 10^{18}\ 1/m^3$$

Assuming a reactor volume of $1\ m^3$, the amount of gold in the particles in moles is equal, at any given time between 20 and 45 min, to $1.41 \times 10^{18} \times \rho m_v {s_m}^3$. At the synthesis time of 25

min, $s_m = 7.86\,nm$, and so the value is $1.41 \times 10^{18} \times 1 \times 10^{5} \times \pi/6 \times (7.86 \times 10^{-9})^3 = 0.036\,mol$. Then, at the synthesis time of 25 min, the amount of $AuCl_3(OH)^-$ in moles is given by the difference between the initial amount of precursor in moles and the current amount of gold present in the particles in moles, i.e. $0.25 - 0.036\,mol = 0.214\,mol$.

Analogously, at synthesis times of 30, 35, and 40 min, from Figure 4.B.1 we obtain $s_m = 8.54$, 9.04, and $9.56\,nm$, respectively. The corresponding amounts of gold in the particles at these times are 0.046, 0.055 and $0.065\,mol$, respectively. As above, we use the differences between the initial amount of 0.25 mol and these amounts of gold in the particles to calculate the amounts of $AuCl_3(OH)^-$ present in the mixture at the three synthesis times considered. As we will see shortly, the same amounts of gold in the particles can be used to calculate the amounts of CtH^{2-} at the different times considered. For the time being, by deducting these amounts from the initial amount of $0.25\,mol$, we find that the amounts of $AuCl_3(OH)^-$ are 0.204, 0.195 and $0.185\,mol$ at 30, 35, and 40 min, respectively. Based on the assumption of $1\ m^3$ of synthesis solution, $C_{AuCl_3(OH)^-}$ is 0.214, 0.204, 0.195 and $0.185\ mol/m^3$ at times 25, 30, 35, and 40 min, respectively.

In the synthesis solution, the initial concentration of Na_3Ct is equal to $2.5\ mol/m^3$. This value is ten times larger than that of the precursor. Given the stoichiometric ratio of the reduction of the precursor as 1.5 (Kumar et al., 2007) and the amount of gold in the particle phase, we can calculate the amounts of citrate consumed as CtH_2^- while reducing $AuCl_4^-$ and as CtH^{2-} while reducing $AuCl_3(OH)^-$. Then, we use the difference between the initial amount of $2.5\ mol$ in $1\ m^3$ synthesis solution and these consumed amounts to calculate the total amount of all citrate species Ct left in $1\ m^3$ of synthesis solution. This amount is distributed among the four citrate species according to their relative mole fractions in Figure 4.C.1 in Section 4.C once the reaction pH is specified. Since the initial molar ratio of sodium citrate to tetrachloroauric acid is greater than five, as discussed in the main contribution, the reaction pH is approximately equal to the pH value at quasi-equilibrium. Following the reasoning in Section 4.A, the pH value at quasi-equilibrium after the precursor and reducing agent solutions are mixed to obtain the synthesis solution, which contains $0.25\ mol/m^3$ $HAuCl_4$ and $2.5\ mol/m^3$ Na_3Ct at $75\ ^0C$, is 6.43, whilst the corresponding values of the relative mole fractions among the four citrate species are 7.48×10^{-8}, 4.32×10^{-4}, 9.97×10^{-2} and 0.9 for CtH_3, CtH_2^-, CtH^{2-} and Ct^{3-}, respectively.

From the amounts of gold in the particles at 25, 30, 35 and 40 min, previously calculated as 0.036, 0.046, 0.055 and $0.065\,mol$, respectively, we can now determine the total amounts of Ct consumed as CtH_2^- in the reduction step and as CtH^{2-} in the surface reduction of the growth step. The sum of these amounts is 1.5 times the amounts of gold in the particles. At

25 min, this sum is given by $0.054\,mol$. By deducting this amount from the initial amount of $2.5\,mol$, we obtain the amount of Ct left, given by $2.45\,mol$. Then, using the relative molar fraction of CtH^{2-} reported above (which is equal to 9.97×10^{-2}), we can calculate the amount of CtH^{2-} present at 25 min in the synthesis solution as $9.97 \times 10^{-2} \cdot 2.45 = 0.244\,mol$. We operate analogously for the three other times of 30, 35 and 40 min; the amounts of CtH^{2-} obtained are 0.242, 0.241, and $0.240\,mol$, respectively. Based on the assumption that the volume of the synthesis solution is $1\ m^3$, $C_{CtH^{2-}}$ becomes 0.244 , 0.242, 0.241 and $0.240\ mol/m^3$, respectively.

Now that we know the values of the variables ds_m/dt, $C_{AuCl_3(OH)^-}$ and $C_{CtH^{2-}}$ in the synthesis solution at the times 25, 30, 35 and 40 min, we can use Eq. (4.B.4) to calculate the respective values of the rate constant k_g. To do so, we can adopt two alternative approaches. We substitute the values of ds_m/dt, $C_{AuCl_3(OH)^-}$ and $C_{CtH^{2-}}$ at times 25, 30, 35 and 40 min into Eq. (4.B.4), to obtain four corresponding rate constants. Then, from these values, we calculate the average value and use it as the value of k_g in the model. Alternatively, we substitute the average values of ds_m/dt, $C_{AuCl_3(OH)^-}$ and $C_{CtH^{2-}}$ into Eq. (4.B.4) to obtain the value for k_g.

We first follow the first approach. At 25 min, the values of ds_m/dt, $C_{AuCl_3(OH)^-}$ and $C_{CtH^{2-}}$ are $2.27 \times 10^{-3}\ nm/s$, $0.214\ mol/m^3$ and $0.244\ mol/m^3$, respectively; so, the resulting value of k_g is $2.17 \times 10^{-6}\,m^4/(mol.s)$. For the other synthesis times, the values are 2.29×10^{-6}, 2.14×10^{-6} and $1.48 \times 10^{-6}\,m^4/(mol.s)$, respectively. These four values yield an average value of $2.0 \times 10^{-6}\,m^4/(mol.s)$.

On the other hand, we substitute the average values of ds_m/dt, $C_{AuCl_3(OH)^-}$ and $C_{CtH^{2-}}$ into Eq. (4.B.4) to obtain one single value for k_g. Over the four synthesis times, the average values of ds_m/dt, $C_{AuCl_3(OH)^-}$ and $C_{CtH^{2-}}$ result to be $1.96 \times 10^{-12}\,m/s$, $0.200\ mol/m^3$, and $0.242\ mol/m^3$, respectively. From these values, the value of k_g is $2.0 \times 10^{-6}\,m^4/(mol.s)$. The values of k_g from these two approaches are identical, yielding $k_g = 2.0 \times 10^{-6}\,m^4/(mol.s)$ at 75 ^{0}C.

4.C Quasi-equilibrium and pH calculations

In this section, we show that Eq. (4.3.27) is valid for initial molar ratios of citrate to gold equal to or greater than five.

To use Eq. (4.3.26) to calculate S, we need the time profiles of $C_{AuCl_4^-}$, $C_{CtH_2^-}$ and C_{OH^-}. However, we do not have all the necessary information to determine them. To overcome

this, we assume a particular profile for each reactant based on the initial and final values of $C_{AuCl_4^-}$, $C_{CtH_2^-}$ and C_{OH^-}. For the initial values, we use those present at quasi-equilibrium, because the reactions involving H^+ ions taking place before the quasi-equilibrium state is reached can be regarded as instantaneous. For the final values, we use the reported experimental values that refer to the end of the synthesis. Because past researchers have reported complete conversion of the precursor into GNPs when the pH value of the reaction condition measured at 25 ^{0}C is in the range 3 – 8, we can assume that at the end of the synthesis $C_{AuCl_4^-}$ vanishes. We cannot, however, do the same for $C_{CtH_2^-}$ and C_{OH^-}, because the synthesis is usually carried out with excess of sodium citrate. In theory, for conditions with excess of sodium citrate, we can calculate the residual amount (at the end of the synthesis) of Ct, representing the sum of all the species of citrate, as the difference between the initial amount of sodium citrate and 1.5 times the initial amount of tetrachloroauric acid. From this residual amount, we can then determine $C_{CtH_2^-}$ if we know the final synthesis pH because the relative amount of each species of citrate (among only the citrate species) depends on the prevailing pH value. The pH variations of the relative mole fractions at equilibrium among the citrate species at 25 and 100 ^{0}C are shown in A and B, respectively, of Figure 4.C.1.

To obtain these diagrams, we considered an aqueous solution containing only sodium citrate and hydrochloric acid. In this system, after the complete dissociation of sodium citrate and hydrochloric acid in water, the only reactions occurring are the speciation reactions in Eqs. (4.2.4) – (4.2.6) and the equilibrium reaction of water in Eq. (4.2.1). As previously illustrated, these reactions occur instantaneously. Since there are no other reactions, for this system the quasi-equilibrium state is the same as the final equilibrium state. By specifying the initial concentrations of sodium citrate and hydrochloric acid, we can then determine the equilibrium amounts of all the reactants including the four citrate species and H^+ ions. In calculating the equilibrium amounts, we write and solve material balance equations for the components with the values of the equilibrium constants at the prevailing temperature of 25 or 100 ^{0}C. From the equilibrium amount of H^+, we can then determine the equilibrium pH of the reaction system. With the concentrations of hydrochloric acid in the range $10^{-4}\ mol/m^3$ to $10^3\ mol/m^3$ for a fixed concentration of $3\ mol/m^3$ sodium citrate in the synthesis solution, we obtained the pH variations of the relative mole fractions at equilibrium among the citrate species at 25 and 100 ^{0}C, as shown in Figure 4.C.1.

The final synthesis pH, itself, is a measure of the final value of C_{OH^-}. Therefore, from the final synthesis pH, we can determine both the final values of $C_{CtH_2^-}$ and C_{OH^-}.

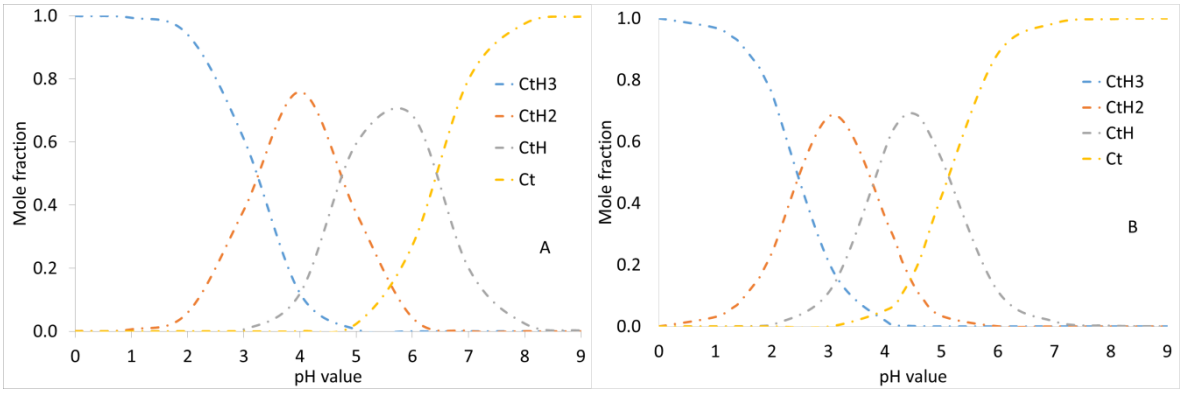

Figure 4.C.1. Relative mole fractions of the citrate species as a function of pH: A. 25 ^{0}C B. 100 ^{0}C.

In their investigation, Ji et al. (2007) reported the value of the pH at the end of the synthesis. As said previously, they investigated the synthesis at 100 ^{0}C. However, the reported pH values were measured at 25 ^{0}C, because most pH meters are not accurate at high temperatures (Barron et al., 2006). Figure 4.C.2 shows how those pH values, indicated as "final equilibrium pH", change with the initial values of the ratio of citrate to precursor. Since the latter are the final equilibrium states at 25 ^{0}C, for comparison, we calculated the pH values at quasi-equilibrium pH at this temperature for the initial ratios of citrate to precursor in the synthesis solution. These pH values at quasi-equilibrium are also indicated in Figure 4.C.2. From this figure, the pH values at quasi-equilibrium are approximately equal to the pH values at final equilibrium for initial molar ratios equal to or greater than five. Similarly, at the synthesis temperature of 100 ^{0}C, we assume that the pH values at quasi-equilibrium are approximately equal to the pH values at final equilibrium for initial molar ratios equal to or greater than five.

Therefore, in Eq. (4.3.26), we can assume that C_{OH^-} remains constant and equal to the quasi-equilibrium value $C_{OH^-,0}$ as the synthesis progresses. Similarly, we can assume that the value of $C_{CtH_2^-}$ does not change significantly with time for values of the initial citrate-to-gold molar ratio equal to or greater than 5, since sodium citrate is in large excess. To show this, using the threshold molar ratio of 5, we apply the stoichiometry of 1.5 of citrate to tetrachloroauric acid reported by Kumar et al. (2007). At quasi-equilibrium, the amount of Ct, representing the sum of all the species of citrate, is five moles for every mole of tetrachloroauric acid present in the reaction solution. At the end of the synthesis, the amount of Ct would be 3.5 moles, whilst that of tetrachloroauric acid would be zero. The final amount of Ct represents 70% of the initial value. This has the same order of magnitude as the initial one. In line with the assumption that the pH value is constant, the relative mole fraction of CtH_2^- is constant. Therefore, the final value of $C_{CtH_2^-}$ is about 70% of the value present at

quasi-equilibrium. This final value has the same order of magnitude as $C_{CtH_2^-,0}$. Hence, to a good approximation, in Eq. (4.3.26) we can replace $C_{CtH_2^-}$ and C_{OH^-} with $C_{CtH_2^-,0}$ and $C_{OH^-,0}$, respectively. Doing so yields Eq. (4.3.27).

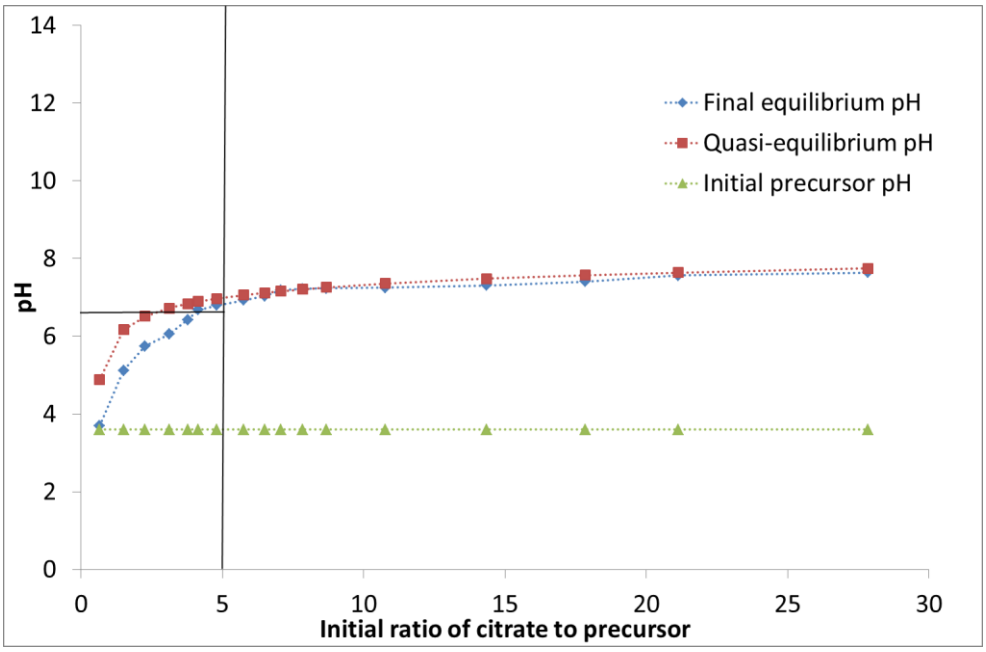

Figure 4.C.2. A comparison of the values of the initial pH of tetrachloroauric acid solution, quasi-equilibrium and final pH of the synthesis mixture at $25\,^0C$ using the data from Ji et al. (2007).

4.D Reduction step calculations

In this section, we illustrate how to calculate the initial reduction rate from the peak absorbance reported by Ji et al. (2007). Then, we employ Eq. (4.3.4) to confirm that CtH_2^-, and not CtH^{2-}, reduces $AuCl_4^-$ in the reduction step.

4.D.1 Peak absorbance as a measure of gold atoms

Figure 2S (b) in the work of Ji et al. shows the time evolution of the peak absorbance of the UV-Vis absorption spectra in the wavelength band between 400 and 800 nm when monitoring the synthesis conducted at a temperature of $100\,^0C$ for a fixed initial value of the concentration of $HAuCl_4$ of $0.25\,mol/m^3$ in the synthesis solution and an initial value of the citrate-to-gold molar ratio spanning the range 0.7-28. Figure 4.D.1 shows the time evolutions of the normalized peaks (of these absorption spectra) and of the normalized UV-Vis absorbance at 400 nm for two values of the citrate-to-gold molar ratio (7.0 and 17.5). We can see that these are nearly identical.

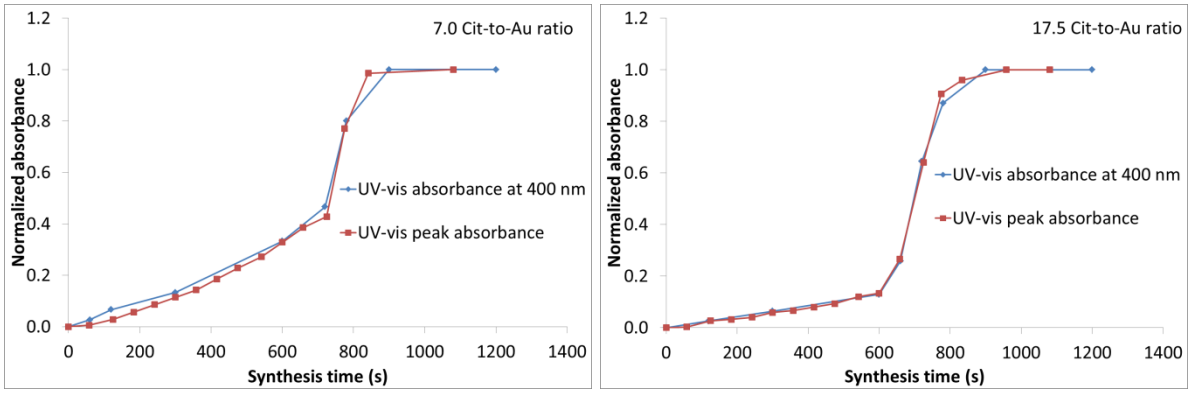

Figure 4.D.1. Time evolution of the peaks (of the UV-Vis absorption spectra in the wavelength band of 400 to 800 nm) and of the UV-Vis absorbance at 400 nm for citrate-to-gold molar ratios of 7.0 and 17.5. The experimental data are taken from Ji et al. (2007).

To show that the peak absorbance relates to the amount of atomic gold present in the solid phase, we consider the (non-normalized) values of the former at the end of the synthesis. These are about unity for all the values of the citrate-to-gold molar ratio investigated. The final mean diameter of the GNPs reported by Ji et al. for these values of the molar ratio varies between a minimum of 13 nm to a maximum of 60 nm. Assuming that the particles are spherical and monodisperse, and that all the gold in the precursor converts into GNPs, we can calculate the number concentration of GNPs at the end of the synthesis as follows:

$$\frac{C_{HAuCl_4}}{\rho m_v {s_f}^3} \tag{4.D.1}$$

where $C_{HAuCl_4} = 0.25\ mol/m^3$, $\rho = 10^5\ mol/m^3$ and $m_v = \pi/6$ for all ratios.

For a final mean diameter s_f of 13 nm, the number concentration is:

$$\frac{0.25\ mol/m^3}{10^5\ mol/m^3 \times \pi/6 \times (13 \times 10^{-9})^3} = 2.17 \times 10^{18}\ GNPs\ per\ m^3$$

For a final mean diameter s_f of 60 nm, the number concentration is:

$$\frac{0.25\ mol/m^3}{10^5\ mol/m^3 \times \pi/6 \times (60 \times 10^{-9})^3} = 2.21 \times 10^{16}\ GNPs\ per\ m^3$$

Thus, the value of the GNP number concentration varies by two orders of magnitude. In contrast, the peak absorbance is almost constant at the value of one. Therefore, the peak absorbance cannot be related to the GNP number concentration. However, for the ratios employed by Ji et al. (2007), assuming complete conversion of the gold in the precursor into GNPs, the final concentration of gold in the particle phase is constant, equal to $0.25\ mol/m^3$,

which is the value of the initial $HAuCl_4$ concentration in the synthesis solution. So, we can relate the final peak absorbance of nearly one to the final concentration of gold of $0.25\ mol/m^3$ in the particle phase, and in general, we can relate the concentration of gold in the particle phase C_{Au} to the peak absorbance P. So, we can write:

$$C_{Au} = bP \tag{4.D.2}$$

where b is a proportionality constant. We obtain its value by relating the final peak absorbance, assumed to be one in Figure 2S (b) of Ji et al. (2007), to the maximum concentration of gold $C_{Au,max}$ in the solution containing the GNPs, which, in the case considered, is equal to $0.25\ mol/m^3$. Therefore, we obtain:

$$b = C_{Au,max} \quad \rightarrow \quad C_{Au} = C_{Au,max}P \tag{4.D.3}$$

4.D.2 Calculation of the initial reduction rate, $r_{r,0}$

Because C_{Au} accounts for the gold from the reduction and growth steps, we consider Figure 2S (b) of Ji et al. (2007) for $t \rightarrow 0$; in this limit, the slope of the function $P(t)$ is related to the reduction step only. Thus, we write:

$$r_{r,0} = dC_{Au}/dt|_0 \tag{4.D.4}$$

where the subscript 0 indicates that the quantity is evaluated in the limit $t \rightarrow 0$. Using Eq. (4.D.3), we then have:

$$r_{r,0} = C_{Au,max}\, dP/dt|_0 \tag{4.D.5}$$

We can calculate $dP/dt|_0$ from the Figure 2S(b) of Ji et al. (2007) by extending the straight line tangent, at time $t = 0$, to each $P(t)$ curve to the final peak absorbance of one and by determining the time $t_{r,0}$ taken to reach this final peak absorbance along the x-axis. Therefore, we have:

$$dP/dt|_0 = 1/t_{r,0} \tag{4.D.6}$$

For the smallest citrate-to-gold molar ratio of 0.7 in the Figure 2S (b) of Ji et al. (2007), where $C_{HAuCl_4,0} = 0.25 \times 10^{-3}\ mol/dm^3$ and $C_{Na_3Ct,0} = 0.175 \times 10^{-3}\ mol/dm^3$ in the synthesis solution, we obtain:

$$dP/dt|_0 = 1/(2.4 \times 60\ s) \quad \rightarrow \quad r_{r,0} = 1.74 \times 10^{-3}\ mol/(m^3.s)$$

We denote the concentrations of precursor and reducing agent in the synthesis solution for $t \rightarrow 0$ as $C_{AuCl_4^-,0}$ and $C_{RA,0}$ (where RA represents the reducing agent, which can be any of the species in which citrate can be present). The values for $t \rightarrow 0$ correspond to those at

quasi-equilibrium, which are obtained when, after mixing the precursor solution with the reducing agent solution, the fast reactions involving the H^+ ions have reached equilibrium, but $AuCl_4^-$ has still not significantly reacted. For the citrate-to-gold molar ratio of 0.7, we have reported the values of $C_{AuCl_4^-,0}$ and $C_{RA,0}$ in Table 4.A.6 of Section 4.A, in which $C_{RA,0}$ is either $C_{CtH_2^-,0}$ or $C_{CtH^{2-},0}$. For $t \to 0$, we write Eq. (4.3.4) as:

$$r_{r,0} = k_r \, C_{AuCl_4^-,0} \, . \left[C_{RA,0}\right]^n \qquad (4.D.7)$$

4.D.3 Test for the reducing agent

Following the procedure above, we obtained the values of $r_{r,0}$, $C_{AuCl_4^-,0}$ and $C_{RA,0}$ for other citrate-to-gold molar ratios. These values are shown in Table 4.D.1.

Table 4.D.1. Initial rates and concentrations for different initial values of citrate-to-gold molar ratio calculated from the data of Ji et al. (2007) at the synthesis temperature $100\,^0C$. The concentrations are at quasi-equilibrium.

Molar Ratio	$r_{r,0}$	$C_{AuCl_4^-,0}$	$C_{CtH_3,0}$	$C_{CtH_2^-,0}$	$C_{CtH^{2-},0}$	$C_{Ct^{3-},0}$
	[mol/(m^{3}s)]	[mol/m^3]				
1.4	3.63E-03	0.25	6.36E-05	1.61E-02	2.06E-01	1.28E-01
2.0	1.59E-03	0.25	1.96E-05	9.40E-03	2.26E-01	2.65E-01
2.8	9.41E-04	0.25	7.50E-06	5.94E-03	2.36E-01	4.58E-01
3.5	6.28E-04	0.25	4.20E-06	4.49E-03	2.40E-01	6.30E-01
4.2	2.76E-04	0.25	2.68E-06	3.61E-03	2.43E-01	8.03E-01
4.9	1.71E-04	0.25	1.86E-06	3.02E-03	2.45E-01	9.77E-01
5.6	9.32E-05	0.25	1.37E-06	2.60E-03	2.47E-01	1.15E+00
6.3	1.10E-04	0.25	1.05E-06	2.28E-03	2.48E-01	1.32E+00
7.0	6.26E-05	0.25	8.34E-07	2.04E-03	2.50E-01	1.50E+00
7.7	6.48E-05	0.25	6.78E-07	1.84E-03	2.51E-01	1.67E+00
8.4	6.34E-05	0.25	5.63E-07	1.68E-03	2.52E-01	1.85E+00
10.5	4.60E-05	0.25	3.52E-07	1.34E-03	2.54E-01	2.37E+00
14.0	3.69E-05	0.25	1.96E-07	1.01E-03	2.58E-01	3.24E+00

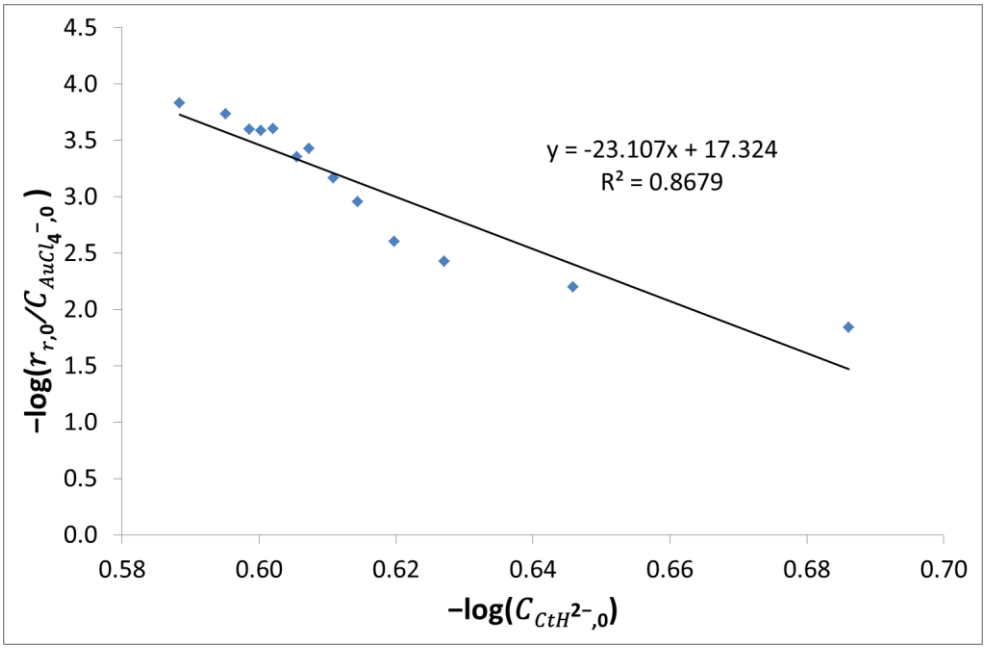

Figure 4.D.2. Plot of Eq. (4.3.6), in which CtH_2^- is replaced by CtH^{2-} as the reducing agent for the reduction step; $y = -\log\left(r_{r,0}/C_{AuCl_4^-,0}\right)$ vs $x = -\log C_{CtH^{2-},0}$.

Table 4.D.1 shows that the rate of the reduction step decreases with increasing initial values of the citrate-to-gold molar ratio. With the values reported in Table 4.D.1, we have produced the diagrams in Figures 4.3.1 (reported in the main contribution) and 4.D.2. The former, which refers to CtH_2^-, shows that as the concentration of CtH_2^- increases, the reduction rate increases, while the opposite trend is observed in Figure 4.D.2, which refers to CtH^{2-}. We expect that the reduction rate should increase with the concentration of reducing agent. Moreover, while the reaction order n results to be 1.85 when CtH_2^- is assumed to be the reducing agent, the reaction order is -23 for CtH^{2-}, a value that appears to be unlikely. In addition, Figure 4.3.1 gives a better correlation for the experimental data. Therefore, we conclude that CtH_2^- is the reducing agent.

4.E Characteristic times' calculations

In this section, we relate the rate constant to the characteristic time for two reactions: 1) a single-phase (i.e., homogeneous) reaction involving two reactants, whose rate is first-order with respect to each reactant, and 2) a fluid-particle surface reaction which leads to particle growth involving two reactants, whose rate is first-order with respect to each reactant and depends on the surface area.

4.E.1 Single-phase reaction

We assume that the single-phase reaction occurs between reactants A and B, where A is the limiting reactant. Since the rate is first-order with respect to each reactant, the consumption rate of component A is given by:

$$\frac{dC_A}{dt} = -k_1 C_A C_B \tag{4.E.1}$$

where k_1 is the reaction rate constant.

We define the characteristic time τ_1 of this reaction as the time that A takes to react significantly. Here “significantly” means that the change in concentration of A has the same order of magnitude as the initial concentration $C_{A,0}$ of A. If we denote as $C_{B,0}$ the initial concentration of B, using Eq. (4.E.1), we can therefore write:

$$\frac{C_{A,0}}{\tau_1} = k_1 C_{A,0} C_{B,0} \quad \rightarrow \quad k_1 = \left(\frac{1}{C_{B,0}}\right)\frac{1}{\tau_1} \tag{4.E.2}$$

If the initial concentrations of reactants A and B are kept constant, we can relate the rate constant to the characteristic time as:

$$k_1 = \frac{b}{\tau_1} \tag{4.E.3}$$

where b is a constant (its value would vary if the value of the initial concentration $C_{B,0}$ changed). Eq. (4.E.3) has been used, as Eq. (4.3.10), in the main contribution.

4.E.2 Surface reaction for particle growth

We assume that the surface reaction for particle growth occurs between reactants P and Q. Since the rate is first-order with respect to each reactant and depends on the surface area, following the same passages shown in Section 4.B to derive Eq. (4.B.4), we can write:

$$\frac{ds}{dt} = k_g \left(\frac{m_a}{3\rho m_v}\right) C_P C_Q \tag{4.E.4}$$

We define the characteristic time τ_g of this process as the time that the particle size takes to increase significantly. Here “significantly" means that the order of magnitude of the particle size change is the same as the order of magnitude of the particle size s_0 taken as reference value. We can thus write Eq. (4.E.4) as:

$$\frac{s_0}{\tau_g} = k_g \left(\frac{m_a}{3\rho m_v}\right) C_{P,0} C_{Q,0} \tag{4.E.5}$$

whence:

$$k_g = \frac{b}{\tau_g} \text{with} \quad b \equiv s_0 \left(\frac{3\rho m_v}{m_a}\right) \frac{1}{C_{P,0} C_{Q,0}} \tag{4.E.6}$$

Here $C_{P,0}$ and $C_{Q,0}$ are reference values for the concentrations of the reactants, which have the same order of magnitude as the reactant concentrations during the particle growth process examined.

In the gold nanoparticles growth process considered in Section 4.3.3, reactants P and Q are $AuCl_3(OH)^-$ and CtH^{2-}, respectively, and their concentrations at the beginning of the growth process are those at the end of the seed formation step. Moreover, the value of s_0 coincides with the size of the seed particles.

In Section 4.3.3, we used Eq. (4.E.6) to obtain the value of k_g. To do so, we considered three syntheses investigated experimentally by Polte et al. (2010), in which the initial concentrations of precursor and reducing agent in the synthesis solutions were $0.25\ mol/m^3$ and $2.50\ mol/m^3$, respectively, while the solution temperatures were 75, 85 and 100 ^{0}C. For these syntheses, we assumed that the parameter b in Eq. (4.E.6) had the same value. This is justified only if in the syntheses the orders of magnitude of $C_{P,0}$, $C_{Q,0}$ and s_0 are the same. This is indeed the case. The experimental data reveal that the size of the seeds does not vary by an order of magnitude. The same is true for the concentration of reducing agent, because CtH^{2-} is in large excess. Therefore, we only need to prove that the concentration of $AuCl_3(OH)^-$ at the beginning of the growth process has the same order of magnitude in all cases. If we denote as $C_{Au,0}$ the initial concentration of precursor in the synthesis (which, as said, is equal to $0.25\ mol/m^3$ for all three syntheses), then a simple mass balance on gold yields:

$$C_{P,0} = \left[1 - \left(\frac{s_s}{s_f}\right)^3\right] C_{Au,0} \tag{4.E.7}$$

where s_s and s_f denote the size of the seed and the final size of the nanoparticles, respectively. Usually, the term $(s_s/s_f)^3$ is far less than unity, but even if its order of magnitude were unity, the orders of magnitude of $C_{Au,0}$ and $C_{P,0}$ would be the same. So, we can indeed regard the parameter b as a constant.

4.F Passivation step calculations

To estimate the value of k_p at the standard synthesis temperature of 100 ^{0}C, we employ the experimental data of Wuithschick et al. (2015), who (when investigating the synthesis at $100\,^0C$ with $0.25\ mol/m^3$ and $2.5\ mol/m^3$ as the initial concentrations of tetrachloroauric acid and sodium citrate, respectively, in the synthesis solution) reported that about 1.3 mol% of

the precursor converted to gold atoms and then seed particles, while the residual precursor grew the latter. From this conversion, we can determine the selectivity S of the reduction step over the passivation step, defined as the ratio of the amount of precursor that forms gold atoms in the reduction step to the amount of precursor that becomes passivated, as $1.3\,\%/98.7\,\% = 1.32 \times 10^{-2}$. From Eq. (4.3.27) in the main contribution, the selectivity S is defined as follows:

$$S = \frac{k_r}{k_p} \frac{\left[C_{CtH_2^-,0}\right]^{1.85}}{\left[C_{OH^-,0}\right]} \tag{4.F.1}$$

Rearranging, we have:

$$k_p = \frac{k_r}{S} \frac{\left[C_{CtH_2^-,0}\right]^{1.85}}{\left[C_{OH^-,0}\right]} \tag{4.F.2}$$

As the synthesis temperature is $100\,^0C$, k_r is equal to $35.48\,[m^3/mol]^{1.85}\,1/s$. Following the procedure described in Section 4A, we find that $C_{CtH_2^-,0}$ and $C_{OH^-,0}$ are equal to $1.4 \times 10^{-3}\,mol/m^3$ and $7.44 \times 10^{-3}\,mol/m^3$ for the synthesis condition that yielded 1.32×10^{-2} as the value of the selectivity S. Thus:

$$k_p = \frac{35.48\,[m^3/mol]^{1.85}\,1/s}{1.32 \times 10^{-2}} \frac{[1.4 \times 10^{-3}\,mol/m^3]^{1.85}}{[7.44 \times 10^{-3}\,mol/m^3]} = 1.9\,m^3/(mol.s)$$

Appendix F

In this appendix, we present two calculations using Eq. (5.2.5). First, we present a simple case calculation and then we use the equation in the citrate synthesis method.

This equation yields the thickness of the electric double layer. To understand the concept of the electric double layer, let us assume a charged surface is immersed in a solution containing ions. This charged surface attracts oppositely charged ions, which surround the surface and form a layer of ions around it, called layer 1. Because of the attraction, there is no relative motion between the surface and layer 1. While the charged surface is all covered by the oppositely charged ions, layer 1 is exposed on one side to the solution environment and can also attract oppositely charged ions, called layer 2, which would be of the same sign as the charged surface. However, the attraction of layer 1 for layer 2 is weak because of the existing attraction between it and the charged surface. Consequently, layer 2 of ions continues to attach and detach from layer 1. Hence, layer 2 is called the diffuse layer and (the order of magnitude of) the distance between the surface and layer 2 is called the electric double layer thickness. To determine this thickness, researchers employ the Debye's length $1/\kappa$, which is expressed in Eq. (5.2.5) as:

$$1/\kappa = \left[\frac{\epsilon_0 \epsilon_c k_B T}{\sum_i (p_i e^2 z_i{}^2)}\right]^{1/2} \qquad \text{(F.1)}$$

where ϵ_0 is the permittivity of free space, whose value is $8.85 \times 10^{-12}\, F/m$; ϵ_c is the dielectric constant of the solution; e is the charge on an electron, whose value is $1.6 \times 10^{-19} C$; p_i is the number concentration of the i-th ion present in the solution measured in $1/m^3$; and z_i is the charge on the i-th ion. As indicated, this length only depends on the condition in the bulk solution, but not on the condition of the surface (Israelachvili, 2011).

A simple case: In this case, we consider an aqueous solution containing 100 mM of sodium chloride and some bio-colloidal particles at $25\,^0C$. We assume the solution to be mainly water with $\epsilon_c = 78.54$ at $T = 298\, K$. For each of Na^+ and Cl^-, $z_i{}^2 = 1$. Thus:

$$1/\kappa = \left[\frac{\epsilon_0 \epsilon_c k_B T}{\sum_i (p_i e^2 z_i{}^2)}\right]^{1/2} = \left[\frac{8.85\times10^{-12} F/m \times 78.54 \times 1.38\times10^{-23}\, J/K \times 298\, K}{[(100\times10^{-3}\times10^3 mol/m^3 \times 6.02\times10^{23}) \times (1.6\times10^{-19} C)^2 \times (1)] \times 2}\right]^{1/2}$$

$$= \left[\frac{2.86\times10^{-30}}{3.08\times10^{-12}}\right]^{1/2} = [9.27 \times 10^{-19}]^{1/2} = 0.96\, nm$$

For this condition in this simple case, Israelachvili (2011) reported a value of $0.95\, nm$ as $1/\kappa$.

The citrate method, on the other hand, presents a complex case with a number of problems. There are many ions in solution, some monovalent such as H^+, OH^-, some divalent such as

CtH^{2-} and some trivalent such as Ct^{3-}. Further, we need to know which ions preferentially attach on the particles, which are called the potential determining ions (PDIs). To overcome these problems, Briggs et al. (1993) assumed the PDIs to be Ct^{3-} and CtH^{2-}. This assumption is consistent with the fact that citrate ions, and in particular Ct^{3-}, provide the electrostatic stabilization for GNPs (Kumar et al., 2007). Thus, we assume Ct^{3-} and CtH^{2-} preferentially attach on the particles. Further, Briggs et al. reported certain values of $1/\kappa$ on a $300\ nm$ gold sphere for different concentrations of sodium citrate, where the citrate species are assumed to be 75% Ct^{3-} and 25% CtH^{2-}. These concentrations of sodium citrate are 6×10^{-6}, 1×10^{-4} and $3 \times 10^{-4}\ mol/dm^3$, yielding 58.8, 15.3, and $8.9\ nm$, respectively, as the values of $1/\kappa$. Using Eq. (E.1) and the assumed composition of 75% Ct^{3-} and 25% CtH^{2-}, we obtained 53.6, 13.1, and $6.9\ nm$, respectively, as the values of $1/\kappa$. The values we obtained are similar to the values reported by Briggs et al. Thus, in Eq. (E.1), we use only the amounts of Ct^{3-} and CtH^{2-} in determining $1/\kappa$.

Appendix G

In this appendix, we derive an approximate expression for Eq. (5.2.3). In this equation, x ranges from $(s + s')/2$ to ∞. In a reactor mixture, V is finite. Thus, for a colloidal system of finite volume, the maximum value of x is finite. To determine the order of magnitude of this distance, we present a sample calculation as follows.

Israelachvili (2011) reported the expression for E_T around a particle (a vesicle) in interaction with another vesicle as:

$$E_T(r) = \frac{s}{4} Z \exp(-\kappa x) - \frac{As}{24x} \qquad \text{(G.1)}$$

where $Z = 9.38 \times 10^{-11} \tanh^2(\varphi_s/107)$ and $A = 10^{-20} J$. φ_s is the surface potential, given as $24.5\, mV$. Similarly, $1/\kappa$ is taken as $0.95\, nm$ and $s = 200\, nm$. Figure G.1 shows the results of how E_T varies with x (this profile is similar to the profile in Elimelech et al. (1995) and Hunter (1995)). From this figure, the upper limit of x in Eq. (5.2.3) is smaller than $8\, nm$. Thus, x is finite as previously stated. Also in this figure, the maximum value $E_{agg} = 1.03 \times 10^{-19}\, J$.

Then, we solve Eq. (5.2.3) numerically.

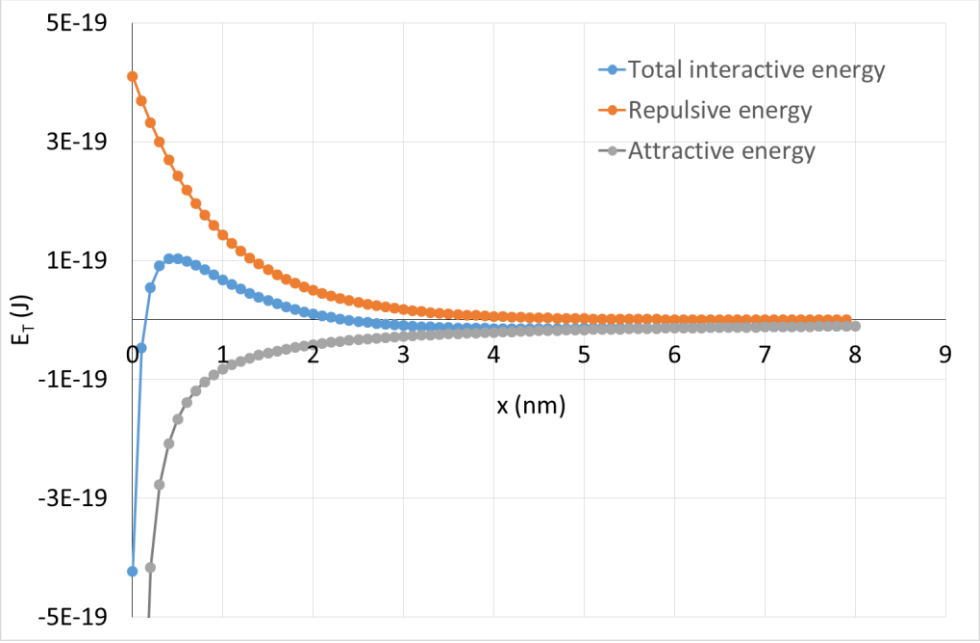

Figure G.1: The calculated profile of $E_T(x)$ using an experimental problem from Israelachvili (2011)

In this example, $T = 310\, K$ (Israelachvili, 2011) and taking $k_B = 1.38 \times 10^{-23}\, J/K$, we calculate E_T/k_BT and integrate the expression $\int_0^{x=8\, nm} \exp[E_T/k_BT]/x^2\, dx$ as Figure G.1

reveals. We solved the expression numerically from $x = 0.1\,nm$ to $8\,nm$. Table G.1 shows the numerical data. From the numerical data, we observed that only the positive values of E_T contribute to the stability factor of the particle. More importantly, while $\int_0^8 \exp[E_T/k_BT]/x^2\,dx = 4.16 \times 10^{20}\,1/m$, $\kappa \exp\left[E_{agg}/k_BT\right] = 6.33 \times 10^{20}\,1/m$. These values are quite close. Therefore, instead of the integral function in Eq. (5.2.3), we can write the equation approximately as:

$$W(\bar{s},\hat{s}) = \frac{\kappa(\bar{s}+\hat{s})}{2}\exp\left[E_{agg}(\bar{s},\hat{s})\Big/k_BT\right] \qquad \text{(G.2)}$$

Table G.1: The numerical data for the experimental problem of Israelachvili (2011)

x (nm)	$E_T/(k_b*T)$	$z=\exp(E_T/(k_b*T))$	z/x^2 (1/m^2)
0.1	-110.9855377	6.30367E-49	6.30367E-29
0.2	-12.45732933	3.88911E-06	9.72278E+13
0.3	14.2944542	1614368.152	1.79374E+25
0.4	23.80017357	21691223526	1.3557E+29
0.5	26.89079374	4.77005E+11	1.90802E+30
0.6	27.12190849	6.01029E+11	1.66952E+30
0.7	25.97636155	1.91157E+11	3.90117E+29
0.8	24.16427519	31218452655	4.87788E+28
0.9	22.0559014	3791021717	4.68027E+27
1.0	19.8543718	419415150.9	4.19415E+26
1.1	17.67390712	47389304.75	3.91647E+25
1.2	15.57866886	5830823.828	4.04918E+24
1.3	13.60347341	808934.6435	4.7866E+23
1.4	11.76546029	128728.433	6.56778E+22
1.5	10.07095463	23646.12738	1.05094E+22
1.6	8.519641937	5012.258729	1.95791E+21
1.7	7.107174884	1220.694067	4.22385E+20
1.8	5.82683264	339.2823461	1.04717E+20
1.9	4.670590805	106.7607986	2.95736E+19
2.0	3.62981584	37.70587208	9.42647E+18
2.1	2.695715505	14.81611597	3.35966E+18
2.2	1.859628286	6.421349425	1.32673E+18
2.3	1.113205334	3.04410013	5.75444E+17
2.4	0.448520058	1.565992891	2.71874E+17
2.5	-0.141871129	0.867733075	1.38837E+17
2.6	-0.664901057	0.514324414	7.60835E+16
2.7	-1.12698617	0.324008292	4.44456E+16
2.8	-1.534035525	0.215663593	2.75081E+16
2.9	-1.891469246	0.15085001	1.7937E+16
3.0	-2.204242802	0.110334038	1.22593E+16
3.1	-2.476874605	0.084005366	8.74145E+15

$$dx = 1 \times 10^{-10}$$

$$\sum(z/x^2) = 4.16 \times 10^{30}$$

$$dx \sum(z/x^2) = 4.16 \times 10^{20}$$

$$[z]_{max} * \kappa = 6.33 \times 10^{20}$$

3.2	-2.713475187	0.06630598	6.47519E+15
3.3	-2.917776748	0.054053729	4.96361E+15
3.4	-3.093162277	0.045358292	3.92373E+15
3.5	-3.242693692	0.039058542	3.18845E+15
3.6	-3.369138675	0.034419271	2.65581E+15
3.7	-3.474995984	0.030961958	2.26165E+15
3.8	-3.562519147	0.028367273	1.96449E+15
3.9	-3.633738499	0.026417239	1.73683E+15
4.0	-3.690481577	0.024959979	1.56E+15
4.1	-3.734391921	0.023887692	1.42104E+15
4.2	-3.766946336	0.023122564	1.3108E+15
4.3	-3.789470715	0.022607565	1.22269E+15
4.4	-3.803154492	0.022300315	1.15188E+15
4.5	-3.809063824	0.022168923	1.09476E+15
4.6	-3.808153595	0.022189111	1.04863E+15
4.7	-3.801278328	0.022342193	1.01142E+15
4.8	-3.789202088	0.022613638	9.81495E+14
4.9	-3.77260747	0.022992034	9.57602E+14
5.0	-3.752103732	0.023468323	9.38733E+14
5.1	-3.728234164	0.024035241	9.24077E+14
5.2	-3.70148275	0.024686895	9.12977E+14
5.3	-3.672280183	0.025418445	9.04893E+14
5.4	-3.641009305	0.026225861	8.99378E+14
5.5	-3.60801001	0.027105733	8.96057E+14
5.6	-3.573583669	0.028055133	8.94615E+14
5.7	-3.537997119	0.029071496	8.94783E+14
5.8	-3.501486256	0.030152536	8.9633E+14
5.9	-3.464259272	0.031296179	8.99057E+14
6.0	-3.426499565	0.032500508	9.02792E+14
6.1	-3.388368363	0.033763722	9.07383E+14
6.2	-3.35000708	0.035084106	9.12698E+14
6.3	-3.311539434	0.036460003	9.18619E+14
6.4	-3.273073347	0.037889799	9.25044E+14
6.5	-3.234702663	0.03937191	9.3188E+14
6.6	-3.196508675	0.040904767	9.39044E+14
6.7	-3.158561507	0.042486814	9.46465E+14
6.8	-3.120921345	0.044116503	9.54077E+14
6.9	-3.083639551	0.04579229	9.61821E+14
7.0	-3.046759651	0.047512633	9.69646E+14
7.1	-3.010318225	0.049275995	9.77504E+14
7.2	-2.974345705	0.051080845	9.85356E+14
7.3	-2.938867085	0.052925655	9.93163E+14
7.4	-2.903902561	0.054808907	1.00089E+15
7.5	-2.869468099	0.056729093	1.00852E+15
7.6	-2.835575944	0.058684717	1.01601E+15
7.7	-2.802235075	0.060674299	1.02335E+15

7.8	-2.769451612	0.062696377	1.03051E+15
7.9	-2.737229173	0.064749508	1.03749E+15
8.0	-2.705569201	0.066832272	1.04425E+15

Nomenclature

Symbol	Meaning	Units
Roman alphabets		
A	Particle surface area per unit volume of solution	m^2/m^3
A_H	Hamaker constant	J
A_s	Seed correlation parameter	–
B_s	Seed correlation parameter	nm
b	Proportionality constant	–
$B(v)$	Birth aggregation rate	$1/(dm^3.cm^3.s)$
B_r	Pre-exponential constant for repulsion energy	J
c, C	Concentration	mol/m^3
C_T	gold (III) chloride	mol/m^3
C_C	Citrate	mol/m^3
C_D	Acetone	mol/m^3
C_M	aurous chloride	mol/m^3
C_S	Dicarboxy acetone	mol/m^3
C_P	Other products	mol/m^3
C	All the four species of citrate	–
C_T, $C_{AuCl_4^-}$	Concentration of tetrachloroauric ion	mol/m^3
C_{Ct}	Concentration of all citrate species	mol/m^3
C_{H^+}	Concentration of H^+ ions	mol/m^3
C_{OH^-}	Concentration of OH^- ions	mol/m^3
C_{Au}	Concentration of gold in the particle phase	mol/m^3

$C_{Au,max}$	Maximum concentration of gold in the particle phase	mol/m^3
C_{RA}	Concentration of the reducing agent, which can be any of the species of citrates	mol/m^3
C_{Pr1}	Concentration of all other products from the reduction step, lumped together	mol/m^3
C_{Pr2}	Concentration of all other products from the growth step, lumped together	mol/m^3
D_{im}	diffusion coefficient for component i in the mixture	m^2/s
D_{ij}	the binary diffusion coefficient of component i relative to component j	m^2/s
D_0	Diffusion coefficient of solute	m^2/s
$D(v)$	Death aggregation rate	$1/(dm^3.cm^3.s)$
D_s	Seed correlation parameter	–
D_z	Stability gradient correlation parameter	–
e	The charge on an electron, whose value	C
E_A	Energy due to the Van der Waal's force of attraction	J
E_R	Energy due to the charge repulsion	J
E_T	the sum of the particles' interaction energy due to the Van der Waal's force of attraction and that due the charge repulsion	J
E_{agg}	the energy barrier to particle aggregation	J
E_{max}	The maximum particles' interactive energy attainable	J
E_a	Activation energy	J/mol

f_a	Fraction of surface occupied by gold species	–
$f(s)$	number of particles per particle-length per total volume of fluid-particle mixture	$1/(m^3.m)$
$f_n(s, \boldsymbol{u}, \boldsymbol{x}, t)$ or $f_n(\boldsymbol{\psi}, t)$	number density function	Depends on the application
$\boldsymbol{F}$	Force	N
F_z	Stability gradient correlation parameter	–
G_s	linear growth rate	m/s
$\langle G_s \rangle$	Average linear growth rate conditioned on s	m/s
$\langle G_s \rangle_{av}$	Average linear growth rate conditioned on s and $\boldsymbol{x}$	m/s
G_v	volume-growth rate	m^3/s
H_N	Nucleation rate	$1/(m^3.m.s)$
$\boldsymbol{J}_i$	Diffusive flux of component i	$mol/(m^2.s)$
$\bar{\boldsymbol{J}}_{\boldsymbol{i}}$	Total molar flux of component i	$mol/(m^2.s)$
k_c	Rate constant for the reaction between citrate and auric acid	$m^3/(mol.s)$
k_d	Rate constant for the reduction with acetone	$m^3/(mol.s)$
k_{MT}	Mass transfer coefficient	m/s
k_{SI}	Surface integration coefficient	$Depends\ on\ application$
k_n	Rate constant for the nucleation step	$(m^3)^4/(mol^5.s)$
k_s	Rate constant for the degradation of dicarboxy acetone	$1/s$
k_h	Rate constant for the growth step	m/s
k_0	Pre-exponential factor	$Depends\ on\ application$

k_r	Rate constant for the reduction step	$[m^3/mol]^{1.85}\,1/s$
k_p	Rate constant for the passivation step	$m^3/(mol.s)$
k_g	Rate constant for the growth step	$m^4/(mol.s)$
$K_{a,w}$	Dissociation constant of water	–
K_{Ri}'s	Equilibrium constants of the speciation of citrate	–
K_{Pi}'s	Equilibrium constants of the speciation of the precursor	–
K_B	Boltzmann constant	J/K
l	Reaction order of the precursor in the reduction step	–
m_i	Mass of species i	kg
m_a	Particles area shape factor	–
m_v	Particles volume shape factor	–
n	Reaction order of the reducing agent in the reduction step	–
N_0	Number of nuclei formed in the model developed by Kumar et al. per unit reactor volume	$1/m^3$
N_P	final number of GNPs per unit reactor volume	$1/m^3$
N_{av}	$Avogadro's\ number = 6.02e23$	–
$n(s,\boldsymbol{x})$	Number of particle per unit size space per unit physical space	$1/(m.m^3)$
P	Peak absorbance	–
$Pr1$	by-products of the reduction step, lumped together	–
$Pr2$	by-products of the growth step, lumped together	–

$P(v)$	number of particles per particle-volume per total volume of fluid-particle mixture	$1/(dm^3.cm^3)$
P_r	Osmotic pressure	N/m^2
p_i	The number concentration of an ion in the bulk of the solution	$1/m^3$
P_z	Stability gradient correlation parameter	–
q_1, q_2	Point charges	C
$q(v, v')$	Aggregation kernel	m^3/s
Q_s	Seed correlation parameter	nm
r_r	Rate of the reduction step	$mol/(m^3.s)$
r_p	Rate of the passivation step	$mol/(m^3.s)$
r_g	Rate of the growth step	$mol/(m^3.s)$
r_m	Particle mean radius	$mol/(m^3.s)$
r_a	Aggregate mean radius	$mol/(m^3.s)$
r	Particle radius	m
R	Universal gas constant	$8.31 J/(mol.K)$
R^a	Citrate-to-gold ratio	–
Re	Reynold's number	–
s	Size	m
s_0	Nucleus diameter ($2\ nm$ in the model of Kumar et al. and size of gold atom i.e. $0.272\ nm$ in the aggregation model)	m
s_s	Seed diameter	m
s_m	Mean diameter with time	m
s_f	Final mean diameter	m
S	Selectivity of the reduction step over the passivation step	–
$\hat{S}$	Supersaturation	–

$\boldsymbol{S}$	physical control surface	m^2
Sc	Schmidt's number	–
Sh	Sherwood's number	–
t	Time	s
$t_{r,0}$	Time taken to reach the final peak absorbance along the x-axis	s
t_s	Synthesis time	s
T	Temperature	K
$\boldsymbol{u_f}$	Fluid velocity	m/s
V	volume of synthesis solution	m^3
V_m	Molar volume of solute	m^3/mol
W	Stability factor	–
$\widetilde{\omega}_A(\bar{s},\hat{s},t)$	Aggregation kernel	m^3/s
$\boldsymbol{x}$	Position vector	m
x	relative mole fraction of CtH_2^- at the quasi-equilibrium pH	–
y_i	mole fraction of component i.	–
y_x	relative mole fraction of CtH_2^- at the quasi-equilibrium pH	–
y_y	relative mole fraction of CtH^{2-} at the quasi-equilibrium pH	–
Y_i	Molar mass of species i	kg/mol
z_i	The charge on the ion	C
Z	The numerator of the stability gradient	J

Greek alphabets

δ	The thickness of the boundary layer	m
ϵ_0	The permittivity of free space	F/m

ϵ_c	The dielectric constant of the solution	$-$
κ	the Debye-Huckel parameter	$1/m$
μ	Fluid viscosity	$kg/(m.s)$
ρ	Molar density of gold	mol/m^3
ρ_f	Fluid density	mol/m^3
ρ_e	Electron densities	$1/m^3$
ρ_x	counterion density profile	$1/m^3$
$\pi_N(s\|\boldsymbol{x},t)$	Probability density function	$1/m$
λ	Chemical potential	J
φ	Surface charge potential	mV
ψ_x	Electrostatic charge potential	V
τ	Characteristic time	s
τ_p	Reaction time for the passivation	s
τ_g	Time for the growth step only in the citrate method	s
γ_s	the interfacial surface energy for the cluster	J/m^2

Glossary

Keyword	Meaning
Aggregation	This is the coalescence of two or more smaller particles to form a bigger particle.
Aggregation frequency	This is the number of collisions per unit time.
Aggregation kernel	This is the volume of successful particles aggregating per unit time.
Auric ion	Gold in +3 oxidation state: Au^{3+}
Aurous ion	Gold in +1 oxidation state: Au^{+}
Classical nucleation theory	This postulates that nucleation only occurs in a supersaturated solution when statistical fluctuation brings a number of monomers together required to form thermodynamically stable clusters, called nuclei.
Colloidal system	An aqueous system containing surfactants and/or nanoparticles not seen by unaided eye and undergoing Brownian motion.
The Gaussian distribution	This is otherwise known as the normal distribution.
Growth	This is the addition of an atom or a monomer into the characteristic arrangement of a particle.
Intra-particle ripening	This is the rearrangement of the monomers in a single particle, changing the shape of the particle from one form to another, for example, a nanowire becoming a nanosphere.
Nanoparticles	These are particles with sizes in the range 1 – 100 nm.

Nanotechnology	The synthesis, modification and application of nanoparticles.
Nucleation	This is the generation of the smallest particles from the aqueous phase.
Nucleation-aggregation-growth mechanism	This is the evolution of particles in the order of nucleation, aggregation and growth.
Number density function	This is the number of particles per unit phase-space volume, where phase space is the abstract space given by the union of size, velocity and physical spaces.
Reducing agent solution	Aqueous solution of sodium citrate
Particle size distribution	This is the list of values or a mathematical function that defines the relative amount, by number or mass, of particles present according to size.
Parsival	The numerical code employed in solving population balance equations.
pH	A measure of the concentration of H^+ ions.
Polydentate	This relates to the shape of a structure with a teeth-like grip.
Polydispersity	Also known as the coefficient of variation – the ratio of standard deviation to the mean size – of the particle size distribution
Population balance equation	An equation describing the number density function or in particle the particle size distribution evolve with time under the influence of processes such as nucleation, growth, aggregation and/or breakage.
Precursor solution	tetrachloroauric acid solution
Quasi-equilibrium	A temporary equilibrium state reached in the citrate synthesis method after fast reactions

	(involving H^+) have completed, but before other synthesis reactions begin to occur significantly.
Sodium citrate	This is a compound with the chemical expression: $[(COONaCH_2)_2C(OH)COONa]$ or simply Na_3Ct.
Seed-mediated mechanism	A description of the formation of gold nanoparticles in the citrate synthesis method, where gold atoms form and aggregate into seed particles before growing to the final particle size, as proposed by Wuithschick et al. (2015).
Solubility	The maximum amount of solute, at a particular temperature and pressure, that can dissolve in a solvent and form a homogeneous solution
Species of hydroxylation of tetrachloroauric ions	These are $AuCl_4^-$, $AuCl_3(OH)^-$, $AuCl_2(OH)_2^-$, $AuCl(OH)_3^-$ and $Au(OH)_4^-$
Species of citrate	These are Ct^{3-}, CtH^{2-}, CtH_2^-, and CtH_3
Stability factor	This is the number that accounts for stabilization by electrostatic repulsion.
Surfactant	A long macromolecule with a characteristic head and tail.
Synthesis mechanism	This is the description of how GNPs form in the citrate synthesis method.
Synthesis solution	A mixture of the precursor solution and reducing agent solution.
Tetrachloroauric acid	This is a compound with the chemical expression: $HAuCl_4$
Turkevich organizer theory	A nucleation-growth mechanism of formation of gold nanoparticle in the citrate synthesis,

	where dicarboxy acetone organises aurous ions in the nucleation step, as proposed by Turkevich et al. (1951)